Alma Mater Studiorum – Università di Bologna

DOTTORATO DI RICERCA IN

Chimica

Ciclo XXVII

Settore Concorsuale di afferenza: 03/B1

Settore Scientifico disciplinare: CHIM 03

BIOMINERALIZATION IN CALCIFYING MARINE ORGANISMS

Presentata da: **Michela Reggi**

Coordinatore Dottorato

Aldo Roda

Relatore

Prof. Giuseppe Falini

Correlatore

Prof. Stefano Goffredo

Esame finale anno 2015

The activities of the three years of Doctorate in Chemistry was aimed to the study of the biomineralization process in marine organisms, playing a particular attention to their response to environmental stress, pH and temperature, associated to the human activities.

The most studied family of organisms was Mediterranean and Read Sea corals, being the PhD project received funding from the European Research Council [249930] (www.coralwarm.eu). The main goals obtained from the research on corals included: (i) the discovery of the species specific role of the intra-crystalline organic matrix molecules in the precipitation of calcium carbonate; (ii) the definition of the role of magnesium ions in the control of the macromolecules assembly/aggregation and in the consequent calcium carbonate polymorphic selectivity; (iii) the discovery that in corals the biomineralization process is not affected by the sea water acidity, as consequence corals are able to construct their skeletons independently from the environmental conditions as far they survive. Michela Reggi has also carried our research on biogenic vaterite, on the shell of *Abalone rufescens* and on the synthesis of biomineralization inspired materials.

She spent six months at the Rudjer Boskovic Institute (Zagreb, Croatia) to carry out experiments on the kinetics of calcium carbonate deposition in the presence of coral organic matrix macromolecules.

During the period of the thesis the candidate has demonstrated reliability, availability, accuracy in work laboratory and ability to self-employment. She has demonstrated the ability to effectively apply new methods of research The work carried out by Michela Reggi has so far resulted in eight articles published in international journals refereed, one of them in Nature Climate Change. Other manuscripts are in an advanced stage of preparation and will soon sent to international journals. She also attended at several national and international conferences and in two of them gave an oral presentation.

She has also regularly shown her work through oral presentations in meetings with the other partners of the ERC project throughout the three-year period.

In conclusion the tutor evaluate the PhD activity of Michela Reggi as excellent.

The Board expresses a score of excellence on the activity carried out by the candidate during the whole cycle of doctorate and considers her worthy to attain the PhD in Chemistry

INDEX

1. INTRODUCTION

Biomineralization is widespread in the biosphere (more than 60 different minerals are produced by 55 phyla, from bacteria to humans), and refers to the process by which organisms form minerals.[1, 2] The organism selectively extracts certain elements from the surrounding environment and incorporates them into functional structures under strict biological control,[3] the obtained biominerals are composite materials, particularly complex, formed both from a mineral phase and an organic matrix with a specific hierarchical structure, which spans from the Ångstrom to the centimetres level. The organic matrix gives softness and elasticity, while the mineral phase gives a considerable hardness. For this reason biominerals have unique properties and high versatility. Most organisms contain only one type of mineral phase; in some cases there are two or more different minerals, located in different areas.[4] Biomineralization offers an organism structural support and mechanical strength but also is involved in a wide variety of important biological functions such as: protection, motion, cutting and grinding, buoyancy, storage, optical detection, magnetic and gravity sensing.[3] Biologically produced minerals are also a reservoir of information about the past. Chemical analyses of fossil shells proxies of the temperature of the sea water thousands of years ago.[5, 6] Is necessary involve a lot of scientists, expert in different disciplines, to understand this complex interdisciplinary field that is the biomineralization.[1]

1.1 Calcium carbonate polymorphism

Calcium carbonates ($CaCO_3$) are the most abundant among the biogenic minerals, both in terms of quantity produced both in terms of diffusion between the taxa.[1] $CaCO_3$ is one of the first biomineral produced in the past, since around 600 million years ago.[7] According to the early ocean chemistry, organisms selected the most easily available ions to produced skeleton building materials of $CaCO_3$; also now in the oceans carbonates are more abundant than the other biominerals[8] and are important for the global carbon cycle.[9] $CaCO_3$ present six different structural forms referred to as calcite, aragonite, vaterite, monohydrate, hexahydrate and amorphous calcium carbonate (ACC).[10] Calcite and aragonite are the most common form of $CaCO_3$ crystals in nature because are more stable than the other polymorphs. There is also another anhydrous form, vaterite, but is rare in nature because of is low stability in solution where spontaneously becomes calcite or aragonite.[3, 11] The other two crystalline forms are monohydrate $CaCO_3$, produced by a limited number of organisms, and hexahydrate $CaCO_3$, of which is not present in the biological world.[12] Recently, it has been discovered that there are two different forms of ACC in biological systems: one more hydrated and the other one anhydrous.[13] During the crystallization process, after an increase of temperature, the ACC undergoes a decrease in the content of water and is subsequently transformed into calcite or aragonite.[14]

Aragonite and calcite have a crystal structure very similar, consisting of alternating layers of Ca^{2+} and CO_3^{2-} perpendicular *c* axis (in the *ab* plane). Calcium ions take up the same position in both polymorphs, unlike the carbonate ions. In the aragonite these are raised in the direction of the *c* axis and form two separate layers, in which the orientation of the ions is different (Fig. 1.1).[15] This structural difference give different properties at the two forms. Aragonite is more thick (2.95 g/mm^3) than calcite (2.71 g/mm^3) and its crystal systems are orthorhombic and growth more along *c* axes acquiring a needle-like shape. Calcite is more stable and its crystal systems is rhombohedral. In biological systems, both forms have a structural and defensive functions (i.e. shells, skeletons, etc)[1] and the kind of polymorphs produced by organism is always under genetic control.[16] Aragonite usually set up spherulitic architecture with high superficial area and porosity, while calcite set up more large crystals but more brittle.[16]

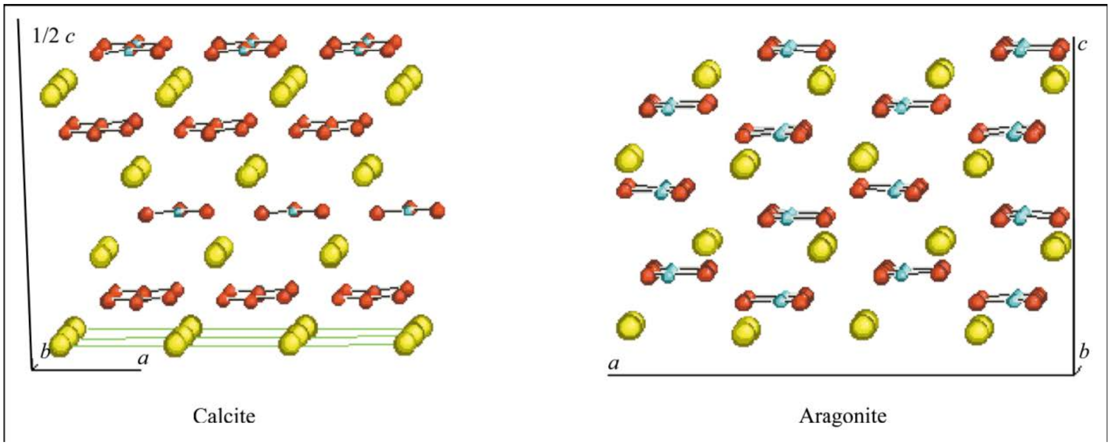

Figure 1.1: Schematic representation of the crystal structure of calcite and aragonite. It is possible observe the distribution of calcium ions planes (yellow) and carbonates ions planes (red carbonate ions, blue oxygen ions).[15]

1.2 Role of magnesium on the precipitation of calcium carbonate

Magnesium, is very important biologically, with proper Ca/Mg balance being crucial to electrolyte balance, cardiac and neurological function, membrane transport, and photosynthesis.[17] Magnesium ions (Mg^{2+}) modify the $CaCO_3$ polymorphism and growth.[18] For this reason, it is very important the ratio between Mg^{2+} and Ca^{2+} concentrations in the seawater, that at present is equal 5. Changing of this ratio may have led the observed polymorphic transitions in carbonate materials in the geologic past.[19, 20]

Magnesium ions inhibit calcite growth. Because of their minor ionic radius with respect to Ca^{2+}, Mg^{2+} can be absorbed on the surface of calcite crystalline nuclei changing crystalline structure, inhibiting the growth and, thus, decreasing the enthalpic contribution on calcite precipitation.[20-23] This inhibition cause an increase of supersaturation and the precipitation of aragonite. Aragonite can't be affected by Mg^{2+} because is more dense. For this reason aragonite tends to precipitate first from seawater, even if its supersaturation is lower respect to calcite.[24]

Mg^{2+} can also promote the precipitation of ACC. Loste *et al.*[10] found that Mg^{2+} could defer ACC transformation into a crystalline phase, and that this effect was intensified with the amount of magnesium.[3, 10] It was demonstrated that the Mg–O bond length in the ACC structure is shorter than the one measured in the other anhydrous polymorphs, but is comparable to those of the hydrated phases. This shortening and the distortion it imposes on the $CaCO_3$ host mineral are important factors in the stabilization of the amorphous structure.[25]

For the above reasons, low values in solution of Mg^{2+} allow the nucleation of calcite and its growth following the classical ion-by-ion addition process.[20, 23, 26, 27] As the magnesium concentration increases, calcite tends to incorporate an increasing number of Mg^{2+} in its structure, which leads to a decrease in the growth of the polymorph. The inhibition of the calcite growth start when the Mg^{2+}/Ca^{2+} ratio is between 1 and 2. On the contrary, when the Mg^{2+}/Ca^{2+} ratio is higher than 2, aragonite precipitation is favoured, and when it is higher than 4, also ACC precipitation can occur.[15, 20, 23, 24, 27, 28] The precipitation of ACC depends also by a rapid increase in carbonate ion concentration (Fig. 1.2).[24]

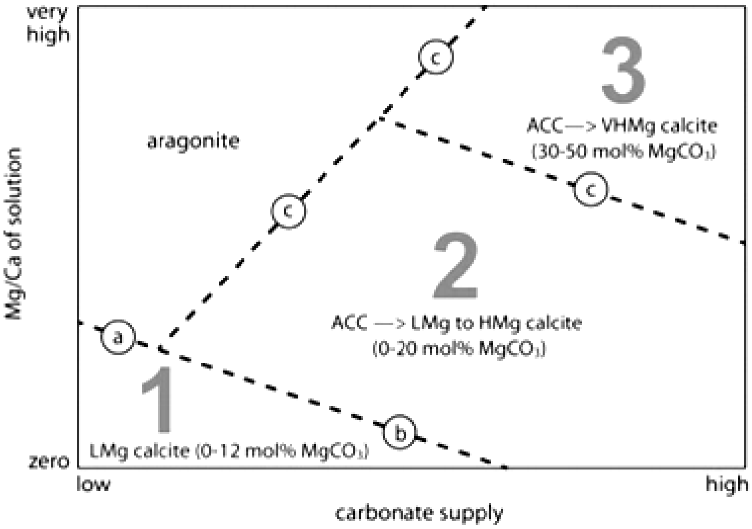

Figure 1.2: Conceptual model for how the interplay of Mg : Ca ratio and carbonate supply bias pathways to $CaCO_3$ mineralization. LMg calcite=low Mg calcite; HMg calcite=high Mg calcite; VHMg calcite=vary high Mg calcite.[24]

1.3 Role of organic matrix on the precipitation of calcium carbonate

The key component of biological materials is the organic matrix (OM), closely involved in the control of nucleation, growth, form and function of the mineral phase.[16] Biosynthesis of the OM is arranged in time and in space at cellular level in closeness of the mineralization sites. For example in corals, OM is synthesized from cells of calicoblastic epithelium and secreted in the adjacent subepithelial space.[29] The OM is a combination of macromolecules. OMs compositions are varied,[30] but they exhibit common chemical features, that is the presence of proteins having residues carrying carboxylate groups (COO^-),[31] polysaccharidic components, which often also contain phosphate and / or sulfate groups, which bind to proteins with a -O- bond.[32, 33] The presence of numerous negative charges makes these macromolecules excellent candidates to interact with mineral cations in solution or with the surfaces of the crystals,[34] and for this reason can be defined "control macromolecules". Examples of this class are glycoproteins rich in Asp, Glu or Ser.[16] The presence of the acid residues, having free COO^-, causes that the abundance of negative charges distributed along the protein chain and provides binding sites for positively charged calcium ions and determines their orientation. This underlines the Asp key role in the control of calcification.[35, 36] Glu and Ser are the major components of different mineralized tissues containing ACC.[16, 37, 38]

However most of the molecules that make up the OM are hydrophobic They are difficult to extract without the complete dissolution of the mineral phase. They are defined as " frame-work macromolecules", alluding to their main function, that of constituting a three-dimensional matrix in which takes place the formation of the mineral phase and where some control macromolecules can interact with it.[31] This is a group protein rich in residues Gly and Ala.[16]

An important fraction of the OM is constituted by free polysaccharides.[38] Their function in the crystallization process is not yet well known. It was noted that they have a strong tendency to associate, forming a gelatinous structure in which the macromolecules acid can be absorbed and exercise control over the precipitation of $CaCO_3$.[33] In different organisms, chitin was observed in the OM and seems to build a insoluble three-dimensional compartment in which the polyanionic polysaccharides or proteins, which control the crystallization, bind constituting a confined space.[33, 39, 40] Another hypothesis is that sugars interact directly with the mineral phase. In a work done on calcite of coccoliths has been shown as the polysaccharides are able to inhibit the growth of calcite crystals. These macromolecules interacting with the hydrogen bonds that are established between the aqueous solution and the surface of the growing crystals,[41] blocking the water an disrupt its ordering. This suggest that polysaccharides may block other cation and anion bonding and thereby inhibit growth on the surfaces.[42]

In addition to proteins and polysaccharides, among the main components of the OM are also lipids. In addition to being structural components of cell membranes and of important signal molecules, it is believed that lipids are involved in the precipitation of $CaCO_3$. In corals, the lipid content varies between different species, and can be affected by environmental conditions or from the diet of the coral itself. Nevertheless some lipids are always present in the OM, as phospholipids, sterols and, in lesser amounts, waxes and sterol esters.[43] The large amount of sterols and sterol esters suggests that different steroids can be involved in the process of biomineralization. Other lipids, such as polar lipids, have already been observed in other carbonate biominerals.[44] This means they could be very common lipids, or components involved in the mechanism of biomineralization. Isa and Okazaki [45] have shown that phospholipids extracted from the skeleton of scleractinian are able to bind calcium, and therefore suggested that they can serve as a nucleation site for the deposition of $CaCO_3$. Furthermore, it has recently been suggested a possible role of lipids in the process of ionic traffic.[46]

Despite the OM involvement in biomineralization is accepted, not clear is its function. It was shown in physiological studies as the synthesis of OM is connected to the calcification process.[47] Pioneering in vitro experiments have shown the influence of acidic glycoproteins on the morphological control of calcite deposition, highlighting an important role of the glycosidic regions in morphology modulation.[32] The capability of OM to determine the aragonite versus calcite polymorphic selection has been determined in mollusc shells.[48, 49] This organic control on the $CaCO_3$ polymorphism has been also verified by the abrupt transition calcite-aragonite in abalone shells, accompanied by the synthesis of specific polyanionic proteins.[49] Acidic macromolecules associated with aragonite or vaterite from fish otoliths influence this polymorphic selection.[50] Families of mixed acidic macromolecules have always been used in all these studies. Only recently a specific protein, Pif1, able to selectively deposit aragonite on a chitin substrate was completely characterized.[51] The function of acid macromolecules can be triggered by the presence of magnesium ions. In a recent research was shown that ACC stabilized by magnesium ions can be converted into calcite by the addition of aspartic acid. The aspartic acid destabilizes the hydration of magnesium ions, thus favoring the precipitation of calcite. This important observation was used to explain how organisms can control the phase transformation from ACC into calcite.[52] Clode and Marshall have suggested that, in corals, the sheath of the OM may act as an inhibitory property, controlling and reducing the deposition of $CaCO_3$, or alternatively assuming a structural role, rather than regulatory.[53] The OM acidic macromolecules usually are absorbed on the specific plane of crystals growing from solution, thus retarding growth in direction perpendicular to the plane; as the crystal growth the adsorbed macromolecules is included within the crystal structure.[54-56] Thus, OM presence not only affects the morphology but also the mechanical properties of the crystal. The mechanism of such interactions is suggest to be a result of both stereochemical recognition and binding energy at the organic-inorganic interface.[56] It was also considered the possibility that the OM transport the mineral component in the state of amorphous at the site.[46, 57] OM protein have also amino acid repeating motifs, which may possibly mimic the repeating lattice of the crystal. [58] However, OM and in particular acidic proteins was found to be present in almost mineralized tissues[59, 60] and were also present in ancient mollusc shells, some 80 milllions years old,[61] so they have a function on biomineralization process.[6]

1.4 Crystallization

In the classical picture of crystallization, crystals growth take place for nucleation in supersaturated environment and later crystals increase their dimensions. Nucleation is the process of generating new phase from an old phase, occurs via the formation of small embryos of the new phase inside the other one.[21] Usually it occurs when the ions concentration reaches a critical point where the surface energy of the aggregate is equal to the bulk energy.[46, 62] At that point molecules will start to aggregate in clusters and when they reach a critical size are called nuclei. Crystals start to growth via layer-by-layer trough the absorption of solute atoms or molecules on nuclei. The addition of a molecule in a growing layer is more favoured respect to the formation of a new layers. The first molecule of a layer takes contact only with the molecules of underlying layer, while a molecule added in a growing layer takes contact in two or three dimensions.[16] The growth in different directions follows kinetic and thermodynamic rules.[16] The difference in crystal morphology are due to the differences in surface energies of the crystal faces, which can be influence by growth environment. The kind of crystal polymorph precipitated is under kinetic control that consist in the modifications of the activation-energy barrier of nucleation and growth.[63] In the case of $CaCO_3$, the Gibbs free energy difference between calcite and aragonite is very low (about 0.21 $kJmol^{-1}$), such that surface energy and/or impurity effects can cause crossovers in stability, and therefore which phase crystallizes at the nanoscale can be controlled by thermodynamic as well as kinetic factors.[17]

Crystallization of $CaCO_3$ involve the control over the concentration of the two ions that react together following this reaction:

$Ca^{2+} + CO_3^{2-} \rightleftarrows CaCO_3$

Every solid state is characterized by a saturation state (Ω):

$\Omega = [Ca^{2+}]*[CO_3^{2-}]/K_{sp}$

where K_{sp} is the solubility constant of $CaCO_3$ polymorph considered. If Ω is major than 1, the precipitation is favoured, if is minor than one the dissolution is favoured. In the ocean, carbonate ions supply is due to the following series of reactions that started with dissolution of CO_2 in the ocean and its transformation before in carbonic acid and then in carbonate ions. Is necessary shift the equilibrium in favour of carbonate ions to obtain the precipitation of $CaCO_3$; for this reason hydrogen ions must be remove from the crystallization site.[64]

$CO_2 + H_2O + Ca^{2+} \rightleftarrows Ca^{2+} + H_2CO_3 \rightleftarrows CaCO_3 + 2H^+$

Recently some studies, showed that crystals can nucleated starting from a transition amorphous phase, that later convert in a crystal phase.[65] This non-classical crystallisation followed the Ostwald's "step rule" which asserts that the crystallization process takes place with a succession of sequential precipitation starting from a metastable phase, similar to its precursor in solution, until reaching the most stable phase. This progression is thermodynamically and kinetically favoured because these steps reveal a lower activation-energy barrier due to a lower critical size necessary to start nucleation and crystal growth. The system visits a series of metastable phases , decreasing its free energy by a series of small and faster steps rather than in one big leap (Fig. 1.3).[17]

Soluble amorphous minerals are used to temporarily store ions or function as solid precursor phases of crystals, because they can easily be modelled in different shapes.[6, 12] In particular, in the process of $CaCO_3$ precipitation, once ions concentration reached the critical point, a prenucleation-stage take place and ACC start to precipitated (Fig. 1.4).[66] ACC is thermodynamically instable and spontaneously crystallize in aqueous solution in short times and leads to the precipitation of the anhydrous forms of $CaCO_3$.[67] There are two forms of ACC, one more stable (ACCI) and the other one less stable but more hydrated (ACCII).[14, 67] These forms show a specific short-range order that corresponds to the long-range order of a particular crystalline polymorph.[66, 68, 69]

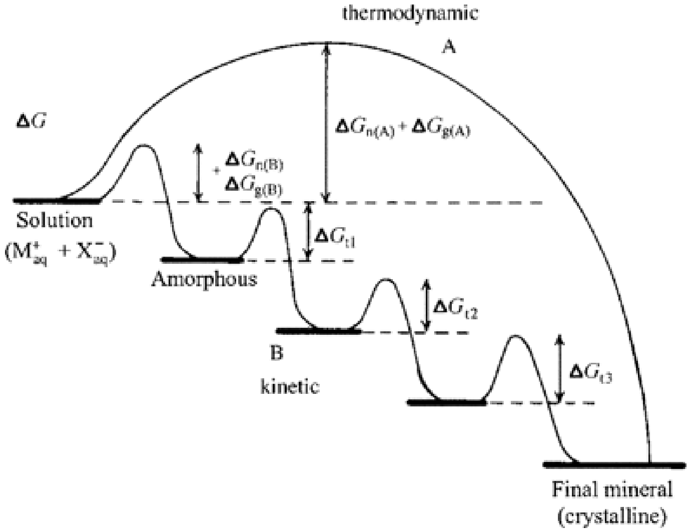

Figure 1.3: Simplified scheme of the crystallization pathways under thermodynamic and kinetic control. Whether a system follows a one-step route to the final mineral phase (pathway A) or proceeds by sequential precipitation (pathway B) depends on the free energy of activation associated with nucleation (n) and growth (g).[70]

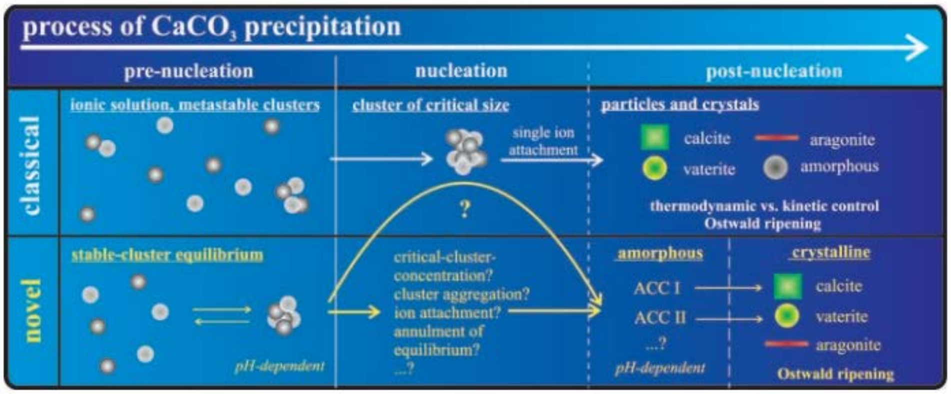

Figure 1.4: Schema of the classical and novel view on precipitation (not to scale). Prenucleation-stage calcium carbonate clusters provide an early precursor species of different ACC phases giving rise to an alternative crystallization-reaction channel.[66]

The transition from a crystalline to an amorphous form is thermodynamically controlled. In the absence of additives, the dominant process is the dissolution of ACC into ions and a consequent growth of the crystal ion-to-ion. The presence of additives change the nature of the transformation in that it stabilizes the ACC, which is well able to resist longer to dissolution and reach the surface of the growing crystal. At the level of this site, the diffusion and the surface tension favours the migration of the particles, which interact with the crystal at the level of an extended area thus stimulating the crystallization (Fig. 1.5).[71]

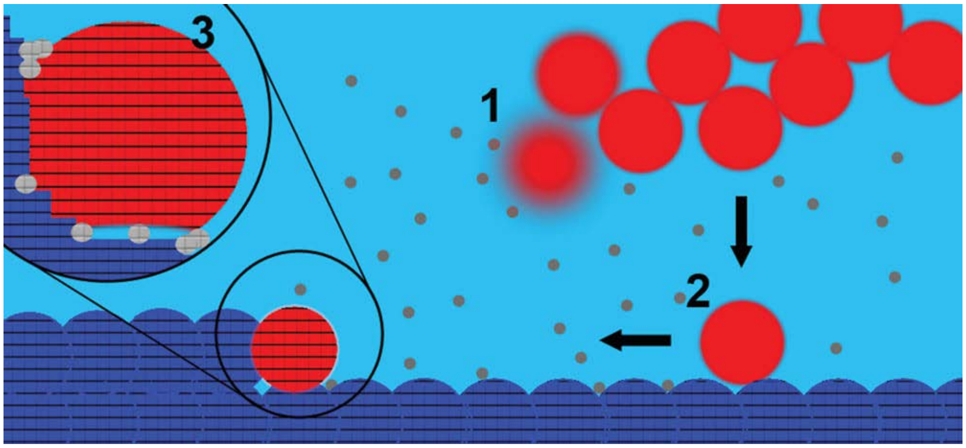

Figure 1.5: Crystal growth pathways. 1) Upon immersion of ACC (red) in water, the ACC particles can undergo partial dissolution (blurred particles) into ions (gray). This process of ACC dissolution into ions, as well as the process of ion-by-ion crystal growth, is slowed down by the presence of additives. (2) An ACC particle can migrate to the crystal surface (blue) where diffusion and surface tension will favor its movement towards steps and kinks on the crystal surface. (3) Particle crystallization at such preferred sites will be favored, whereby they will become integral parts of the crystal. Ion-by-ion attachment to the crystal is occurring concomitantly with particle accretion.[71]

1.5 Biomineralization process

As just discuss above, biomineralization is a process which involves mineral phase, macromolecules that make up the framework in which the minerals form and the interphase that link the two.[65] Biomineralization processes are divided into two fundamentally different groups based upon their degree of biological control: “biologically induced” and “biologically controlled” mineralization.[60] The first one involves the precipitation of inorganic materials by reaction of extraneous ions with metabolic products extruded across or into the cell wall.[72] In this case also relatively minor disturbances, such as the introduction of a biologically final product obtained from the metabolism, the release of particular cations by the cells, or the construction of charged surfaces (for example a surface of the cells), can cause minerals precipitation in certain circumstances.[1] The biological system has little control over the type and habit of minerals deposited, although the metabolic processes employed by the organism within its particular redox environment mediate pH, pCO_2 and the compositions of secretion products.[60] The minerals product are closely associated with the cell wall and are poorly defined and heterogeneous.[72] In “biologically controlled” mineralization, the organism uses cellular activities to direct the nucleation, growth, morphology and final location of the mineral that is deposited.[60] the minerals product are distinguished by reproducible and species-specific crystallochemical properties as uniformity of particles size, complex morphology, higher order assembly into hierarchical structure, ecc.[72] The way in which the crystallization process is controlled varies between different organisms. Some produce the organic matrix that interacts with the growth of crystals in the extracellular space. Single-celled organisms that exist as a community use the epithelial surfaces of cells as the organic substrate for nucleation and growth with a preferred orientation. Controlled mineralization can also occur also within specialized vesicles or vacuoles that direct the nucleation of biominerals within the cell.[60]

In biological systems, the microenvironment where the crystallization occurs is the key to control the growth of the crystal. The crystals are generally formed in a predefined space, delimited by an extracellular matrix and cell membranes, or within vesicles. Within this space defined crystals grow under limitations of shape, size, concentration and composition imposed directly or indirectly by specialized cells in the surrounding area.[16] Recently, some studies have shown that many organisms do not form their crystals for nucleation and growth in a supersaturated solution, but before producing a phase colloidal, and from this nucleate and grow crystals mature. In the case of $CaCO_3$ phase precursor disordered transient is the ACC, as described above. Therefore, much attention must be given to the intracellular environment in terms of control over mineral formation.[65]

This new crystallization pathway was observed in many different organisms where the crystals grow from an amorphous precursor that is formed within the cells and depend by environmental conditions such as pH, temperature and additives.[46, 65, 73] Weiner and Addadi,[46] proposed three different models for different organisms organizations using an amorphous phase as a precursor (Fig. 1.6):

- Mineralization of extracellular matrix (Fig. 1.6a)
- Mineralization within a large vesicle (syncytium) (Fig. 1.6b)
- Mineralization within vesicles that are located in the intracellular space (Fig. 1.6c)

In all these models the first stage is to acquire, through a process of endocytosis, the ions from the surrounding environment, or the sea water. Inside of the vesicles created, the formation of the first amorphous mineral phase takes place, then it is transported to the site of crystallization or in a large vesicles. On site, the conversion of the amorphous phase into a crystalline phase occurs. In this way develops the mineralized tissue mature.

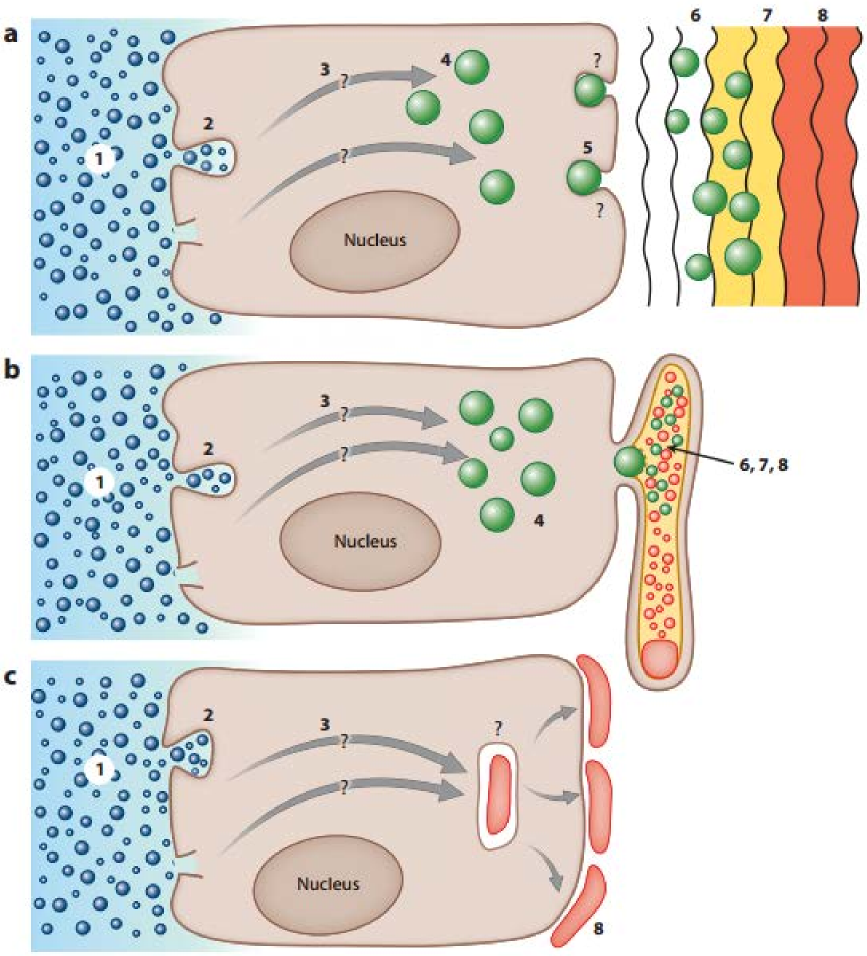

Figure 1.7: Schemes of generalized crystallization pathways involving (a) an extracellular matrix, (b) a vesicle-confined space (syncytium), and (c) the formation of mature mineralized elements within a vesicle inside the cell. Crystallization pathways. (1) The medium from which the ions are derived (seawater or body fluids). (2) The ion-sequestering process: endocytosis of seawater droplets and/or ion channels and/or transporters. (3) Transport within the cell to specialized vesicles. (4) Specialized vesicles in which the formation of the first disordered mineral phase occurs. (5) Transport of the mineral-bearing vesicles and their contents into the extracellular environment or into the syncytium. (6) The translocation of the disordered phase to the crystallization front. (7) Transformation of the initial disordered phase into more ordered phases. (8) The mature mineralized tissue. In the case of the crystallization pathway shown in panel c, the mature mineralized product may remain within the cell or may be transported to the cell. Very little is known about transient precursor phases in the crystallization pathway shown in panel c.[46]

1.5.1 Corals biomineralization

Corals are a major source of biogenic $CaCO_3$,[74] and create coral reefs that, in tropical environments, covering about 15% of the shallow seabed (up to 30 m).[75, 76] The reefs are fundamental elements in the ecosystem, as they are able to provide a habitat for numerous heterogeneous species, facilitating the diversification of biologic niches. Furthermore hosting a very high biological diversity they provide resources for fishing and also a valuable attraction for tourism. In addition to the tropical seas, corals also colonized temperate environments up to higher latitudes and depths (up to 4000 m). Corals can be present as solitary or aggregated in isolated colonies, in small reef, or in large reef in the ocean depths, up to 300 m with a diameter of several kilometers. Even the cold water corals, although still partly unexplored, are complex habitats.

Corals give the opportunity of investigating many phenomena of geochemical, biochemical, mineralogical, ecological and paleontological interest.[74, 77] Nowadays, corals relevance as $CaCO_3$ crystallizers is of extreme importance in view of the effects of global warming and ocean acidification.[78, 79]

The scleractinian are anthozoa benthic cnidarians. The corals are constituted by cnidarians with polyp form, benthic, equipped with an exoskeleton of $CaCO_3$ consists mainly of aragonite. (Fig. 1.8) The body of the polyp is composed of two tissues, an outer layer, ectoderm, and an inner, gastroderm, separated by a layer of collagen, with or without free cells, called mesoglea. The polyp is equipped with a crown of tentacles, used to predation, which surrounds the mouth, which opens into the gastro-vascular cavity.[76] The epiderm contains specialized cells as cnidociti, mucociti epithelial cells and muscle. The gastroderm is instead characterized by the presence of zooxanthellae, single-celled algae that live in symbiosis with the polyp, which provide energy and nutrients[80] and favour calcification process[29, 81] through photosynthesis. The zooxanthellae, in turn, receive inorganic nutrients from the metabolism of the polyp.[82] The epidermis aboral, also called calicoderm, is composed of a single layer of cells, calicoblastic cells, that are in close contact with the skeleton below. The interface between these two tissues takes the name of calcifying extracellular matrix (ECM), and is the site where biomineralization takes place.[64] The ECM is composed primarily of proteoglycans and adhesive glicoprotine, forming a gel in which are embedded collagen fibrils.[83]

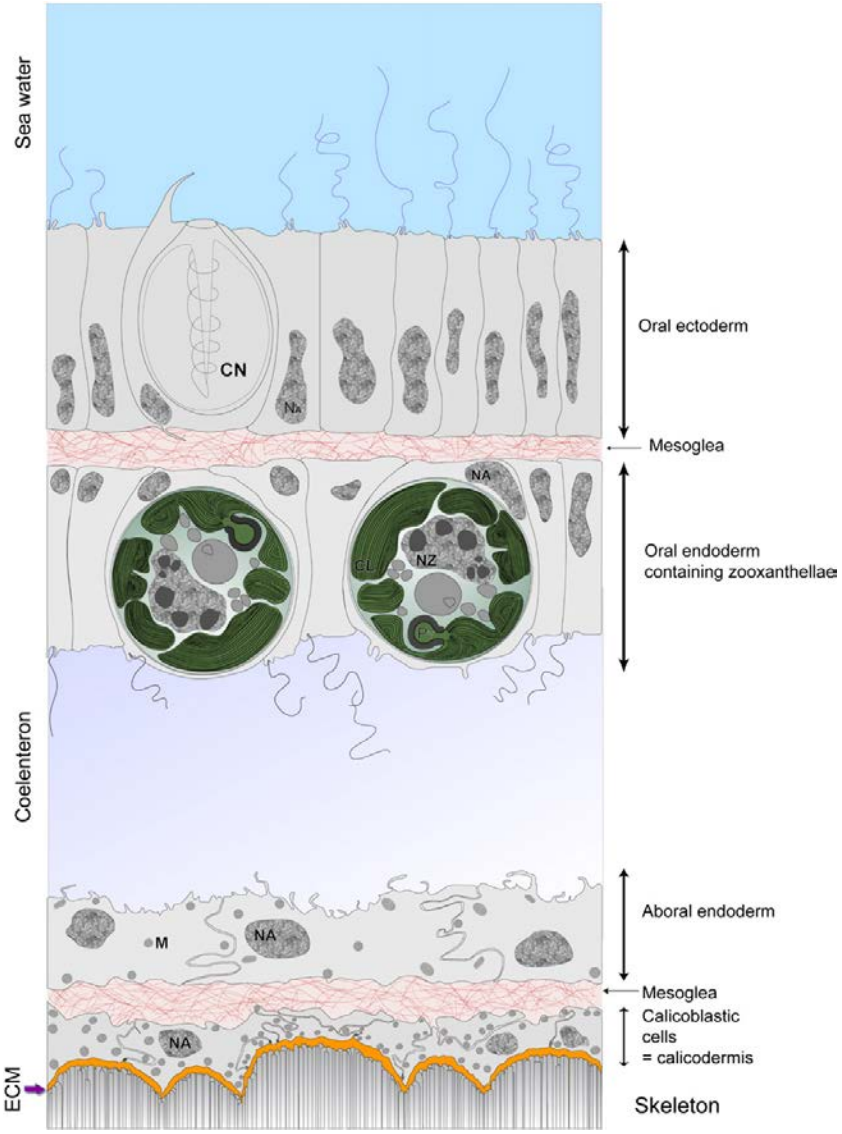

Figure 1.8: Schematic representation of the histology of the coenosarc (drawn from a picture in transmission electronic microscopy of the coral S. pistillata). CL = Chloroplast. CN = Cnidocyte. M=Mitochondria. NA= Nucleus of animal cell. NZ =Nucleus of zooxanthella. PY=Pyrenoid. ECM = Extracellular Calcifying Medium.[64]

The skeleton of corals is a composite structure with both inorganic (aragonite) and organic components.[84] The merging of data from several investigations[85, 86] has revealed that the actual growth unit of the skeleton is a few micrometer thick mineralizing growth layer synchronically increasing the "sclerodermites", forming a given skeletal unit (e.g. a septum) (Fig. 1.9). The mineralizing growth layer simultaneously increases the two distinct mineralizing areas that have been extensively described from a structural point of view. At the growth edge of any structural components (e.g. septal spines) a granular and porous nanocrystalline phase (randomly oriented) forms the initial skeletal framework (also the earliest appearing mineralized elements after larval metamorphosis, according to Vandermeulen and Watabe[87]). These early mineralizing zones (EMZ), usually called “center of calcification”, are laterally reinforced by deposition of a second structural layer made of dense large acicular crystals: the fibers.[88]

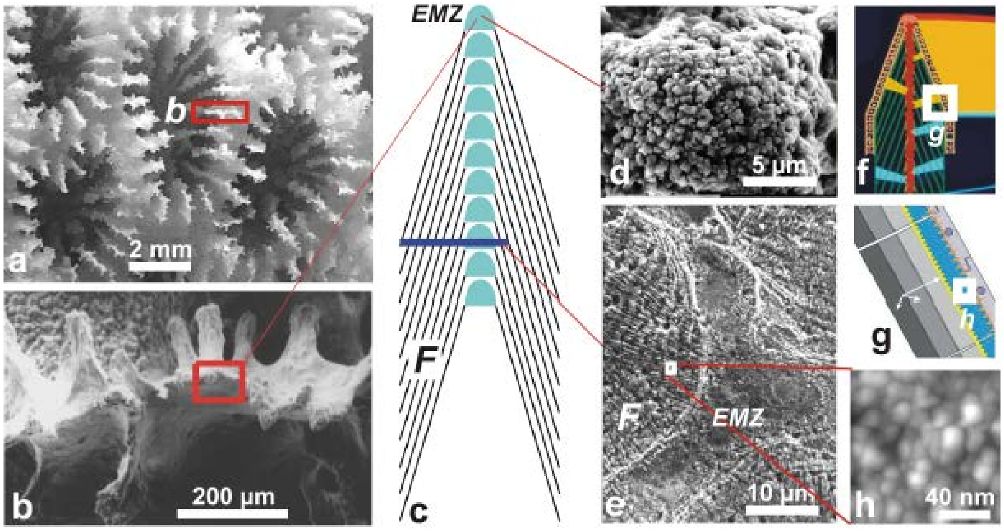

Figure 1.9: From corallite morphology to skeletal nanograins of a septal growth layer in *Favia stelligera*. Measurements now possible at the micrometre range impose a good understanding of the skeletal features. (a–b) corallite (a) and septum growth edge (sight of the top); (c) scheme of superimposed growth layers (EMZ: early mineralization zones); (d) tiny isodiametric crystals in EMZ; (e) microstructure in the median part of a septum (F: fibre zone after etching); (f–g) scheme of growing surface with basal ectoderm; (h) nanometre structure of a fibre growth layer.[89]

The morphological relationship between OM and mineral phases in coral unit crystals is poorly understood. OM is synthesized by cells of the calicoblastic epithelium and then secreted into the adjacent subepithelial space in which calcification takes place.[29] The OM of scleractinian corals was investigated in detail in its structure and relation with the mineral phase.[37, 64, 90-94] The whole OM is made of glycoproteins in which the proteic regions assume preferentially a α-helical conformation in all the coral species studied, except in one case,[37] where a β-sheet conformation was observed. The amino-acid analysis of OM from representative coral skeletons showed a similar composition characterized by a high content of Glu, Asp and Gly. Moreover, Gln, Ser, and Thr were demonstrated to act respectively as N- and O- linking sites for glucidic regions, which were found to be sulphated.[91, 95] X-ray Absorption Near Edge Structure (XANES) mapping of the EMZ and the fibrous zone, the two main structural entities of the coral skeleton, has shown the correspondence between S-polysaccharides and the spatial arrangement of mineral growth and have evidenced 1) a biochemical zonation that corresponds to the step by step growth, and 2) the general coordination by polyp physiology.[37, 90-92]

These molecules have a different role in the biomineral synthesis according to diverse biomineralization models. In physicochemical models, involving a liquid layer with chemical properties called calcifying fluid,[96] the OM acts as a support for calcium carbonate oriented crystallization.[74] In these models crystal growth occurs through a primarily inorganic process, which involves a coral controlled transcellular ions transport to the calcifying fluid (ref. 64 and references there in). A recent model of ionic transport shows a direct and rapid seawater transport to the calcification site.[97] In contrast to physicochemical models, Clode and Marshall[53] have suggested a molecular model in which calcification occurs within a gel secreted at the interface between the calicoblastic cells and the skeleton. According to this model the glycoproteins form an architectural framework bearing the sites for development of the mineral phase.[98] In this model, OM interacts with the growing crystal changing its shape[46, 99, 100] and biomineralization cycle can be schematize in four principal phases (Fig. 1.10):[89]

a) at the starting point, the basal ectoderm of the polyp is in close contact with the upper surfaces of aragonite fibres;
b) basal ectoderm secrets organic macromolecules and take conctact with aragonite fibers;
c) in this phase the ions are secreted and starting crystallization, and a new layers starts to growth;
d) a new skeletal layer growth.

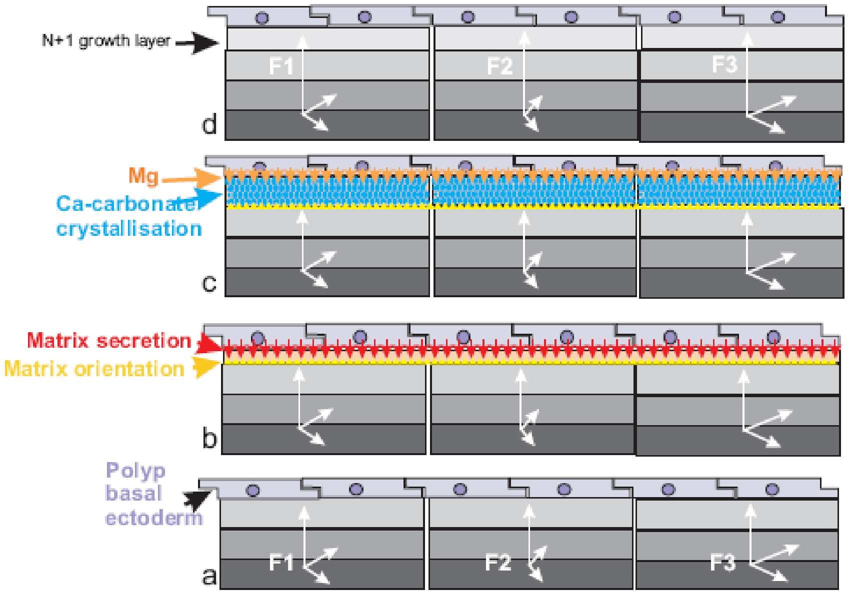

Figure 1.10: Scheme of a growth layer formation in a coral skeleton, summarizing the structural, chemical and biochemical data. F1, F2, F3: upper mineralized layers in three adjacent fibres; arrows: over- all crystallographic orientations.[89]

Several clues support the existence of a biological influence over the mineral deposition. First, the ultra-structural organization of the aragonite crystals in coral skeleton shows differences from the one of aragonite precipitated abiologically and is species specific. Second, in the coral skeleton, EMZ rich of biological macromolecules were identified, suggesting a controlled release of macromolecules in space and time by the organism.[37, 90-94, 101]

Many aspects of OM role in the dynamics of skeleton formation of corals are enigmatic.[102] It has been recently shown, by *in vitro* studies, that the OM from different corals species influences polymorphism and morphology of calcium carbonate. Goffredo *et al.*[79] showed that the intra-skeletal OM from Mediterranean zooxanthellate solitary coral *Balanophyllia europaea* can favor the precipitation of aragonite and that a transient phase of amorphous calcium carbonate (ACC) stabilized by lipids is involved.

Moreover, an important recent study has shown that four highly acidic proteins, derived from the expression of genes obtained from the common coral *Stylophora pistillata* can spontaneously catalyze the precipitation of calcium carbonate *in vitro* from seawater.[103]

1.6 Biomineralization and ocean acidification

Currently, one of the issues most discussed, is that of global warming. Over the past two centuries because of the use of fossil fuels, deforestation and changes of land use on the part of man, there was an increase in the concentration of greenhouse gases in the atmosphere (Fig.1.11).[104]

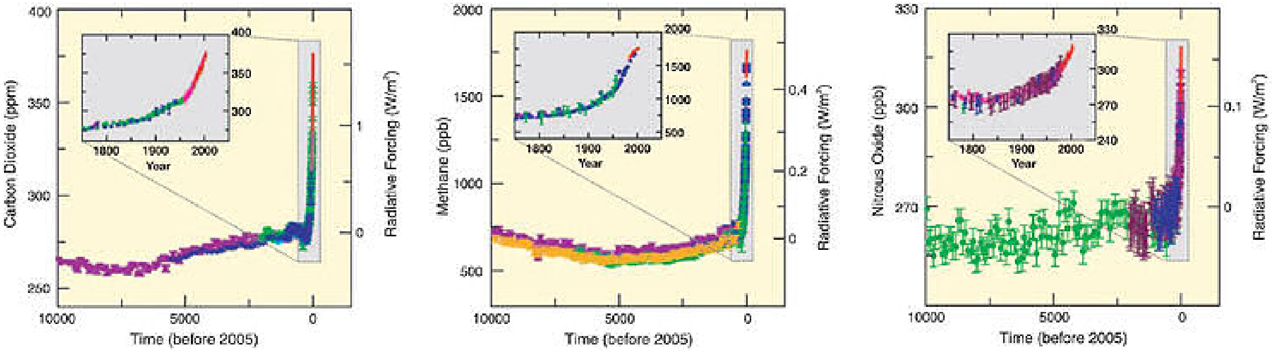

Figure 1.11: Atmospheric concentrations of carbon dioxide, methane and nitrous oxide over the last 10,000 years (large panels) and since 1750 (inset panels). Measurements are shown from ice cores (symbols with different colours for different studies) and atmospheric samples (red lines). The corresponding radiative forcings are shown on the right hand axes of the large panel.[105]

Greenhouse gases, absorbing terrestrial infrared radiation dissipated as a result of absorption of sunlight, trap some of the thermal energy warming the atmosphere at a temperature that enables life on the planet. But the increase in the amount of these gases, caused precisely by air pollution, caused a rise in average global temperature.[106] Consequently are also increased temperatures of the seas, in fact, last century the surface temperature of the ocean waters has increased by 0.4-0.8 °C and the most recent report of the Intergovernmental Panel on Climate Change (IPCC) predicts a further increase of 1.1 to 6.4 °C by the end of the century. It is expected that this strong climatic variation causes the rise of the sea level, the rise of the intensity of extreme weather events, changing precipitation regimes, changes in agricultural yields, modifications of trade routes, retreat of glacier and the extinction of species.

A further consequence of global warming is the ocean acidification. This phenomenon is mainly due to the increase of only one of the main greenhouse gases: CO_2. The increasing of its levels in the atmosphere is caused, as mentioned earlier, by human activities. Half of the CO_2 released in the last few decades by human activity has remained in atmosphere, while the remainder was absorbed by the terrestrial biosphere and the oceans causing a lowering of ocean pH values.[104] Whereas the concentration of CO_2 in the seas will only increase, there will be a drastic decrease of marine pH in the coming decades, and also a change in the saturation state of aragonite, calcite and other biominerals essential for the survival of some marine organisms (e.g. Foraminifera, coralline algae, corals, molluscs, worms, sea urchins) (Fig. 1.12).

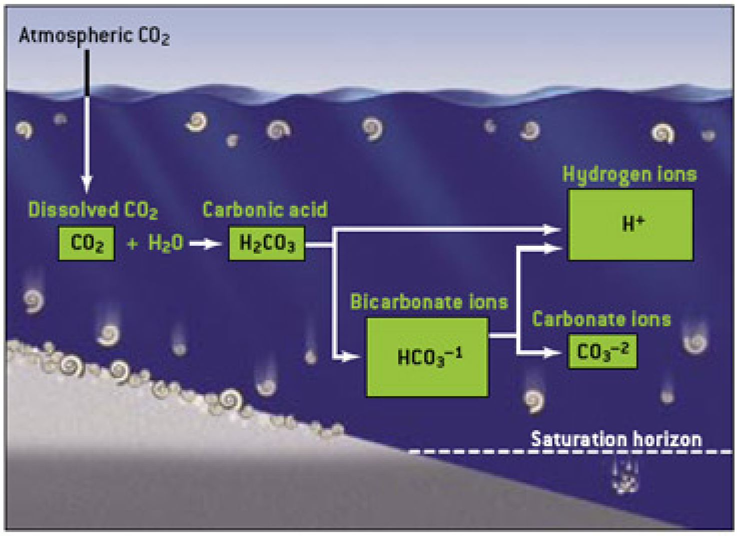

Figure 1.12: Carbon dioxide absorbed from the air combines with water to form carbonic acid. A portion of this compound persists in the ocean, but most of it dissociates into acidifying hydrogen ions along with bicarbonate ions. Some of the latter also dissociate, forming carbonate ions and yet more hydrogen ions. These chemical changes cause an upward shift in the "saturation horizons" for calcite and aragonite—the water levels deep in the sea below which shells of marine organisms made of these minerals dissolve.[107]

1.7 Objective of the thesis

The importance of biomineralization in biology is widely recognized, biominerals make up important ecosystems (e.g. coral reefs), carry out functions of support (e.g. in humans) and of protection (e.g. in mollusks and in eggs) in different organisms. Despite that, the mechanism of interaction between cells and minerals is not yet clear. It is know that there are several levels of control depending on the type of organism taken into account, and that in these processes are involved a wide variety of macromolecules with different functions.

In vitro crystallization experiments and characterization of biominerals can help to better understand both the degree of control exercised by different organisms both the effect of the organic and inorganic additives on the crystallization process.

In the light of this, in this thesis were chosen different calcifying organisms and their crystalline structures were characterized by different techniques, and the effects of additives, magnesium ions and organic matrix, on $CaCO_3$ precipitation were also investigated through *in vitro* crystallization experiments.

2. CONTROL OF ARAGONITE DEPOSITION IN COLONIAL CORALS BY INTRA-SKELETAL MACROMOLECULES

2.1. Introduction

Scleractinian corals possess several records in terms of their mineralization activity. They represent the biggest source of biogenic calcium carbonate[74, 108] and they are among the fastest marine mineralizing organisms.[109] Despite their great relevance in biomineralization, and the plethora of articles published in this field[64] and references therein), many aspects of their mechanism of mineralization are still a source of discussions and controversies. The main issue is the relative level of biological and environmental control over calcification.

It has long been recognized that coral skeletons comprise both inorganic (aragonite) and organic components,[84] but the main issue is the relative level of biological and environmental control over calcification. In geochemical research area, opinions inspired by the spherulitic crystallization model[110] are still prevalent. If presence of an organic component has become accepted, its active role in the biomineralization process is still considered doubtful.[111] The intra-skeletal OM shows an unusual amino-acid composition (high concentrations of acidic amino acids) and has been suggested to play an important role in the coral mineralization process.[35, 79, 112] Morphology of coral colonies are dramatically affected by habitat conditions,[113] nevertheless the changes always remain within the species-specific ‘‘vocabulary’’ controlled by the taxon’s DNA.[85]

However, the mode of action of these organic compounds is still debatable. Initial models favored the ‘‘template mechanism’’ in which organic layers were acting as a scaffold for Ca-carbonate oriented crystallization. In contrast to models involving a liquid layer with chemical properties close to sea-water[96, 114] as the place where crystallization occurs,[53] have established the existence of direct contact between cells and skeleton. Calcification occurs within a gel secreted, or a high viscous sol, at the interface between the calicoblastic cells and the skeleton. In situ XANES mapping of organic components (proteins and sulfated polysaccharides) have shown that organic and mineral components were not distributed among alternating layers, but associated within each growth layer at a submicrometer scale.[91]

Molecular models suggest formation of a glycoproteic architectural framework bearing sites for development of a crystalline structure.[98] More recently attention was drawn to the potential role of OMs as carriers of the mineral component, possibly in amorphous status, crystallization itself trapping the organic phases along the boundaries of the grains.[46, 57, 115] This model is supported by $CaCO_3$ crystallization experiments in gel and partial gels.[116]

The real role of the OM in the dynamics of skeleton formation of corals is enigmatic and is related to the information on its properties once extracted from the skeleton. However, bearing in mind these limits, but supported by many analogous studies on mollusk shells, it has been recently demonstrated, by in vitro studies, that the OM from a coral species (*Balanophyllia europaea*) influences the polymorphism and morphology of $CaCO_3$.[79]

Here, we extended this study to different species of colonial corals, *Montipora caliculata*, *Acropora digitifera* (French Polynesia) and *Lophelia pertusa* (Atlantic Ocean), living in different habitats and having diverse calcification rates. Respectively, first and second largest coral genus in the present-day seas with respect to taxonomical diversity, *Acropora* and *Montipora* belong to the most successful and most studied coral family *Acroporidae*. According to Veron,[76] *Acroporidae* and *Caryophyllidae* (the Family to which the deep-sea coral *Lophelia* belongs) are distributed into two major supra-ordinal lineages, possibly distinct since the Triassic times. The aim of the present study is to determine whether the OM extracted from different corals shows a different capability to interact with $CaCO_3$ and if this is related with the coral species.

2.2 Experimental section

Coral skeletons:

Samples of *Montipora caliculata* and *Acropora digitifera* from Mangareva atoll (French Polynesia), were collected during by SCUBA diving and *Lophelia pertusa* from Bay of Biscay (French coast, Atlantic Ocean) by deep-sea dredging. After collection the coral tissue was completely dissolved and the skeletons were analyzed (see Appendix A).

Extraction of the organic components:

After decalcification process obtained aqueous solution containing the OM was centrifuged at 350g for 5 min to separate the soluble (SOM) and the insoluble (IOM) OM fractions, which were then lyophilized and weighted. The OM fractions were also characterized with different techniques (see Appendix A).

Calcium carbonate crystallization experiments:

Overgrowth and crystallization experiments were performed in a crystallization chamber using microplates for cellular culture (for major details see Appendix A). In each well, 750 μL of 10 mM $CaCl_2$ solutions having Mg/Ca ratio equal to 0 or 3 ($CaCl_2.2H_2O$, Merck; $MgCl_2.6H_2O$, Sigma Aldrich) were poured. Eight microlitre (for *L. pruvoti*) or 20 μL (for *M. caliculata* of *L. pertusa*) of a solution obtained dissolving lyophilized SOM in water (17.5 mg/mL (hereafter reported as c_s) were added to 750 μL of 10 mM $CaCl_2$ solution (without or with magnesium ions). This quantity was chosen keeping in consideration SOM concentration in the pristine skeleton and on the bases of the experience from previous work carried out in our lab.[79] In a second set of experiments 0.5 mg of IOM (here after reported as c_i) were added to 750 μL of 10 mM $CaCl_2$ solution (without or with magnesium ions). SOM (c_s) and the IOM (c_i) were added in each well in a third set of experiments. The crystallization tests of

$CaCO_3$ in the different conditions were replicated six times, starting from different batches of OM fractions. The precipitates were analyzed by optical microscopy, scanning electronic microscopy (SEM) observation and spectroscopic Fourier transform infrared (FTIR) analysis (see Appendix A).

Microscopic observations:

Scanning electron microscopy (SEM). Several fractured and polished sections of coral skeletons were cut perpendicular and parallel to the surface of the septa and walls. Polished sections and some fractures were etched with various acids and enzymes to reveal microstructural features. Detailed procedures of sample preparation are given in the legend of figures. SEM observations were conducted using a Philips XL30 and a Phenom Pro-X at IDES laboratory (Université Paris-Sud) and a Phenom^{TM} Pro X (FEI).

Atomic force microscopy (AFM). AFM observations were obtained with a Dimension 3100 Nanoscope III (Veeco Instruments) housed at UMR IDES. Samples were imaged at room temperature and in air using tapping mode. In phase imaging, a variant of tapping mode, the phase lag of the cantilever oscillation relative to the signal sent to the cantilever's piezo driver is used as a basis for image generation. Phase images were generated as a consequence of variations in material properties such as composition, adhesion, friction, etc. Thus, understanding of the contribution of the individual factors to the phase shift is not simple. Despite the complications involved in interpretation, phase contrast is a commonly used technique for mechanical and composition characterization of sample surfaces. In organo-mineral samples such as biominerals, a detailed interpretation of phase image is not possible. The probe consists of a cantilever with an integrated silicon nitride tip (Digital Instruments).

AFM has several advantages over most SEM, e.g., samples do not require coating. However, disadvantages are the small image size and a reduced depth of field on the order of micrometers. Thus, observation of fractured surfaces is difficult, and most samples have to be polished and cleaned.

Depending upon the structures of the coral skeletons, different preparative processes were used. $CaCO_3$ precipitates were dried in open air on a glass support and observed without any further preparation.

2.3 Results

2.3.1. Skeletal structures in corals

Scanning electron microscope (SEM) images of the studied species showed the common structural pattern of the coral skeleton (Fig. 2.1): the early mineralization zone (EMZ) was composed of small rounded granules. EMZs were more sensitive to etching than the fibers.[90] Then, fibers were produced with a rhythmic growth. Growth layers are about 2–3 lm thick. However, the size and arrangement of EMZ and fibers depend upon the species (Fig. 2.1 a, b, f, j). The inner structure of EMZ and fibers becomes visible using atomic force microscopy. Both EMZ and fibers are composed of rounded small granules (Fig. 2.1 d, g–i, k, l). These granules are surrounded by a cortex, the exact nature of which remains still unknown. Nevertheless, from phase image contrast, it can be said that the cortex is probably a mixture of organic and amorphous components. The inner part of the granules is also heterogeneous, as shown by the changes in colors in phase images.

2.3.2 Studies on the intra-skeletal organic matrix

In *M. caliculata*, *A. digitifera* and *L. pertusa* the OM was embedded in a skeleton of pure aragonite, as shown by the X-ray powder diffraction patterns (not show. A first quantification of the OM content in the skeleton was carried out by thermogravimetric analysis (TGA). The skeletons' thermograms showed a first weight loss in a range around 150–220 °C followed by one between about 280 and 450 °C (Fig. 2.2). The total weight loss (water + OM; see Cuif *et al.* [117] was of 3.4 ± 0.1 (0.9 ± 0.1 + 2.5 ± 0.1), 2.7 ± 0.1 (1.0 ± 0.1 + 1.7 ± 0.1) and 3.9 ± 0.1 (1.3 ± 0.1 + 2.6 ± 0.1) % (w/w) in

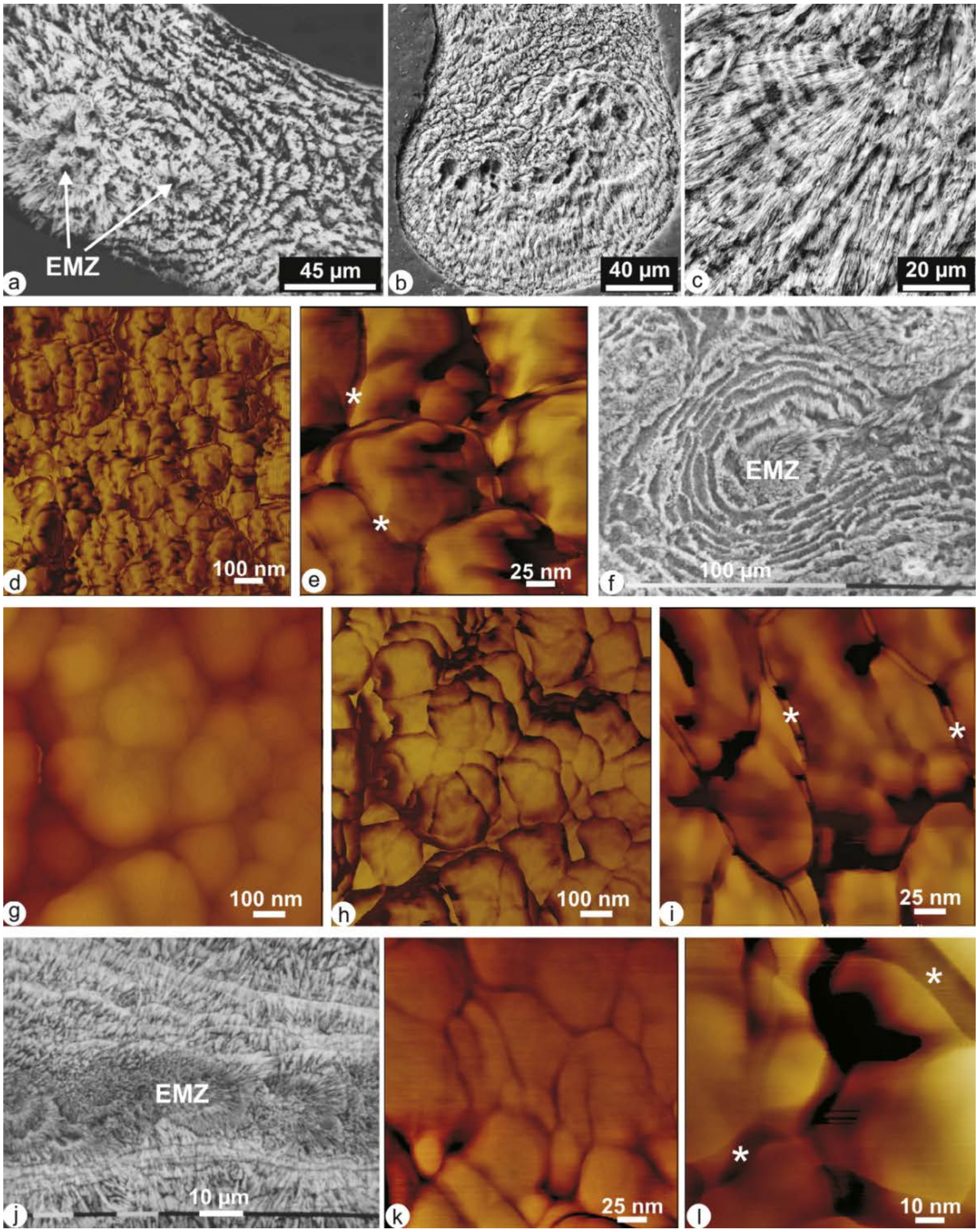

Figure 2.1: a–e: *M. caliculata*. Etching clearly shows the dual structure of coral skeletons: the superposed growth layers (a–b) cover the framework built by the small round shaped units which are formed at the tip of the skeletal units (EMZ: early mineralization zones); c: etching also demonstrates the coordinated stepping growth mode of fibers; d–e: atomic force microscopy reveals the reticulate structure of the skeleton. a–c: Alcalase etching of polished sections; d–e: polished section, etched with formic acid (5%) and glutaraldehyde (0.1%) for 5 s. f–i: *A. digitifera*. f: A typical view of skeletal organization: instead of continuous and regularly superposed growth layer, EMZ are surrounded by densely packed digitiform units with a spiral mode of growth (EMZ); polished and etched section, formic acid 5% for 5 s. g: Detail of the granular structure shown by AFM (polished and etched section) g: height image, polished section, etched with formic acid (5%) and glutaraldehyde (0.1%) for 5 s. h: Phase image of the same, i: same sample, granules surrounded by a thin cortex (⁄) of organic matrix ± ACC, AFM phase image. j–l: *L. pertusa*. j: typical for this genus is the wide EMZ median of the septa, covered by regular layers forming fibers; polished and etched section (HCl 1% for 5 s). k–l: Both domains are built by a reticulate composite material, with round shaped mineral units covered by a non crystallized phase strongly interacting with AFM probe tip (⁄). Polished sections, etched with formic acid (5%) and glutaraldehyde (0.1%) for 5 s.

M. caliculata, *A. digitifera* and *L. pertusa*, respectively. The OM concentration was also determined after acetic acid extraction from the skeleton. This material, formed by the soluble (SOM) and insoluble (IOM) fractions of OM, was about 0.3, 0.2 and 0.1% (w/w) in *M. caliculata*, *A. digitifera* and *L. pertusa*, respectively. The quantification of the relative amount of the OM fractions, SOM and IOM, was a difficult task, since a significant variability was observed from one extraction to another. However, as the result of six extractions the mass ratio between SOM and IOM was roughly estimated to be 1.4 in *M. caliculata*, 5.0 in *A. digitifera*, and 1.5 in *L. pertusa*.

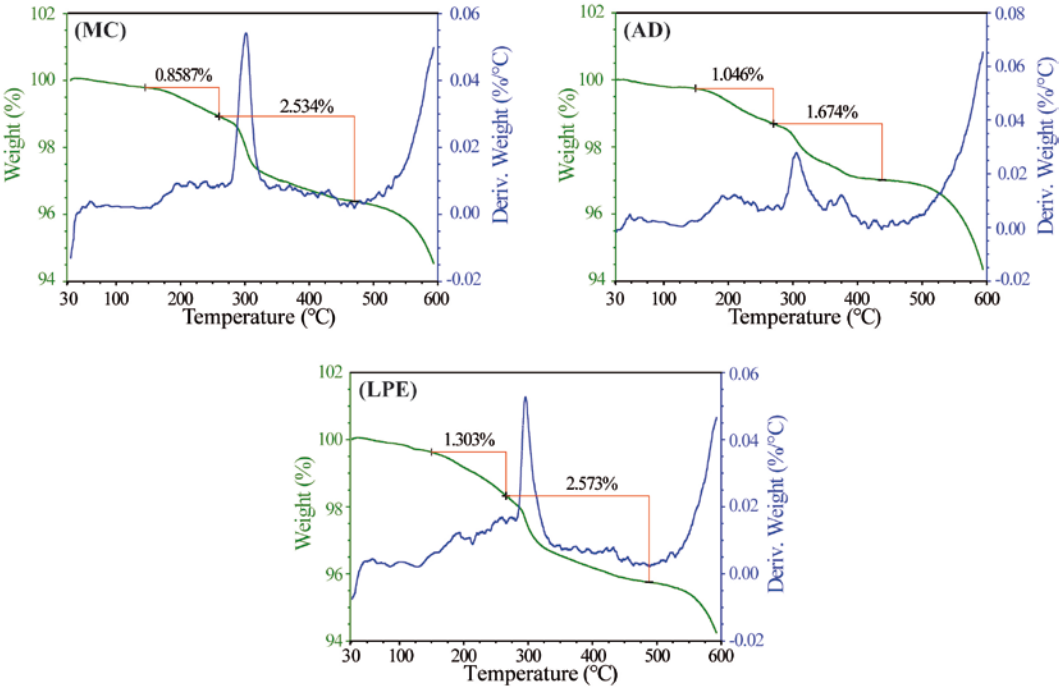

Figure 2.2. Thermo gravimetric profiles from powdered coral skeleton samples from *M. calyculata* (MC), *A. digitifera* (AD) and *L. pertusa* (LPE).

The chemical–physical characterization of the OM fractions was performed by Fourier transform infrared spectroscopy (FTIR), polyacrylamide gel electrophoresis (SDS–PAGE) and amino-acidic analyses (AAA). Table 2.1 summarizes the observations from the FTIR spectra of SOM and IOM obtained from six extraction processes from different coral skeletons of each species. In Fig. 2.3

the most representative spectra are shown. In general SOM and IOM showed the same absorption bands, regardless of the coral species; however, differences were observed in their relative intensities, and to a minor extent in their maxima. Two marked bands at about 2920 cm^{-1} and 2851 cm^{-1} and a weak one at 1737/35 cm^{-1} were observed in all fractions. In the SOMs the amide I bands were centered around 1654 cm^{-1}, this band partially shifted towards lower wave numbers, around 1636 cm^{-1}, in the IOMs. The amide II band, at around 1542 cm^{-1} , was weak with respect to the amide I band, in both SOM and IOM, particularly in *M. caliculata*. The band at around 1460 cm^{-1} was well defined in the IOM but weak in the SOM from all the species. An opposite trend was observed for the band at about 1460 cm^{-1} , which was more evident in SOM than IOM, except that in the IOM from *L. pertusa*. The band around 1250 cm^{-1} was evident only in the SOM from *M. caliculata*. The bands in the region between 1080 and 1030 cm^{-1} were observed in the spectra of all the extracts. To estimate the relative amounts of the main functional groups of the OM from the FTIR spectra, three zones (1–3) were defined (Fig. 2.4, Table 2.2). In the zone 1 (3000–2800 cm^{-1}) the absorption bands due to the methylene and methyl groups' vibration modes were present, they could mainly be related to the presence of fatty acids, mainly in IOM, or to molecules bearing alkylic chain regions. In the zone 2 (1750–1500 cm^{-1}) were located the absorption bands mainly associable to the amide I and II vibration modes of proteins (and of some sugars). In zone 3 (1100–950 cm^{-1}) ether bonds and C–C single bond vibration modes, mainly associable to polysaccharides, were present.[118] The integrated intensities of the absorption zones 1 and 3 were normalized to that of zone 2 (Table 2.2). Then a Mann–Whitney statistical test was carried out to verify if the differences in the relative zone absorption intensities between SOM and IOM of the same species and among different species were significant. In the SOM from *A. digitifera* and *M. caliculata* significant lower relative absorption intensity in the zone 1 with respect to IOM was observed. In the comparison among OM fractions from different species only the SOM from *L. pertusa* showed a significant higher absorption in zone 3.

Table 2.1: Main absorption bands in the FTIR spectra of soluble (SOM) and insoluble (IOM) OM fractions extracted from the skeleton of *A. digitifera* (*AD*), *M. caliculata* (*MC*) and *L. pertusa* (*LPE*). Their relative intensity is indicated in brackets: strong (*s*), medium (*m*) or weak (*w*).

	SOM			IOM		
	MC	*AD*	*LPE*	*MC*	*AD*	*LPE*
CH stretching	2920 (*s*)	2920 (*s*)	2922 (*s*)	2919 (*s*)	2920 (*s*)	2922 (*s*)
CH stretching	28501 (*m*)	2851 (*m*)	2851/4 (*m*)	2851 (*m*)	2851 (*m*)	2852 (*m*)
Carboxylic stretching	1735 (*w*)	1735 (*w*)	1736 (*w*)	1735 (*w*)	1732/7* (*w*)	1737 (*w*)
Amide I (α-helix, r.c.)	1655 (*s*)	1650/55 (*s*)	1655 (*s*)	1652 (*w*)	1650 (*w*)	1653 (*m*)
Amide I (β-sheet)	1637 (*w*)	1637 (*w*)	1639 (*w*)	1639 (*s*)	1632/8 (*s*)	1639 (*s*)
Amide II	1540/7 (*w*)	1542 (*w*)	1542 (*m*)	1544 (*w*)	1542 (*w*)	1545 (*w*)
CH_2 bending	1457/63 (*w*)	1459 (*m*)	1456/62 (*w*)	1457/63 (*m*)	1465 (*m*)	1460 (*m*)
Carboxylate stretching	1429 (*m s*)	1420/31 (*m*)	1420 (*m*)	1428/32 (*w*)	1422/8 (*w*)	1420 (*w*)
CH_3 bending	1384 (*w*)	1385 (*m*)	1384 (*m*)	1385 (*w*)	1384 (*w*)	1384 (*w*)
sugar groups**	1074/7 (*s*)	1080 (*s*)	1073/8 (*s*)	1060/80 (*s*)	1078 (*s*)	1079 (*s*)

*Two values are reported to indicate that this band maximum appeared in one of the two positions among different extraction products.

**The sugar groups region presents several bands, here the most intense one is reported-

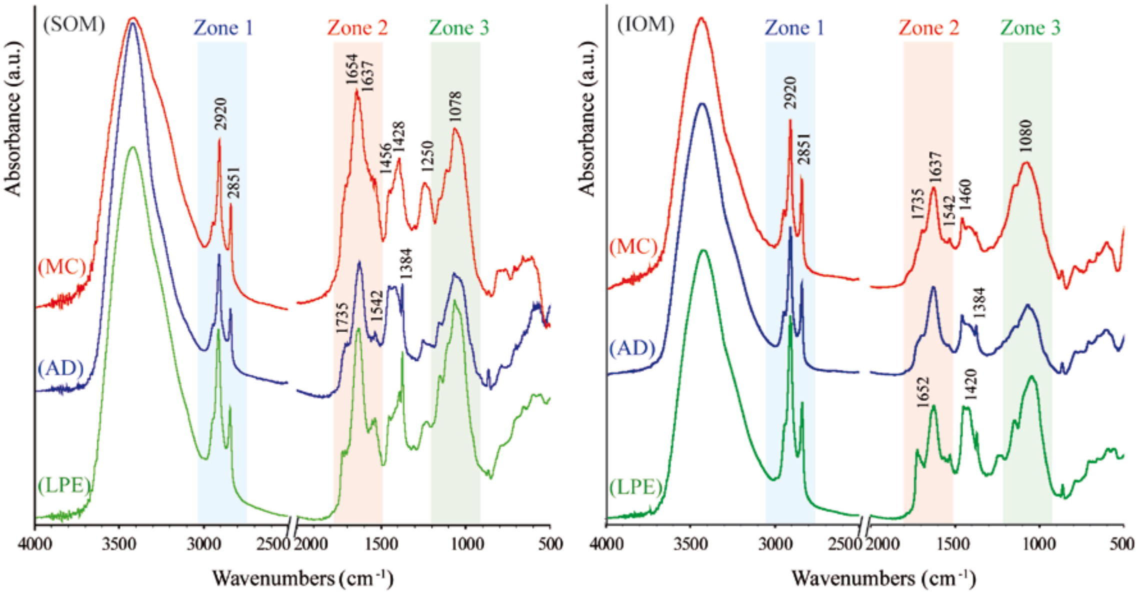

Figure 2.3: FTIR spectra of intra-skeletal soluble (SOM) and insoluble (IOM) organic matrix extracted from the aragonitic skeleton of *A. digitifera* (AD), *M. caliculata* (MC) and *L. pertusa* (LPE). The maximum of the absorption bands are indicated. The three zones define diagnostic regions of functional groups which could be mainly associated to the presence of lipids (zone 1), protein and polysaccharides (zone 2) and polysaccharides (zone 3).

Table 2.2: Average relative intensities of zone 1 (3000-2800 cm^{-1}) and zone 3 (1100-950 cm^{-1}) normalized to that of zone 2 (1750-1500 cm^{-1}) of the OM fractions, SOM and IOM, from *M. caliculata*, *A. digitifera* and *L. pertusa*. The intensity of the zone 1-3 can be considered a rough approximation of the content of lipids, proteins and polysaccharides, respectively. In parentheses standard deviations are reported.

		Zone 1	**Zone 3**
M. calyculata	SOM	0.7 (0.2)	0.9 (0.2)
	IOM	1.6 (1.3)	1.0 (0.5)
A. digitifera	SOM	0.8 (0.3)	0.8 (0.2)
	IOM	1.8 (1.3)	0.9 (0.2)
L. pertusa	SOM	1.0 (0.5)	0.7 (0.1)
	IOM	2.2 (1.7)	2.2 (1.5)

The macromolecules comprising SOM fractions were also investigated by SDS–PAGE (Fig. 2.3). *L. pertusa* SOM was characterized by the presence of many bands, gathered around 65, 43 and 35 kDa. *M. caliculata* showed two weak bands at 64 and 41 kDa. In A. digitifera no bands were detected. The PAS stain did not underline glycoprotein in any of the species. The AAA from SOM and IOM was reported in Table 2.3. SOM was always characterized by a higher content of aspartic (and aspargine) acidic residues than that of IOM. In *L. pertusa* the difference in aspartic residue content between SOM and IOM was lower than in the other two species. The content of hydrophobic residues, Gly, Ala, Val, Ile and Leu, was always higher in IOM (43–51 mol%) than in SOM (19– 30 mol%). The calculated average protein pIs[119] show that OMs were acidic, and IOM was less acidic than the SOM within a species.

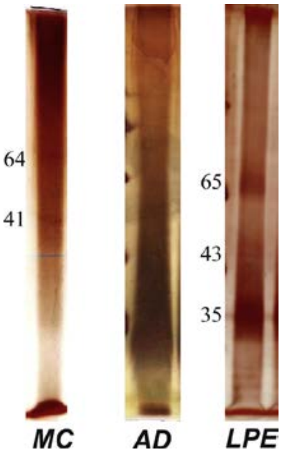

Figure 2.3: SDS-PAGE of intra-crystalline SOM extracted from aragonitic skeleton of *A. digitifera* (*AD*), *M. caliculata* (*MC*), *L .pertusa* (*LPE*). The side numbers indicate the molecular weight (kDa) of the silver stain marked bands. This dye did not express any band from the SOM of *A. digitifera*.

Table 2.3: Ammino acids composition (mol %) of soluble (SOM) and insoluble (IOM) fractions of OM proteins extracted from skeleton of *A. digitifera* (*AD*), *M. caliculata* (*MC*), *L .pertusa* (*LPE*).

	SOM			IOM		
	AD	*LPE*	*MC*	*AD*	*LPE*	*MC*
Asx[#]	46.77	30.97	34.62	16.95	24.66	13.80
Glx[$]	2.38	3.71	3.62	2.42	3.31	5.69
Ser	6.09	6.91	5.62	0.46	6.46	6.93
Gly	14.16	16.59	21.92	25.28	30.27	21.76
His	5.13	8.26	3.47	0.76	1.15	4.70
Thr	4.90	6.97	6.02	6.38	2.47	5.17
Arg	6.71	7.04	6.34	6.16	3.69	4.64
Ala	1.17	6.35	4.14	9.24	7.41	9.01
Tyr	6.83	2.47	1.30	0.50	1.94	2.63
Cys	-[*]	-	-	-	-	-
Val	0.35	1.80	1.39	3.49	1.32	3.81
Met	-	-	-	-	-	-
Phe	2.43	1.65	2.29	0.87	-	7.34
Ile	1.72	2.29	2.83	5.86	1.84	4.39
Leu	1.35	2.90	2.53	7.31	6.14	6.89
Lys	-	2.08	3.92	14.31	9.33	3.25

[#] Indicates the sum of Asp and Asn
[$] Indicates the sum of Glu and Gln
[*] Not quantified

2.3.3. Overgrowth of $CaCO_3$ onto coral skeleton sections

The results of the $CaCO_3$ overgrowth experiments onto coral skeleton cross sections are illustrated in Fig. 2.4. As substrate a surface section, normal to the oral-aboral axis, close to the growing tips, was used. The growing media was a 10 mM $CaCl_2$ solution. $CaCO_3$ crystals were observed sticking onto the skeleton cross sections and outside them (on the surface of the embedding resin). The overgrowth of aragonite was always observed onto the surface of the skeletons. These crystals appeared as long hexagonal needles in different orientations, probably reflecting the orientation of the underlying fibers of aragonite. The average cross section of these prisms was about 2 µm for *L. pertusa* and *M. caliculata* and less than 1 µm for *A. digitifera*. Onto the coral skeleton of *L. pertusa* and *M. caliculata* calcite crystals were also observed. Outside the skeleton of *A. digitifera*, *L. pertusa* and *M. caliculata* the precipitation of aggregates of needle-like crystals of aragonite (Fig. 2.4 *AD*2), of rhombohedral {10.4}calcite crystals (Fig. 2.4 *LPE*2) and of aragonite crystals and calcite crystals showing {hk.0} and {10.4} faces (Fig. 2.4 *MC*2), respectively, was observed.

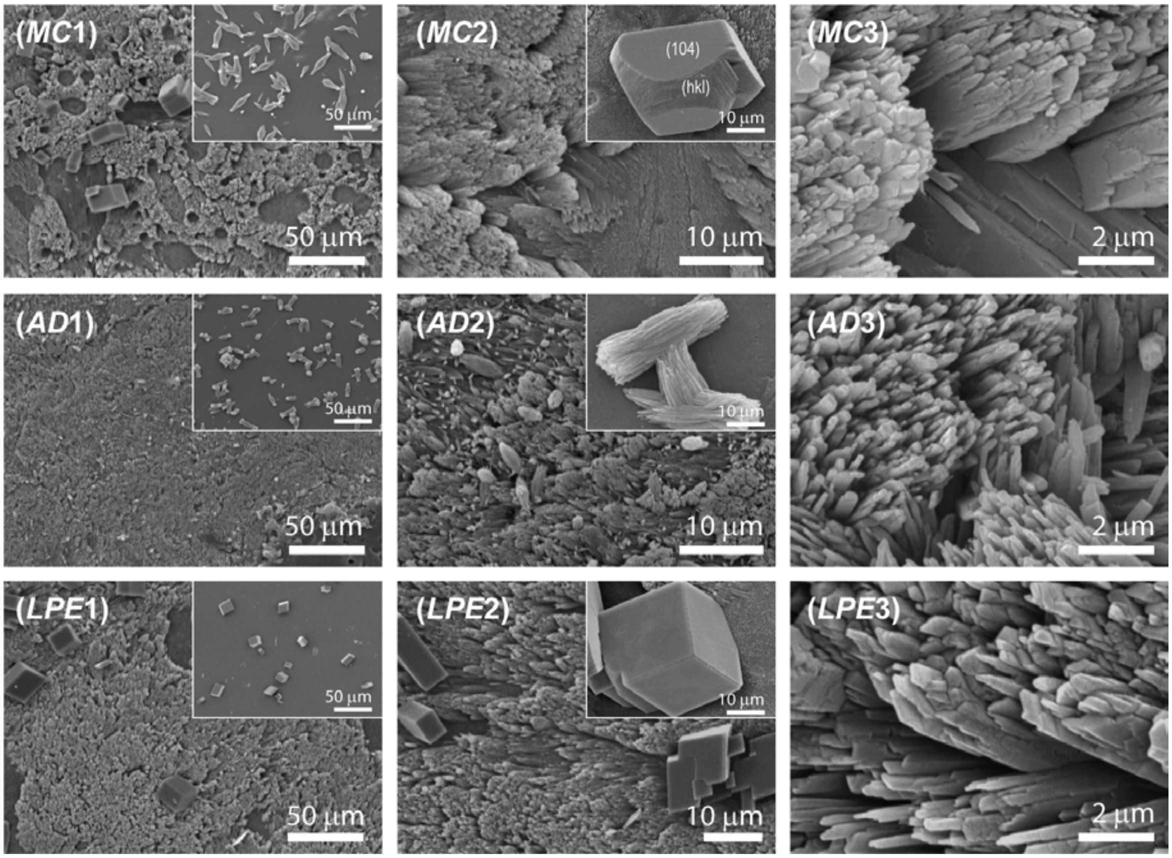

Figure 2.4: SEM pictures at increasing magnifications (1–3) of sections of coral skeleton of *A. digitifera* (*AD*), *L. pertusa* (*LPE*) and *M. caliculata* (*MC*) after the calcium carbonate overgrowth experiment. The insets in *AC*1, *LPE*1 and *MC*1 show the crystals precipitated outside the coral skeleton. The inset in *AD*2 shows a magnification of an aragonite crystal overgrown outside the skeleton. The insets in *LP*2 and *MC*2 show magnification of calcite crystals (over)grown on the coral skeleton section. The crystals of calcite overgrown on *M. caliculata* showed an additional {hk.0} faces other than the {10.4} faces. These crystals also appeared outside the skeleton with the precipitated aragonite ones. Their extension was generally higher in the crystals observed on the skeleton than outside it.

2.3.4 Precipitation of $CaCO_3$ in the presence of OM fractions and magnesium ions

In a first set of experiments the precipitation of $CaCO_3$ from 10 mM $CaCl_2$ solutions containing the OM fractions was studied. In the absence of OM only rhombohedral calcite crystals precipitated (Fig. 2.5). The presence of OM fractions changed the particles' morphology and the polymorphism of the precipitated $CaCO_3$. This presence induced also an inhibition of the precipitation and a reduction of average particle sizes (Fig. 2.6 and Table 2.4). Six crystallization experiments were carried out for each combination using different batches of OM components. The reported results summarize the observed trends (Table 2.5). The presence of SOM (c_s = 0.44 mg/mL) always induced an aggregation of the $CaCO_3$ particles (Fig. 2.6 SOM). In the presence of *M. caliculata* SOM peanut and dumbbell shaped aggregates were observed; these shapes appeared to be formed by the association of nanometric sub-particles (Fig. 2.6 SOM *MC*, inset). In the presence of *A. digitifera* SOM dumbbells and spherical aggregates were also observed, but differing from the previous case, these particles showed surfaces formed by stacked multilayers (Fig. 2.6 SOM *AD*, inset). In the presence of *L. pertusa* SOM many different shapes were observed. The most representative one was that of spherical particles formed by the aggregation of nanoparticles (Fig. 2.6 SOM *LPE*, inset) and showing a rough superficial mammillated topography.[120] The FTIR spectra of these precipitates always showed the characteristic absorption bands of calcite (ν_3 = 1420 cm^{-1}; ν_2 = 875 cm^{-1}; ν_4 = 712 cm^{-1}) plus additional bands. In the presence of *M. caliculata* SOM additional bands at 1082 cm^{-1}, 1030 cm^{-1} and 1474 cm^{-1} were observed together with a relative weakening of the band at 712 cm^{-1}. These features may agree with the co-presence of amorphous calcium carbonate (ACC).[12] In the presence of *L. pertusa* SOM the other bands were at 1487 cm^{-1}, 1464 cm^{-1}, 1437 cm^{-1} and 744 cm^{-1}, suggesting the co-precipitation of vaterite (Table 2.4). In the presence of dispersed IOM (c_i = 0.625 mg/mL), that sometime floated at the air-solution interface, the deposition of mineral particles was mainly observed on the IOM surface. The

FTIR spectra showed the presence of the typical absorption bands of calcite, together with those of IOM. Onto IOM from *M. caliculata*, *L. pertusa* or *A. digitifera* calcite crystals showing truncation of rhombohedral corners and edges (Fig. 2.6 IOM and insets) were observed. Rare crystals like those precipitated in presence of SOM and spherulitic particles were also observed with IOM form *M. caliculata* and *A. digitifera*, respectively. The co-presence of SOM (c_s) and IOM (c_i) favored the precipitation of small particles clustered into big aggregates (Fig. 2.6 SOM + IOM and insets). With *M. caliculata* and *A. digitifera* OM fractions the surface of the IOM was covered by particles having a rough surface formed by the aggregation of nanoparticles. In the presence of *L. pertusa* SOM and IOM particles having the shapes and the morphologies observed in the presence of the two single fractions were observed. The distribution among these shapes and morphologies changed from one experiment to another (Fig. 2.6 SOM + IOM). The FTIR spectra of these materials showed the same absorption bands observed in the presence of SOM. In the presence of *A. digitifera* SOM and IOM absorption bands (1457 and 744 cm^{-1}) associable to vaterite were also observed.

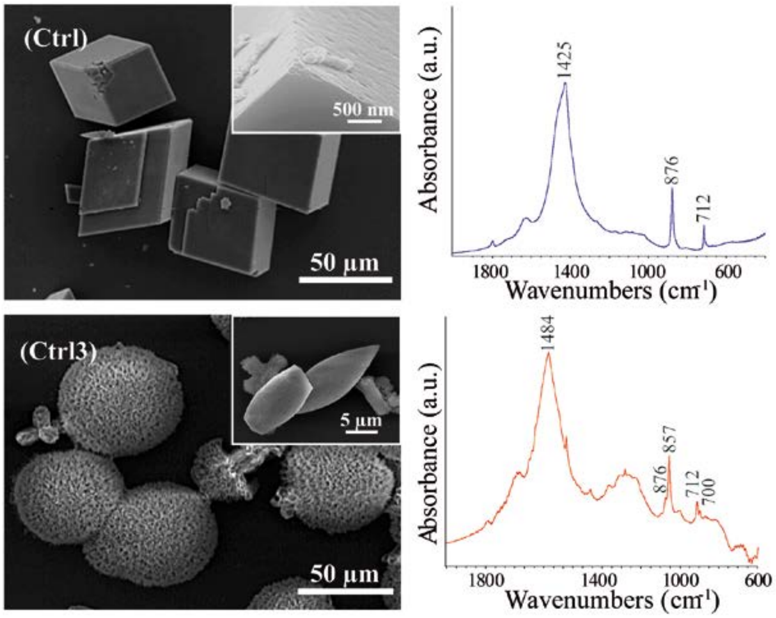

Figure 2.5: Scanning electron microscopy pictures of calcium carbonate precipitated in the absence of OM fractions from a 10 mM $CaCl_2$ solution (Ctrl) and from a 10 mM $CaCl_2$ solution containing magnesium ions with a Mg/Ca molar ratio equal to 3 (Ctrl3). On the right of the figure the respective FTIR spectra are shown.

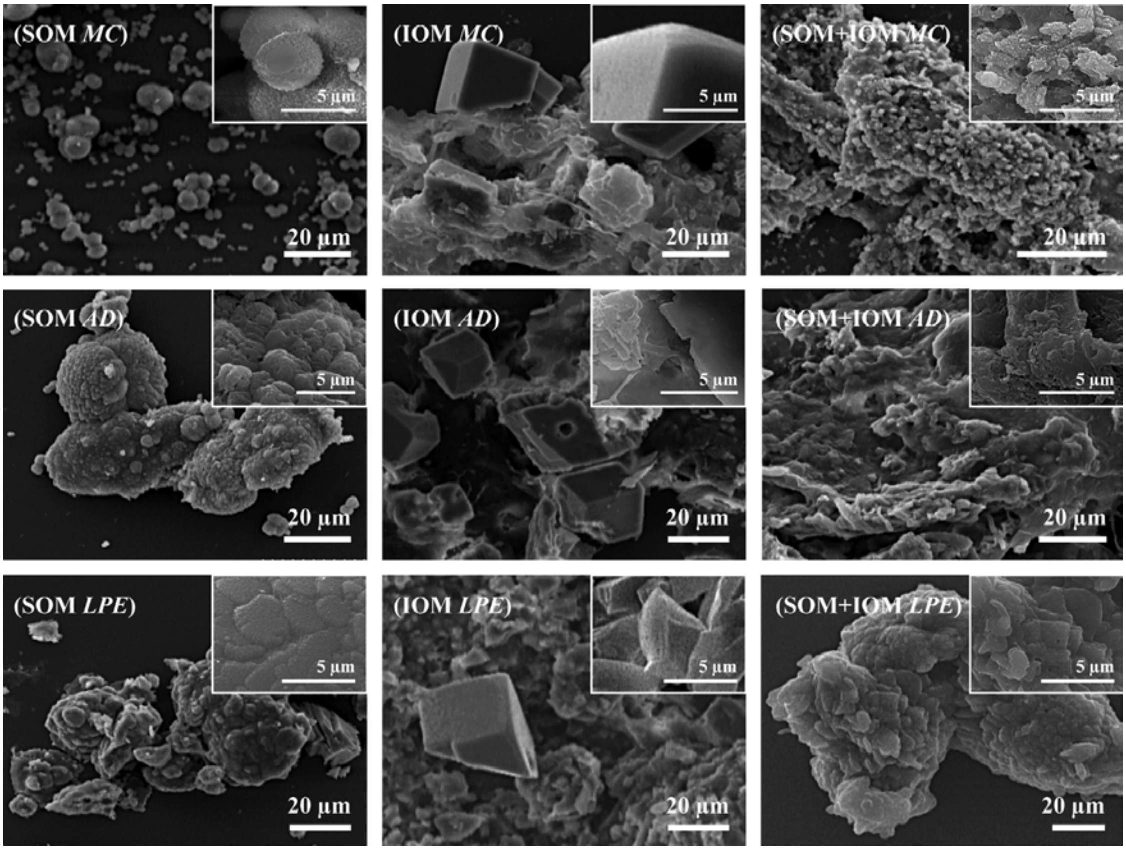

Figure 2.6: SEM pictures of particles obtained from precipitation experiments of $CaCO_3$ from 10 mM $CaCl_2$ solutions in the presence of OM fractions. In the first, second and third columns are shown particles obtained in the presence of SOM, IOM and SOM + IOM, respectively. The first, second and third rows refer to the extracts from, *M. caliculata* (*MC*), *A. digitifera* (*AD*) and *L. pertusa* (*LPE*), respectively. In the insets are reported high magnification pictures of the particles. The calcite crystals on IOMs showed a light truncation of rhombohedral {104} corners and edges (probably the presence of small {108} and {hk0} faces). These pictures are the most representative of the populations of observed particles.

Table 2.4: Features $CaCO_3$ particles precipitated in a 10 mM $CaCl_2$ solution with or without Mg ions with Mg/Ca molar ratio equal to 3 using as additives SOM (cs = 0.44 mg/mL), IOM (ci = 0.50 mg) or both of them, SOM (cs) + IOM (ci). The additives were extracted from the skeleton of *A. digitifera* (AD), *M. caliculata* (MC) and *L. pertusa* (LPE). When two phases were obtained the main one is indicated as first.

	Ca solution												Mg/Ca solution											
				SOM			IOM			SOM + IOM						SOM			IOM			SOM + IOM		
	p	*s*	*D*	*p*	*s*	*d*	*p*	*s*	*d*	*p*	*s*	*d*	*p*	*s*	*d*	*P*	*s*	*d*	*p*	*s*	*d*	*p*	*s*	*d*
MC	C	rh	30	C	pn, db	5	C	rh	20	C	sp	4	A	sp	45	MgC	db	4	MgC	sp	5	MgC	db	3
				ACC	nd					ACC	nd		MgC	rd	5	ACC	nd					ACC	nd	
AD	C	rh	30	C	db, sp	9	C	rh	40	C	sp	4	A	sp	45	MgC	db	6	A	sp	56	MgC	db	6
										V			MgC	rd	5	ACC	nd		MgC	rd		ACC	nd	
LPE	C	rh	30	C	sp	9	C	rh	45	C	sp	3	A	sp	45	MgC	db	3	MgC	sp	7	MgC	db	6
				V	sp					V			MgC	rd	5	ACC	nd		A	nd		ACC	nd	

C, A, V, MgC and ACC indicate calcite, aragonite, vaterite, magnesium calcite and amorphous calcium carbonate, respectively. p, s and d indicate phase, shape and average size along the main axis (lm) of the $CaCO_3$ precipitated particles. In the case of V and ACC the size of particles or aggregates was in a very wide range of dimensions such to make the average size not significant. In these cases is not reported. The shapes were named according to the literature[63, 120, 121]; rh = rhombohedra; pn = peanuts; db = dumbbells; sp = spherulites, nd = not definable shape originated by the aggregation of nano-sized spherical particles.

A second set of $CaCO_3$ precipitation experiments was conducted using a 10 mM $CaCl_2$ with Mg/Ca molar ratio equal to 3, solution to which SOM, IOM or SOM plus IOM were added. The co-presence of Mg ions and OM fractions had an inhibitory effect on the precipitation process and caused, once more, variability in the $CaCO_3$ polymorphism and morphology of the precipitates (Table 2.5), the presented results reveal a general trend (Fig. 2.7, Table 2.4). In the absence of OM fractions crystals elongated along the c-axis and needle shaped crystal aggregates typical of magnesium calcite and aragonite, respectively, were observed (Fig. 2.5) together with rare botryoidal aggregates. The addition of c_s of SOM provoked a strong inhibition of the precipitation and only few aggregates were observed (Fig. 2.7 SOM and insets). The FTIR spectra of these materials showed only typical absorption bands of magnesium calcite (ν_2 band at 876 cm^{-1}) and suggested the presence of ACC (very weak ν_4 band at 712 cm^{-1} and splitting of the ν_3 band at 1462 and 1420 cm^{-1}). These aggregates showed the rod, dumbbell and, sometimes, spherical shapes, already observed in the control experiments; however, sometimes in the presence of *L. pertusa* and *A. digitifera* SOMs the particles' crystalline habits were partially or completely lost (Fig. 2.7 SOM *LPE*) and the particle surfaces were quite smooth (Fig. 2.7 SOM *AD*, inset). In the presence of IOM the precipitate was observed on and around it. The mineral particles appeared elongated and showed spherulitic aggregation (Fig. 2.7 IOM). In the presence of *A. digitifera* and *M. caliculata* IOM, and particularly of *L. pertusa* IOM, the particles observed on the IOM lose their crystalline habit (Fig. 2.7 IOM). The FTIR spectra of these materials showed the same absorption bands of magnesium calcite (875/6 cm^{-1}) and aragonite (858 cm^{-1}) observed in the absence of OM. However, in some cases the band at 858 cm^{-1} was not observed. Once more the calcitic ν_4 band was very weak compared to the ν_2 one. In the co-presence of SOM and IOM a strong inhibition of the $CaCO_3$ precipitation was observed and only few particles precipitated outside the IOM. In the presence of *M. caliculata* OM fractions these particles grew also on the IOM (Fig. 2.7 SOM + IOM *MC*). In the presence of *A. digitifera* and *L. pertusa* OM fractions the IOM was covered by aggregates of nanoparticles (Fig. 2.7 SOM + IOM *AD*, inset) and the mineral particles showed an irregular framboid spherical shape surface (Fig. 2.7 SOM + IOM *LPE*), respectively. The FTIR spectra of these materials showed the same pattern observed in presence of only SOM. Broad absorption bands at 1030 cm^{-1} and 1082 cm^{-1} were also present.

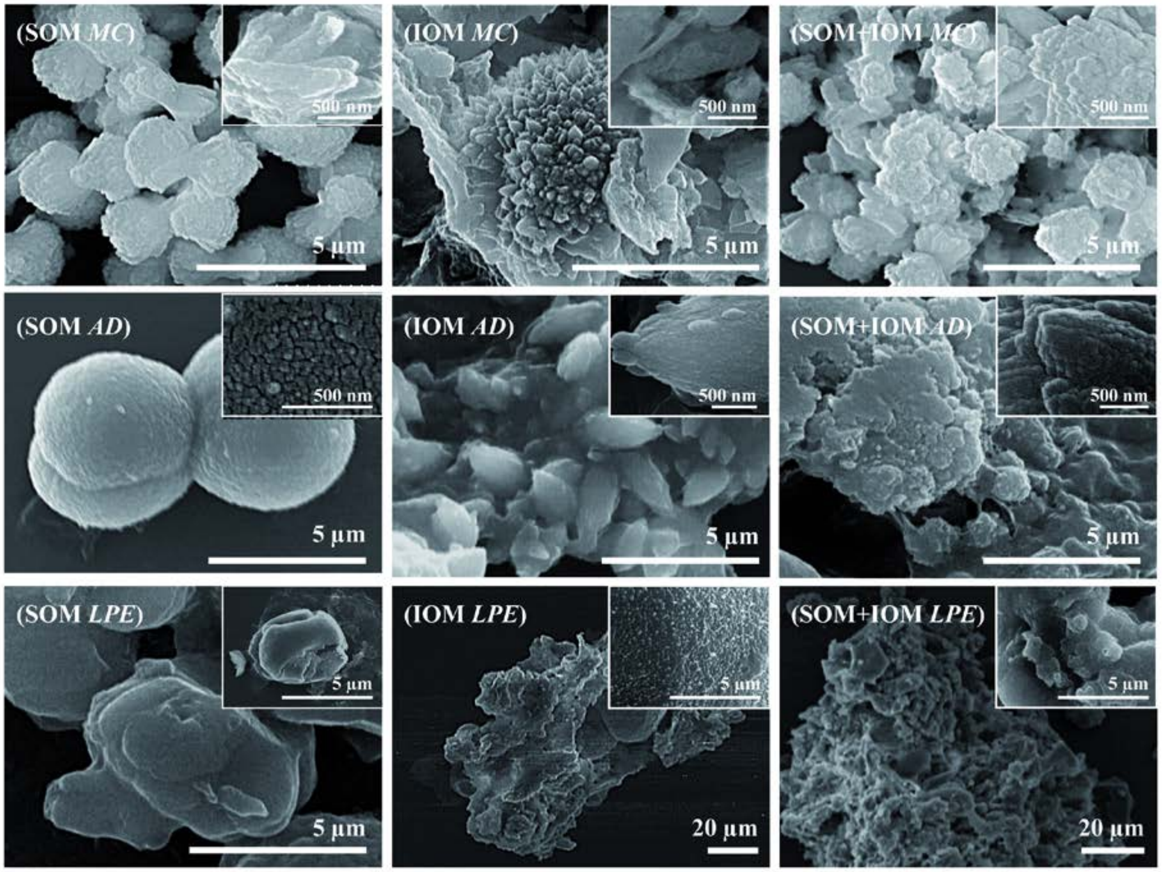

Figure 2.7: SEM pictures of particles obtained from precipitation experiments of $CaCO_3$ from 10 mM $CaCl_2$ solutions with Mg/Ca ratio equal 3 in the presence of OM fractions. In the first, second and third columns are shown particles obtained in the presence of SOM, IOM and SOM + IOM, respectively. The first, second and third rows refer to the extracts from *M. caliculata* (*MC*), *A. digitifera* (*AD*), and *L. pertusa* (*LPE*), respectively. In the insets are reported high magnification pictures of the particles. These pictures are the most representative of the populations of observed particles.

Table 2.5: Results of all the crystallization experiments with soluble (SOM), insoluble (IOM) or both (SOM+IOM) organic matrix fractions in a 10 mM calcium chloride solutions with Mg ions (Mg/Ca molar ratio equal to 3; Ctrl3) or without (Ctrl) Mg ions. The OM fraction were extracted from the skeleton of *A. digitifera* (AD), *M. caliculata* (MC) and *L. pertusa* (LPE). The activity of the OM fractions was evaluated checking their promoting or inhibiting role in the precipitation of aragonite with respect to the control experiment. In some cases was observed the precipitation of vaterite (V) and amorphous calcium carbonate (ACC) parenthetical indicated in this table along the times that were observed.

MC	**SOM**			**IOM**			**SOM + IOM**		
N=6	promotes A	inhibits A	no effect	promotes A	inhibits A	no effect	promotes A	inhibits A	no effect
Ctrl			**6** (5 ACC)			**6**			**6** (6ACC)
Ctrl3		**5** (3 ACC)	1	2	**4** (1 ACC)			**5** (3 ACC)	1

AD	**SOM**			**IOM**			**SOM+IOM**		
N=6	promotes A	inhibits A	no effect	promotes	inhibits A	no effect	promotes A	inhibits A	no effect
Ctrl			**6** (1V)			**6** (2ACC)			**6** (4V)
Ctrl3	1	**5** (5ACC)		1	**3**	2	2	**4** (3ACC)	

LPE	**SOM**			**IOM**			**SOM+IOM**		
N=6	promotes A	inhibits A	no effect	Promotes A	inhibits A	no effect	promotes A	inhibits A	no effect
Ctrl			**6** (4V)			**6**			**6** (3V)
Ctrl3		**5** (3ACC)	1		**4**	2		**5** (3ACC)	1

N indicates the total number of replica. In bold the number of replica which gave the reported general trend. Each replica was carried out starting from a new batch of OM fractions extracted from different skeletons of the same species.

2.3.5. AFM observations of $CaCO_3$ precipitated in the presence of OM fractions

Precipitates obtained using the OM fractions extracted from *M. caliculata*, *L. pertusa* and *A. digitifera*, with or without Mg, have been studied by AFM. Only the data related to *M. caliculata* are presented here. The shape of the mineral precipitations is better seen with SEM, but similar morphologies have been observed. The surface of the precipitates obtained with the SOM of *M. caliculata* was rough and composite in height (= morphological) images (Fig. 2.8a). They were probably dispersed in a thin OM. Phase images show that the elements seen in height images were composed of granules, the shape and size of which were irregular (Fig. 2.8b). However, the observed morphologies of these granules were not like those of purely crystalline minerals: they were devoid of angle and facets. These granules were surrounded by a more or less distinct cortex (Fig. 2.8b). The color of each granule is non uniform in phase images, indicative of a heterogeneous composition. The precipitates obtained using IOM of *M. caliculata* were rhombohedral, as seen using SEM. Height images showed a layered structure with rounded denticulate outlines (Fig. 2.8c). The phase image shows that the layers were not compact and they were rich in OM (in black in Fig. 2.8d). Again, granules within a layer are heterogeneous in composition, and irregular in shape and size. Shapes obtained using SOM and IOM differ: the units were elongated and composite (Fig. 2.8e, f), with nano growth lines (Fig. 2.8f). Rounded granules were also present. Addition of Mg to the SOM of *M. caliculata* resulted in various morphologies (Fig. 2.8g, h). Nevertheless, granules within these precipitates were irregular in shape and size (Fig. 2.8g), while the elongated units showed faint growth lines (Fig. 2.8h). Addition of IOM generated flat units (Fig. 2.8i), the inner structure of which consisted of rounded granules (Fig. 2.8j). The mixture of SOM, IOM and Ca/Mg leads to more angular crystals (Fig. 2.8k), but as for the previous samples, granules were heterogeneous in composition and surrounded by a cortex (Fig. 2.8l).

2.4 Discussion

Corals challenge some widespread notions about biomineralization and the importance of OM components in promoting and organizing mineral growth. They do incorporate organic materials into their skeletons, but they do not shape or organize their skeletal crystals with anything approaching the care seen in molluscan shells.[1, 64] However, corals calcify a hundred times faster than inorganic calcification rates on the reef, and faster than most other animals, and thereby display a strong command over the biomineralization process.[109] Despite the fact that an extracellular calcification occurs outside the ectodermal cell layer, the control of skeletal organization remains an unresolved question.[79]

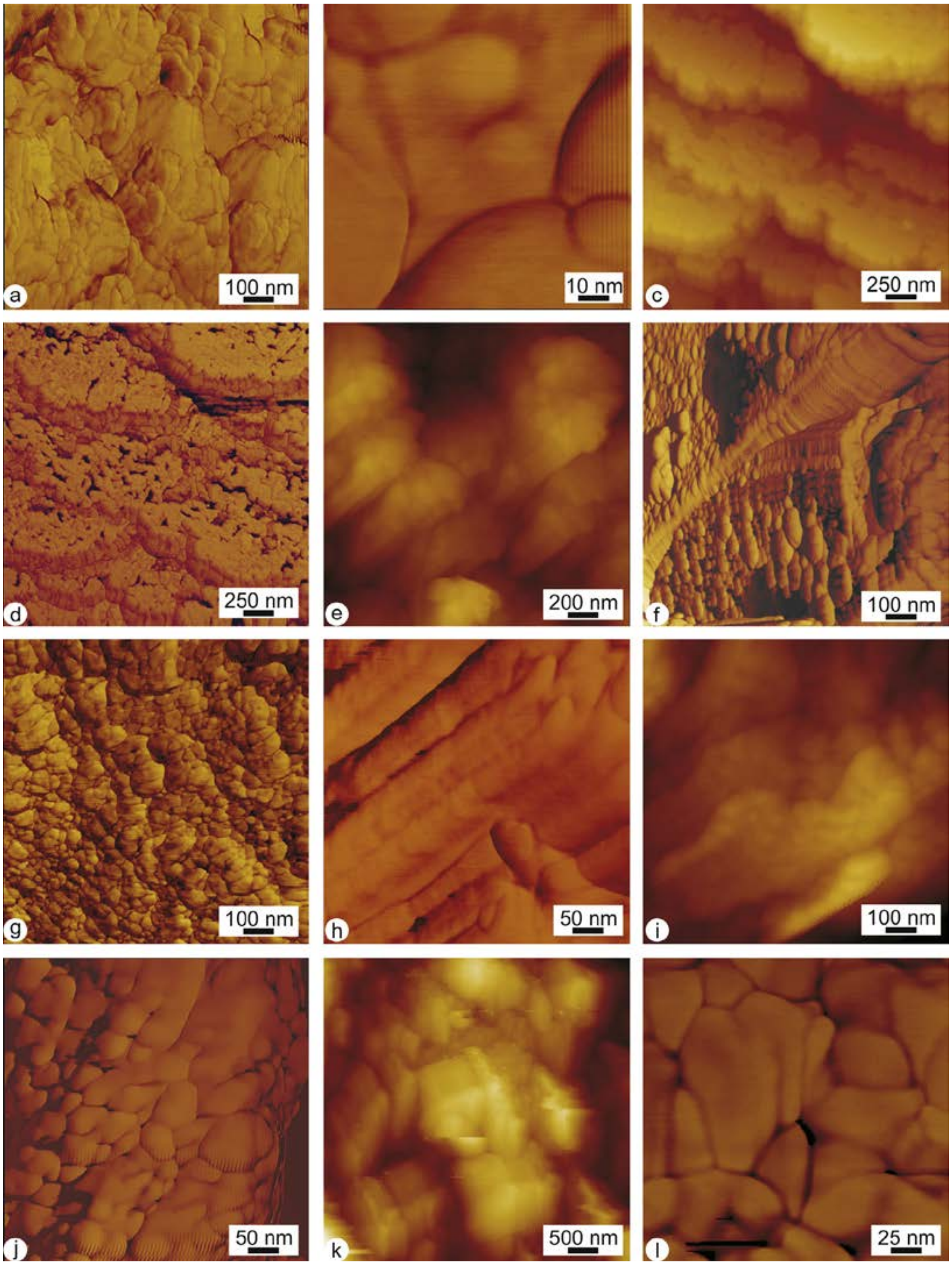

Figure 2.8: AFM images of crystallization experiments using OM extracted from *M. caliculata*. a–b: 10 mM $CaCl_2$ solution and SOM; irregular rounded granules; phase image. c–d: 10 mM $CaCl_2$ solution and IOM; lamellar units are a mixture of organic and minerals components as shown in phase image (d). e–f: 10 mM $CaCl_2$ solution and SOM and IOM; height image showing elongated granular units (e); phase image confirms the presence of granules and thin growth lines (f). g–h: 10 mM $CaCl_2$ solution and SOM with Mg/Ca ratio equal 3; granular structures (g) and elongated, but not flat units (h) in phase images. i–j: 10 mM $CaCl_2$ solution and IOM with Mg/Ca ratio equal 3; flat units (i, height image) are composed of round granules (j, phase image). k–l: 10 mM $CaCl_2$ solution and SOM and IOM with Mg/Ca ratio equal 3; height image showing angular shape of the precipitation (k), but the inner structure is granular without any facets (l, phase image).

In this study the skeleton from three colonial coral species, *A. digitifera*, *M. caliculata* and *L. pertusa* was used. *A. digitifera* and *M. caliculata* are tropical corals living in hot waters, while *L. pertusa* lives on the North Atlantic coast in cold waters. *A. digitifera* shows a rate of calcification higher than the other two species.[122] The skeleton of these species, as that of all corals, shows differences in the textural organization of the fibers and EMZ zone regions.[90, 123] This species specific difference comes from the coral's biological activities in which, among many processes (i.e. ion trafficking[97]), there is the release of the OM molecules in the confined extracellular calcification site.[102] Some of these molecules are then entrapped in the forming mineral phase, with which they interact. If these molecules are subject to re-organization,[124] and eventually degradation, while being hosted in the mineral matrix is still unclear.[64] It has been demonstrated that in mollusk shells the OM control on the biomineralization process requires that specific macromolecules are located in a specific gelling environment.[48, 51, 116] Much less information is available for corals on the mechanism of action of the OM molecules. The general features of OM from the three species of the studied corals are quite similar, but different in several aspects from those associated to mollusk shells. The OM matrix content ranges around 2.5% (w/w), but is lower in *A. digitifera*, in agreement with what reported for other coral species.[117] The fact that the amount of extracted OM is one order of magnitude lower, around 0.2% (w/w), is due to the extraction procedure, as also observed by other researchers.[94] The relative mass amount of the two fractions of OM shows a significant higher content of SOM than IOM. This, that occurs in *A. digitifera* (5 to 1) more than in *M. caliculata* (1.4 to 1) and *L. pertusa* (1.5 to 1), is not observed in mollusk shells where the IOM, which builds the scaffold on which the mineralization occurs, is the dominant fraction.[125] A high content of intra-crystalline SOM with respect to IOM is observed in organisms like algae, in which a lower control on the mineral deposition is present.[1] OM from corals shows also other peculiarities. The SOM from *A. digitifera* is very rich in aspartate residues compared with other species and mollusk shells.[125] It was shown that aspartate sequences have an important role in the control of calcium carbonate precipitation.[27, 126] The IOMs are acidic (about 20 mol% of aspartate). This is unusual since the IOM is typically rich in hydrophobic residues, which also represent a significant fraction of coral IOMs (about 45 mol%). IOMs are also significantly rich in lipids, as was already reported for other coral species in the whole OM.[43] Lipids could have a role in the mineralization process.[45, 127] Goffredo *et al.*[79] observed that the OM from *B. europaea* devoid of lipids was unable to stabilize ACC. Recently, and importantly, several researchers suggested that lipids can be involved in processes of ionic trafficking (see ref. 46 and references therein), although different processes were suggested to be present in corals.[97] The conformation of proteins in SOM appears to be mainly in α-helix or random coil, while in IOM is mainly in β-sheet. Other characterizations of coral OM, which focused only on the SOM, confirmed the absence of β-sheet conformation in it.[37, 92, 93] These different conformations could play a role in discriminating the molecules' aggregation and solubility.[128] It was shown that in corals SOM and IOM are constituted by the same macromolecules, in the IOM richer in high molecular weight, and less hydrophilic, than those in SOM.[79] Thus, it cannot be excluded that the extraction procedure could be partially responsible of familiarization in SOM and IOM. The above observations narrow, at least for corals, the distinction between IOM and SOM. *A. digitifera* produces almost only SOM that does not stain bands after the SDS–PAGE, suggesting that it is composed of low molecular weight acidic molecules (pI = 3.7) very mobile[129] and with low tendency to aggregate and precipitate in water. SOM and IOM are both present in the OM matrix of *M. caliculata* and *L. pertusa*. These acidic IOMs have a tendency to form a gel. Very importantly it was recently demonstrated using ''proto-polyp'' cell cultures from *Stylophora pistillata* that the precipitation of aragonite occurs in a gel environment.[130]

The capability of intra-crystalline OM molecules to influence the precipitation of $CaCO_3$ was studied both by $CaCO_3$ overgrowth on the coral skeleton sections and by $CaCO_3$ precipitation from solutions.

Overgrowth experiments allow to study specific crystal-macromolecules interactions under conditions that minimally affect the macromolecules native state.[55] They are certainly more conducive to preserving their structure that after isolation and separation procedures. Moreover, not all the intra-skeletal macromolecules could be released by the skeletal elements. The presence of aragonite overgrowth on the coral skeleton suggests a capability of the OM components to stabilize this polymorph, even in the absence of magnesium ions. However, the possibility of a direct secondary nucleation on aragonite cannot be excluded, unless aragonite was observed as unique phase outside the skeleton. Aragonite was likewise observed in the precipitate as the unique phase when *A. digitifera* skeleton was used. This observation can be related to the peculiar features of the OM of *A. digitifera* described above. On the surface of *M. caliculata* and *L. pertusa* was observed the co-presence of calcite crystals, as well on the surrounding of the skeleton. In *L. pertusa* calcite crystals growth was not affected by the OM molecules and they showed only the cleavage {10.4} faces of calcite. This was not the case of the ones that grew on the skeleton of *M. caliculata*, where additional {hk.0} faces developed as a result of selective re-adsorption of the soluble macromolecules released from the coral skeleton.[98] The higher expression of the {hk.0} faces in the crystals on the skeleton with respect to those outside it, could be related to the diffusion process of the macromolecules. In *M. caliculata* aragonite precipitation was observed also outside the skeleton. These divergent results have to be related to the release of different OM molecules from diverse skeletons species. Indeed, different distributions of families of molecules were observed (see FTIR, AAA and SDS–PAGE data).

Calcium carbonate precipitation experiments were also conducted to evaluate the SOM and IOM fractions influence on the calcification process (Table 2.4). This was done using an in vitro assay[36] far from the real biological environment, but able to simulate the mineralization process by increasing concentration of carbonate ions. In the absence of magnesium ions, and in the presence of the OM fractions, the precipitation of calcite was always observed. The presence of SOM stabilized also the precipitation of ACC and vaterite in *M. caliculata* and *L. pertusa*, respectively. The SOM from *A. digitifera*, once more, acted diversely having no effect on the polymorphism of $CaCO_3$ (i.e. only calcite precipitated). However, in this set of experiments the main effect of OM fractions was on the precipitate's morphology. Aggregates of calcite particles having the shape of dumbbells, rods and peanuts[63, 121] were observed in the presence of the SOM from all the species. These aggregates always appeared to be formed by the assembly of sub micron sized particles, and the AFM observations showed that they were covered by an organic shell. The granular structure suggests that their precipitation occurred by a non-classical mechanism in which the precipitation took place by the assembly of preformed units.[131] Indeed, the coral skeleton is composed of nanosized grains.[57, 115] The precipitation of these particles may occur through a transient ACC phase under conditions of high supersaturation.[131] Accordingly, the presence of SOM from *M. caliculata* seems to stabilize ACC.

In the magnesium ions free $CaCO_3$ precipitation experiments aragonite was observed only when few components of the SOM were released in solution (i.e. overgrowth experiments), but not when all the extracted components of the OM were in solution. It should be also considered that in the extraction procedure the low molecular weight (MW < 3500 Da) molecules are lost, and they could have a role in the control of the precipitation process. Moreover, in corals, the calicoblasts express and secret in the nucleation site the OM molecules at different times and spaces. Thus, the use of all the extracted intra-crystalline molecules, considering the denaturation associated to the extraction process, could bring to lower level of polymorphism control on the precipitation of $CaCO_3$ *in vitro*. However, these molecules influence the morphology of the precipitating phase.

The presence of magnesium ions in the extracytoplasmic calcifying fluid, at the nucleation site of corals, has been reported.[111, 132] The analysis of the results of the $CaCO_3$ precipitation in the presence of magnesium ions and OM fractions show, differently from what observed in their absence, a strong effect on the polymorphism and a lower effect on the morphology of the precipitated particles. While in the control experiments the coprecipitation of magnesium calcite and aragonite was observed in the presence of SOM from all the species the precipitation of aragonite was inhibited and that of ACC favored. Magnesium ions have an inhibitory effect on the precipitation of $CaCO_3$, while they stabilize ACC in the presence of additives.[12, 133] As a seemingly opposite effect, magnesium ions favor the precipitation of aragonite.[28, 52, 134] This apparent dichotomy could be explained by considering the role of OM components. Some of these components having strong affinity for aragonite (they are in an aragonitic skeleton) could interact with the aragonite nuclei inhibiting their growth, favoring the precipitation of other phases, and changing the final crystal's shape. Thus, from these observations it seems that magnesium ions, together with some specific OM molecules, could play also important roles in the control of fibers' shape (i.e. fibers length) in the coral skeleton.[57]

2.5. Conclusion

This work on the intra-crystalline OM from *M. caliculata*, *A. digitifera* and *L. pertusa*, and its influence of the precipitation of $CaCO_3$ shows that (*i*) among species the OM has similar chemical features that differs from that from mollusk shell; (*ii*) the OM from *A. digitifera* appears more acidic and formed by a family of more soluble small molecules which are less prone to aggregate with respect to those from *M. caliculata* and *L. pertusa*; (*iii*) OM molecules of *A. digitifera* are able to induce the deposition only of aragonite in CaCO3 overgrowth experiments; (*iv*) in the presence of OM fractions and magnesium ions the SOM inhibits the precipitation of aragonite and induces changes in the morphology of calcite, which are species specific; (*v*) the peculiarity OM molecules from *A. digitifera* could be involved in the control of the high calcifying rate of this species. Thus, based on our results we may safely conclude that the OM components and magnesium ions influence, in species specific way, the fine scale characteristics of the crystals of which the coral skeleton is constructed.

This work has been published (see Falini G, Reggi M, Fermani S, Sparla F, Goffredi S, Levy O, Dubinsky Z, Dauphin Y, Cuif JP. Control of aragonite deposition in colonial corals by intra-skeletal macromolecules. Journal of Structural Biology. 2013, 183: 226-238.)

3. Biomineralization in Mediterranean corals: The role of the intra-skeletal organic matrix

3.1. Introduction

The influence of coral intra-skeletal OM molecules in the precipitation of $CaCO_3$ was proved for the tropical species *Acropora digitifera*, *Lophelia pertusa* and *Montipora caliculata*, as described in chapter 3.[135]

This study deepened the investigations using the OM from skeletons of *Leptopsammia pruvoti* (solitary, non-zooxanthellate), *Balanophyllia europaea* (solitary, zooxanthellate), *Astroides calycularis* (colonial, non-zooxanthellate) and *Cladocora caespitosa* (colonial, zooxanthellate). These Mediterranean coral species were chosen because represent the combination among different growth forms and trophic strategies. Solitary corals are single autonomous individuals (polyps), while colonial corals are modular organisms constituted by cloned polyps living in close connection (physical and physiological) one to each other. Symbiosis determines the synthesis of molecules essential to the biomineralization process,[136] such as precursors for the OM.[29, 38, 64, 137] The first link between photosynthesis and calcification was found by Kawaguti and Sakumoto;[138] they pointed out that calcification rate is higher in the light than in the dark.[64, 101, 139] It was also shown that in presence of light the calcification rate is higher in zooxanthellate corals than in non-zooxanthellate corals [81]. However, from a general point of view, it is clear that coral's calcification is not dependent on the presence of symbionts[140] and non-zooxanthellate corals have an efficient calcification as well. Moreover, tissues that calcify at the highest rates, or which initiate calcification, do not possess zooxanthellae[64, 101, 139]. It was also shown that photosynthesis increases calcification rate because fixes CO_2 and increase the skeleton surface pH.[141]

The main goals of this study are: a) to evaluate whether the intra-skeletal OM from different coral species shows a different capability to govern the formation and stability of calcium carbonate precipitates; b) to infer possible relationships between the organism ecology (growth form and trophic strategy) and its OM capabilities.

3.2. Experimental section

Coral skeletons:

The samples of *L. pruvoti*, *B. europaea*, *C. caespitosa* from Calafuria and *A. calycularis* from Palinuro (Italian coast, Nord-Western Mediterranean Sea) were randomly collected by scuba diving at 16, 6 and 9 m depth, respectively, between 1 July 2010 and 25 February 2012 (see Appendix A).

Extraction of the organic matrix:

The soluble (SOM) and the insoluble (IOM) OM fractions were extracted throw decalcification using a 0.1 M CH_3COOH solution as reported above. The whole OM (*w*OM) was obtained using the same procedure without the separation step between SOM and IOM (see Appendix A).

Calcium carbonate crystallization experiments

Overgrowth and crystallization experiments were carried out for vapour diffusion in a crystallization chamber using microplates for cellular culture (see Appendix A). In each well, 750 μL of 10 mM $CaCl_2$ solutions ($CaCl_2.2H_2O$, Merck) or of modified (increased of 10 times the Ca^{2+} and Mg^{2+} concentration) artificial sea water (ASW),[142] were poured. In the first sets of experiments OM fractions, separately or together, were added to 750 μL of 10 mM $CaCl_2$ solution. 8 μL (for *L. pruvoti* and *A. calycularis*) or 20 μL (for *B. europaea* and *C. caespitosa*) of a solution obtained dissolving lyophilized SOM in water (17.5 mg/mL) were added to the solution. This quantity was chosen keeping in consideration SOM concentration in the skeleton [79, 135]. In other wells 0.5 mg of IOM were added to

750 μL of 10 mM $CaCl_2$ solution. SOM and the IOM (*e*OM) were added in the lasts wells. In the second sets of experiment the whole OM (*w*OM) was added to 750 μL of 10 mM $CaCl_2$ solution and to ASW. The quantity of *w*OM added was of 0.4 and 0.2 mg.

Characterization of $CaCO_3$ precipitates

FTIR spectra of samples were collected as described in appendix A.

Atomic absorption measurements. Atomic absorption measurements of calcium and magnesium were carried out with Perkin Elmer AAnalyst 100 flame and graphite furnace (HGA 800) spectrometer equipped with a Zeeman effect background corrector, and an automatic data processor. A 20-μl volume sample solution obtained by precipitated dissolution in 0.1 M HNO_3, was injected by an auto sampler. A multi element hollow cathode lamp of analytes was used as radiation source. Three measurements were carried out for each sample.

Thermal treatment of $CaCO_3$ precipitates. The samples that showed the presence of ACC in the precipitate from ASW solution with *w*OMs were heated at 105° for 18 hr, 36 hr and 72 hr [143]. At the end the same samples were heated at 300° C for 8 hr. FTIR spectra were collected after each thermal treatment.

Differential scanning calorimetry. To detect phase transitions during the heating of ACC precipitated during the crystallization experiments, differential scanning calorimetric (DSC) analyses on a DSC Q100 simultaneous thermal analysis instrument (TA instrument) was carried out. The analysis was performed in nitrogen flow from 30 to 100 °C with a heating rate of 10 °C/ min, an isothermal at 100 °C for 5 min, and another cycle from 120 to 550 °C with a heating rate of 10 °C/ min.

3.3. Results

3.3.1 Skeletal structures of corals

Scanning electron microscope images of septum cross sections showed the typical textural pattern of the coral skeleton (Fig. 3.1): the EMZ was composed of small rounded granules and fibers are produced with a rhythmic growth. EMZs are more sensitive to acidic etching than the fibers[90] and thus appear rich of cavities. Size and spatial distribution of EMZs and fibers vary upon species. In *L. pruvoti* and *B. europaea* the EMZs were observed as shallow cavities from which fibers radially extend having in *L. pruvoti* a smaller diameter and a less compact structure than in *B. europaea* (Fig. 3.1 *LPR*1-3 and *BEU*1-3). In *A. calycularis* in the EMZs were observed as granular particles that cover the fiber tips. In *A. calycularis* and *C. caespitosa* the cavities are deep and episodically aligned parallel to the long axis of the septa and the fibers are similar to those of *B. europaea* (Fig. 3.1 *ACL*1-3 and *CCA*1-3).

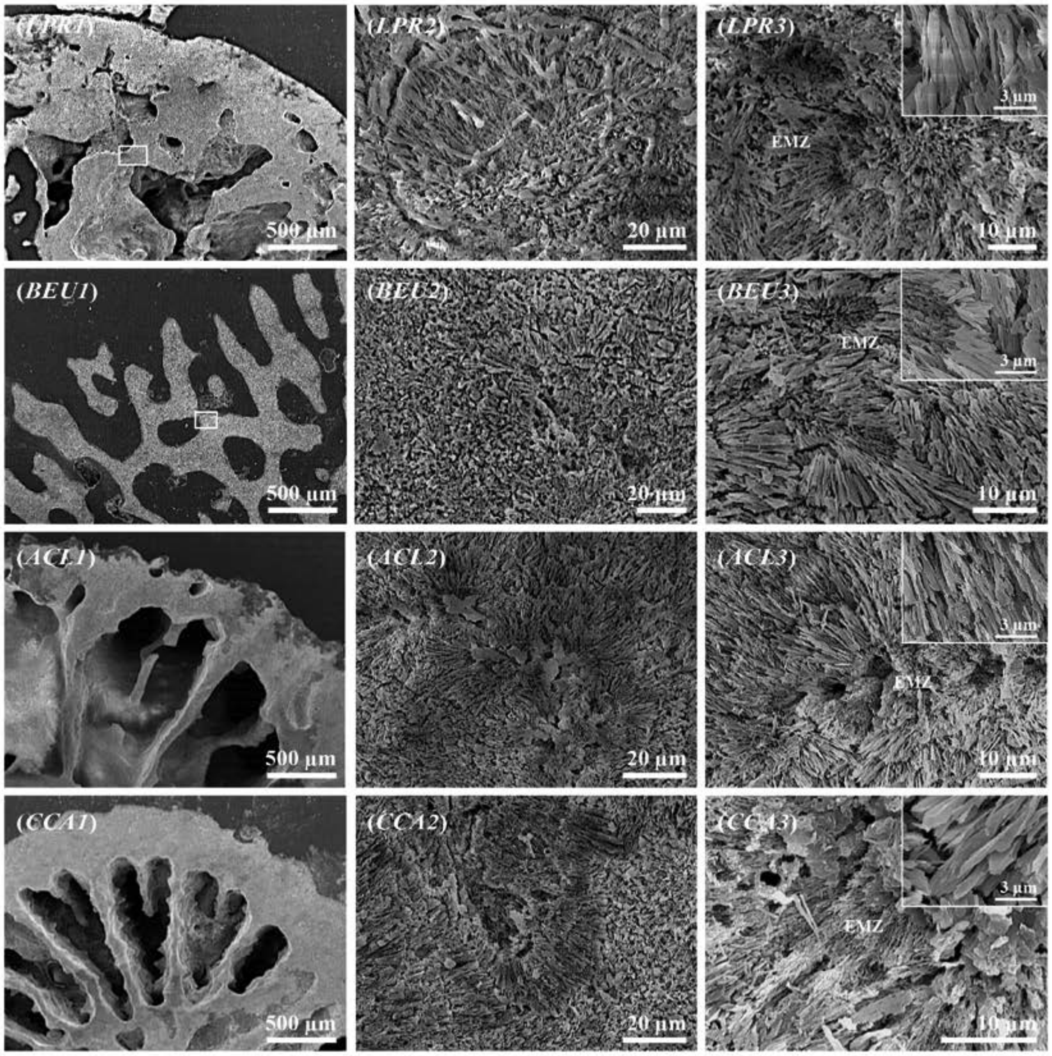

Figure 3.1: SEM pictures at increasing magnifications (1−3) of sections of coral skeleton of *L. pruvoti* (*LPR*), *B. europaea* (*BEU*), *A. calycularis* (*ACL*) and *C. caespitosa* (*CCA*) after etching. The pictures with suffix 3 show early mineralization zones (EMZ) surrounded by fibers, which are shown in the insets at higher magnifications.

3.3.2 Studies on the intra-skeletal OM

In *L. pruvoti*, *B. europaea*, *A. calycularis* and *C. caespitosa* the mineral skeleton hosting the OM was expected to be of pure aragonite; however, in the insoluble residue obtained after decalcification, few silica needles were observed, constantly in *A. calycularis* and rarely in the other species. The presence of this impurity, which was not possible to remove, was considered not influencing the calcium carbonate precipitation assays. The skeleton TGA showed a first weight loss (bounded water) in the range 150-220 °C followed by a second one (OM pyrolysis) between 280 and 450 °C (Fig. 3.2).[117] The overall weight loss was of 3.4 ± 0.1, 3.9 ± 0.1, 3.5 ± 0.1 and 3.4 ± 0.1 % (*w*/*w*) in *L. pruvoti*, *B. europaea, A. calycularis* and *C. caespitosa*, respectively (Table1, OM composition). After extraction the OM separated in SOM and IOM fractions; the median amount of IOM was higher than that of SOM in all species, except in *B. europaea* (Table 3.1, OM composition).

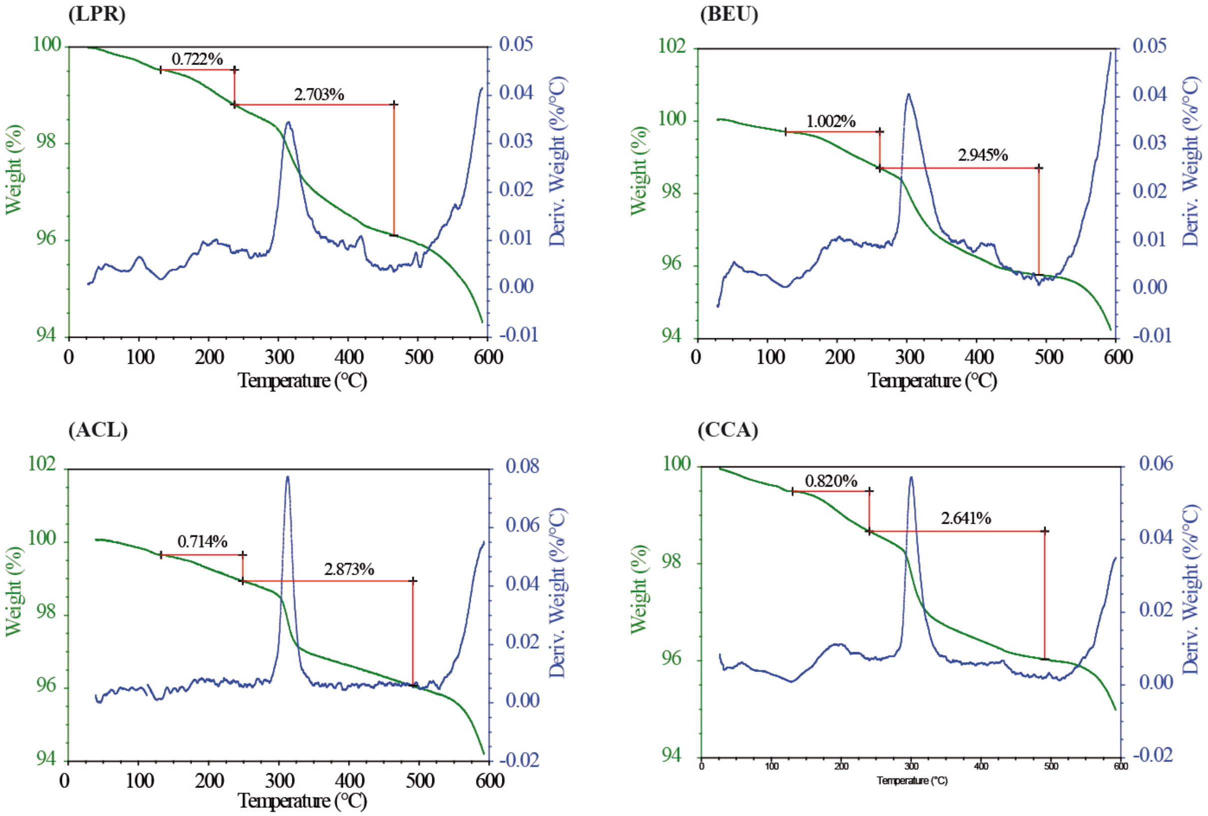

Figure 3.2: Thermogravimetric profiles from powdered coral skeleton samples from *L. pruvoti* (LPR), *B. europaea* (BEU), *A. calycularis* (ACL) and *C. caespitosa* (CCA).

The OM fractions were analyzed by FTIR, SDS-PAGE and AAA. The most representative FTIR spectra of SOM and IOM are shown in Fig.3.3. In SOM and IOM the same absorption bands were detected with different relative intensities (according to 79, 85, 135).

Table 3.1. Summary of the *in vitro* calcium carbonate crystallization experiments in the presence of organic matrix (OM) extracted from *L. pruvoti*, *B. europaea*, *A. calycularis* and *C. caespitosa*.

	OM composition			$CaCO_3$ overgrowth		$CaCO_3$ precipitation				
Medium				10 mM $CaCl_2$		10 mM $CaCl_2$				ASW
Species		SOM[$]	IOM[$]	C	A	SOM (C)	IOM (C)	*e*OM (**C**, A)*	*w*OM (**C**, A)*	*w*OM (**ACC**[#], MgC, A)
LPR *sol. azo.*	2.5±0.1[a] 0.3[b] -[c]	*p* (=) *s* (-) *l* (=)	p (=) s (+) l (=)	s. cryst. {10.4} (7-29)[&]	needle bundles (1-3)[&]	db., s. ag. (s. m. layers) (5-57)[&]	cr. ag. {10.4} {10.8} (12-72)[&]	s. ag. (ag. nano p.) (5-32)[&]	**cr. ag**., s. ag. (ag. nano p.) (3-28)[&]	nanoparticles[|] 2D struct. ACC1 (19.8±0.5)
BEU *sol. zoo.*	2.9±0.1[a] 1.5[b] +[c]	*p* (=) *s* (-) *l* (=)	p (=) s (+) l (=)	**s. cryst.** **{10.4}{hk.0**} (6-33)[&]	prisms (0.3-1)[&]	db., s. ag. (add. part.) (2-20)[&]	cr. ag. {10.4}{10.8} (16-53)[&]	flat. ag. * (ag. nano p.) (3-10)	**cr. ag**., flat. ag. (ag. nano p.) (38-124)[&]	nanoparticles 3D struct. ACC2 (20.3±0.6)
ACL *col. azo.*	2.7±0.1[a] 0.2[b] +[c]	*p* (=) *s* (-) *l* (-)	p (=) s (+) l (+)	s. cryst. {10.4} (10-50)[&]	fused prisms (2-5)[&]	db., s. ag. (add. part.) (4-40)[&]	s. cr. {10.4} {10.8} (4-21; 113-139)[&]	ag. (ag. nano p.) (37-68)	**cr. ag**.,ag. (ag. nano p.) (7-24; 54-106)[&]	nanoparticles 3D struct. ACC2 (19.4±0.5)
CCA *col. zoo.*	2.5±0.1[a] 0.3[b] -[c]	p (=) s (-) l (-)	p (=) s (+) l (+)	**s. cryst.** **{10.4} {hk.0}** (4-28)[&]	fused prisms (1-4)[&]	db., s. ag. (ag. nano p.) (7-10)[&]	cr. ag. {10.4}{10.8} (26-85)[&]	s. ag. (ag. nano p.) (3-16)[&]	**cr. ag**., s. ag. (ag. nano p.) (10-42)[&]	nanoparticles 2D struct. ACC1 (19.6±0.5)

The main features of the OM fractions are also reported. [a] Mass percentage of OM entrapped in the skeleton. [b] Mass ratio between SOM and IOM. This data showed a great variability from one experiment to another and the median value is reported. [c] Relative content of acidic amino acid between SOM and IOM: (+) indicates higher and (-) indicates lower. [$] *p*, *s* and *l* indicate protein, sugars and lipids, respectively and their relative content between SOM and IOM is evaluated as higher (+), equal (=) or lower (-). [&] Indicates the range of dimension of the particles (in µm). [*] Only in the presence of BEU the precipitation of aragonite was observed. [#] Two forms of ACC were observed, having the FTIR ν_2 band at 868 cm^{-1} (ACC1) and 871 cm^{-1} (ACC2). In parenthesis the magnesium content with respect to calcium as mol percentage is reported. [|] The presence of few the elongated rhombohedral single crystals and of aggregates of needle like crystals (only BEU) was observed. When indicated the errors are reported as standard deviations.

To estimate the relative amounts of the main molecular components of the OM from the FTIR spectra, three zones (1-3) were defined (Fig. 3.3, Table 3.2).[135] In the zone 1 (3000-2800 cm^{-1}) the bands were related to fatty acids or to molecules bearing alkylic chain regions, in the zone 2 (1750-1500 cm^{-1}) were located the bands associable to proteins (and some sugars) and in the zone 3 (1100-950 cm^{-1}) bands linked to polysaccharides.[118] The integrated intensities of the bands in zones 1 and 3 were normalized to that of zone 2 (Table 3.2). Then a Mann-Whitney test was carried out to check for significant differences between SOM and IOM. In all the species SOM showed a lower absorption than IOM in the zone 3, and only in *A. calycularis* and *C. caespitosa* in the zone 1. Comparing OM fractions among all the species, the absorption of IOM from *A. calycularis* is the highest and *B: europaea* and *C. caespitosa* reveal a higher content of lipids than the azooxhantellate species.

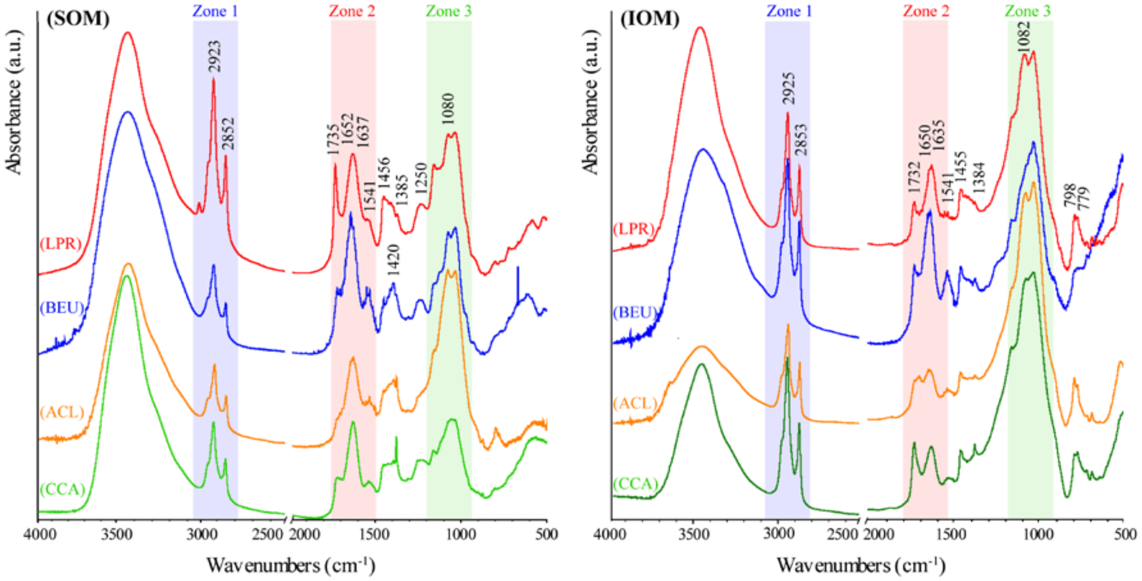

Figure 3.3: FTIR spectra of intra-skeletal soluble (SOM) and insoluble (IOM) organic matrix from aragonitic skeleton of *L. pruvoti* (LPR), *B. europaea* (BEU), *A. calycularis* (ACL), and C. *caespitosa* (CCA). The wavenumbers of the main absorption bands are indicated. The three marked zones define diagnostic regions of functional groups, which could be mainly associated with the presence of lipids (zone 1), protein and polysaccharides (zone 2), and polysaccharides (zone 3).

Table 3.2: Average relative intensities of zone 1 (3000-2800 cm^{-1}) and zone 3 (1100-950 cm^{-1}) normalized to that of zone 2 (1750-1500 cm^{-1}) of the OM fractions, SOM and IOM, from *L. pruvoti*, *B. europaea*, *A. calycularis*, *C. caespitosa*. The intensity of the zone 1-3 can be considered a rough approximation of the content of lipids, proteins and polysaccharides, respectively. In parentheses standard deviations are reported.

		Zone1/**Zone2**	**Zone3**/**Zone2**
L. pruvoti	SOM	0.9 (0.6)	1.4 (0.4)
	IOM	1.3 (0.5)	4.6 (1.9)
B. europaea	SOM	0.9 (0.5)	1.0 (0.3)
	IOM	1.5 (0.4)	1.9 (1.2)
A. calycularis	SOM	0.6 (0.2)	1.8 (0.7)
	IOM	2.1 (0.8)	8.2 (3.3)
C. caespitosa	SOM	1.2 (0.7)	1.1 (0.3)
	IOM	3.2 (1.5)	2.3 (0.9)

SDS-PAGE observations (Fig. 3.4) of SOMs showed many bands gathered around 45 and 30 kDa in *L. pruvoti* and bands clustered in two groups having molecular masses from ca. 40 to 34 kDa and from 73 to 60 kDa[79] in *B. europaea*. In *A. calycularis* and *C. caespitosa* many bands distributed from ca. 104 to 30 kDa and from 62 to 28 kDa, respectively, were revealed.

The AAA from SOM and IOM was reported in Table 3.3. SOM was characterized by a content of aspartic (and asparagine) higher than that in IOM. The content of hydrophobic residues was always higher in IOM (33-50 mol %) than in SOM (24-34 mol %). The calculated average protein pI[46] shows that OMs were acidic, and IOM was less acidic than the SOM within a species.

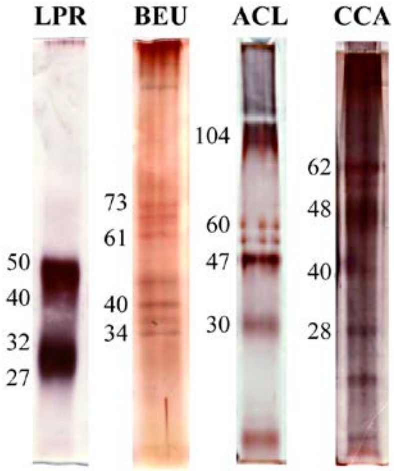

Figure 3.4: SDS-PAGE of intracrystalline soluble organic matrix extracted from aragonitic skeleton of *L. pruvoti* (LPR), *B. europaea* (BEU), *A. calycularis* (ACL), and *C. caespitosa* (CCA). The side numbers indicate the molecular weight (kDa) of silver stain marked bands.

Table 3.3: Amino acids composition (mol %) of soluble (SOM) and insoluble (IOM) fraction of OM proteins extracted from the skeleton of *L. pruvoti* (LPR), *B. europaea* (BEU), *A. calycularis* (ACL) and *C. caespitosa* (CCA).

	SOM				IOM			
	LPR	BEU	ACL	CCA	LPR	BEU	ACL	CCA
Asx**	33.1	46.4	45.8	34.8	19.5	13.0	20.9	18.4
Glx***	9.4	6.6	5.7	3.4	10.0	8.6	1.5	1.4
Ser	17.4	12.9	3.9	5.4	8.9	9.5	6.1	6.1
Gly	20.9	17.8	17.8	16.0	15.1	22.9	26.5	19.4
His	3.7	2.4	4.6	3.1	5.4	4.3	4.2	6.6
Thr	-*	0.3	4.1	1.9	3.4	1.1	5.9	5.2
Arg	-	0.5	4.2	5.5	4.6	3.6	6.1	9.6
Ala	6.8	4.1	2.6	3.9	7.1	13.6	5.4	2.7
Tyr	-	0.2	3.6	4.5	1.9	2.0	0.9	3.6
Cys	1.2	1.0	1.0	-	1.1	1.0	1.0	1.0
Val	2.9	2.6	0.9	3.6	6.3	4.9	6.3	4.5
Met	-	-	-	-	-	-	-	-
Phe	0.8	1.1	0.8	4.0	-	3.1	0.9	6.8
Ile	1.5	1.6	1.4	2.6	4.7	3.7	4.2	7.7
Leu	2.1	1.9	2.2	3.1	8.2	5.5	5.3	3.2
Lys	-	0.5	1.5	8.1	3.7	3.3	4.8	3.7

* Indicates the absence of a relative quantitaty

** Indicates the sum of Asp and Asn

*** Indicates the sum of Glu and Gln

3.3.3 Overgrowth of CaCO3 onto coral skeleton sections

The results of the calcium carbonate overgrowth experiments on skeleton cross sections are illustrated in Fig. 3.5. Surfaces normal to the oral-aboral axis and close to the growing tips were used. The overgrowth occurred in a 10 mM calcium chloride solution under diffusion of ammonium carbonate vapors. Calcium carbonate crystals were observed on the skeleton cross section and outside it (on the surface of the embedding resin). On the resin only calcite crystals appearing almost as perfect {10.4} faced rhombohedra (see Fig. 3.5 *ACL1* on the right) were observed. The crystals with the typical morphology of aragonite were observed only on the surface of the skeletons. They appeared as bundles of needle-like crystals in *L. pruvoti* and as single hexagonal prisms in *B. europaea*, the bundles were about 3 µm in diameter, while the needle like crystals and the single prisms had an average diameter smaller than 1 µm. In *A. calycularis* and *C. caespitosa* the hexagonal prisms observed on *B. europaea* were coherently fused in big prisms having a diameter usually above 4 µm. On the coral skeleton calcite crystals were also observed and they exhibited additional {hk.0} faces to {10.4} ones, which were wider in those grown on the skeleton of *B. europaea* and *C. caespitosa* (Fig. 3.5 *CCA2* and *BEU2*) than in those on the *A. calycularis* and *L. pruvoti* skeletons (Fig. 3.5 *ACL2* and *LPR2*).

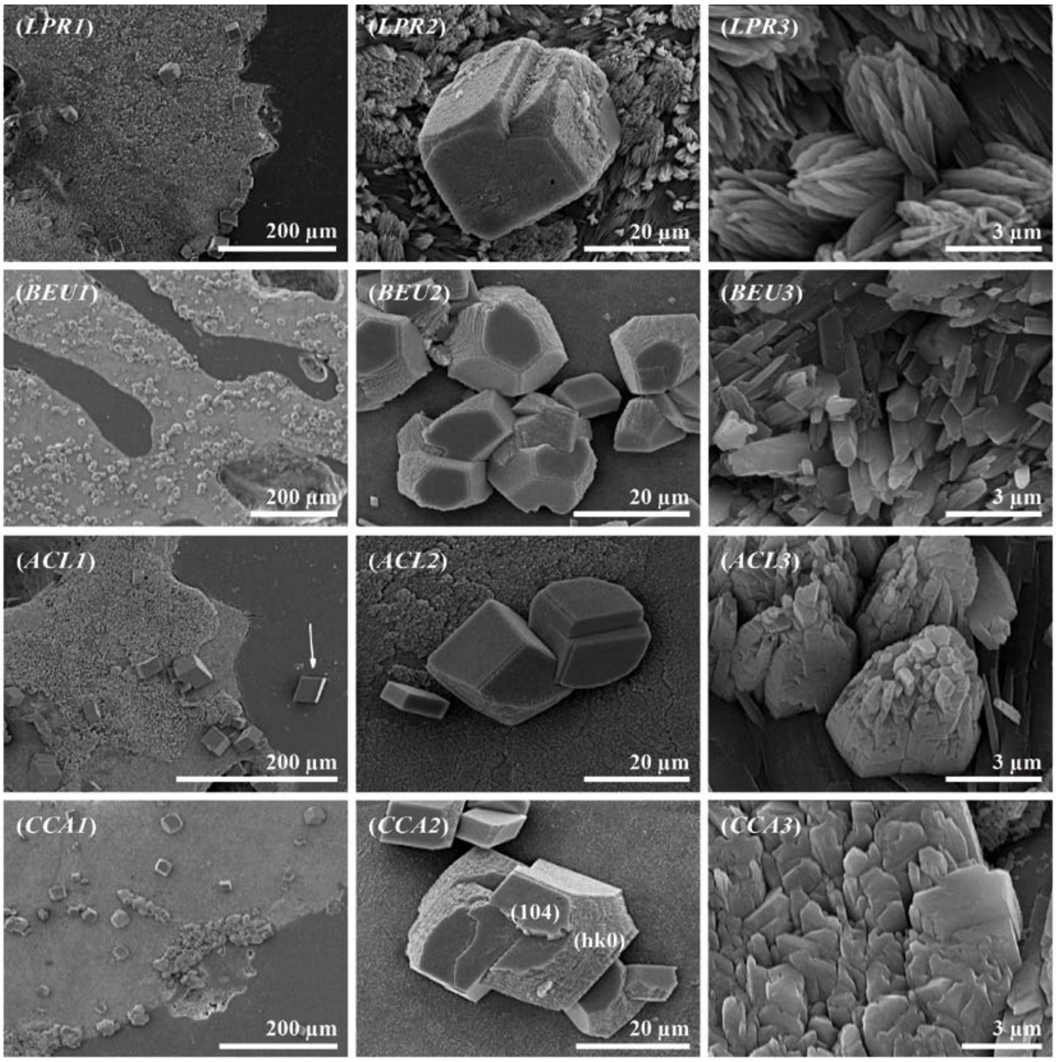

Figure 3.5: SEM pictures at increasing magnifications (1–3) of sections of coral skeleton of *L. pruvoti* (*LPR*), *B. europaea* (*BEU*), *A. calycularis* (*ACL*), and *C. caespitosa* (*CCA*) after calcium carbonate overgrowth experiments. A new layer of crystals with aragonite typical morphology grew on the skeleton surfaces in all the species (magn. 3). On these new layers more or less smoothed calcite crystals were observed (magn. 2) that in some cases they showed additional {hk0} faces to the rhombohedral {10.4}. Outside the skeletons sections only rhombohedra of calcite precipitated (*ACL1*, indicated by the arrow).

3.3.4 Precipitation in the presence of OM fractions

A first set $CaCO_3$ precipitation trials was carried out from 10 mM $CaCl_2$ solutions containing the OM fractions. Without OM only the deposition of rhombohedral crystals of calcite was observed. The presence of OM fractions induced an inhibition of the precipitation and a reduction of the average particle sizes, as a monotone function of the additive concentration. On the basis of a set of preliminary studies and previous similar experiments[79, 135] a SOM concentration of 185 µg/mL was used for *L. pruvoti* and *A. calycularis* and 455 µg/mL for *B. europaea* and *C. caespitosa*, while 666 µg/mL of IOM were dispersed in the calcium chloride solution.

The reported results are the trends observed from six precipitations. In the presence of SOM aggregates having the shape of dumbbell and sphere were always observed (Fig. 3.6 SOM). These particles (5-69 µm) showed surfaces formed by stacked of multilayers (Fig. 3.6 SOM *LPR*, inset) in the presence of *L. pruvoti* SOM, while with *B. europaea* and *A. calycularis* SOMs they showed (4-20 µm and 4-80 µm, respectively) smooth surface and were co-present with aggregates having various shapes (Fig. 3.6 SOM *BEU* and *ACL,* inset). In the presence of *C. caespitosa* SOM the dumbbells and spherical shaped aggregates (7-80 µm) appeared formed by the association of sub-micrometer particles (Fig. 3.6 SOM *CCA,* inset). The FTIR spectra of these precipitates showed the characteristic absorption bands of calcite plus those due to the SOM. In the presence of dispersed IOM, which sometime floated at the air solution interface, the formation of mineral particles was observed both on the matrix surface and outside it. On the IOMs framework, from all the species, calcite crystals grew showing truncation of rhombohedral corners and edges (Fig. 3.6 IOM and insets). On *A. calycularis* IOM only few calcium carbonate particles were observed, together with the needle-like silica contaminants (see materials and methods section). On *L. pruvoti, C. caespitosa* and *B. europaea* IOM, and outside it, the calcite crystals assembled showing overlapping edges (Fig. 3.6 IOM *LPR*, IOM *BEU*). The FTIR spectra showed only the presence of the absorption bands of calcite, with those of IOM.

When the *e*OM was used (Fig. 3.7 *e*OM and inset) few aggregates formed by small particles (submicron sized) precipitated, this observation effect was prominent for *A. calycularis*. In the presence of *L. pruvoti*, *B. europaea* and *C. caespitosa e*OM, the surface of the IOM was covered by aggregates of sub-micrometer units having a rough surface. In addition, crystals, like those precipitated in presence of SOM, were observed around the IOM, particularly for *C. caespitosa*

(Fig. 3.7 *e*OM *CCA* inset). In the presence of *A. calycularis* *e*OM few aggregates with shape changing from one experiment to another were observed (the most representative in Fig. 3.7 *e*OM *ACL*). The FTIR spectra of these materials showed the absorption bands of calcite, except for *B. europaea* where the aragonite bands were observed as well (as reported ref. 79).

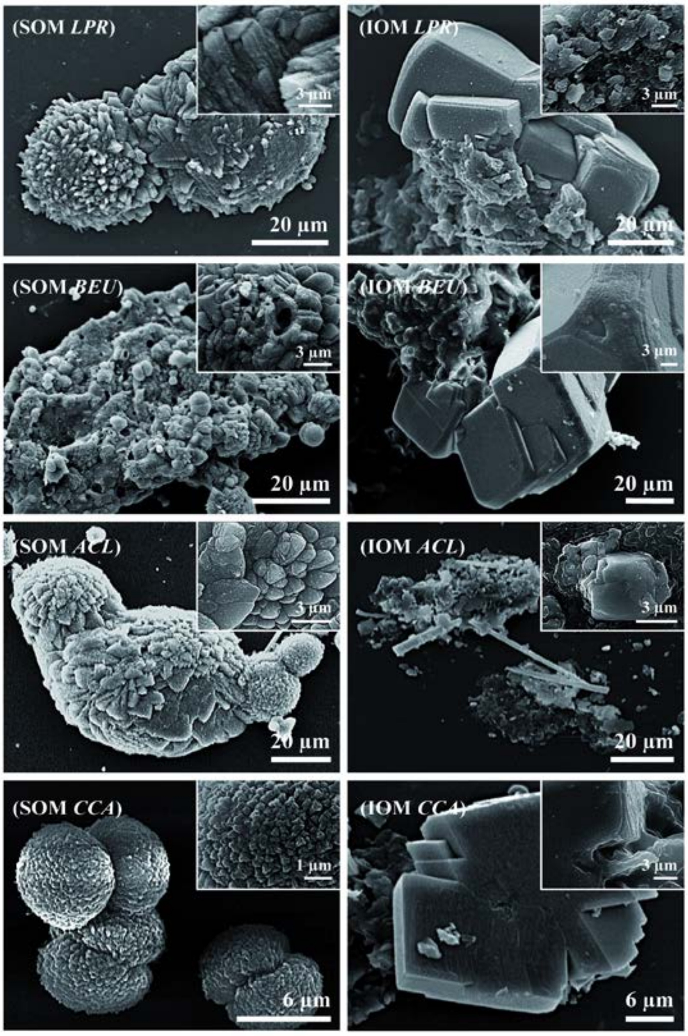

Figure 3.6: SEM pictures of particles obtained from precipitation experiments of $CaCO_3$ from 10 mM $CaCl_2$ solutions in the presence of OM fractions. In the first and second columns are shown particles obtained in the presence of soluble (SOM) or insoluble (IOM) organic matrix, respectively. In the rows are shown, from top to bottom, particles obtained in the presence of *L. pruvoti* (*LPR*), *B. europaea* (*BEU*), *A. calycularis* (*ACL)*, and *C. caespitosa* (*CCA*). In the insets are reported high magnification pictures of the particles. The calcite crystals on IOMs show truncation of rhombohedral {104} corners and edges (probably the presence of small {108} and {hk0} faces). These pictures are the most representative of the populations of observed particles.

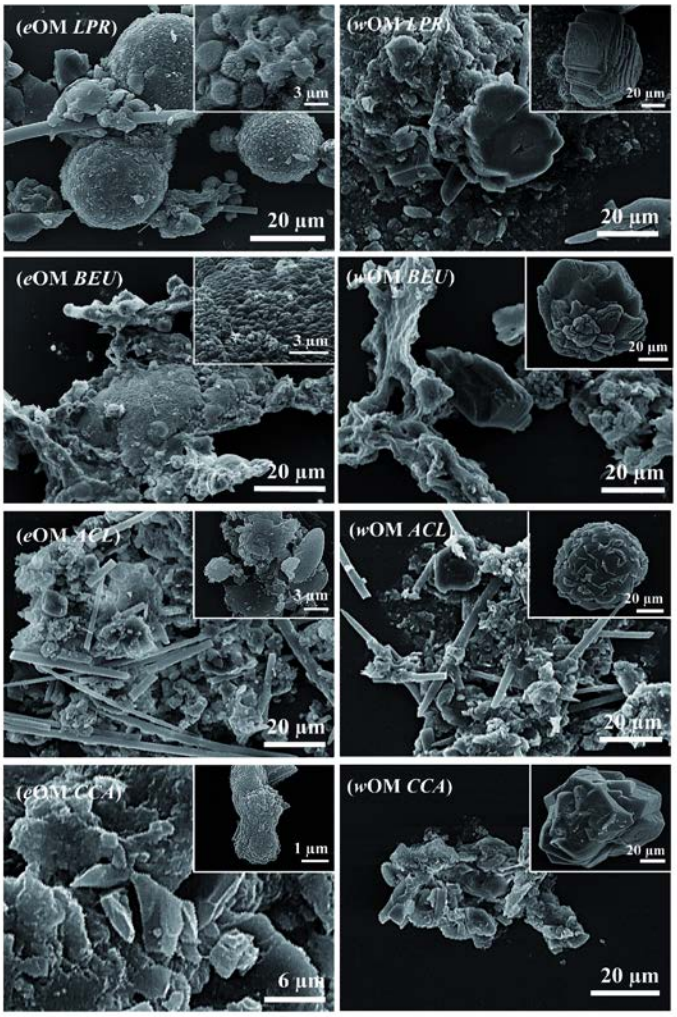

Figure 3.7: SEM pictures of particles obtained from precipitation experiments of $CaCO_3$ from 10 mM $CaCl_2$ solutions in the presence of the entire organic matrix (*e*OM) or the whole organic matrix (*w*OM). The *e*OM and *w*OM were extracted from *L. pruvoti* (*LPR*), *B. europaea* (*BEU*), *A. calycularis* (*ACL*), and *C. caespitosa* (*CCA*). In the picture *ACL* needle-like silica spicules are present. In the insets are reported high magnification images of representative features of the associated particles. These pictures are the most representative of the populations of observed particles.

3.3.5. Precipitation in the presence of the whole OM

A second set of $CaCO_3$ precipitation trials, in which the *w*OM whole was added into a 10 mM $CaCl_2$ solution or into a ASW[142] solution (Fig. 3.7, Tables 3.1), was carried out. The experiments were carried out using 0.25 mg/mL or 0.5 mg/mL of *w*OM, but the latter inhibited the precipitation over four days.

From the 10 mM $CaCl_2$ solution containing *w*OM precipitated $CaCO_3$ particles (Fig. 3.7 *w*OM) similar to those observed in the presence of *e*OM (Fig. 3.7 *e*OM), but showing morphological features closer to those observed in the presence of the respective IOM (Fig. 3.6 IOM).

From the precipitation in ASW, aggregates having the shape of peanut, dumbbell and spherulite and formed by submicron size elongated rhombohedral crystals and needle-like crystals were observed (Fig. 3.9 *ASW*). These aggregates were formed of magnesium calcite and aragonite (Fig. 3.9a). The addition of the *w*OM to the ASW produced the massive precipitation of spherical sub-micrometer particles (Fig. 3.8 ASW + *w*OM) and of few elongated rhombohedral crystals and needle-like crystals (only BEU). The aggregation of the sub-micrometer particles was species specific. They appeared as forming long chains associated in a two dimensional network for *L. pruvoti* and *C. caespitosa*, while for *B. europaea* and *A. calycularis* three-dimensional architectures were generated. The FTIR spectra showed the presence of the typical absorption bands of ACC [12]. The presence of ACC was also verified by X-ray powder diffraction. The diffraction pattern of the precipitated obtained in the presence of *w*OM showed only diffraction peaks due to presence of halite and a very weak broad peak at about 29.7 °. From ASW diffraction peaks owing to aragonite and magnesium calcite were observed. Despite these observations the presence of traces of hydrated forms of calcium carbonate could not be excluded. ACC was further investigated by FTIR experiments upon thermal treatment of the precipitates (Fig. 3.9). The ν_3 and ν_2 showed a different position and profile bands after the thermal treatments. In the ACC obtained from *L. pruvoti* and *C. caespitosa* the ν_2 band was at 868 cm^{-1} and in the ones from *B. europaea* and *A. calycularis* was at 871 cm^{-1}. Upon thermal treatment at 105 °C for 18 hr for all the ACC the ν_2 band was at 871 cm^{-1}, and after 76 hr this band moved at 875 cm^{-1} for all the samples, the same value showed in the precipitate formed from ASW without OM. When the same samples were thermally treated for 8 hr at 300 °C they all showed the ν_2 band at 877 cm^{-1}. Moreover, a second band at 860 cm^{-1} clearly appeared in the precipitated obtained from *B. europaea*, analogously to that obtained from pure ASW, and was present as shoulder in *A. calycularis* precipitate. The profile of the ν_3 band showed three main maxima centered at 1431, 1466 and 1480 cm^{-1}. By thermal treatment the maximum at

1431cm^{-1} strengthened, while the one at 1480 cm^{-1} weakened. This change in intensities was more difficult in *B. europaea* that in the other species. The analysis of the absorption band at about 3300 cm^{-1}, due to the OH groups stretching, did not reveal any clear trend. This difficulty can be ascribed to the diverse contributes (e.g. water solvatation, carbohydrates) to this bands and the presence of moisture.

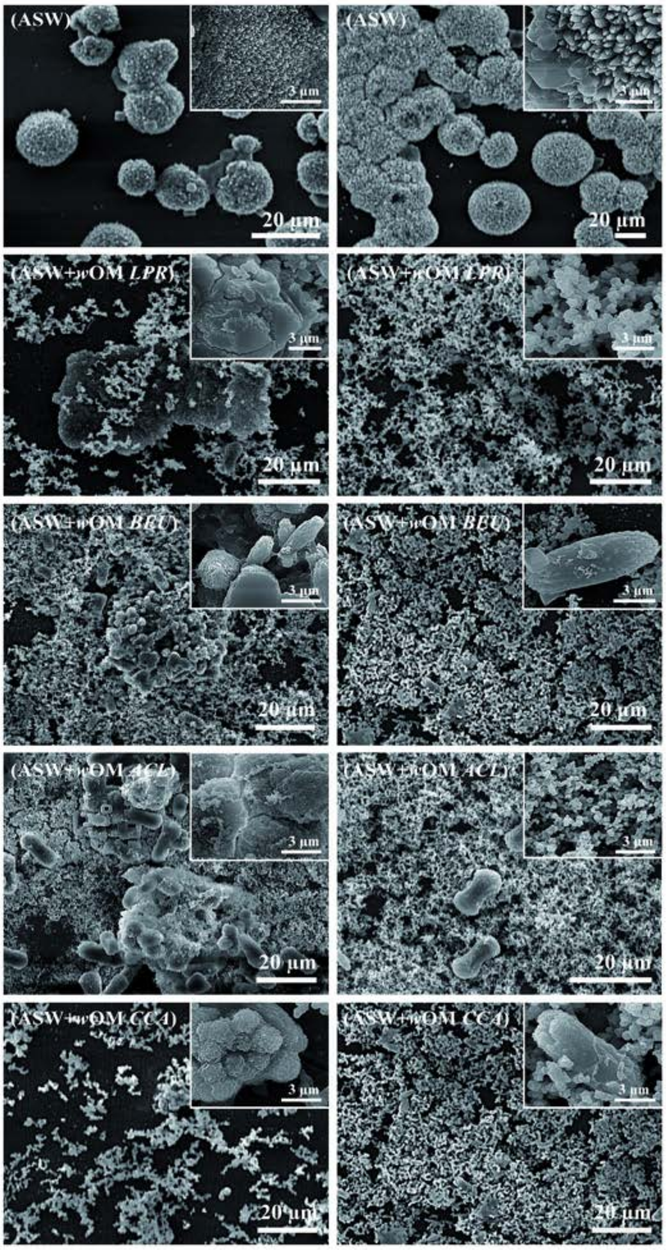

Figure 3.8: SEM pictures of particles obtained from precipitation experiments of $CaCO_3$ from artificial seawater (ASW) in the presence of the whole organic matrix (*w*OM), after the synthesis (left), and after the thermal treatment at 300 °C for 12 h (right). The spherical nanoparticles (2nd–4th row) were made of ACC before the thermal treatment and of magnesium calcite after the thermal treatment. In the presence of the *w*OM from *B. europaea*, aragonite coformed with magnesium calcite. The *w*OM was extracted from *L. pruvoti* (*LPR*), *B. europaea* (*BEU*), *A. calycularis* (*ACL*), and *C. caespitosa* (*CCA*). These pictures are the most representative of the populations of observed particles.

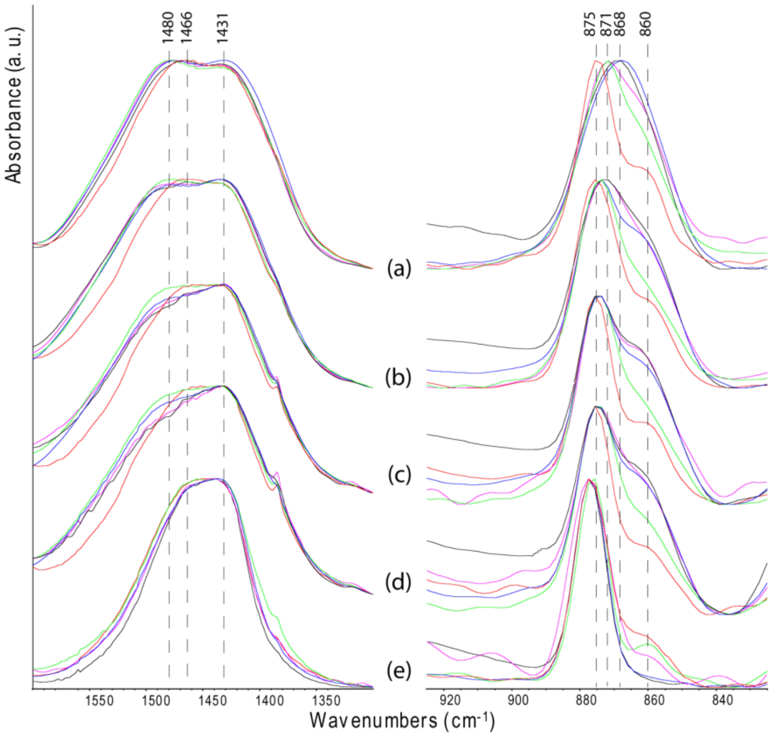

Figure 3.9: FTIR spectra of calcium carbonate precipitated from artificial seawater in the presence of the whole organic matrix (*w*OM), which was extracted from *L. pruvoti* (blue), *B. europaea* (green), *A. calycularis* (magenta), and *C. caespitosa* (black). The spectra from calcium carbonate precipitated from artificial seawater in the absence of wOM are also reported (red). Only the diagnostic ranges from 800 to 900 cm−1 and 1300 to 1600 cm−1 are shown. (a) Spectra collected without any thermal treatment of the samples. (b−d) Spectra collected after a thermal treatment of the samples at 105 °C for 18 h (b), 36 h (c), and 72 h (d). (e) Spectra collected after a thermal treatment of the samples at 300 °C for 12 h.

DSC analyses were carried out to monitor the trend in the phase transition of the ACC. After each test, the samples were analyzed by FTIR spectroscopy. From spectra obtained with DSC analyses (Fig. 3.10), it was possible observe how the presence of OM changes the temperature and the quantity of transitions of $CaCO_3$ when the temperature increases. The pattern obtained from the sample precipitated in ASW without OM, was not detected in any other samples, in fact the only one endothermic peak observed even in the presence of the OM extracted from all species is the one at 325 °C. Because the values of the individual peaks may be subject to variation due to the presence of the OM, it was possible observe that the peak at 171 °C obtained in the absence of the OM was present only in *L. pruvoti*, the one at 417 °C could be associated at peaks observed in the presence of the OM of *L. pruvoti* and *A. calycularis* around at 420 °C, and the peak at 502 °C was present only in *C. caespitosa* (Table 3.4). In the presence of the organic matrix of *A. calycularis* less peaks were observed than in the other species. Although in general all species exhibit a different trend compared to precipitation in only ASW, *B. europaea* shows a unique behavior. It presents less enthalpy changes than the others, and is the only one with a peak around at 518 °C. After DSC analysis, FTIR spectra were collected. The sample with precipitated ACC is heated up to 550 °C during DSC analysis and the FTIR spectrum after the heating showed the bands at 1431 cm^{-1}, 876 cm^{-1} and 712 cm^{-1}, characteristic of calcite. This means that the ACC, precipitated during the crystallization process, was converted into calcite. This applies to all species. In the precipitates from the ASW the Mg/Ca molar ratio was measured the atomic absorption spectroscopy (n = 6). It was of 19.8 ± 0.5, 20.3 ± 0.6, 19.4 ± 0.5 and 19.6 ± 0.5 in *L. pruvoti*, *B. europaea*, *C. caespitosa*, and *A. calycularis*, respectively, while in the absence of OM it was of 5.1 ± 0.1 (Table 3.1).

Table 3.4: temperatures and enthalpies of the thermally induced transitions in crystallization experiments in sea water (ASW) with or without intra-skeletal OM. *BEU = B. europaea*, *LPR = L. pruvoti*, *CCA = C. caespitosa*, *ACL = A. calycularis*

	T_{tr} (°C)	ΔH (J/g)
ASW	172	3.1
	325	3.3
	417	16.1
	502	3.4
BEU	204	0.7
	290	1.4
	324	2.5
	518	6
LPR	180	2.6
	327	4.3
	425	26.0
CCA	222	4.0
	322	2.2
	408	14.6
	501	19.8
ACL	325	1.5
	425	6.3

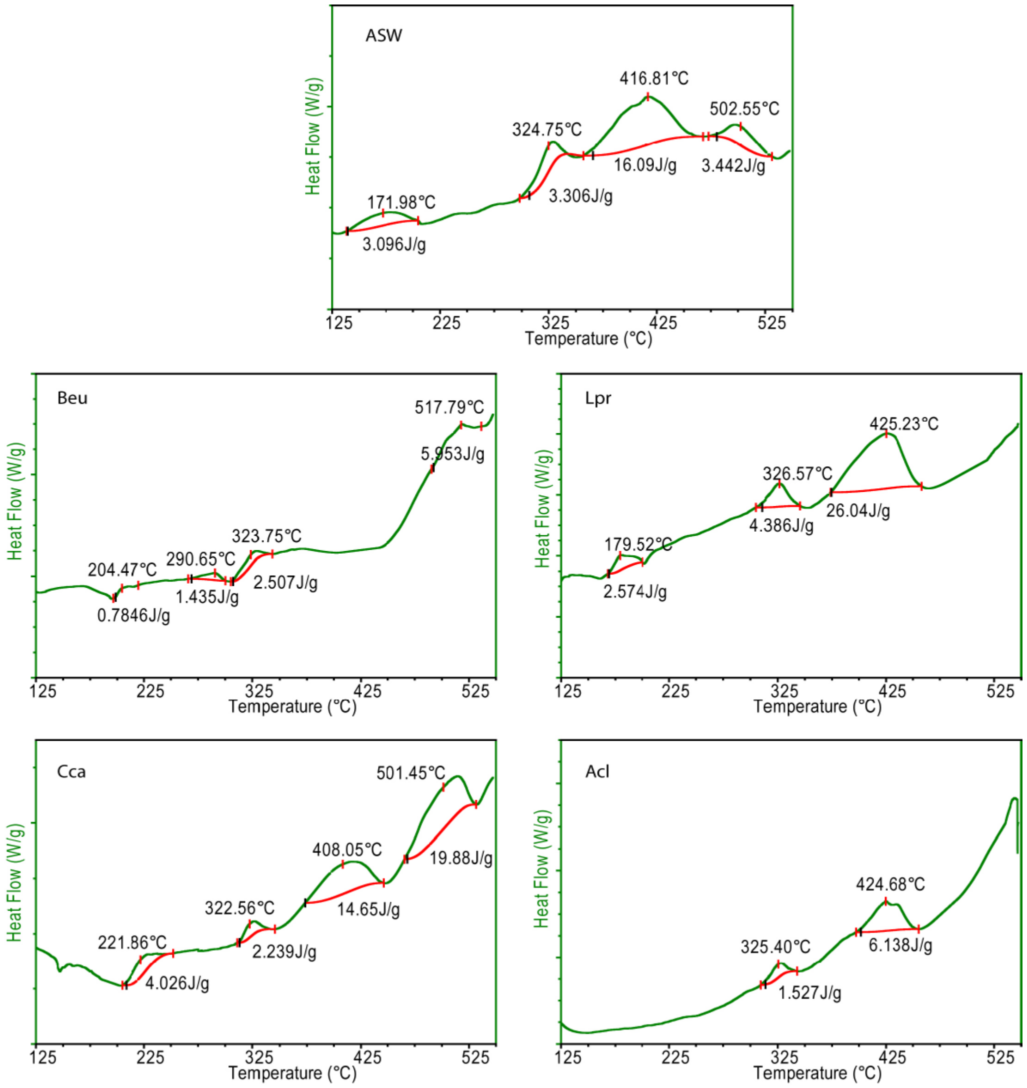

Figure 3.10: DSC profiles of crystallization experiments in seawater (ASW) with or without intra-skeletal organic matrix. Beu = *B. europaea*, Lpr = *L. pruvoti*, Cca = *C. caespitosa*, Acl = *A. calycularis*.

3.4 Discussion

The precipitation of aragonite in corals occurs in a confined environment in a sea water like fluid that contain biomineralizing (macro)molecules.[43, 144] The understanding of the role of sea water ions (mainly magnesium) and of biomineralizing macromolecules in the *in vivo* calcification process lays objective difficulties, although terrific results were achieved.[72] The *in vitro* mineral precipitation in the presence of OM components represents an alternative approach. This assay has the disadvantage, and limitation, that only intra-skeletal macromolecules upon an extraction process, are considered. However, the assay was validated by a plethora of studies that have proved that the intra-skeletal macromolecules were effective modifiers of the nucleation and growth processes of minerals deposited by organisms.[60, 63, 72] Until few years ago this assay was almost ignored in the study of the biomineralization of corals. Recently, few *in vitro* studies have shown that the intra-skeletal OM of coral influenced the aragonite precipitation.[79, 103, 135] Scleractinian corals, differently from many other marine calcifiers, show diverse growth forms (solitary *vs* colonial) and trophic strategies (zooxanthellate *vs* non-zooxanthellate). The presence of zooxanthellae was reported to have an influence on the calcification process.[64, 101] A study on the OM amino acid composition showed differences between different species with different trophic strategies in the content of acidic residues [38]. Here, the study on the composition of OMs from the corals *L. pruvoti*, *B. europaea*, *A. calycularis* and *C. caespitosa* showed the absence of any clear correlation among coral ecology (growth form or trophic strategy) and OM content, mass ratio between SOM and IOM, protein features and macromolecule distribution (Table 3.1). The only difference that can be correlated with the different trophic strategy is the higher total lipids content in the *w*OM of *B. europaea* and *C. caespitosa* respect to the azooxhantellate species. In fact, the presence of zooxanthellae contributes to the energy supply of the polyp,[80] causing a different origin and a different amount of certain metabolites compared to azooxanthellate species that feed themselves through the predation. An emerging feature was the high mass ratio SOM/IOM (1.5) in *B. europaea* (Table 3.1), a non unique behavior since in *Acropora digitifera* a ratio of about 5 was observed.[135] Overgrowth experiments showed that aragonite formed on the surface of all coral skeletons. This effect, which could be due to secondary nucleation events, brought to the growth of crystals having size and texture species specific. On the skeleton of the zooxanthellate species, *B. europaea* and *C. caespitosa*, the overgrowth of numerous calcite crystals having a modified morphology was also observed. This can be related with the release in solution of molecules able to interact specifically with the {*hk*.0} faces of calcite.[99] The band's distribution revealed by SDS-PAGE seemed to exclude that this effect was related to the presence of a significant amount of low molecular weight molecules more easily released from the skeleton, keeping in consideration that some molecules could be not stained or fixed by the gel.[129] The $CaCO_3$ precipitation experiments in the presence of SOM, IOM and the *e*OM gave results in agreement to what observed for other coral species.[79, 135] The SOM molecules were strong modifiers of the morphology of the calcite particles. These changes in morphology were due either to the aggregation of modified single crystalline units of calcite, as in case of *L. pruvoti*, *A. calycularis* and *C. caespitosa*, or to the assembly of sub-micrometer particles, as with *B. europaea*. The presence of IOM lightly affected the precipitation of calcite, and the crystals were slightly modified from their rhombohedral morphology, suggesting the limited release of IOM molecules in solution, favored by the crystallization conditions (pH and ionic strength).[79, 135] According to reported data[79, 135] the *e*OM effect on the precipitation was dominated by the SOM fraction, unless for *B. europaea* where the co-presence of SOM and IOM allowed the precipitation of aragonite together with calcite in a $CaCl_2$ solution Mg ions free, where usually precipitated calcite.[135] The favored precipitation of aragonite by OM molecules has been observed also for *Stylophora pistillata*,[103] but these experiments were carried out in sea water where the presence of magnesium ions (Mg/Ca molar ratio equal to 5) favors the precipitation of aragonite. The trials in which the *w*OM was used instead *e*OM, were performed to exclude possible artifacts associated to the separation process between SOM and IOM (e.g. re-aggregation and re-precipitation). The results with *w*OM were in line with those obtained using *e*OM, but the morphological effects were more similar to those observed in the presence of IOM, suggesting that in the *w*OM a lower content of SOM was present with respect to the *e*OM.

More information respect to what is already known, was obtained from precipitation experiments in ASW using the *w*OM. In fact, previously described experiments showed that *w*OM behaved similarly to *e*OM and it was definitely more representative of the OM entrapped in the skeleton. These two OMs differed for the extraction mode. In the *e*OM experiments the soluble and insoluble organic matrices were separated during the extraction process and then used together, with the *w*OM the whole organic matrix was extracted in one step. The fact that these two procedures gave materials having similar functions in the precipitation of calcium carbonate indicated that (*i*) soluble and insoluble fractions activity was not affected by the extraction process and that (*ii*) the interaction between soluble and insoluble fraction was a reversible process. The use of ASW was in line with recent researches showing direct seawater transport to the calcifying site in corals.[97] The presence of magnesium ions in the extracytoplasmic calcifying fluid, at the nucleation site of corals, has been also reported.[111, 132, 142] The addition of *w*OM to ASW induced the precipitation of almost only ACC instead of aragonite and Mg-calcite, as revealed by the FTIR and X-ray diffraction analyses. ACC appeared in two forms having different FTIR spectra and thermal stability. The thermally less stable form of ACC, which precipitated in the presence of *w*OM from *L. pruvoti* and *C. caespitosa*, converted in the one more stable, which precipitated in the presence of *w*OM from *B. europaea* and *A. calycularis*, upon heating at 105° C for 18 hr. According to Radha *et al.* [14] a hydrated ACC transformed with aging or heating into a less hydrated form, crystallizing with time as calcite or aragonite. Two ACC forms, anhydrous ACC and hydrated ACC containing about 1 mol of water that persists for longer time periods, exist in biogenic sources.[13] So we could infer that in our experiment the ACC thermally less stable forms (probably the hydrated ACC) converted in less hydrated, or anhydrous, ones upon heating (the complexity of the material did not allowed accurate thermal analyses). The less hydrated ACC showed a different behavior when subject to a further heating process. It converted in poor crystalline Mg calcite in the presence of *w*OM from *L. pruvoti*, *A. calycularis* and *C. caespitosa,* while the one from *B. europaea* formed in Mg calcite and aragonite. This polymorphic selectivity in the solid state crystallization of the ACC was attributed to the *w*OM, since the same heating profile was used, excluding effects due to the annealing rate.[145] Moreover, an increase in the crystallinity of Mg-calcite was observed after annealing.[143] The existence of two forms of ACC, which had a diverse binding strength, was reported as precursors of diverse crystalline phases.[146] DSC analysis confirm what it was observed with the heating experiments: the OM of each species stabilizes the ACC differently. In particular *B. europaea* differs most from the others in agreement with previous analyses.

The wet transition from ACC to specific crystalline phases was reported to rely on the Mg/Ca molar ratio and the presence of additives in the precipitating solution.[147, 148, 10, 69] In particular it was observed that in conditions of Mg/Ca molar ratio > 4 the transition from ACC to aragonite[147] occurred through monohydro-calcite as transition phase[10] in times shorter (< 4 days) than those used in this study. This strongly indicated a stabilization of the ACC by the *w*OM, indeed in its absence the ACC precipitation was not observed.

It has been reported that the formation and stability of different hydrated ACC forms has to been ascribed to the co-presence of Mg ions and OM from diverse mineralized tissues.[12, 25] However, our data suggests that *w*OM play a primary role in the ACC formation. Here, the *w*OM stabilization of two forms of ACC was not related to the content of Mg^{2+} hosted in ACC, being the same in all the precipitates (Table 3.1). Moreover, the co-precipitation of ACC with crystalline phases was observed also in the absence of magnesium ions.

The stabilization of ACC by *w*OM suggested that also coral biomineralization followed a crystallization pathway involving the formation of a transient form, as reported for foraminifera, mollusks and echinoderms.[46] This agreed with recent observations on growing coral that reported the presence of transient granules that convert in aragonite fibers.[88] However, the presence of ACC was not detected in coral recruits.[149]

3.5 Conclusions

In conclusion this research added three important observations to the study on *in vitro* precipitation of calcium carbonate: (*i*) the capability of OM to affect morphology and polymorphism was not related to the coral growth form or trophic strategy; (*ii*) in simulated sea water the OM stabilized the formation of diverse forms of ACC which converted species specifically in aragonite or magnesium calcite upon thermal treatment (*iii*) *B. europaea* showed distinguished in *in-vitro* biomineralization features: under overgrowth and solution precipitation experiments, its OM was the most prone to favor the precipitation of aragonite in absence of magnesium ions; under thermal treatments, its ACC was unique with being the most stable, and was the only one that partially converted in aragonite instead of magnesium calcite. These features suggested a stronger control of *B. europaea* OM over the mineral phases and a higher independence from crystallization environment compared to the other species. The reasons of the peculiar behavior of the OM from *B. europaea* were unknown. However, this species distinguished also for the ecological properties being the only one able to tolerate the effects of ocean acidification.[150]

This work has been published (see Reggi M., Fermani S., Landi V., Sparla F., Caroselli E., Gizzi F., Dubinsky Z., Levi O., Cuif J-P., Dauphin Y., Goffredo S., Falini G. Biomineralization in Mediterranean corals: The role of the intra-skeletal organic matrix. Crystal Growth and Design. 2014,14 (9), pp 4310–4320).

4. EXPRESSION AND PURIFICATION OF AN INTRA-SKELETAL ORGANIC MATRIX PROTEIN

4.1 Introduction

Galaxin is a soluble protein of the OM for which the complete primary structure has been determined and was identified for the first time in the exoskeleton of the coral *Galaxea fascicularis* where it is most abundant.[151] In recent years many genes related to galaxin were identifying also in other coral species and is the first completely.[152, 153] Its role in biomineralization processes is unknown. It was demonstrated that this protein did not reveal neither acidic regions nor Ca^{2+}-binding domains.[103, 151] Galaxin contains many tandem repeated cysteine-rich domains (Fig. 4.1) usually associated at proteins having a structural role in the organic matrix, as a framework,[129, 154] and commonly found in extracellular matrix and cell surface receptor proteins. So it is supposed that this protein have a key role in the biomineralization process.[152, 154] Galaxin exhibits, also, putative post-translational modifications, in particular N-glycosylations and phosphorylations on Ser, Thr and Tyr residues and attachment sites for glycosaminoglycans (Ser-Gly-X-Gly-).[40] Reyes-Bermudez et al. showed that the expression of three galaxin genes takes place in different time during calcification process of *Acropora millepora*. In particular two galaxin-like genes are expressed in the early stage of calcification, while the other galaxin gene continues to be expressed also in the adult and it was suggested that is involved in controlling fiber-like aragonite deposition characteristic of adults skeletons.[152]

To better understand the role of this protein in the precipitation of $CaCO_3$ in organisms, this study proposes to produce galaxin through a recombinant prokaryotic system and then to characterize its structure through mass spectroscopy and protein crystallization.

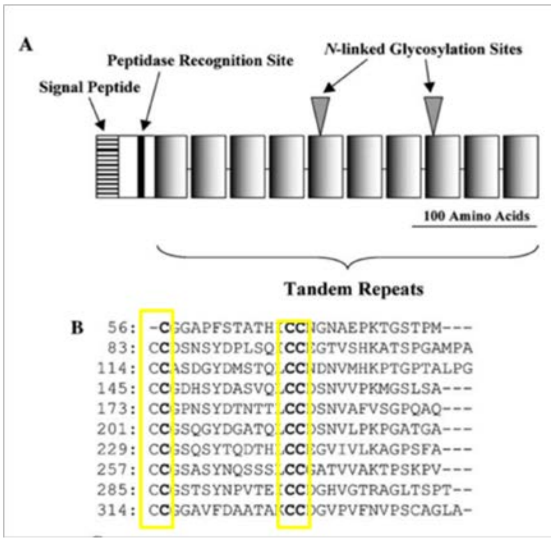

Figure 4.1: (A) schematic representation of the primary structure of galaxin. (B) The tandem repeat structure in galaxin. The numbers on the left represent the amino acid positions and ‘‘–’’ indicates a gap. Below the alignment is shown a deduced consensus sequence in which only the amino acids that are observed in at least five sequences are shown and ‘‘–’’ represents an arbitrary amino acid.

4.2 Experimental section

<u>Insertion of encodind cDNA inside of the expression vector</u>

The cDNA for Galaxin from *Stylophora pistillata* inserted in the pGEM was kindly provided by Oren Levi’s group, and then was transferred in pET-28 (Novagen) expression vector through endonuclease *Nde*I (Promega). At a later stage Galaxin cDNA was transferred in pET-22b (Novagen) expression vector through endonucleases *Nco*I and *Sac*I (Promega) because this vector has an N-terminal pelB signal sequence that allows to localize the express protein in the periplasm, the space between cell wall and cell membrane.

To transfer cDNA from pET-28 to pET-22b, point mutations for restrictin sites were introduced by PCR. Primers were as follows: NcoI-Up-L: 5’ - GCC GCG CGG CAG CCC CAT GGA GCC ATC TGT TGC CTT – 3’ and NcoI-Up-R: 5’ - AAG GCA ACA GAT GGC TCC ATG GGG CTG CCG CGC GGC – 3’; Sac-Down1-L: 5’ – CGT ACC ATG TAG CAT CGC GTT CAG GAC TAG CAT AGA ATC -3’ and Sac-Down1-R: 5’ – GAT TCT ATG CTA GTC CTG AAC GCG ATG CTA CAT GGT ACG -3’; SacDown2-L: 5’ – CGT ACC ATG TAG CAT CG**A** G**C**T CAG GAC TAG CAT AGA ATC – 3’ and SacDown2-R: 5’ – GAT TCT ATG CTA GTC CTG

A**G**C **T**CG ATG CTA CAT GGT ACG -3’. PCR and transformation reactions were performed according to the QuickChangee Site-Directed Mutagenesis kit (Stratagene) (in bold are indicated mutated nucleotides).

Fragments were ligated into NcoI/SacI-predigested pET-22b (Novagen) with His tag and the ligation mixture was used to transform *Escherichia coli* cells, strain BL21 (DE3) and Rosetta-gami™ 2 (DE3). One colony was picked up, transferred into liquid culture (LB medium supplied with ampicillin (50 µg/mL)) and grown overnight at 37°C with vigorous shaking (150– 170 rpm). Plasmid DNA was extracted and sequenced (Fig. 4.2). Is possible observed that Galaxin cDNA is between two His tag (bolt and italic), up and down, useful to detect the protein during the expression and purification processes.

```
gcctaacgtcttcccctctagaataattttgtttaactttaagaaggagatatacatatg
                                                          M
aaatacctgctgccgaccgctgctgctggtctgctgctcctcgctgcccagccggcgatg
 K  Y  L  L  P  T  A  A  A  G  L  L  L  L  A  A  Q  P  A  M
gccatgggcagcagccatcatcatcatcatcacagcagcggcctggtgccgcgcggcagc
 A  M  G  S  S  H  H  H  H  H  H  S  S  G  L  V  P  R  G  S
catatgaagccatctgttgccttccgtagcctttgtgtagttttgctcagccttgcaact
 H  M  K  P  S  V  A  F  R  S  L  C  V  V  L  L  S  L  A  T
tactgtttttccttcccaagtgattccttgaagagagacgcccatagtgacgccaacgca
 Y  C  F  S  F  P  S  D  S  L  K  R  D  A  H  S  D  A  N  A
ttaaaaactagagatcggcgtcaggctccagcatttcagctctcgtgtggaggggttttg
 L  K  T  R  D  R  R  Q  A  P  A  F  Q  L  S  C  G  G  V  L
tacaatcccgcaacagagatttgctgtcacggaaatgtagagcccagagtgggagcatcg
 Y  N  P  A  T  E  I  C  C  H  G  N  V  E  P  R  V  G  A  S
cctatgtgttgtgaaagtacctcgtatgacccgtccactcaggtgtgttgtgaaggtaca
 P  M  C  C  E  S  T  S  Y  D  P  S  T  Q  V  C  C  E  G  T
gtctcgaacaagccaccgggaattgcaatgtgctgcggcagtgaggcatacgatgcgaac
 V  S  N  K  P  P  G  I  A  M  C  C  G  S  E  A  Y  D  A  N
agtcagatatgctgcaatggcaatataaataccaaggcaaccggcccaacagcccaacca
 S  Q  I  C  C  N  G  N  I  N  T  K  A  T  G  P  T  A  Q  P
ggatgctgtggagagttctcatataatgcagcttctcagttgtgttgtgacagccatcct
 G  C  C  G  E  F  S  Y  N  A  A  S  Q  L  C  C  D  S  H  P
gtgctaatggttggctcattaccaagctgctgtggtcgaaatgggtacgatgctaacaca
 V  L  M  V  G  S  L  P  S  C  C  G  R  N  G  Y  D  A  N  T
tcgttgtgttgcggtgacaacgacgtcgcgtttgtgtccggaccccaagctgcatgctgt
 S  L  C  C  G  D  N  D  V  A  F  V  S  G  P  Q  A  A  C  C
ggggacatgggttataacagaaacacacacttatgctgtgacagcaacgttttaccgaag
 G  D  M  G  Y  N  R  N  T  H  L  C  C  D  S  N  V  L  P  K
ccagcggtgggagcatgctgtggtagctggacccacagccagcaaactcatctgtgctgt
 P  A  V  G  A  C  C  G  S  W  T  H  S  Q  Q  T  H  L  C  C
gagggtgttcaactttacaaaggcatgaatacagcttgctgtggatcagtaggatacaac
 E  G  V  Q  L  Y  K  G  M  N  T  A  C  C  G  S  V  G  Y  N
caggtaaattccttatgttgtgaaggcactgtcgtaccgataacaccttcaaagcccgtt
 Q  V  N  S  L  C  C  E  G  T  V  V  P  I  T  P  S  K  P  V
tgctgtggtacaacgtcttacaatcctatgaccgaattgtgctgtgatggaatagccttt
 C  C  G  T  T  S  Y  N  P  M  T  E  L  C  C  D  G  I  A  F
cctaaaacaggatttacaagaccgacttgctgtggaggagcgatttacgatgcaactctt
 P  K  T  G  F  T  R  P  T  C  C  G  G  A  I  Y  D  A  T  L
gcaagatgctgtgacggagtccctacgtaccatgtagcatcgagctccgtcgacaagctt
 A  R  C  C  D  G  V  P  T  Y  H  V  A  S  S  S  V  D  K  L
gcggccgcactcgagcaccaccaccaccaccactgagatccggctgctaacaaagcccga
             A  A  A  L  E  H  H  H  H  H  H  -
```

Figure 4.2:Nucleotide sequence above and translation of ORF below. The pelB is highlighted, His-tag up and down were highlighted bolt and italic and trombone site is highlighted and in italic.

Protein expression

Once sequence was confirmed, the construct was transferred into *E. coli* BL21 (DE3) and Rosetta-gami^{TM} 2 (DE3). The clones with pET-22b-Gal were grown in LB medium in presence of ampicillin for 24h at 37 °C under shaking (70 rpm) and Galaxin was expressed by induction with 0.4mM IPTG at an optical density at 600nm of around 0.4 Abs. At the end of the growth, cells were centrifuged at 10000 rpm at 4°C for 20 min, and the pellet was conserved at -80°C. Frozen cells were thawed on ice and resuspended in 50mM TRIS pH 7.6 (about 50mL of buffer to 1L of cell colture). Resuspended cells were broken by addition of 100µg/mL lysozyma and incubated for 20 min at 30°C. Then the cell debris was incubaterd for 20 min at room temperature with 10mM $MgCl_2$, 1µg/mL of RNAsi and DNAsi. Cell debris was precipitated by centrifugation at 10000 rpm at 4°C for 20 min. Both supernatant and pellet were analysed by Wester blot.

In order to solubilize Galaxin from the pellet, it was resuspended in Binding Buffer 1X (5mM Imidazole, 0.5 M NaCl, 20 mM Tris HCl pH 7.9) with 6 M Urea, 8M Urea and in 4% 2-Mercaptoethanol solution (100mM Tris pH 7.6; 0.2% Triton; 1mM EDTA; 200mM NaCl; 4% 2-Mercaptoethanol) with increasing time of treatment. Every step was resolved by 12.5% SDS-polyacrylamide gel electrophoresis and Western blot.

Western blot. The results of SDS-polyacrylamide gel electrophoresis were transferred onto a nitrocellulose membrane. The membranes were blocked with 3% non fat dry milk in TBST (10 mM Tris-HCl (pH 8.0), 100 mM NaCl, and 005% Tween 20) for 40 min at room temperature and then incubated with the primary mouse anti-polyHis antibody at 1:2000 dilution overnight at 4 °C, followed by incubation with anti-mouse secondary antibody coupled to peroxidase at 1:2000 dilution for 3h at room temperature. Signal were visualized by enhanced chemioluminescence.[155]

4.3 Results and Discussion

At the beginner the cDNA of galaxin was inserted in pET-28 expression vector but cells died, probably because the protein is toxic for the cells. So it was inserted in pET-22b because this vector carries an N-terminal pelB signal sequence for potential periplasmic localization, in this way protein should not affect cell metabolism and thus not interrupts the cells growth. Two different *E. coli* cells were transformed with pET 22b, BL21 (DE3) and Rosetta-gami^{TM} 2 (DE3), to understand what is the best way to produced the protein. The first host strain is the most widely used host background for protein expression; the second one combines the enhanced disulfide bond formation with enhanced expression of eukaryotic protein that contain codons rarely used in *E. coli*. The colonies with the plasmid construct were grown in LB medium in presence of ampicillin for 24h and galaxin were expressed by induction with IPTG 0.4mM. Is possible observed in the Fig. 4.3 that both colonies when IPTG was added interrupt the growth for few hours and then restart to growth. The causes of this unusual growth can be due at the fact that the recombinant protein interferes with cell proliferation and probably is toxic for the cell metabolism, however after more time, cell culture restarts to grow probably because the protein arrives in the periplasm.

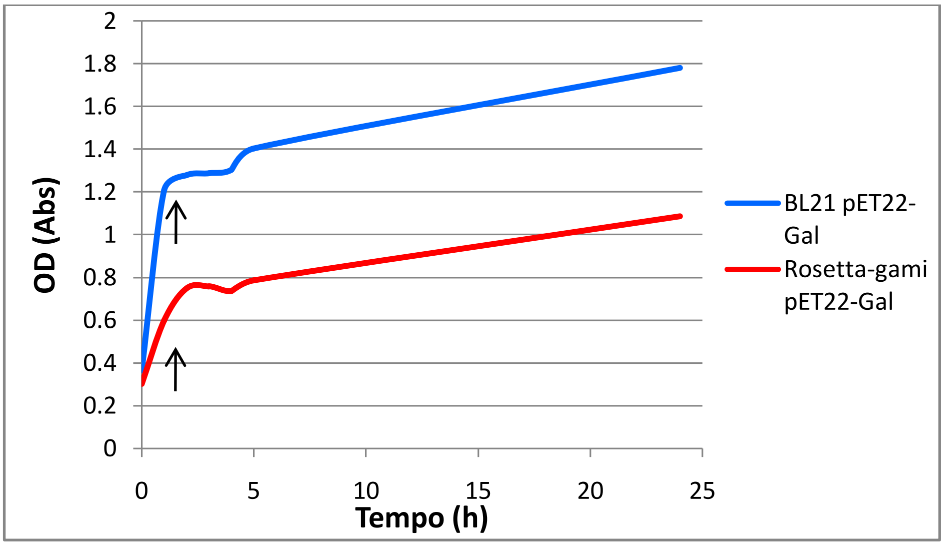

Figure 4.3: Growth curves of the cells of *E. coli* BL21 (blue) and Rosetta-gami2 (red) transformed with the expression vectors pET22-Gal obtained by monitoring over time the absorption at 600 nm. Arrows indicate the time of addition of 0.4 mM IPTG.

Western blot analyses was carried out to observed if the cells produced Galaxin. The results showed that only the cells of *E. coli* Rosetta-gami^{TM} 2(DE3) produced the protein probably because of their particular features described above (Fig. 4.4). So it was decided to use this kind of cells for the expression and purification of the protein.

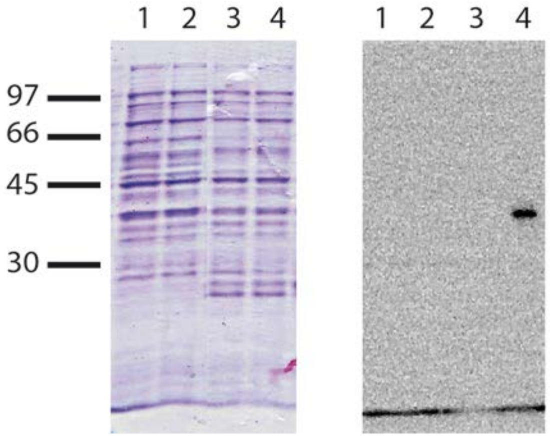

Figure 4.4: SDS-PAGE (on the left) and Western blot (on the right) of BL21(DE3) (lane 1, 2) and Rosetta-gami^{TM} 2 (DE3) (lane 3, 4), both transformed with pET22-Gal, collected during the bacterial growth before (lane 1 and 3) and after (lane 2 and 4) induction with IPTG. The black lines indicate the marker's bands with corresponding molecular weight in kDa.

The following step was resuspended protein in a buffer for carry on purification process. Usually proteins are dissolved in Binding Buffer 1X, but in this case Galaxin is not dissolved and remains in the pellet probably because is embedded in inclusion bodies. Denatured conditions are necessary to dissolve the protein. So part of the pellet was resuspended in Binding Buffer 1X with 6M Urea for 2h at 4°C and another part was resuspended in 2-Mercaptoethanol solution overnight because usually is used when protein have many cystein to better dissolved them. In both cases the solution was under shaking. After the necessary time, the solution was centrifuged at 10000 rpm for 20 min at 4°C to separate the pellet and supernatant. Through Western blot was checked if the protein was in the supernatant. In Fig. 4.5 is possible observed as Galaxin only partially was dissolved in presence of 6M Urea, infact is present both in pellet both in supernatant, while was not resuspended in 2-Mercaptoethanol solution where stands in the pellet.

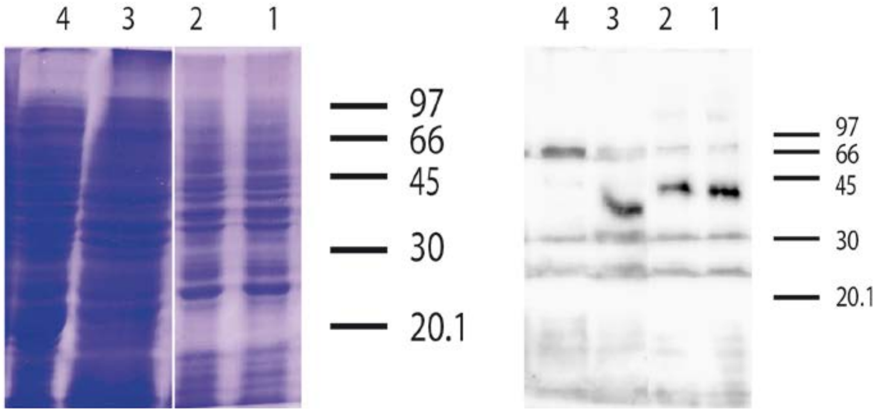

Figure 4.5: SDS-PAGE (on the left) and Western blot (on the right) of pellets and supernatants obtained after dissolution in 6M Urea (1 = pellet, 3 = supernatant) and 2-Mercaptoethanol (2 = pellet, 4 = supernatant). The black lines indicate the marker's bands with corresponding molecular weight in kDa.

To improve the system and obtain a major quantity of the protein in supernatant, Urea concentration and the time of stir at 4°C were increased. The pellet was resuspended half in 6M Urea and half in 8M Urea for 2, 4, 6, 18 and 24 hours at 4°C under shaking. The results showed that increasing the concentration of Urea decreases the time necessary to resuspend all the protein in the supernatant, while a lower concentration of Urea needs of more time to completely dissolve the protein (Fig. 4.6). In some cases also in pellet appeared some signals but probably are due to aspecific signals. However in all the SDS-PAGE electrophoretic gels there were not clear evidence of an increase of concentration of the band at 44 kDa that corresponds at Galaxin molecular weight. This indicates that the sistem yield is not so high probably because of the toxicity of the Galaxin that inhibits the cell growth.

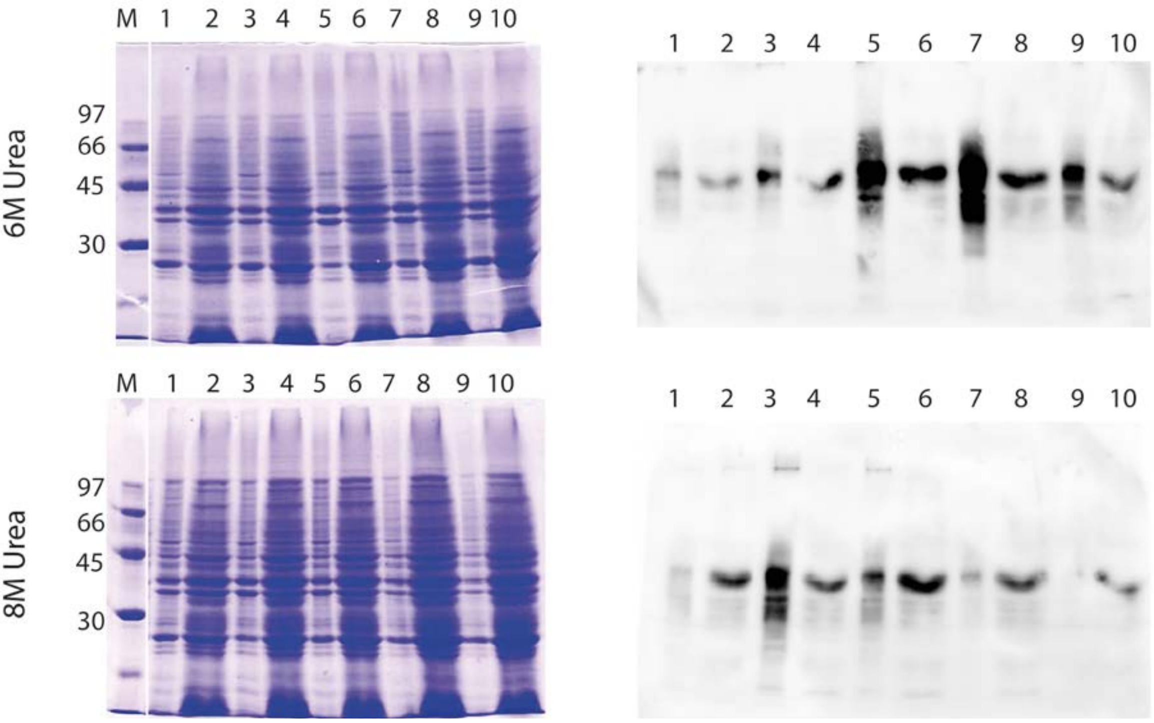

Figure 4.6: SDS-PAGE (on the left) and Western blot (on the right) of pellets (pel.) and supernatants (super.) obtained after dissolution in 6M Urea and 8M Urea for 2h (1 = pel., 2 = super.), 4h (3 = pel., 4 = super.), 6h (5 = pel., 6 = super.), 18h (7 = pel., 8 = super.) and 24h (9 = pel., 10 = super.). Lane M correspond to the marker and the corresponding molecular weight in kDa are writed on the left.

4.4 Conclusions

To better understand the role of Galaxin, an OM protein, in the biomineralization process, in this study its expression and purification were carried out.

The fact that through conventional techniques is difficult to express and purify Galaxin may be due to the presence of many cysteine residues in its structure. In this study have been tried several methods to purify the protein and it was concluded that:

- the best way to express Galaxin is to use a vector that carries an signal sequence for potential periplasmic localization for not affect *E. coli* cell metabolism;
- Galaxin is not resuspended in 2-Mercaptoethanol solution;
- To completely dissolve Galaxin are necessary a high concentration of Urea and a greater time of incubation in denaturing solution.

5. Biomineralization control related to population density under ocean acidification

5.1. Introduction

Several studies on the influence of pH on crystallography and texture of calcified regions are *ex situ*, short-term experiments on isolated organisms,[156] providing important information, but unrepresentative of natural ecosystems and failing to assess long-term effects.[157] There is a great need for long-term analyses on ocean acidification effects on marine ecosystems acclimated to high pCO_2, as found around CO_2 vents. Vents are not perfect predictors of future oceans, owing to pH variability, proximity of unaffected populations, and co-varying environmental parameters.[158] However, vents acidify sea water on sufficiently large temporal and spatial scales to integrate ecosystem processes,[157] acting as `natural laboratories'. In Papua New Guinea vents, reductions in coral diversity, recruitment and abundance, and shifts in competitive interactions, are found.[159] In Mediterranean vents, decreased diversity, biomass, trophic complexity and abundance in many calcifying and non-calcifying organisms, and increases in macroalgae and seagrasses, are observed.[158, 160, 161]

We assessed, along a natural pH gradient, the effect of pCO_2 on the mineralization and abundances of the aragonitic scleractinian *B. europaea*, the aragonitic tube-forming gastropod *V. triqueter*, the brown alga *P. pavonica*, which deposits aragonite on the thalli surface, and the green alga *A. acetabulum*, whose cups' outer surfaces are calcified with aragonite and a small amount of whewellite (calcium oxalate). The mineralization is biologically controlled in *V. triqueter* (that is, mineral is deposited in confined nucleation sites under complete biological control with minimal environmental effects), biologically induced in *P. pavonica* and *A. acetabulum* (that is, it is strongly affected by the environment with minimal biological control), whereas *B. europaea* may represent an intermediate and still controversial situation.[1] We aimed to assess changes in the mineralization and abundance of species along a pCO2 gradient in relation to their control over biomineralization.

5.2. Experimental section

Study site

The Island of Panarea belongs to the Aeolian Archipelago (Italy), located in the southern Tyrrhenian Sea in the Mediterranean (Fig. 5.1), and is part of an active volcanic system.[162] In the main vent, a crater 20 x 14 m wide and 10 m deep generates a sustained column of bubbles from the seabed to the sea surface. The hydrothermal system of Panarea is characterized by very active discharges of hydrothermal water and gas from the seafloor at a shallow depth (up to 150 m).[163] On the seafloor, at depths ranging from 8 to 40 m, in an area delimited by the islets of Dattilo, Bottaro, Lisca Nera and Lisca Bianca, there is a widespread presence of gas vents and hot water springs.[164]

As reported, the hydrothermal activity at Panarea was limited to only light gas bubbling in the years of first investigations (mid-80‘s) and the system was considered almost static and interpreted as the declining activity of a cooling and extinct volcano.[165] During the night of the 3rd of November 2002, a sudden and huge outgassing phenomenon was observed on the sea surface near the islets of Bottaro and Lisca Bianca, off the eastern coast of Panarea.[166] Several active spots were identified by direct observations and bathymetric investigations.[167] After the crisis, investigations on the Panarea hydrothermal system have intensified and were performed by co-authors of this study.[163, 165, 168]

Between November 2002 and March 2003 the monitored submarine gas exhalations displayed a complex combination of temporal and spatial changes of their chemical compositions. The pre-2002 conditions were restored relatively rapidly, reaching a stationary hydrothermal condition starting from March 2003.[169]

Carbonate chemistry

Four sampling Sites were selected (Fig. 5.1): a control site (Site 1), two intermediate pCO2 sites (Site 2 and Site 3), and a high pCO2 site (Site 4). pH (NBS scale), temperature and salinity were measured at each Site during several surveys between July 2010 and May 2013 with a multi-parametric probe (600R, YSI Incorporated) powered from a small boat and operated by SCUBA divers. Bottom-water samples for determination of total alkalinity were collected and analysed using standard methods. Further temperature data were recorded every three hours by sensors (Thermochron iButton, DS1921G, Maxim Integrated Products) attached in each Site from July 2010 to May 2013. Measured pH was converted to the total scale using CO2SYS software. Median pH (back transformed hydrogen ion concentrations) were calculated for each Site. The pH, total alkalinity, salinity and temperature were used to calculate other carbonate system parameters using the software CO2SYS.

Benthic survey

Photographs of benthos (5 to 10 per Site, 50 _ 50 cm for the animals, 21.0 _ 29.7 cm for the algae) were used to measure the percentage of cover for *B. europaea*, *V. triqueter*, *P. pavonica*, *A. acetabulum* at each Site.

Vent gas

Gas was sampled during five surveys (June 2011_May 2013) and analysed at the Laboratory of Fluid and Rock Geochemistry of the University of Florence using standard methods. Water samples were collected and tested for dissolved $H2S$

Statistical analyses.

Analysis of variance and the post hoc Fisher least significant difference test were used to test for differences among Sites using arcsine and log-transformation for percentage of cover and environmental data, respectively, when necessary. Otherwise, the non-parametric Kruskal-Wallis and Spearman's rank correlation coefficients were used. All analyses were performed using SPSS v.20.

.

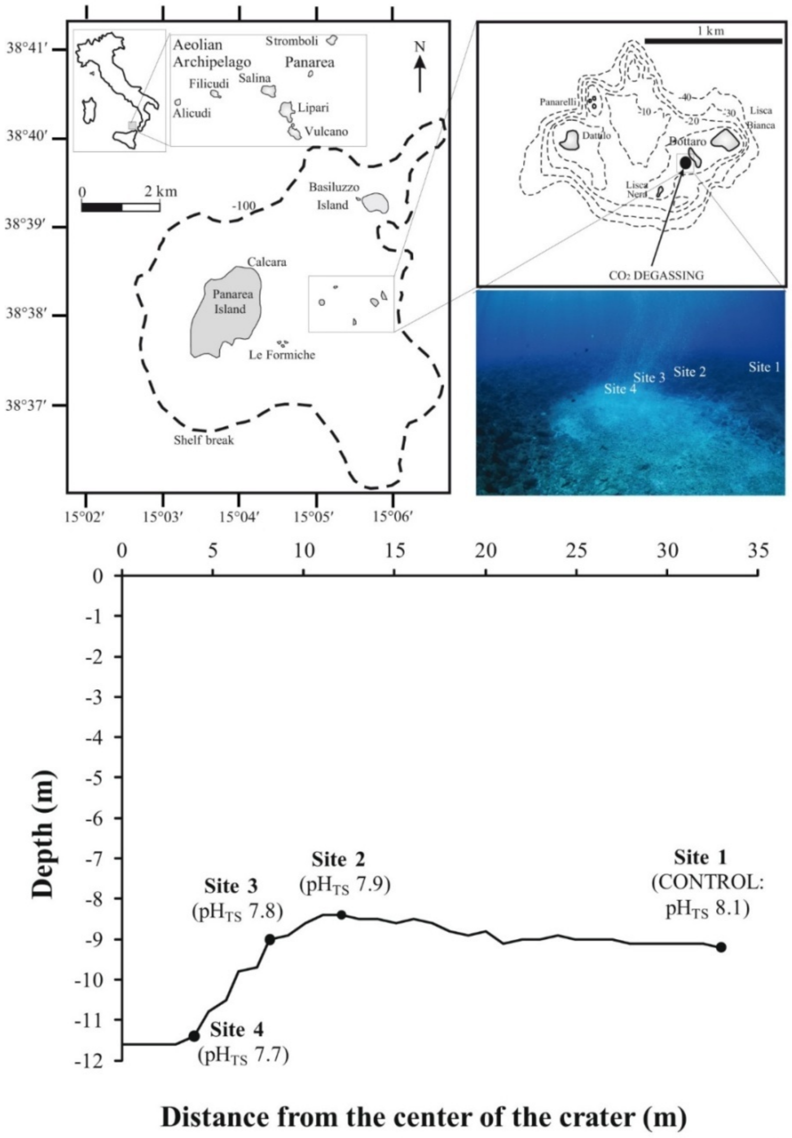

Figure 5.1: Map of vent site off Panarea Island (Aeolian Archipelago) and bathymetric profile of the experimental area. Underwater volcanic crater with localized CO_2 emissions a few tens of meters SE of Bottaro, one of the islets surrounding Panarea. Depth along the pCO_2 gradient goes from 11.6 m in the center of the crater to 9.2 m in the control site, at a distance of 34 m from the crater. pH values in brackets are expressed as medians at the total scale.

Sampling

Along these sites were collected different calcifying organisms: *Vermetus triqueter* (mollusc, gastropoda), *Balanophyllia europaea* and two species of macroalgae, *Padina pavonica* and *Acetabularia acetabulum*. After collection, all organism samples were rinsed with deionized water, cleaned from ground contaminations and stored in ethanol at 4°C. The skeletons of *B. europaea* and the shelltubes of *V. triqueter* were cleaned from the live tissues by treatment with a 0.5% (v/v) sodium hypochlorite for 10 minutes. The remaining skeletons and shell-tubes were then washed with deionized water and dried at room temperature. Each skeleton and shell-tube was inspected under a binocular microscope to remove fragments of rock and calcareous deposits produced by other organisms, such as serpulid tubes and bryozoan colonies. For some characterizations, the samples, or regions of them, were dusted using an agate mortar. Attention was paid to avoid high local increase of temperature. For microscopic observation and mechanical measurements, the samples were embedded in resin (Technovit 5071, Buehler), and were then lightly polished using colloid alumina (average size of 1 µm, PACE Technologies).

Spectroscopic measurements.

For spectroscopic measurements, the samples were sandwiched in a KBr disk and then polished normally to the disk surface. The demineralization process of the algae was carried out treating the samples with a 0.3% (v/v) acetic acid solution overnight. A series of considerations and tests were applied to get confidence on the presence of hydrated calcium sulphate salts in the tip of the thallus of *P. pavonica*.

i. *A. acetabulum* and *P. pavonica* were subject to the same procedure of sampling, cleaning and washing. Calcium sulphate salts were observed only on the surface of *P. pavonica*.

ii. A set of samples after collection were stored in sea water instead that in ethanol. Also in these sample was observed the presence of calcium sulphates salts.

iii. A third set of samples was stored in a saturated solution of $CaCO_3$, but unfortunately the algae decomposed.

iv. Upon drying of ethanol solution used to keep the algae, no detectable amounts of calcium sulphate were observed.

Despite all of the above facts we cannot completely exclude the possibility that the presence of calcium sulphate salts can be an unavoidable effect associated to the drying process, specific for *P. pavonica.*

X-ray powder diffraction. X-ray powder diffraction patterns of the samples were collected using a PanAnalytical X'Pert Pro equipped with X'Celerator detector powder diffractometer using Cu Kα radiation generated at 40 kV and 40 mA. The diffraction patterns were collected within the 2θ range from 10° to 60° or from 20° to 60° with a step size (Δ2θ) of 0.02 ° and a counting time of 1200 s. The X-ray powder diffraction patterns were analyzed using the X'Pert HighScore Plus software (PANalytical).

Fourier transform infrared spectroscopy. Low amount powder samples were analyzed by means of Fourier transform infrared (FTIR) spectroscopy analyses (for details see Appendix A).

Attenuated Total Reflection Fourier transform Infrared (FTIR ATR) spectra of sample cross sections were acquired in the range 4000–650 cm−1 with a Thermo-Nicolet Nexus 5700 spectrometer connected to a Thermo Continuum IR microscope, fitted with an MCT type A detector cooled by liquid nitrogen. Measurements were made with the microscope in reflection mode, using a 15× Thermo-Electron Infinity Reflachromat objective and a tube factor of 10×. A micro slide-on ATR with a silicon crystal (contact area diameter 120 μm) was connected to the 15× objective.

Thermal analyses. An estimation of the organic matter content in the sample was determined by thermo-gravimetric analysis (TGA) on a SDT Q600 simultaneous thermal analysis instrument (TA instrument) (see Appendix A)

Microscopy. Several fractured and polished sections of samples were cut perpendicular to the surface. Polished sections and some fractures were etched with various acids and enzymes to reveal microstructural features. The optical microscope observations of samples were made with a Leica microscope equipped with a digital camera. The scanning electron microscopy (SEM) observations were conducted in a Phenom™ microscope (FEI) for uncoated samples and a Hitachi FEG 6400 microscope for samples after coating with gold. Presented images are representative of the entire population of each sample. The aragonitic fiber diameter in the coral skeleton was measured from high magnification SEM images (see Fig. 5.4). About 20 fibers were measured from three different skeleton fragments for each site.

Mechanical analyses. The mechanical properties of coral skeletons and mollusc shell-tubes were measured using a Nanoindentation Tester, model NHT-TTX by CSM Instruments, equipped with a Berkovich diamond tip. The maximum applied load in the test was always 50 mN, corresponding to a penetration depth in the range from 700 to 900 nm. The instrumented (IT) values of the elastic Young's modulus (EIT) and hardness (HIT) were determined by Oliver-Pharr analysis of the loaddepth curvesS18. The reported values are the average of at least 10 measurements.

5.3 Results and Discussion

Mean pH, CO2, saturation of calcite (Ω_{calc}), and of aragonite (Ω_{arag}) di_ered among Sites (Kruskal-Wallis test/analysis of variance, $p<0.001$). The median pH values were 8.1 (Site 1), 7.9 (Site 2), 7.8 (Site 3) and 7.7 (Site 4), with increasing variability towards Site 4 (Table 5.1).

Aragonite was the only mineral phase in *B. europaea* skeletons (Fig. 5.2). Organic matrix content was homogeneous among Sites (Kruskal-Wallis test, $p> 0.05$; Table 5.1). Skeletal texture exhibited fibres evolving from a centre of calcification (Fig. 5.3), but the morphology of these centres, and fibre thickness (600-200 nm), were not related to pCO_2 (Fig. 5.4). Hardness was homogeneous among sample regions and study Sites (5100±600MPa). The elastic Young's modulus decreased (that is, the skeleton became less stiff) along the aboral to oral direction and was lower at Sites 2 and 3 than at Site 1. Crystal quality and fibre thickness usually increases when crystallization occurs under lower supersaturation.[111] Although a reduction of precipitation rate with pCO_2 could increase crystal quality, other mechanisms could involve OM molecules. Corals seem to maintain a high pH at the nucleation sites within the calicoblastic layer, possibly expending a significant amount of energy.[144] This is supported by the lack of increase in aragonite fibre thickness with decreasing seawater Ω_{arag}, which would be expected if Ω_{arag} of the calcification site decreased.[111]

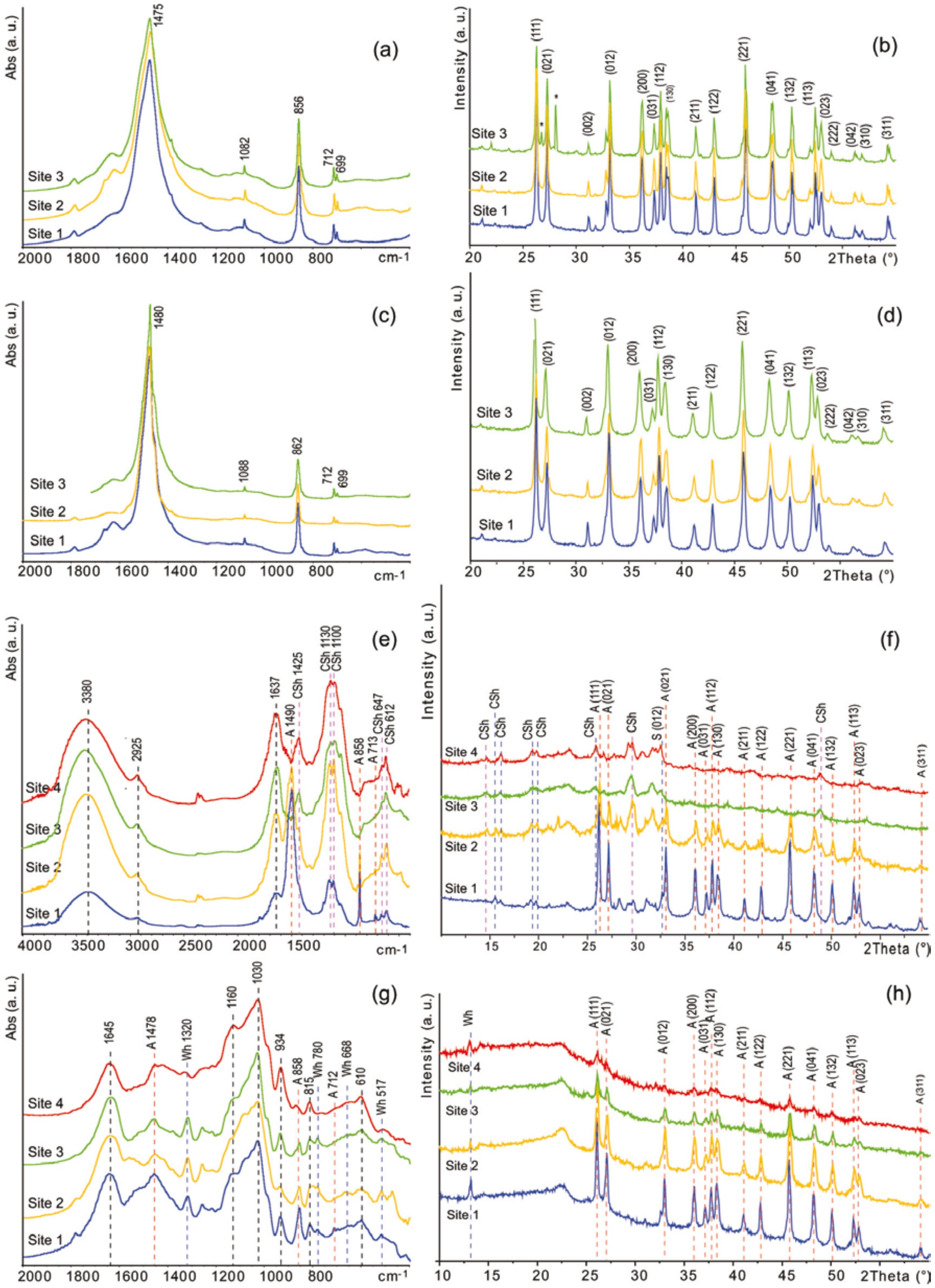

Figure 5.2: Fourier transform infrared spectra (a, c, e, g) and X-ray powder diffraction patterns (b, d, f, h) from ground skeletons of *Balanophyllia europaea* (a, b) and ground tubes of *Vermetus triqueter* (c, d) collected at Sites 1 to 3 along the pCO_2 gradient, and from ground samples of *Padina pavonica* (e, f) and *Acetabularia acetabulum* (g, h) collected at Sites 1 to 4. In (a-d) only absorption bands and diffraction peaks due to aragonite are observable. In *P. pavonica* (g, h) absorption bands and diffraction peaks due to aragonite (A) and mono hydrate calcium sulphate minerals (CSh) are marked. In *A. acetabulum* (e, f) only absorption bands and diffraction peaks due to aragonite (A) and whewellite (Wh) are observable. The diffraction peaks are indicated according to the Miller indices. Spectra are vertically offset to increase their readability.

Table 5.1: Summary of the main effects of ocean acidification on the mineral distribution and content in the calcified organisms with increasing proximity to the CO**2** seep (declining pH).

			B. europaea		*V. triqueter*		*P. pavonica*		*A. acetabulum*	
	Median pH	**Median Ω_{arag}**	**Mineral phase**	**Mineral phase (%)**[†]	**Mineral phase**	**Mineral phase (%)**	**Mineral phases**	**Mineral phases (%)**	**Mineral phases***	**Mineral phases (%)**
Site 1	8.1	3.6	A	97.4 ± 0.4	A	98.0 ± 0.5	**A** CSh[‡]	73.9 ± 8.3	**A** Wh	42.9 ± 3.9
Site 2	7.9	2.4	A	97.80 ± 0.04	A	98.3 ± 0.2	A CSh	71.5 ± 10.6	**A** Wh	24.2 ± 6.9
Site 3	7.8	2.1	A	97.8 ± 0.2	A	98.1 ± 0.1	A **CSh**	59.6 ± 4.9	A **Wh**	22.7 ± 7.6
Site 4	7.7	1.5	-	-	-	-	A[‡] **CSh**	61.6 ± 4.5	Wh	25.4 ± 8.0

Uncertainties are one standard deviation. A, Wh and CSh indicate aragonite, whewellite and monohydrate calcium sulphate salts. The percentage of mineral phase(s) is reported as mass ratio. *Amorphous globular particles were also detected. [†]The content of organic matrix is the complement to 100 in *B. europaea* and *V. triqueter* where no significant amounts of water were detected in the skeletons and shell-tubes. *P. pavonica* and *A. acetabulum* contained a significant amount of bounded water and their percentage of organic matrix significantly increased with *p*CO2. [‡]This phase was detected in traces. When two phases were present, the most abundant one is indicated in bold.

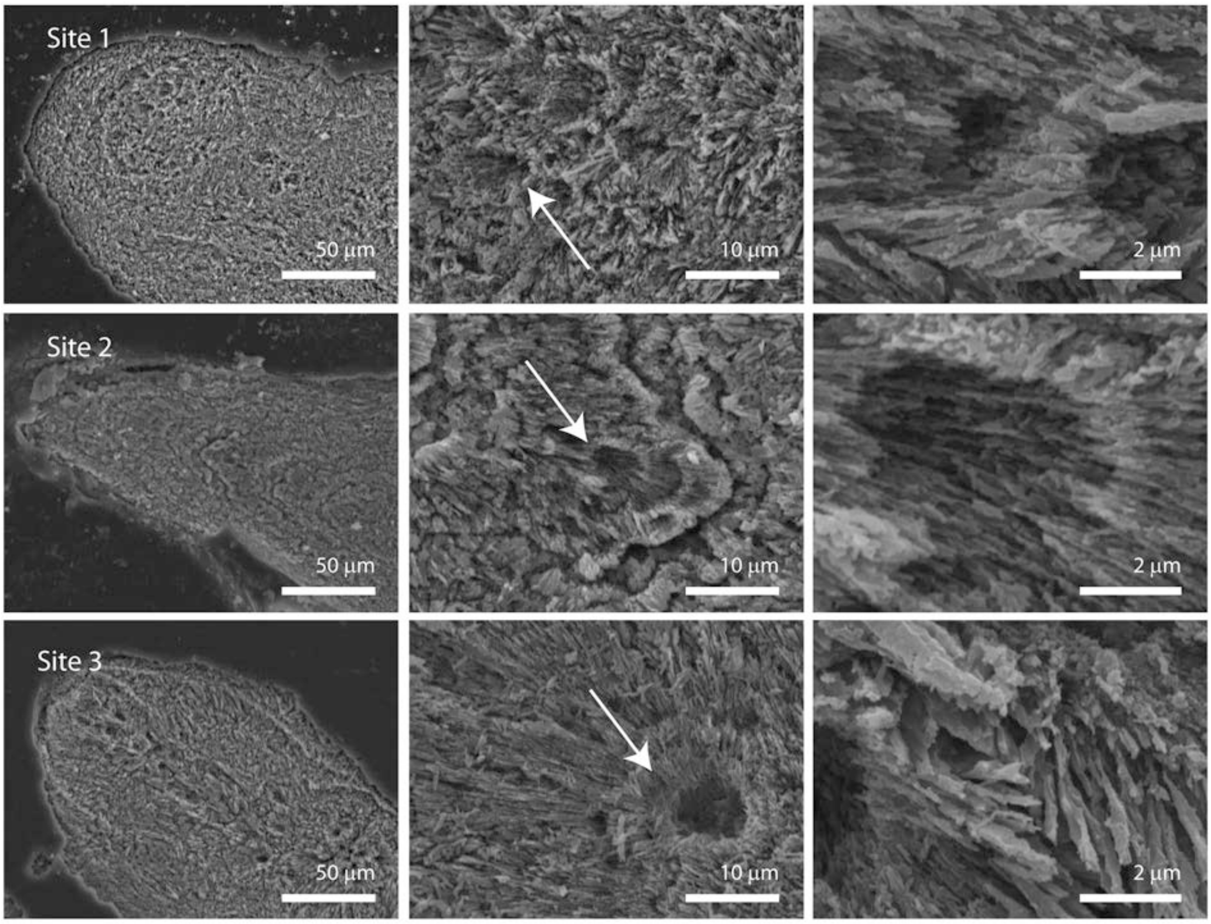

Figure 5.3. SEM images of *Balanophyllia europaea* skeletons. Centers of calcification (indicated by arrows) and fibers were observed. Their size, shape and distribution were not related to pCO_2.

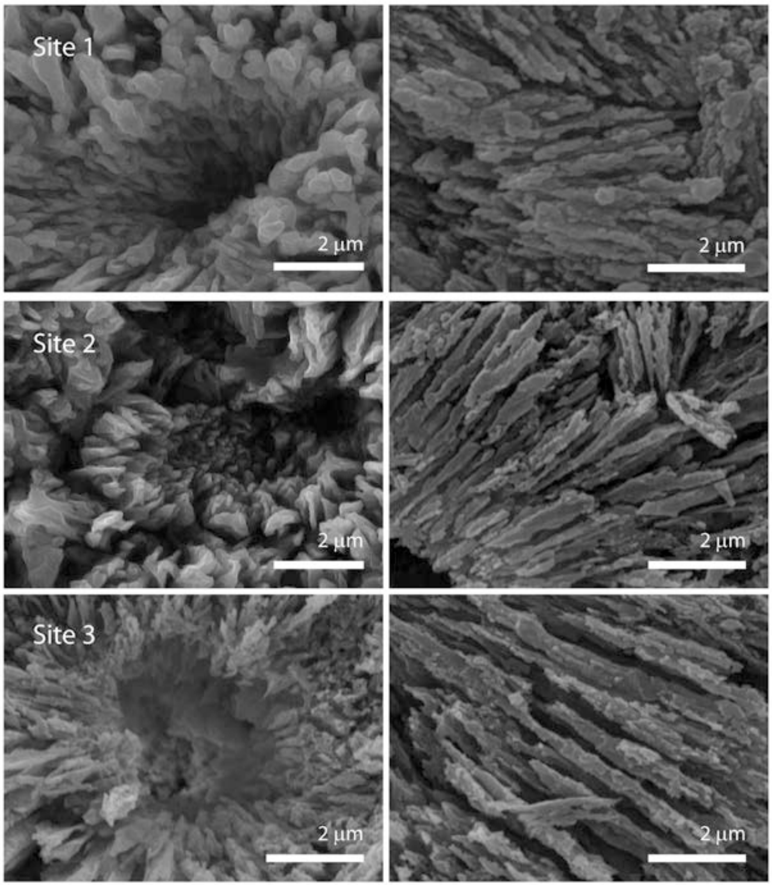

Figure 5.4. Scanning electron microscope images of the cross sections of the tip regions of septa of *Balanophyllia europaea* skeletons collected atSites 1 to 3 along the pCO_2 gradient. The two structural entities constituting the coral skeleton, centers of calcification and fibers, are illustrated in the left and right columns, respectively. The observed differences were not statistically significant.

The apical regions of *V. triqueter* shell-tubes of similar diameter (~5 mm) were analysed. Aragonite was the only mineral phase (Fig. 5.2). Shell-tubes from Site 1 had four layers with different crystal texture and variable relative thickness among samples (Fig. 5.5). The first two layers were prismatic, with the second one made of regular prisms with a square section (500nm side). The third was cross-lamellar with regular fibres 500nm thick. The fourth external layer was spherulitic, with several bores and channels (Fig. 5.5). In one of six samples from Site 2, and in four of six from Site 3, the two internal layers were not present. Different hardnesses and elastic Young's moduli were associated with different textures, without significant variations among Sites. OM content was homogeneous among Sites (Kruskal-Wallis test, $p>0.05$; Table 5.1). The unaffected mineralogy of *V. triqueter* shell-tubes is possibly due to the exquisite control of biological macromolecules on mollusk mineralization, which occurs in confined sites resulting in complex crystalline textures (Fig. 5.5). During shell-tube growth, the external layers are the first to be deposited, followed by the internal ones.[1] A pH reduction can reduce the growth rates (calcification) of mollusk shells,[170] which probably explains the absence of the internal layers in shell-tubes from the most acidic Sites.

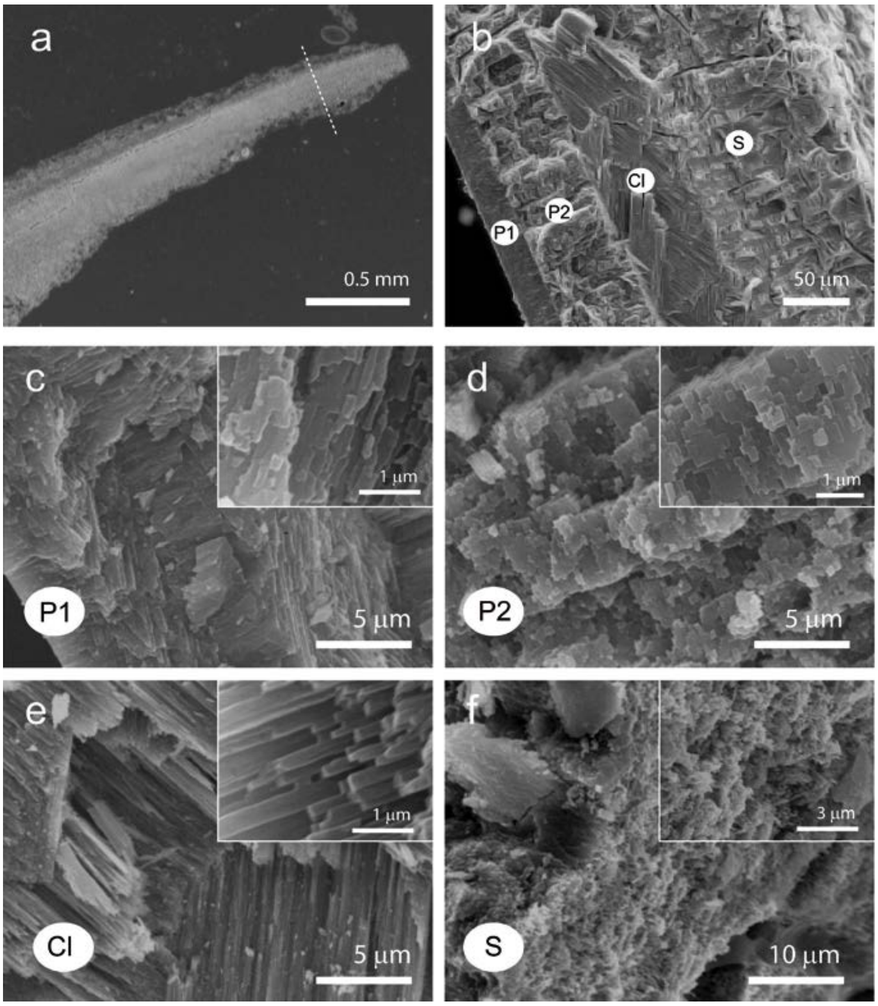

Figure 5.5. Scanning electron microscope images of a longitudinal section of *Vermetus triqueter* shell-tube. **a**) Apical region of shell-tube. High-magnification images were taken along the dotted line from inside (P1) to outside (S) the tube; **b**) shell-tubes in Site 1 consisted of four layers (P1, P2, Cl, S); **c**) first prismatic layer (P1); **d**) second prismatic layer (P2), with square cross-sections; **e**) cross-lamellar layer (Cl); **f**) spherulitic layer (S) containing bores and channels. The first two layers were not present in one sample from Site 2 and in most of the samples from Site 3.

Padina pavonica thallus tips from Site 1 were mainly aragonitic with traces of hydrate calcium sulphate salts (CSh). Aragonite concentration decreased with increasing pCO_2, and almost only CSh was observed at Site 4 (Fig. 5.2). The presence of CSh was investigated in detail by further tests and considerations (see 5.2 Experimental section). The overall mineral content differed among Sites (Kruskal-Wallis test, $p< 0.05$; Table 1), and declined with increasing pCO_2 (Spearman's rho of the correlation with pH D 0.592, $p< 0.01$). In all samples, many aragonite needle-like crystals were aggregated or merged forming bundles. CSh crystals appeared as prisms or tablets (Fig. 5.6 and 5.8). The decalcification left the thalli free of mineral deposits (Fig. 5.8). In *P. pavonica*, CSh increased with increasing pCO_2. Some stabilization of CSh salts by algal molecules,[171, 172] probably polysaccharides, is expected, as in sea water CSh converts to gypsum.

Acetabularia acetabulum was mainly aragonitic, with minor presence of whewellite (Fig. 5.2). All samples contained about 10% (w/w) of water. The content of mineral phases, estimated after pyrolysis and release of water, differed among Sites (Kruskal-Wallis test, $p < 0.01$; Table 1) and declined with increasing pCO_2 (Spearman's rho of the correlation with pH D 0.555, $p< 0.01$). The aragonite/whewellite ratio decreased with increasing pCO_2. Globular granules of amorphous material rich in Ca and S were observed on the surface of needle-like aragonite aggregates at Sites 1-4 (Fig. 5.6 and 5.8). Whewellite was the only phase detected at Site 4 (Fig. 5.2 and 5.6), where it appeared as prisms. After decalcification, the cup surface was free of mineral deposits (Fig. 5.8). In line with a mainly chemical mineralization control,[172] increasing pCO_2 did not affect deposition of whewellite in *A. acetabulum*. The persistence of amorphous globular particles rich in calcium and sulphur was unexpectedly observed when aragonite disappeared. This phase, soluble in acetic acid solution, may be the result of interactions between Ca ions and the sulphonated groups of polysaccharides.

Within each sample, *P. pavonica* and *A. acetabulum* showed a marked reduction of mineralized areas with increasing pCO_2 (Fig. 5.7). Their aragonite content decreased with decreasing arag. At a Ω_{arag} of 1.5, aragonite was not observed, probably because this saturation level is too low to sustain its nucleation process. The observed changes in morphology of aragonite crystals (Fig. 5.6) are associated with seawater chemistry.[173]

The percentage of cover for all species, except *A. acetabulum*, differed among Sites (Kruskal-Wallis test, $p<0.001$), and decreased with increasing pCO_2. *B. europaea* and *V. triqueter* were not found at Site 4 (pH=7.7, Ω_{arag}=1.5). Densities of *A. acetabulum* were homogeneous among Sites (Kruskal-Wallis test, p> 0.05). This suggests that *P. pavonica* and *A. acetabulum* are not obligate calcifiers, persisting in high pCO_2.

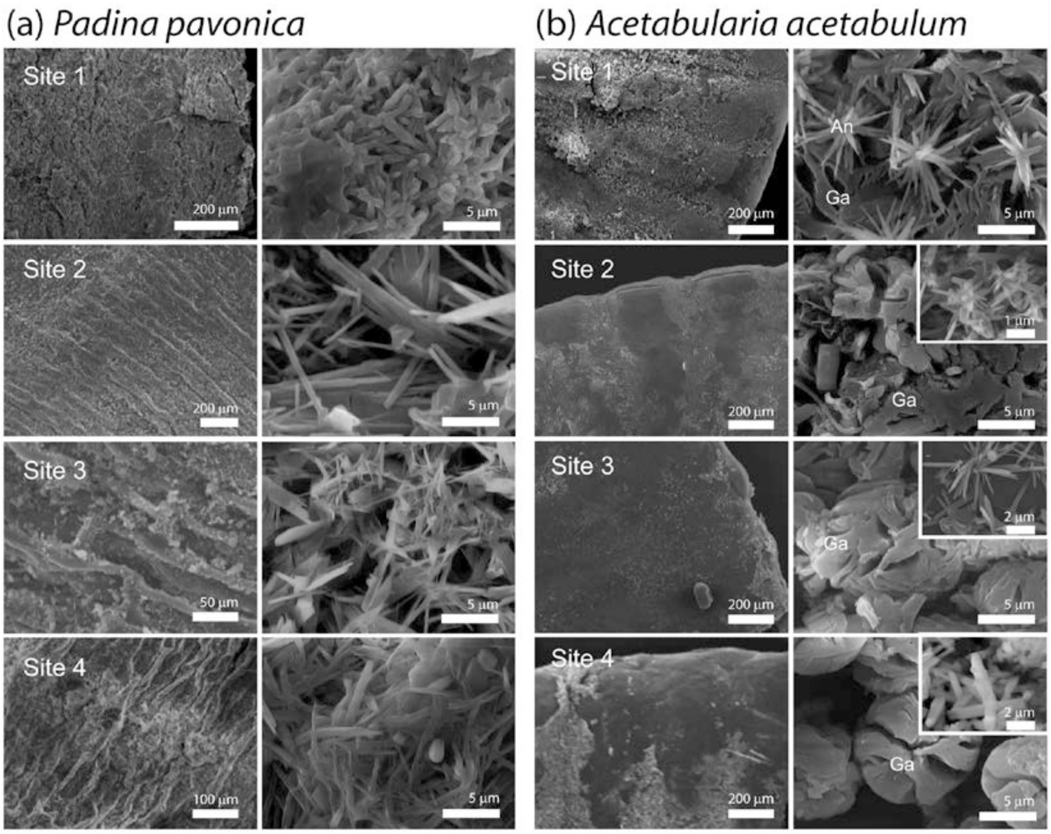

Figure 5.6. SEM images of *Padina pavonica* thalli and *Acetabularia acetabulum* cups. Left column: low magnification, right column: high magnification images. *P. pavonica* became less mineralized with increasing pCO_2. The aggregation and shape of aragonite crystals was lightly affected by pCO_2. In *A. acetabulum*, needle-like crystals of aragonite (An) were above and among the globular aggregates (Ga). The amount of biomineralized material was reduced with increasing pCO_2, while the center of the cup became more populated by spherical aggregates. Aragonite needles are shown in the inset for Site 2 and 3, while whewellite is shown in the inset for Site 4.

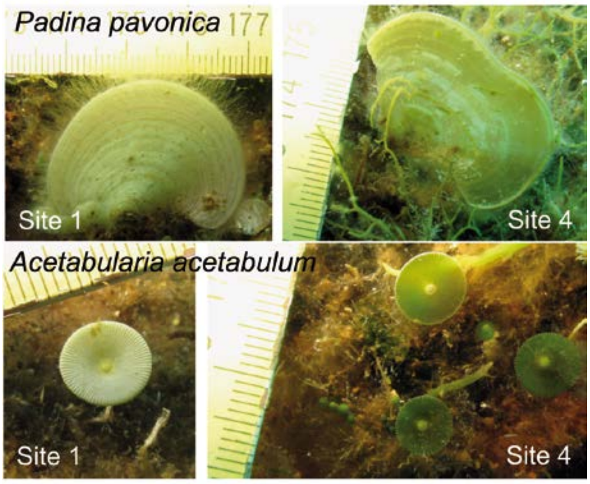

Figure 5.7.. *In situ* pictures of *Padina pavonica* and *Acetabularia acetabulum* at Sites 1 and 4, showing the reduction of calcified material (white areas) with increasing pCO_2.

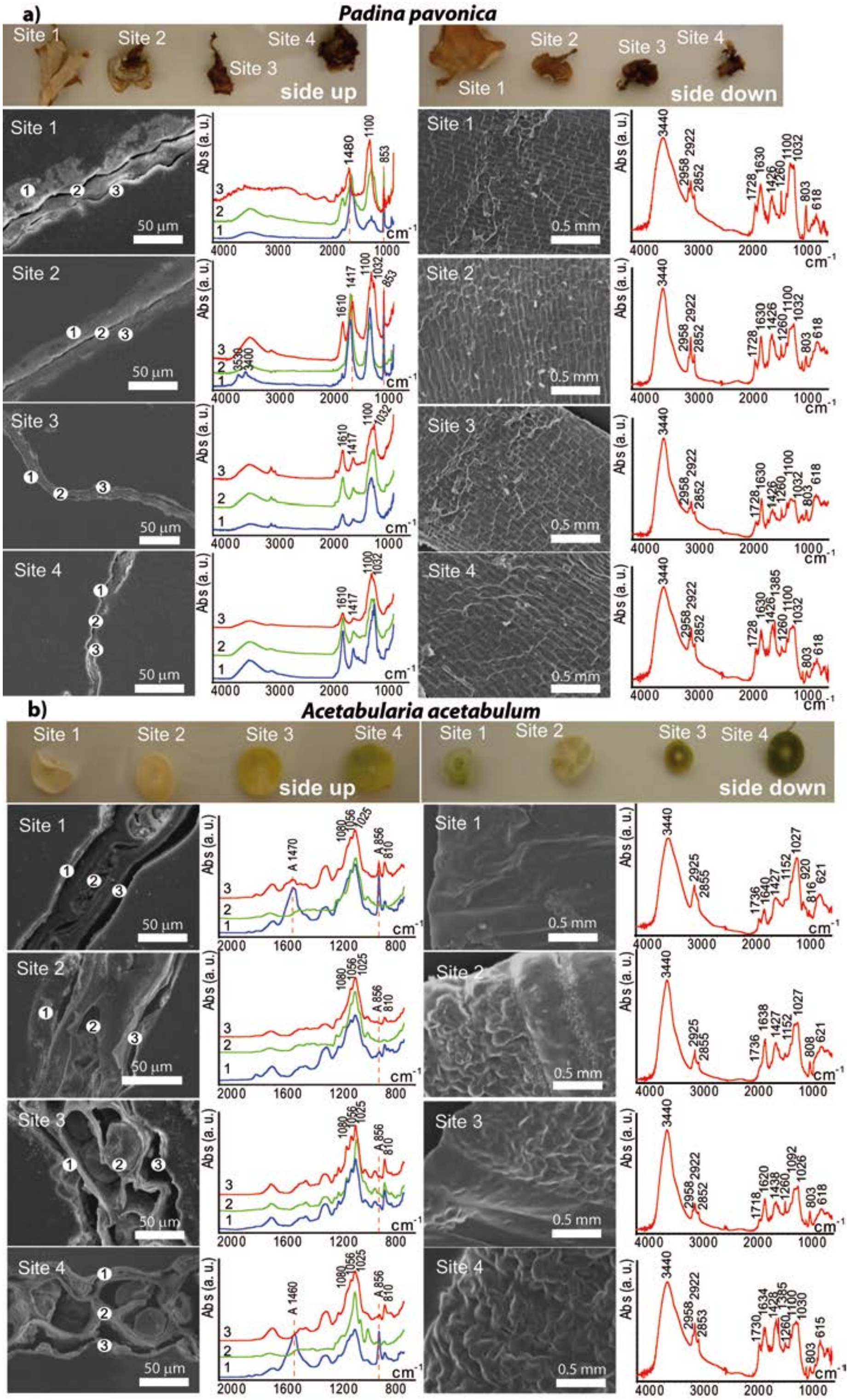

Figure 5.8. *first row* Dry thalli of *Padina pavonica*(a) and dry cups of *Acetabularia acetabulum*(b) collected atSites 1 to 4 along the pCO_2 gradient. The calcified regions appeared white, with the upwards facing surfaces being more heavily calcified than the downward facing surfaces. Scanning electron microscope images (*first column*) of the cross sections of the thalli (a) and the cups (b) and corresponding ATR FTIR spectra (*second column*) at three points, the two surfaces (1, upward; 3, downward) and inside the algae (2), for each sample at each site. The dotted line in the ATR FTIR spectra indicate the band associated to aragonite. The image shows that the upward pointing face is more calcified than the downward facing surface and that mineral phases were not detected inside the algae thalliorcups. Scanning electron microscope images (*third column*) of the surface of the thalli (a) and cups (b) after overnight treatment with a 0.3% acetic acid solution and corresponding FTIR spectra (*fourth column*). The surfaces are completely free of mineral phases and FTIR spectra do not show any absorption band clearly associable to mineral phases.

A changing benthic community was associated with the pCO_2 gradient. The coverage of a coral, a mollusc, and one macroalgae declined with increasing pCO_2. This is in agreement with previous investigations at CO_2 vents, documenting marked reductions in calcifying macroalgal abundance.[158, 159] Calcifying organisms seem the most sensitive to elevated pCO_2,[174] even if their response is not consistent.[159, 170, 175] *A. acetabulum*, *B. europaea* and *V. triqueter* were previously found only outside vent areas, at a pH_{TS} of 8.14.[158] Instead, in our survey *B. europaea* and *V. triqueter* survived up to pH_{TS} 7.8 and algal species up to pH_{TS} 7.7. The response of macroalgae to pCO_2 is expected to vary among species. As an example, increased cover with decreasing pH was observed for *Padina spp*. at CO_2 seeps in Vulcano and Papua New Guinea[176] which contrasts with our data.

We related the biological control over biomineralization with changes in the abundance of organisms along natural pCO_2 gradients. The content of biomineralized products decreased with increasing pCO_2 only in the two calcifying algal species (with a weak control over their biomineralization), but the two species with stronger biomineralization control (*B. europaea* and *V. triqueter*) tolerated less severe pCO_2 increases (pH 7.8) than the algae ($pH \leq 7.7$). Moreover, the more tolerant algae continued to grow despite their biomineralization products being profoundly altered by pCO_2. Even if biomineralization in algae is only induced,[172] we cannot exclude that the switch from aragonite to other biominerals may represent a phenomenon of phenotypic plasticity,[177] which is increasingly being found to strongly contribute to persistence in the face of climate change.[178] The control over biomineralization may not be the only cause of the observed differences, because the coral and the mollusc have a biology completely dependent on calcification, whereas the algae do not. Moreover, the algae may benefit from pCO_2 increase in terms of photosynthesis, whereas the coral may be less dependent on the photosynthetic process and the mollusc does not photosynthesize.

5.5 Conclusions

This study adds new evidence to field studies on ocean acidification effects,[161, 179] all indicating major ecological shifts as CO_2 rises. It documented that the mineralization response to ocean acidification seems connected with the organisms' control of biomineralization, increasing pCO_2 profoundly affects the abundance of many benthic organisms, and only the species with weaker control were observed at the lowest pH.

This work has been published (see Goffredo S., Prada F., Caroselli E., Capaccioni B., Zaccanti F., Pasquini L.,Fantazzini P., Fermani S., Reggi M., Levy O., Fabricius K. E., Dubinsky Z. Biomineralization control related to population density under ocean acidification. Nature Climate Change. 2014, 4, 593–597).

6. Evidence of structural variability among synthetic and biogenic vaterite

6.1 Introduction

Calcium carbonates occur widely in nature, having an important role in many biological functions and processes in living organisms.[1, 72, 180] In addition, they are the major minerals in many sedimentological environments. Calcium carbonates are also valuable in many industrial applications, such as paper, rubber, plastics, and paint production.[181]

Under ambient conditions of temperature and pressure, calcium carbonates appear in the form of three polymorphs and several hydrated phases. Of these, vaterite is thermodynamically unstable with respect to the other anhydrous crystalline polymorphs, aragonite and calcite, which explains its rare appearance as a mineral in geological settings. At the same time, during the early stages of conventional precipitation systems, vaterite formation was observed and explained by Ostwald's rule of stages.[182] On the other hand, vaterite is stable with respect to hydrated modifications and ACCs,[183] so it plays an important role as a precursor in several carbonate-forming processes.[184] However, the natural occurrence of vaterite is usually associated with biogenic activities. In the case of pathological mineralization, vaterite appears in pancreatic and gallstone formation or clogging in human heart valves.[185] As a biomineral, vaterite is present in fish otoliths,[186, 187] crustacean statoliths,[188] green turtle eggshells,[189] freshwater lackluster pearls,[190] aberrant growth of mollusk shells after an injury,[191] or spicules of the ascidian *Herdmania momus*.[192]

Preparation of synthetic vaterite has been extensively investigated and described, either in the precipitation systems without the addition of the additive,[193] or under additive assisted[194] or template-directed[195] conditions.

One of the most striking features of vaterite is the wide variety of shapes and morphologies it can hold,[184] which is related to its high surface energy.[196] On the other hand, researchers not yet succeeded in producing single crystals of vaterite of suitable quality for accurate structure determination by X-ray diffraction. Consequently, the crystal structure of vaterite has been controversial and not well understood. Only recently, Kabalah-Amitai et al. [197] used a high-resolution, aberration-corrected transmission electron microscope (HR-TEM) and found that in a ‘‘single crystal’’ of vaterite, isolated from the biogenic spicules of *H. momus*, a predominantly hexagonal structure coexists with one, or even more, distinct crystallographic structures.

At the same time, Demichelis et al.[198] proposed theoretically the existence of several stable vaterite structures, which required just room-temperature thermal energy for their inter-conversions. The authors also concluded that the vaterite is not a single ‘‘disordered’’ structure, but it should be considered as a combination of different forms. The possible presence of biological molecules was not considered in the described studies and their potential effect on the structure inter-conversions was not discussed, in spite of the fact that biological macromolecules have a demonstrated role in the stabilization of vaterite. Specifically, it was observed that the biogenic vaterite is stable in water solution for months, while under similar conditions, synthetic samples rapidly convert to calcite.[197, 199] Consequently, the possibility that the control of the distribution of vaterite structures is species specific and caused by particular macromolecules cannot be excluded.

Although recent studies contributed to the understanding of the vaterite structure[197, 198] and explained discrepancies among experimental and theoretical data, the question of the role of organisms in the formation of species specific vaterite structures remained open. In this study the structural features of synthetic and biogenic vaterite samples were compared (Fig. 6.1). More specifically, the biogenic vaterite samples were isolated from the asteriscus otolith from the *Condrostoma nasus,* the Chinese freshwater cultured lackluster pearl (from *Hyriopsis cumingii* mussels) and the spicule of the ascidian *H. momus*. Synthetic vaterite samples were precipitated by mixing solutions of $CaCl_2$ and at lower initial concentrations, ci(Ca) = ci(CO_3) = 1.0 mM (vat1), and at higher initial concentrations, ci(Ca) = ci(CO_3) = 2.5 mM (vat2). Synthetic vaterite samples were also prepared in the presence of poly-L-aspartate (pAsp) dissolved in the carbonate solution, applying a similar protocol and keeping the Ca^{2+}/pAsp molar ratio constant. The pAsp concentrations, c = 1.25 ppm (vat1-pAsp) or c = 3.00 ppm (vat2-pAsp), were used in the 1.0 mM or 2.5 mM systems, respectively. This polypeptide was used as a synthetic analogue of the intra-skeletal acidic macromolecules of biogenic vaterite.[186] In the system of higher concentrations, the supersaturation was, $S_{vat} = 6.36$, while in the lower concentration system, $S_{vat} = 3.71$.[193, 194]

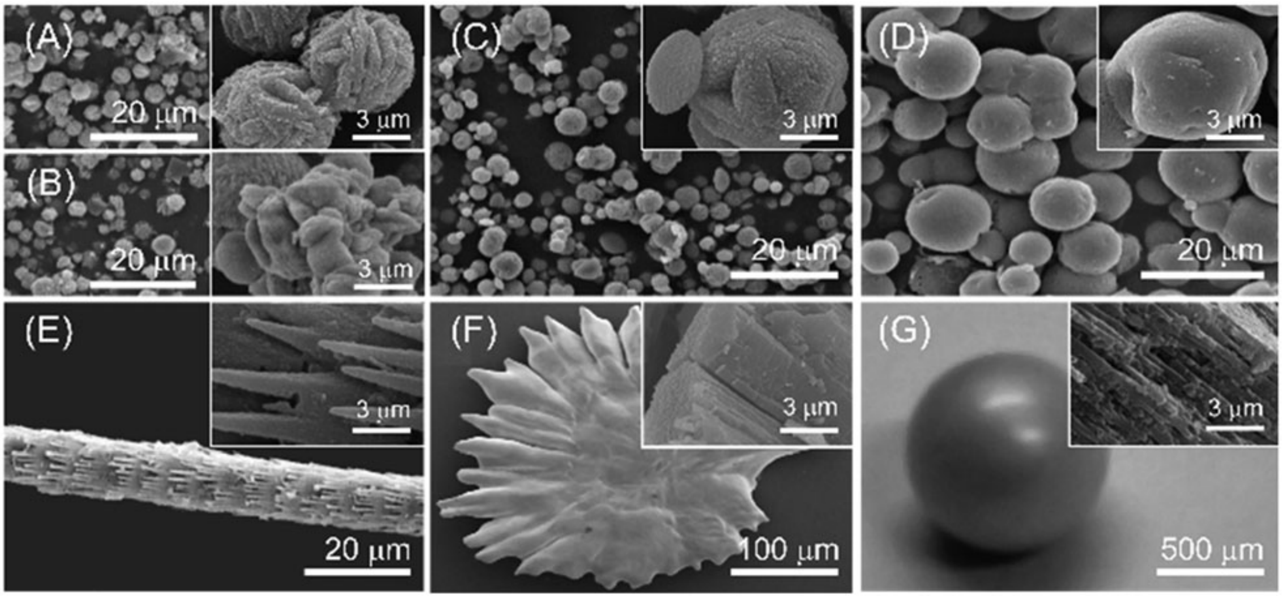

Figure 6.1 Scanning electron microscope pictures of: (A) vat1 (B) vat2 (C) vat1-pAsp (D) vat2-pAsp (E) *H. momus* spicule. (F) *C. nasus* asteriscus otolith. (G) lackluster pearl.

6.2 Experimental section

Synthetic vaterite minerals preparation

The chemicals used to prepare the reactant solutions, $CaCl_2$, Na_2CO_3 and $NaHCO_3$ (all Merck), were analytically pure and the deionized water was of high quality (conductivity <0.055 µS cm^{-1}). Na_2CO_3/$NaHCO_3$ solution was prepared by dissolving anhydrous Na_2CO_3 and/or $NaHCO_3$ in water, while $CaCl_2$ solution was made by diluting an appropriate amount of $CaCl_2$ stock solution.

The preparation of the respective vaterite seed was performed in a thermostated double walled glass vessel with a 400 cm^3 capacity. The vessel was tightly closed by a Teflon cover, thus minimizing the exchange of CO_2 between the air and the reaction system. Precipitation was always initiated by mixing the equal volumes (200 cm^3) of $CaCl_2$ and freshly prepared Na_2CO_3/$NaHCO_3$ solutions. The appropriate amount of pAsp additive was always added to the carbonate solution, to which $CaCl_2$ solution was then rapidly added. The initial concentrations of reactants, total calcium and total carbonate, were equimolar for the two systems,

vat1: $c_i(Ca) = c_i(CO_3) = 1.0 \cdot 10^{-3}$ mol dm^3 ($pH_i = 10.37$; $S_v = 3.71$) and

vat2: $c_i(Ca) = c_i(CO_3) = 2.5 \cdot 10^{-3}$ mol dm^3 ($pH_i = 10.01$; $S_v = 6.36$).

During the experiments, the systems were continuously stirred at a constant rate by means of a Teflon-coated magnetic stirring bar and all experiments were carried out at 25 °C. The progress of the reaction was followed by measuring the pH of the solution using a combined glass-calomel electrode (GK2401C) connected to a digital pH meter (PHM 290, Radiometer).

At a predetermined time (about 400 or 2500 sec), the total volume of the suspension was filtered through a 0.22 µm cellulose nitrate membrane filter (Millipore), washed with small portions of water, and dried at 105 °C.

Calculations of the initial solution composition, as well as of the composition at any time during the process, were based on pH measurements. The total $CaCl_2$ and $Na_2CO_3/NaHCO_3$ concentrations initially added to the system were used for calculating the molar concentrations and activities of the 11 ionic species assumed to be present in solution in significant amounts. The supersaturation was defined as, $S_{vat} = (\Pi/K_{sp}^{o})^{½}$, where Π is the ion activity product, $\Pi = a(Ca^{2+}) \cdot a(CO_3^{2-})$, and K_{sp}^{o} is the thermodynamic equilibrium constant of dissolution of vaterite at 25 °C: ($K_{sp}^{o} = 1.221 \cdot 10^{-8}$).

The detailed calculation procedure, which takes into account the respective protolytic equilibria and equilibrium constants, as well as the charge and mass balance equations, is given in previous papers (e.g. Njegić Džakula *et al.*[194]).

Biogenic vaterite samples preparation

The asteriscus otoliths for this study were taken from the head of the fish *Chondrostoma nasus* collected from the Isonzo River (Italy). After dissecting them from the fish ears, they were washed with sodium hypochlorite (NaOCl) for 1 hr to remove any superficial contaminant organic tissue, then with Milli-Q water (resistivity 18.2 MΩ cm at 25 °C; filtered through a 0.22 μm membrane), and finally air-dried. No distinction was made between sex and left or right ear otoliths.

Herdmania momus specimens for this study were collected by scuba diving from marine floats in Eilat at the northern tip of the Gulf of Aqaba (Red Sea), Israel. Specimens were cut into small tissue pieces, which were then treated with 7% NaClO to remove the organic tissues. NaOCl was replaced frequently and vials were shaken gently for 6 weeks until all organic tissues were removed. Spicules were filtered to remove debris and washed 3 times in 100% ethanol.

The treatment with the NaClO solution is supposed not to affect the content and structure of the intracrystalline organic matrix. Organic matrix is entrapped into the mineral phase, which is insoluble in the NaClO solution.

Pearls were kindly supplied by Prof. Feng (China). Unfortunately, the authors did not succeed in obtaining a geological vaterite sample to be used as a standard and compared with the biogenic ones.

Characterization of different vaterite samples

XRD profiles, FTIR analyses and SEM observations were conducted as just described in Appendix A. DSC analysis were perform in the same way described in Chapter 3.2.

6.3 Results and Discussion

The X-ray diffraction analyses showed the presence of vaterite as a unique crystalline phase in all biogenic samples while, in the synthetic samples, traces of calcite were detected (Fig. 6.2).

The differences between the particle shapes and morphologies of synthetic and biogenic vaterite were significant, as shown in Fig. 6.1. The synthetic vaterite appeared predominantly as spherical structures, built up of hexagonal plate-like aggregates.

The shape and morphology of the vat1-pAsp particles were similar to those of pure synthetic vaterite, while the surfaces of the vat2-pAsp particles appeared much smoother. The shapes of the biogenic vaterite samples, as well as the respective primary building blocks, were found to be species specific. The ascidian spicule was built up from acicular prisms, the asteriscus otolith from prisms and the primary building blocks of lackluster pearls were tablets.

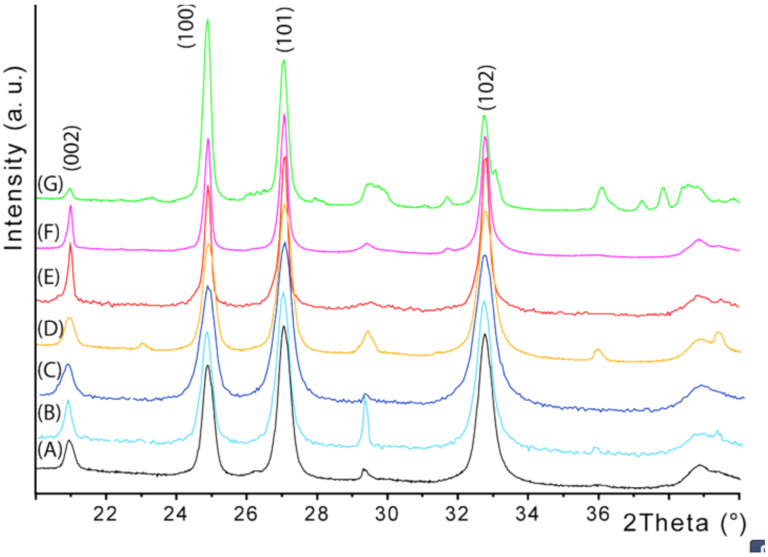

Figure 6.2: X-ray diffraction pattern of the vaterite samples: (A) vat1; (B) vat2; (C) vat1-pAsp; (D) vat2-pAsp; (E) *H. momus* spicules; (F) *C. nasus* asteriscus otolith; (G) lacklustre pearl. The Miller index are the main reflection are indicated in parenthesis.

The initial indication of structural diversities among the samples was gained by the grinding curves (Fig. 6.3). The curves were obtained by repeated grinding of the sample and plotting the intensity of the ν_2 band (normalized with respect to ν_3 band) against the normalized ν_4 band, after each grinding. For each sample, a curve with a well-defined trend line was obtained. The offsets between curves reflected the differences in short range atomic disorder.[200] The results indicated that the grinding curves obtained for biogenic vaterite samples were localized in the same region of the graph, thus pointing to a similar atomic order. The samples of pure synthetic vaterite showed curves localized far from the biogenic ones. However, the curves of synthetic vat1-pAsp and vat2-pAsp samples were localized in the graph region between the curves of the pure synthetic and the biogenic vaterite, with the latter closer to the biogenic and the former to the pure synthetic ones.

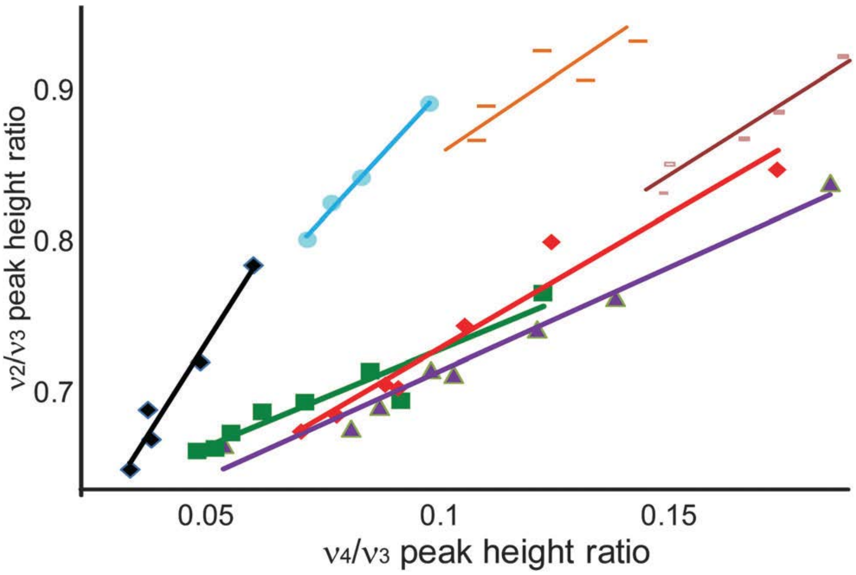

Figure 6.3: Grinding curves of vaterite samples. (E) vat1; (◆) vat2; (●) vat1- pAsp; (–) vat2-pAsp; (–) *H. momus* spicule; (◆) *C. nasus* asteriscus; (■) lackluster pearl.

The different number of peaks in the ν_3 band of the FTIR spectra of vaterite samples offered additional information on their structure (Fig. 6.4).[201] The synthetic vaterite samples showed a central peak at 1465 cm^{-1} and two weaker side peaks at 1492 and 1437 cm^{-1}. In the *H. momus* spicule the peak at 1492 cm^{-1} was the most intense and an additional peak appeared at 1408 cm^{-1}. In *C. nasus* asteriscus, the most intense vibration was that at 1437 cm^{-1}, while in a lackluster pearl those at 1492 and 1465 cm^{-1} were the most intense. Diverse profiles were also observed in Raman spectra, where the symmetric stretching vibration (ν_1) of carbonates revealed a triplet in some studies and a doublet in others.[187] The split in the degenerate ν_3 carbonate stretching mode results from the modification of the electrostatic environment of the Ca–O bond.[202] Thus, the observed source specific profile of the ν_3 band in the vaterite samples is in agreement with a possible co-existence of diverse crystalline structures,[197] which depend on various Ca^{2+} coordination geometries. However, these vibrations could not be assigned to specific structural domains in vaterite samples.

The ν_3 band appeared to be more structured in the biogenic samples than in the synthetic ones. In addition, it could be observed that the ν_3 band of the vat2-pAsp was more structured than for the other synthetic vaterites.

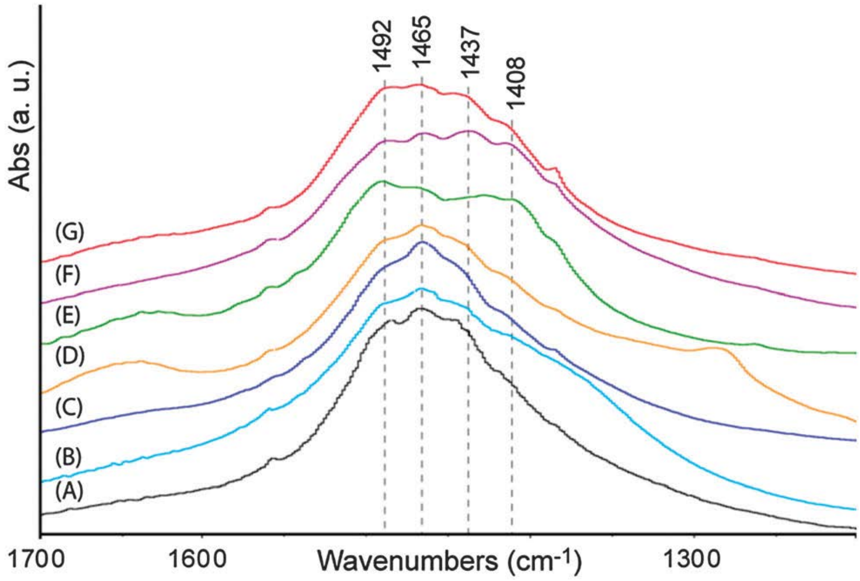

Figure 6.4: FTIR spectrum in the range of the ν_3 band of: (A) vat1; (B) vat2; (C) vat1-pAsp; (D) vat2-pAsp; (E) *H. momus* spicule; (F) *C. nasus* asteriscus; (G) lackluster pearl.

In Fig. 6.5 the DSC profiles of vaterite samples are shown, while the results of their analysis are summarized in Table 6.1. It can be seen that only the samples of pure synthetic vaterite showed a sharp endothermic band centred at 477 °C, while the other vaterite samples showed broader endothermic bands. The maximum of the vat1-pAsp profile was at 465 °C with a shoulder at 477 °C, while the vat2-pAsp profile's maximum was at 463 °C and has a broad shoulder at about 419 °C. Vaterite from spicules and otoliths showed endothermic band maxima at 420 °C and at 431 °C, respectively. The vaterite isolated from pearls showed a band with the maximum at about 533 °C, in agreement with the reported data.[203] In all samples vaterite converted completely to calcite after the thermal treatment, at temperatures corresponding to the maximum of the reported endothermic bands. Therefore, these temperatures represented the temperature of vaterite to calcite transition. The observed different metastability of the vaterite samples has been supposed to be caused by the co-presence of the organic matrix, polypeptides, foreign ions and/or water molecules.[204] Nevertheless, the possibility that the different co-existing crystalline structures contributed to the observed differences cannot be excluded. On the other hand, the broadening of the endothermic bands could be a result of additional thermal events, such as (i) the co-presence of small amounts of amorphous calcium carbonate that converted into the vaterite[13, 205] and/or (ii) the transition between vaterite structures differently stabilized (or destabilized) by the organic matrix.

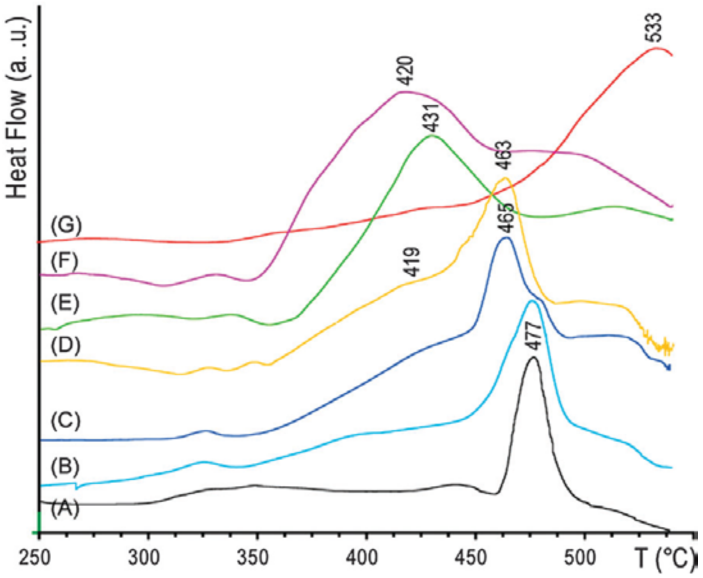

Figure 6.5: DSC profiles of: (A) vat1; (B) vat2; (C) vat1-pAsp; (D) vat2-pAsp; (E) *H. momus* spicule; (F) *C. nasus* asteriscus; (G) lackluster pearl.

Table 6.1: Transition temperatures and enthalpies of the thermal induced transition from vaterite minerals to calcite.

	T_{tr} (°C)	ΔH (J/g)
vat1	477	26.8
vat2	395	27.4
vat1-pAsp	478	24.8
vat2-pAsp	431	25.4
otolith	420	31*
spicule	431	29*
pearl	533	-**

* The endothermic band was very broad and did not allow an accurate measure of the transition enthalpy.
** The enthalpy was not measurable due to instrumental limitation of the highest temperature.

The enthalpy of the transition from vat1 or vat2 to calcite was about 27 J g^{-1}, in agreement with previously published data.[204, 206] The transition enthalpies of vat1-Asp and vat2-Asp samples were slightly lower, at about 25 J g^{-1}. The broadening of the transition band of the biogenic samples reduced the precision of the estimate of the corresponding transition enthalpy. However, the measured values were found to be similar to other vaterite samples (Table 6.1). Indeed, the observed broadening of the band pointed to a possibility of more than one thermal transition in a given temperature range.

6.4 Conclusion

In conclusion, the obtained results show that vaterite can have structures with different degree of disorders and/or a combination of two or more crystalline structures. [197, 198] However, the obtained results cannot exclude the co-presence of ACCs. The differences observed by applying the different techniques (Fig. 6.3–6.5) could be related to their varying detection limits for vaterite structures. Despite this, a higher structural variability was observed in the biogenic samples than in the synthetic ones. In the samples of biogenic vaterite, the organic matrix could (de)stabilize metastable phases, which would be consistent with proposed concept of stabilization of the metastable mineral phase (e.g. ACCs) by biomineralizing organisms, for functional purposes.[12] The presented data also suggest that the distribution among different crystalline structures is wider in biogenic than in synthetic samples. Moreover, it was observed that the presence of pAsp favored the structural heterogeneity.

Finally, on the basis of the presented experimental data it could be concluded that certain organisms are able to control the co-existence of different crystalline structures of vaterite, thus enabling optimization for specific functions.

This work has been published (see Falini G., Fermani S., Reggi M., Njegić Džakula B., Kralj D. (2014) Evidence of structural variability among synthetic and biogenic vaterite. Chem. Commun 50(97):15370-3).

7. CONCLUSIONS

In this thesis biomineralization in different marine organisms was investigated and *in vitro* $CaCO_3$ precipitation experiments was carried out to better understand the effects of different additives, magnesium ions and OM, on the crystallization process. In particular this research added important observations about the role of OM in corals calcification. Every coral species have a specific content of organic matrix characterized by different amount of lipids, protein and polysaccharides that differs from that from other organisms (e.g. mollusc). Crystallization experiment in $CaCl_2$ 10mM solution with and without Mg^{2+} and in ASW in presence of OM added important consideration: (*i*) the role of the OM in coral mineralization appears to be regulated by magnesium ions; (*ii*) OM composition and Mg^{2+} influence the fine scale characteristics of the crystals of which the coral skeleton is constructed; (*iii*) the influence of the intra-crystalline OM on *in vitro* crystallization did not appeared related to the growth form and trophic strategy of the coral (*iv*) the presence of OM does not influence noticeably the polymorphism of $CaCO_3$, except in *B. europaea* that seems has a stronger control on the process; (*v*) the stabilization of ACC by OM suggested that also coral biomineralization followed a crystallization pathway involving the formation of a transient form (chapter 2, 3 and 4).

This thesis shows also that the mineralization response to decreasing pH suggests a link with the degree of control over the biomineralization process by the organism, as only species with lower control managed to thrive in the lowest pH (chapter 5).

The results of the investigation on different kind of vaterite, also confirm the importance of the organism control on the biomineralization process and in particular on the co-existence of different crystalline structures of vaterite for enabling optimization of specific functions, through the employment of OM and acidic macromolecules (chapter 6).

REFERENCES

1. Lowenstam, H. A.; Weiner, S., On Biomineralization. New York, 1989.

2. Dauphin, Y., Biomineralization. In *Encyclopedia of Inorganic Chemistry*, Second Edition ed.; King, R. B., Ed. 2005; Vol. I, pp 391-404.

3. Ren, D.; Feng, Q.; Bourrat, X., Effects of additives and templates on calcium carbonate mineralization in vitro. *Micron* **2011,** *42* (3), 228-245.

4. Weiner, S.; Dove, P., An overview on biomineralization process and the problem of vital effect. In *Biomineralization*, Dove, P.; DeYoreo, J.; Weiner, S., Eds. 2003; Vol. 54, pp 1-29.

5. Epstein, S.; Buchsbaum, R.; Lowenstam, H. A., Revised carbonate-water isotopic temperature scale. *Geological Society of America Bulletin* **1953,** *64*, 1315-1326.

6. Addadi, L.; Weiner, S., Biomineralization: mineral formation by organisms. *Physica Scripta* **2014,** *89*.

7. Pruss, S. B.; Finnegan, S.; Fischer, W. W.; Knoll, A. H., Corbonates in skeleton-poor seas: new insights from cambrian and ordovician strata of Laurentia. *Palaios* **2010,** *25* (1-2), 73-84.

8. Sahni, A., Biomineralization: Some complex crystallite-oriented skeletal structures. *Journal of Biosciences* **2013,** *38* (5), 925-935.

9. Morse, J. W.; Mackenzie, F. T., Geochemistry of Sedimentary Carbonates. Elsevier: Amsterdam, 1990.

10. Loste, E.; Wilson, R. M.; Seshadri, R.; Meldrum, F. C., The role of magnesium in stabilising amorphous calcium carbonate and controlling calcite morphologies. *Journal of Crystal Growth* **2003,** *254* (1-2), 206-218.

11. Li, Z.; Feng, Q., Analysis of polymorphs of Carp's Otoliths. *Rare Metal Materials and Engineering* **2007,** *36*, 47-49.

12. Addadi, L.; Raz, S.; Weiner, S., Taking advantage of disorder: Amorphous calcium carbonate and its roles in biomineralization. *Advanced Materials* **2003,** *15* (12), 959-970.

13. Raz, S.; Hamilton, P. C.; Wilt, F. H.; Weiner, S.; Addadi, L., The transient phase of amorphous calcium carbonate in sea urchin larval spicules: The involvement of proteins and magnesium ions in its formation and stabilization. *Advanced Functional Materials* **2003,** *13* (6), 480-486.

14. Radha A.V., F. T. Z., Killian C. E., Gilbert P.U.P.A, Navrotsky A., Transformation and crystallization energetic of synthetic and biogenic amorphous calcium carbonate. *Proceedings of the National Academy of Sciences USA* **2010,** *105*, 17362-17366.

15. Falini, G.; Fermani, S.; Gazzano, M.; Ripamonti, A., Polymorphism and architectural crystal assembly of calcium carbonate in biologically inspired polymeric matrices. *Journal of the Chemical Society-Dalton Transactions* **2000,** (21), 3983-3987.

16. Weiner, S.; Addadi, L., Design strategies in mineralized biological materials. *Journal of Materials Chemistry* **1997,** *7* (5), 689-702.

17. Navrotsky, A., Energetic clues to pathways to biomineralization: Precursors, clusters, and nanoparticles. *Proceedings of the National Academy of Sciences of the United States of America* **2004,** *101* (33), 12096-12101.

18. De Groot, K., Duyvis, E.M., Crystal form of precipitated calcium carbonate as influenced by adsorbed magnesium ions. *Nature* **1966,** *212*, 183-184.

19. Stanley, S. M.; Hardie, L. A., Secular oscillations in the carbonate mineralogy of reef-building and sediment-producing organisms driven by tectonically forced shifts in seawater chemistry. *Palaeogeography Palaeoclimatology Palaeoecology* **1998,** *144* (1-2), 3-19.

20. Davis, K. J.; Dove, P. M.; De Yoreo, J. J., The role of Mg^{2+} as an impurity in calcite growth. *Science* **2000,** *290* (5494), 1134-1137.

21. De Yoreo, J. J.; Vekilov, P. G., Principles of Crystal Nucleation and Growth. *Reviews in Mineralogy and Geochemistry* **2003,** *54* (1), 57-93.

22. Davis, K. J.; Dove, P. M.; Wasylenki, L. E.; De Yoreo, J. J., Morphological consequences of differential Mg2+ incorporation at structurally distinct steps on calcite. *American Mineralogist* **2004,** *89* (5-6), 714-720. Dove, P. M., De Yoreo, J. J., Davis, K. J. Inhibition of CaCO3 crystallization by small molecules: the magnesium example In *Nanoscale Structura and Assembly at a Solid-Fluid Interfaces,* Liu, X. Y., L.; De Yoreo, J. J., Eds. Kluwer Academic Publishers: 2004; Vol. II, p 55.

23. Wasylenki, L. E.; Dove, P. M.; De Yoreo, J. J., Effects of temperature and transport conditions on calcite growth in the presence of Mg^{2+}: Implications for paleothermometry. *Geochimica Et Cosmochimica Acta* **2005,** *69* (17), 4227-4236.

24. Wang, D.; Hamm, L. M.; Giuffre, A. J.; Echigo, T.; Rimstidt, J. D.; De Yoreo, J. J.; Grotzinger, J.; Dove, P. M., Revisiting geochemical controls on patterns of carbonate deposition through the lens of multiple pathways to mineralization. *Faraday Discussions* **2012,** *159*, 371-386.

25. Politi, Y.; Batchelor, D. R.; Zaslansky, P.; Chmelka, B. F.; Weaver, J. C.; Sagi, I.; Weiner, S.; Addadi, L., Role of Magnesium Ion in the Stabilization of Biogenic Amorphous Calcium Carbonate: A Structure-Function Investigation. *Chemistry of Materials* **2010,** *22* (1), 161-166.

26. Chernov, A. A., Modern Crystallography III: Crystal *Growth*. Springer: Berlin, 1984.

27. Stephenson, A. E.; DeYoreo, J. J.; Wu, L.; Wu, K. J.; Hoyer, J.; Dove, P. M., Peptides Enhance Magnesium Signature in Calcite: Insights into Origins of Vital Effects. *Science* **2008,** *322* (5902), 724-727.

28. Falini, G.; Fermani, S.; Tosi, G.; Dinelli, E., Calcium Carbonate Morphology and Structure in the Presence of Seawater Ions and Humic Acids. *Crystal Growth & Design* **2009,** *9* (5), 2065-2072.

29. Muscatine, L.; Goiran, C.; Land, L.; Jaubert, J.; Cuif, J. P.; Allemand, D., Stable isotopes (delta C-13 and delta N-15) of organic matrix from coral skeleton. *Proceedings of the National Academy of Sciences of the United States of America* **2005,** *102* (5), 1525-1530.

30. Dove, P. M., The Rise of Skeletal Biominerals. *Elements* **2010,** *6* (1), 37-42.

31. Weiner, S.; Traub, W.; Lowenstam, H. A., Organic Matrix in Calcified Exoskeletons. In *Biomineralization and Biological Metal Accumulation*, Westbroek, P.; de Jong, E. W., Eds. Springer Netherlands: 1983; pp 205-224.

32. Albeck, S.; Weiner, S.; Addadi, L., Polysaccharides of intracrystalline glycoproteins modulate calcite crystal growth in vitro. *Chemistry-a European Journal* **1996,** *2* (3), 278-284.

33. Arias, J. L.; Fernandez, M. S., Polysaccharides and Proteoglycans in Calcium Carbonate-based Biomineralization. *Chemical Reviews* **2008,** *108* (11), 4475-4482.

34. Sikes, C. S.; Wierzbicki, A.; Fabry, V. J., From atomic to global scales in biomineralization. *Bulletin de l'Institut océanographique* **1994**, 1-47.

35. Mitterer, R. M., Amino Acid Composition and Metal Binding Capability of the Skeletal Protein of Corals. *Bulletin of Marine Science* **1978,** *28* (1), 173-180.

36. Addadi, L.; Moradian, J.; Shay, E.; Maroudas, N. G.; Weiner, S., A chemical model for the cooperation of sulfates and carboxylates in calcite crystal nucleation – relevance to biomineralization. *Proceedings of the National Academy of Sciences of the United States of America* **1987,** *84* (9), 2732-2736.

37. Dauphin, Y.; Cuif, J.-P.; Williams, C. T., Soluble organic matrices of aragonitic skeletons of Merulinidae (Cnidaria, Anthozoa). *Comparative Biochemistry and Physiology B-Biochemistry & Molecular Biology* **2008,** *150* (1), 10-22.

38. Cuif, J. P.; Dauphin, Y.; Gautret, P., Compositional diversity of soluble mineralizing matrices in some resent coral skeletons compared to fine-scale growth structures of fibres: discussion of consequences for biomineralization and diagenesis. *International Journal of Earth Sciences* **1999,** *88* (3), 582-592.

39. Cartwright, J. H. E.; Checa, A. G., The dynamics of nacre self-assembly. *Journal of the Royal Society Interface* **2007,** *4* (14), 491-504; Wainwright, S. A., Skeletal Organization in the Coral, Pocillopora Damicornis. *Quarterly Journal of Microscopical Science* **1963,** *s3-104* (66), 169-183.

40. Ramos-Silva, P.; Kaandorp, J.; Herbst, F.; Plasseraud, L.; Alcaraz, G.; Stern, C.; Corneillat, M.; Guichard, N.; Durlet, C.; Luquet, G.; Marin, F., The Skeleton of the Staghorn Coral Acropora millepora: Molecular and Structural Characterization. *Plos One* **2014,** *9* (6), 15.

41. Young, J. R.; Henriksen, K., Biomineralization Within Vesicles: The Calcite of Coccoliths. *Reviews in Mineralogy and Geochemistry* **2003,** *54* (1), 189-215; Marsh, M. E., Polyanion-mediated mineralization - A kinetic analysis of the calcium-carrier hypothesis in the phytoflagellate Pleurochrysis carterae. *Protoplasma* **1996,** *190* (3-4), 181-188.

42. Yang, M. J.; Stipp, S. L. S.; Harding, J., Biological Control on Calcite Crystallization by Polysaccharides. *Crystal Growth & Design* **2008,** *8* (11), 4066-4074.

43. Farre, B.; Cuif, J. P.; Dauphin, Y., Occurrence and diversity of lipids in modern coral skeletons. *Zoology* **2010,** *113* (4), 250-257.

44. Rousseau, M.; Bedouet, L.; Lati, E.; Gasser, P.; Le Ny, K.; Lopez, E., Restoration of stratum corneum with nacre lipids. *Comparative Biochemistry and Physiology B-Biochemistry & Molecular Biology* **2006,** *145* (1), 1-9; Farre, B.; Dauphin, Y., Lipids from the nacreous and

prismatic layers of two Pteriomorpha Mollusc shells. *Comparative Biochemistry and Physiology B-Biochemistry & Molecular Biology* **2009,** *152* (2), 103-109.

45. Isa, Y.; Okazaki, M., Some observations on the Ca2+-binding phospholipid from Scleractinian coral skeletons. *Comparative Biochemistry and Physiology B-Biochemistry & Molecular Biology* **1987,** *87* (3), 507-512.

46. Weiner, S.; Addadi, L., Crystallization Pathway in Biomineralization. *Annual Review of Material Research* **2011,** *41*, 21-40.

47. Young, S. D., Collagen and other mesoglea protein from the coral lbophyllia crymbosa (anthozoa, scleractinla). *International Journal of Biochemistry* **1973,** *4* (22), 339-344; Allemand, D.; Tambutte, E.; Girard, J. P.; Jaubert, J., Organic matrix synthesis in the scleractinian coral Stylophora pistillata: Role in biomineralization and potential target of the organotin tributyltin. *Journal of Experimental Biology* **1998,** *201* (13), 2001-2009.

48. Falini, G.; Albeck, S.; Weiner, S.; Addadi, L., Control of aragonite or calcite polymorphism by mollusk shell macromolecules. *Science* **1996,** *271* (5245), 67-69.

49. Belcher, A. M.; Wu, X. H.; Christensen, R. J.; Hansma, P. K.; Stucky, G. D.; Morse, D. E., Control of crystal phase switching and orientation by soluble mollusc-shell proteins. *Nature* **1996,** *381* (6577), 56-58.

50. Falini, G.; Fermani, S.; Vanzo, S.; Miletic, M.; Zaffino, G., Influence on the Formation of Aragonite or Vaterite by Otolith Macromolecules. *European Journal of Inorganic Chemistry* **2005,** *2005* (1), 162-167.

51. Suzuki, M.; Saruwatari, K.; Kogure, T.; Yamamoto, Y.; Nishimura, T.; Kato, T.; Nagasawa, H., An Acidic Matrix Protein, Pif, Is a Key Macromolecule for Nacre Formation. *Science* **2009,** *325* (5946), 1388-1390.

52. Tao, J. H.; Zhou, D. M.; Zhang, Z. S.; Xu, X. R.; Tang, R. K., Magnesium-aspartate-based crystallization switch inspired from shell molt of crustacean. *Proceedings of the National Academy of Sciences of the United States of America* **2009,** *106* (52), 22096-22101.

53. Clode, P. L.; Marshall, A. T., Low temperature FESEM of the calcifying interface of a scleractinian coral. *Tissue & Cell* **2002,** *34* (3), 187-198.

54. Albeck, S.; Aizenberg, J.; Addadi, L.; Weiner, S., Interactions of various skeletal intracrystalline components with calcite crystals. *Journal of the American Chemical Society* **1993,** *115* (25), 11691-11697.

55. Aizenberg, J.; Albeck, S.; Weiner, S.; Addadi, L., Crystal protein interactions studied by overgrowth of calcite on biogenic skeletal elements. *Journal of Crystal Growth* **1994,** *142* (1-2), 156-164.

56. Orme, C. A.; Noy, A.; Wierzbicki, A.; McBride, M. T.; Grantham, M.; Teng, H. H.; Dove, P. M.; DeYoreo, J. J., Formation of chiral morphologies through selective binding of amino acids to calcite surface steps. *Nature* **2001,** *411* (6839), 775-779.

57. Cuif, J. P.; Dauphin, Y.; Farre, B.; Nehrke, G.; Nouet, J.; Salome, M., Distribution of sulphated polysaccharides within calcareous biominerals suggests a widely shared two-step crystallization process for the microstructural growth units. *Mineralogical Magazine* **2008,** *72* (1), 233-237.

58. Marin, F.; Luquet, G., Unusually Acidic Proteins in Biomineralization. In *Handbook of Biomineralization*, Wiley-VCH Verlag GmbH: 2008; pp 273-290.

59. Veis, A.; Perry, A., The phosphoprotein of the dentin matrix. *Biochemistry* **1967,** *6* (8), 2409-16; Weiner, S., Aspartic acid-rich proteins: major components of the soluble organic matrix of mollusk shells. *Calcified tissue international* **1979,** *29* (2), 163-7.

60. Weiner, S.; Dove, P. M., An Overview on Biomineralization Processes and the Problem of the Vital Effect. *Biomineralization* **2003,** *54*, 1-24.

61. Weiner, S.; Lowenstam, H. A.; Hood, L., Characterization of 80-million-year-old mollusk shell proteins. *Proceedings of the National Academy of Sciences of the United States of America* **1976,** *73* (8), 2541-5.

62. Frenkel, J., *Kinetic Theory of Liquids*. Oxford, UK, 1946.

63. Meldrum, F. C.; Coelfen, H., Controlling Mineral Morphologies and Structures in Biological and Synthetic Systems. *Chemical Reviews* **2008,** *108* (11), 4332-4432.

64. Tambutte, S.; Holcomb, M.; Ferrier-Pages, C.; Reynaud, S.; Tambutte, E.; Zoccola, D.; Allemand, D., Coral biomineralization: From the gene to the environment. *Journal of Experimental Marine Biology and Ecology* **2011,** *408* (1-2), 58-78.

65. Weiner, S., Biomineralization: A structural perspective. *Journal of Structural Biology* **2008,** *163* (3), 229-234.

66. Gebauer, D.; Volkel, A.; Colfen, H., Stable Prenucleation Calcium Carbonate Clusters. *Science* **2008,** *322* (5909), 1819-1822.

67. Rodriguez-Blanco, J. D.; Shaw, S.; Benning, L. G., The kinetics and mechanisms of amorphous calcium carbonate (ACC) crystallization to calcite, via vaterite. *Nanoscale* **2011,** *3* (1), 265-271.

68. Hasse, B.; Ehrenberg, H.; Marxen, J. C.; Becker, W.; Epple, M., Calcium carbonate modifications in the mineralized shell of the freshwater snail Biomphalaria glabrata. *Chemistry-a European Journal* **2000,** *6* (20), 3679-3685; Sinn, C. G.; Dimova, R.; Antonietti, M., Isothermal titration calorimetry of the polyelectrolyte/water interaction and binding of Ca2+: Effects determining the quality of polymeric scale inhibitors. *Macromolecules* **2004,** *37* (9), 3444-3450; Politi, Y.; Levi-Kalisman, Y.; Raz, S.; Wilt, F.; Addadi, L.; Weiner, S.; Sagi, I., Structural characterization of the transient amorphous calcium carbonate precursor phase in sea urchin embryos. *Advanced Functional Materials* **2006,** *16* (10), 1289-1298.

69. Lam, R. S. K.; Charnock, J. M.; Lennie, A.; Meldrum, F. C., Synthesis-dependant structural variations in amorphous calcium carbonate. *CrystEngComm* **2007,** *9* (12), 1226-1236.

70. Colfen, H.; Mann, S., Higher-order organization by mesoscale self-assembly and transformation of hybrid nanostructures. *Angewandte Chemie-International Edition* **2003,** *42* (21), 2350-2365.

71. Gal, A.; Kahil, K.; Vidavsky, N.; DeVol, R. T.; Gilbert, P.; Fratzl, P.; Weiner, S.; Addadi, L., Particle Accretion Mechanism Underlies Biological Crystal Growth from an Amorphous Precursor Phase. *Advanced Functional Materials* **2014,** *24* (34), 5420-5426.

72. Mann, S., *Biomineralization: Principles and Concepts in Bioinorganic Materials Chemistry*. 2001.

73. Taylor, M.; Simkiss, K.; Greaves, G. N., Amorphous structure of intracellular mineral granules. *Biochemical Society Transactions* **1986,** *14* (3), 549-552; Beniash, E.; Addadi, L.; Weiner, S., Cellular Control Over Spicule Formation in Sea Urchin Embryos: A Structural Approach. *Journal of Structural Biology* **1999,** *125* (1), 50-62.

74. Cohen, A. L.; McConnaughey, T. A., Geochemical perspectives on coral mineralization. *Biomineralization* **2003,** *54*, 151-187.

75. Smith, S. V., Coral-reef area and the contributions of reefs to processes and resources of the world's oceans. *Nature* **1978,** *273* (5659), 225-226.

76. Veron, J. E. N., *Corals of the World*. Australian Institute of Marine Science: Townsville, 2000.

77. Nakamura, M.; Ohki, S.; Suzuki, A.; Sakai, K., Coral Larvae under Ocean Acidification: Survival, Metabolism, and Metamorphosis. *Plos One* **2011,** *6* (1), 7.

78. Fine, M.; Tchernov, D., Scleractinian coral species survive and recover from decalcification. *Science* **2007,** *315* (5820), 1811-1811; Hoegh-Guldberg, O.; Mumby, P. J.; Hooten, A. J.; Steneck, R. S.; Greenfield, P.; Gomez, E.; Harvell, C. D.; Sale, P. F.; Edwards, A. J.; Caldeira, K.; Knowlton, N.; Eakin, C. M.; Iglesias-Prieto, R.; Muthiga, N.; Bradbury, R. H.; Dubi, A.; Hatziolos, M. E., Coral reefs under rapid climate change and ocean acidification. *Science* **2007,** *318* (5857), 1737-1742.

79. Goffredo, S.; Vergni, P.; Reggi, M.; Caroselli, E.; Sparla, F.; Levy, O.; Dubinsky, Z.; Falini, G., The Skeletal Organic Matrix from Mediterranean Coral Balanophyllia europaea Influences Calcium Carbonate Precipitation. *Plos One* **2011,** *6* (7), 12.

80. Rodriguez-Lanetty, M.; Loh, W.; Carter, D.; Hoegh-Guldberg, O., Latitudinal variability in symbiont specificity within the widespread scleractinian coral Plesiastrea versipora. *Marine Biology* **2001,** *138* (6), 1175-1181.

81. Gattuso, J. P.; Allemand, D.; Frankignoulle, M., Photosynthesis and calcification at cellular, organismal and community levels in coral reefs: A review on interactions and control by carbonate chemistry. *American Zoologist* **1999,** *39* (1), 160-183.

82. Muscatine, L., The Role of Symbiotic Algae in Carbon and Energy Flux in Reef Corals. *Coral Reefs* **1990,** *25*, 1-29.

83. Harel, R.; Tanzer, M. L., Extracellular-matrix. 3. Evolution of the extracellular matrix in invertrebates. *Faseb Journal* **1993,** *7* (12), 1115-1123; Czaker, R., Extracellular matrix (ECM) components in a very primitive multicellular animal, the dicyemid mesozoan Kantharella antarctica. *Anatomical Record* **2000,** *259* (1), 52-59.

84. Wilfert, M.; Peters, W., Vorkommen von chitin bei coelenteraten. *Zeitschrift für Morphologie der Tiere* **1969,** *64* (1), 77-84; Young, S. D., Organic material from scleractinian coral skeletons I. Variation in composition between several species. *Comparative Biochemistry and Physiology Part B: Comparative Biochemistry* **1971,** *40* (1), 113-120.

85. Cuif, J. P.; Lecointre, G.; Perrin, C.; Tillier, A.; Tillier, S., Patterns of septal biomineralization in Scleractinia compared with their 28S rRNA phylogeny: a dual approach for a new taxonomic framework. *Zoologica Scripta* **2003,** *32* (5), 459-473.

86. Cuif, J.-P.; Dauphin, Y., Microstructural and physico-chemical characterization of ‘centers of calcification’ in septa of some Recent scleractinian corals. *Paläontologische Zeitschrift* **1998,** *72* (3-4), 257-269.

87. Vandermeulen, J. H.; Watabe, N., Studies on reef corals. I. Skeleton formation by newly settled planula larva of Pocillopora damicornis. *Marine Biology* **1973,** *23* (1), 47-57.

88. van de Locht, R.; Verch, A.; Saunders, M.; Dissard, D.; Rixen, T.; Moya, A.; Kröger, R., Microstructural evolution and nanoscale crystallography in scleractinian coral spherulites. *Journal of Structural Biology* **2013,** *183* (1), 57-65.

89. Cuif, J. P.; Dauphin, Y., The Environment Recording Unit in coral skeletons - a synthesis of structural and chemical evidences for a biochemically driven, stepping-growth process in fibres. *Biogeosciences* **2005,** *2* (1), 61-73.

90. Cuif, J. P.; Dauphin, Y., The two-step mode of growth in the Scleractinian coral skeletons from the micrometre to the overall scale. *Journal of Structural Biology* **2005,** *150* (3), 319-331.

91. Cuif, J. P.; Dauphin, Y.; Doucet, J.; Salome, M.; Susini, J., XANES mapping of organic sulfate in three scleractinian coral skeletons. *Geochimica Et Cosmochimica Acta* **2003,** *67* (1), 75-83.

92. Dauphin, Y., Comparative studies of skeletal soluble matrices from some Scleractinian corals and Molluscs. *International Journal of Biological Macromolecules* **2001,** *28* (4), 293-304.

93. Watanabe, T.; Fukuda, I.; China, K.; Isa, Y., Molecular analyses of protein components of the organic matrix in the exoskeleton of two scleractinian coral species. *Comparative Biochemistry and Physiology B-Biochemistry & Molecular Biology* **2003,** *136* (4), 767-774.

94. Puverel, S.; Tambutte, E.; Pererra-Mouries, L.; Zoccola, D.; Allemand, D.; Tambutte, S., Soluble organic matrix of two Scleractinian corals: Partial and comparative analysis. *Comparative Biochemistry and Physiology B-Biochemistry & Molecular Biology* **2005,** *141* (4), 480-487.

95. Cuif, J. P.; Dauphin, Y.; Freiwald, A.; Gautret, P.; Zibrowius, H., Biochemical markers of zoaxanthellae symbiosis in soluble matrices of skeleton of 24 Scleractinia species. *Comparative Biochemistry and Physiology a-Molecular and Integrative Physiology* **1999,** *123* (3), 269-278.

96. McConnaughey, T. A.; Whelan, J. F., Calcification generates protons for nutrient and bicarbonate uptake. *Earth-Science Reviews* **1997,** *42* (1-2), 95-117.

97. Gagnon, A. C.; Adkins, J. F.; Erez, J., Seawater transport during coral biomineralization. *Earth and Planetary Science Letters* **2012,** *329*, 150-161.

98. Addadi, L.; Joester, D.; Nudelman, F.; Weiner, S., Mollusk shell formation: A source of new concepts for understanding biomineralization processes. *Chemistry-a European Journal* **2006,** *12* (4), 981-987.

99. Addadi, L.; Weiner, S., Control and desogn principles in biological mineralization. *Angewandte Chemie-International Edition in English* **1992,** *31* (2), 153-169.

100. Didymus, J. M.; Oliver, P.; Mann, S.; Devries, A. L.; Hauschka, P. V.; Westbroek, P., Influence of low molecular weight and macromolecular organic additives on the morphology of calcium carbonate. *Journal of the Chemical Society-Faraday Transactions* **1993,** *89* (15), 2891-2900.

101. Tambutte, E.; Allemand, D.; Zoccola, D.; Meibom, A.; Lotto, S.; Caminiti, N.; Tambutte, S., Observations of the tissue-skeleton interface in the scleractinian coral Stylophora pistillata. *Coral Reefs* **2007,** *26* (3), 517-529.

102. Allemand, D.; Tambutte, E.; Zoccola, D.; Tambutte, S., Coral Calcification, Cells to Reefs. In *Coral Reefs: an Ecosystem in Transition*, Dubinsky, Z.; Stambler, N., Eds. Springer: Dordrecht, 2011; pp 119-150.

103. Mass, T.; Drake, J. L.; Haramaty, L.; Kim, J. D.; Zelzion, E.; Bhattacharya, D.; Falkowski, P. G., Cloning and Characterization of Four Novel Coral Acid-Rich Proteins that Precipitate Carbonates In Vitro. *Current Biology* **2013,** *23* (12), 1126-1131.

104. Sabine, C. L.; Feely, R. A.; Gruber, N.; Key, R. M.; Lee, K.; Bullister, J. L.; Wanninkhof, R.; Wong, C. S.; Wallace, D. W. R.; Tilbrook, B.; Millero, F. J.; Peng, T. H.; Kozyr, A.; Ono, T.; Rios, A. F., The oceanic sink for anthropogenic CO2. *Science* **2004,** *305* (5682), 367-371.

105. IPCC. Climate Change 2007: The Physical Science Basis. Contribution of Working Group I to the Fourth Assessment. Report of the Intergovernmental Panel on Climate Change. Cambridge University Press: 2007.

106. Harley, C. D. G.; Hughes, A. R.; Hultgren, K. M.; Miner, B. G.; Sorte, C. J. B.; Thornber, C. S.; Rodriguez, L. F.; Tomanek, L.; Williams, S. L., The impacts of climate change in coastal marine systems. *Ecology Letters* **2006,** *9* (2), 228-241.

107. Doney, S. C., The Dangers of Ocean Acidification *Scientific American* **2006,** *294*, 58-65.

108. Spalding, M. D.; Ravilious, C.; Green, E. P., *World Atlas of Coral Reefs*. Berkeley, California, 2001.

109. Marshall, A. T.; Clode, P., Calcification rate and the effect of temperature in a zooxanthellate and an azooxanthellate scleractinian reef coral. *Coral Reefs* **2004,** *23* (2), 218-224.

110. Bryan, W. H. W. H.; Hill, D., *Spherulitic crystallization as a mechanism of skeletal growth in the Hexacorals*. University of Queensland Press: Brisbane, 1941.

111. Holcomb, M.; Cohen, A. L.; Gabitov, R. I.; Hutter, J. L., Compositional and morphological features of aragonite precipitated experimentally from seawater and biogenically by corals. *Geochimica Et Cosmochimica Acta* **2009,** *73* (14), 4166-4179.

112. Constantz, B.; Weiner, S., Acidic macromolecules associated with the mineral phase od Scleractinian coral skeletons. *Journal of Experimental Zoology* **1988,** *248* (3), 253-258.

113. Jokiel, P. L., Effects of water motion on reef corals. *Journal of Experimental Marine Biology and Ecology* **1978,** *35* (1), 87-97.

114. Adkins, J. F.; Boyle, E. A.; Curry, W. B.; Lutringer, A., Stable isotopes in deep-sea corals and a new mechanism for “vital effects”. *Geochimica et Cosmochimica Acta* **2003,** *67* (6), 1129-1143.

115. Motai, S.; Nagai, T.; Sowa, K.; Watanabe, T.; Sakamoto, N.; Yurimoto, H.; Kawano, J., Needle-like grains across growth lines in the coral skeleton of Porites lobata. *Journal of Structural Biology* **2012,** *180* (3), 389-393.

116. Asenath-Smith, E.; Li, H. Y.; Keene, E. C.; Seh, Z. W.; Estroff, L. A., Crystal Growth of Calcium Carbonate in Hydrogels as a Model of Biomineralization. *Advanced Functional Materials* **2012,** *22* (14), 2891-2914.

117. Cuif, J. P.; Dauphin, Y.; Berthet, P.; Jegoudez, J., Associated water and organic compounds in coral skeletons: Quantitative thermogravimetry coupled to infrared absorption spectrometry. *Geochemistry Geophysics Geosystems* **2004,** *5*.

118. Parker, F. S., *Applications of infrared, Raman, and resonance Raman spectroscopy in biochemistry*. Springer Science & Business Media.: 1983.

119. Sillero, A.; Ribeiro, J. M., Isoelectric points of proteins: Theoretical determination. *Analytical Biochemistry* **1989,** *179* (2), 319-325.

120. Braissant, O.; Cailleau, G.; Dupraz, C.; Verrecchia, A. P., Bacterially induced mineralization of calcium carbonate in terrestrial environments: The role of exopolysaccharides and amino acids. *Journal of Sedimentary Research* **2003,** *73* (3), 485-490.

121. Sommerdijk, N.; de With, G., Biomimetic CaCO3 Mineralization using Designer Molecules and Interfaces. *Chemical Reviews* **2008,** *108* (11), 4499-4550.

122. Veron, J. E. N., *Corals of Australia and the indo-pacific*. University of HawaiPress: Honolulu, 1993; De'ath, G.; Lough, J. M.; Fabricius, K. E., Declining Coral Calcification on the Great Barrier Reef. *Science* **2009,** *323* (5910), 116-119; Takahashi, A.; Kurihara, H., Ocean acidification does not affect the physiology of the tropical coral Acropora digitifera during a 5-week experiment. *Coral Reefs* **2013,** *32* (1), 305-314.

123. Cuif, J.-P.; Dauphin, Y.; Denis, A.; Gautret, P.; Marin, F., The organo-mineral structure of coral skeletons : a potential source of new criteria for Scleractinian taxonomy. *Bulletin de l'Institut océanographique* **1996,** *14* (4), 359-367.

124. Adamiano, A.; Bonacchi, S.; Calonghi, N.; Fabbri, D.; Falini, G.; Fermani, S.; Genovese, D.; Kralj, D.; Montalti, M.; Dzakula, B. N.; Prodi, L.; Sartor, G., Structural Changes in a Protein Fragment from Abalone Shell during the Precipitation of Calcium Carbonate. *Chemistry-a European Journal* **2012,** *18* (45), 14367-14374.

125. Worms, D.; Weiner, S., Mollusk shell organic matrix: Fourier transform infrared study of the acidic macromolecules. *Journal of Experimental Zoology* **1986,** *237* (1), 11-20.

126. Elhadj, S.; Salter, E. A.; Wierzbicki, A.; De Yoreo, J. J.; Han, N.; Dove, P. M., Peptide controls on calcite mineralization: Polyaspartate chain length affects growth kinetics and acts as a stereochemical switch on morphology. *Crystal Growth & Design* **2006,** *6* (1), 197-201.

127. Tester, C. C.; Brock, R. E.; Wu, C. H.; Krejci, M. R.; Weigand, S.; Joester, D., In vitro synthesis and stabilization of amorphous calcium carbonate (ACC) nanoparticles within liposomes. *Crystengcomm* **2011,** *13* (12), 3975-3978.

128. Falini, G.; Weiner, S.; Addadi, L., Chitin-silk fibroin interactions: Relevance to calcium carbonate formation in invertebrates. *Calcified Tissue International* **2003,** *72* (5), 548-554.

129. Gotliv, B. A.; Addadi, L.; Weiner, S., Mollusk shell acidic proteins: In search of individual functions. *Chembiochem* **2003,** *4* (6), 522-529.

130. Mass, T.; Drake, J. L.; Haramaty, L.; Rosenthal, Y.; Schofield, O. M. E.; Sherrell, R. M.; Falkowski, P. G., Aragonite Precipitation by "Proto-Polyps" in Coral Cell Cultures. *Plos One* **2012,** *7* (4), 8.

131. Kulak, A. N.; Iddon, P.; Li, Y. T.; Armes, S. P.; Colfen, H.; Paris, O.; Wilson, R. M.; Meldrum, F. C., Continuous structural evolution of calcium carbonate particles: A unifying model of copolymer-mediated crystallization. *Journal of the American Chemical Society* **2007,** *129* (12), 3729-3736; Song, R.-Q.; Cölfen, H.; Xu, A.-W.; Hartmann, J.; Antonietti, M., Polyelectrolyte-Directed Nanoparticle Aggregation: Systematic Morphogenesis of Calcium Carbonate by Nonclassical Crystallization. *ACS Nano* **2009,** *3* (7), 1966-1978.

132. Tambutte, E.; Tambutte, S.; Segonds, N.; Zoccola, D.; Venn, A.; Erez, J.; Allemand, D., Calcein labelling and electrophysiology: insights on coral tissue permeability and calcification. *Proceedings of the Royal Society B-Biological Sciences* **2012,** *279* (1726), 19-27.

133. Weiss, I. M.; Tuross, N.; Addadi, L.; Weiner, S., Mollusc larval shell formation: Amorphous calcium carbonate is a precursor phase for aragonite. *Journal of Experimental Zoology* **2002,** *293* (5), 478-491.

134. Lipmann, F., *Sedimentary carbonate mineral*. Springer Berlin Heidelberg: 1973; Vol. 6.

135. Falini, G.; Reggi, M.; Fermani, S.; Sparla, F.; Goffredo, S.; Dubinsky, Z.; Levi, O.; Dauphin, Y.; Cuif, J.-P., Control of aragonite deposition in colonial corals by intra-skeletal macromolecules. *Journal of Structural Biology* **2013,** *183* (2), 226-238.

136. Muscatine, L.; Cernichiari, E., Assimilation of photosynthetic products of zooxhantellae by a reef coral. *The Biological Bulletin* **1969,** *137* (3), 506-523.

137. Johnson, I. S., The ultrastructure of skeletogenesis in hermatypic corals. *International Review of Cytology* **1980,** *67,* 171–214.

138. Kawaguti, S.; Sakumoto, D., The effect of light on the calcium deposition of corals. *Bull. Oceanogr. Inst. Taiwan* **1948,** *4* (65-70).

139. Pearse, V. B.; Muscatine, L., Role of Symbiotic Algae (Zooxanthellae) in Coral Calcification. *Biological Bulletin* **1971,** *141* (2), 350-363.

140. Goreau, T. F., The physiology of skeleton formation in corals. I. A method for measuring the rate of calcium deposition by corals under different conditions. *The Biological Bulletin* **1959,** *116* (1), 59-75; Gautret, P.; Cuif, J. P.; Freiwald, A., Composition of soluble mineralizing matrices in zooxanthellate and non-zooxanthellate scleractinian corals: Biochemical assessment of photosynthetic metabolism through the study of a skeletal feature. *Facies* **1997,** *36,* 189-194.

141. Marshall, A. T.; Clode, P. L., Effect of increased calcium concentration in sea water on calcification and photosynthesis in the scleractinian coral Galaxea fascicularis. *Journal of Experimental Biology* **2002,** *205* (14), 2107-2113; Al-Horani, F. A., Effects of changing seawater temperature on photosynthesis and calcification in the scleractinian coral Galaxea

fascicularis, measured with O-2, Ca2+ and pH microsensors. *Scientia Marina* **2005,** *69* (3), 347-354; Al-Horani, F. A.; Al-Moghrabi, S. M.; de Beer, D., The mechanism of calcification and its relation to photosynthesis and respiration in the scleractinian coral Galaxea fascicularis. *Marine Biology* **2003,** *142* (3), 419-426.

142. Kester, D. R.; Duedall, I. W.; Connors, D. N.; Pytkowicz, R. M., Preparation of artificial seawater. *Limnology and Oceanography* **1967,** *12*, 176-179.

143. Xu, X.; Han, J. T.; Kim, D. H.; Cho, K., Two modes of transformation of amorphous calcium carbonate films in air. *Journal of Physical Chemistry B* **2006,** *110* (6), 2764-2770.

144. Venn, A. A.; Tambutte, E.; Holcomb, M.; Laurent, J.; Allemand, D.; Tambutte, S., Impact of seawater acidification on pH at the tissue-skeleton interface and calcification in reef corals. *Proceedings of the National Academy of Sciences of the United States of America* **2013,** *110* (5), 1634-1639.

145. Noel, E. H.; Kim, Y. Y.; Charnock, J. M.; Meldrum, F. C., Solid state crystallization of amorphous calcium carbonate nanoparticles leads to polymorph selectivity. *Crystengcomm* **2013,** *15* (4), 697-705.

146. Gebauer, D.; Gunawidjaja, P. N.; Ko, J. Y. P.; Bacsik, Z.; Aziz, B.; Liu, L. J.; Hu, Y. F.; Bergstrom, L.; Tai, C. W.; Sham, T. K.; Eden, M.; Hedin, N., Proto-Calcite and Proto-Vaterite in Amorphous Calcium Carbonates. *Angewandte Chemie-International Edition* **2010,** *49* (47), 8889-8891.

147. Zhang, Z. N.; Xie, Y. D.; Xu, X. R.; Pan, H. H.; Tang, R. K., Transformation of amorphous calcium carbonate into aragonite. *Journal of Crystal Growth* **2012,** *343* (1), 62-67.

148. Raiteri, P.; Gale, J. D., Water Is the Key to Nonclassical Nucleation of Amorphous Calcium Carbonate. *Journal of the American Chemical Society* **2010,** *132* (49), 17623-17634.

149. Clode, P. L.; Lema, K.; Saunders, M.; Weiner, S., Skeletal mineralogy of newly settling Acropora millepora (Scleractinia) coral recruits. *Coral Reefs* **2011,** *30* (1), 1-8.

150. Goffredo, S.; Prada, F.; Caroselli, E.; Capaccioni, B.; Zaccanti, F.; Pasquini, L.; Fantazzini, P.; Fermani, S.; Reggi, M.; Levy, O.; Fabricius, K. E.; Dubinsky, Z.; Falini, G., Biomineralization control related to population density under ocean acidification. *Nature Climate Change* **2014,** *4* (7), 593-597.

151. Fukuda, I.; Ooki, S.; Fujita, T.; Murayama, E.; Nagasawa, H.; Isa, Y.; Watanabe, T., Molecular cloning of a cDNA encoding a soluble protein in the coral exoskeleton. *Biochemical and Biophysical Research Communications* **2003,** *304* (1), 11-17.

152. Reyes-Bermudez, A.; Lin, Z.; Hayward, D. C.; Miller, D. J.; Ball, E. E., Differential expression of three galaxin-related genes during settlement and metamorphosis in the scleractinian coral Acropora millepora. *BMC Evolutionary Biology* **2009,** *9*, 12pp.

153. Ramos-Silva, P.; Kaandorp, J.; Huisman, L.; Marie, B.; Zanella-Cleon, I.; Guichard, N.; Miller, D. J.; Marin, F., The Skeletal Proteome of the Coral Acropora millepora: The Evolution of Calcification by Co-Option and Domain Shuffling. *Molecular Biology and Evolution* **2013,** *30* (9), 2099-2112; Shinzato, C.; Shoguchi, E.; Kawashima, T.; Hamada, M.; Hisata, K.; Tanaka, M.; Fujie, M.; Fujiwara, M.; Koyanagi, R.; Ikuta, T.; Fujiyama, A.; Miller, D. J.; Satoh, N., Using the Acropora digitifera genome to understand coral responses to environmental change. *Nature* **2011,** *476* (7360), 320-U82; Spies, N. P.; Takabayashi, M.,

Expression of galaxin and oncogene homologs in growth anomaly in the coral Montipora capitata. *Diseases of Aquatic Organisms* **2013,** *104* (3), 249-256.

154. Shen, X. Y.; Belcher, A. M.; Hansma, P. K.; Stucky, G. D.; Morse, D. E., Molecular cloning and characterization of lustrin A, a matrix protein from shell and pearl nacre of Haliotis rufescens. *Journal of Biological Chemistry* **1997,** *272* (51), 32472-32481.

155. Durrant, I., Light-based detection of biomolecules. *Nature* **1990,** *346* (6281), 297-298.

156. Hahn, S.; Rodolfo-Metalpa, R.; Griesshaber, E.; Schmahl, W. W.; Buhl, D.; Hall-Spencer, J. M.; Baggini, C.; Fehr, K. T.; Immenhauser, A., Marine bivalve shell geochemistry and ultrastructure from modern low pH environments: environmental effect versus experimental bias. *Biogeosciences* **2012,** *9* (5), 1897-1914.

157. James P. Barry, T. T., Lina Hansson, Gian-Kasper Plattner and Jean-Pierre Gattuso, Atmospheric CO_2 targets for ocean acidification perturbation experiments. In *Guide to best practices for ocean acidification research and data reporting,* Riebesell U., F. V. J., Hansson L. & Gattuso J.-P., Ed. Publications Office of the European Union: Luxembourg, 2010.

158. Hall-Spencer, J. M.; Rodolfo-Metalpa, R.; Martin, S.; Ransome, E.; Fine, M.; Turner, S. M.; Rowley, S. J.; Tedesco, D.; Buia, M. C., Volcanic carbon dioxide vents show ecosystem effects of ocean acidification. *Nature* **2008,** *454* (7200), 96-99.

159. Fabricius, K. E.; Langdon, C.; Uthicke, S.; Humphrey, C.; Noonan, S.; De'ath, G.; Okazaki, R.; Muehllehner, N.; Glas, M. S.; Lough, J. M., Losers and winners in coral reefs acclimatized to elevated carbon dioxide concentrations. *Nature Climate Change* **2011,** *1* (3), 165-169.

160. Porzio, L.; Buia, M. C.; Hall-Spencer, J. M., Effects of ocean acidification on macroalgal communities. *Journal of Experimental Marine Biology and Ecology* **2011,** *400* (1-2), 278-287.

161. Cigliano, M.; Gambi, M. C.; Rodolfo-Metalpa, R.; Patti, F. P.; Hall-Spencer, J. M., Effects of ocean acidification on invertebrate settlement at volcanic CO2 vents. *Marine Biology* **2010,** *157* (11), 2489-2502.

162. De Astis, G.; Ventura, G.; Vilardo, G., Geodynamic significance of the Aeolian volcanism (Southern Tyrrhenian Sea, Italy) in light of structural, seismological, and geochemical data. *Tectonics* **2003,** *22* (4), 17.

163. Gugliandolo, C.; Italiano, F.; Maugeri, T. L., The submarine hydrothermal system of Panarea (Southern Italy): biogeochemical processes at the thermal fluids-sea bottom interface. *Annals of Geophysics* **2006,** *49* (2-3), 783-792.

164. Gamberi, F.; Marani, M.; Savelli, C., Tectonic, volcanic and hydrothermal features of a submarine portion of the Aeolian arc (Tyrrhenian Sea). *Marine Geology* **1997,** *140* (1-2), 167-181.

165. Tassi, F.; Capaccioni, B.; Caramanna, G.; Cinti, D.; Montegrossi, G.; Pizzino, L.; Quattrocchi, F.; Vaselli, O., Low-pH waters discharging from submarine vents at Panarea Island (Aeolian islands, southern Italy) after the 2002 gas blast: Origin of hydrothermal fluids and implications for volcanic surveillance. *Applied Geochemistry* **2009,** *24* (2), 246-254.

166. Esposito, A.; Giordano, G.; Anzidei, M., The 2002-2003 submarine gas eruption at Panarea volcano (Aeolian Islands, Italy): Volcanology of the seafloor and implications for the hazard scenario. *Marine Geology* **2006,** *227* (1-2), 119-134.

167. Anzidei, M.; Esposito, A.; Bortoluzzi, G.; De Giosa, F., The high resolution bathymetric map of the exhalative area of Panarea (Aeolian Islands, Italy). *Annals of Geophysics* **2005,** *48* (6), 899-921.

168. Caracausi, A.; Ditta, M.; Italiano, F.; Longo, M.; Nuccio, P. M.; Paonita, A., Changes in fluid geochemistry and physico-chemical conditions of geothermal systems caused by magmatic input: The recent abrupt outgassing off the island of Panarea (Aeolian Islands, Italy). *Geochimica Et Cosmochimica Acta* **2005,** *69* (12), 3045-3059; Chiodini, G.; Caliro, S.; Caramanna, G.; Granieri, D.; Minopoli, C.; Moretti, R.; Perotta, L.; Ventura, G., Geochemistry of the submarine gaseous emissions of panarea (Aeolian Islands, Southern Italy): Magmatic vs. hydrothermal origin and implications for volcanic surveillance. *Pure and Applied Geophysics* **2006,** *163* (4), 759-780.

169. Capaccioni, B.; Tassi, F.; Vaselli, O.; Tedesco, D.; Poreda, R., Submarine gas burst at Panarea Island (southern Italy) on 3 November 2002: A magmatic versus hydrothermal episode. *Journal of Geophysical Research-Solid Earth* **2007,** *112* (B5); Capaccioni, B.; Tassi, F.; Vaselli, O.; Tedesco, D.; Rossi, P. L., The November 2002 degassing event at Panarea Island (Italy): five months of geochemical monitoring. *Annals of Geophysics* **2005,** *48* (4-5), 755-765.

170. Ries, J. B.; Cohen, A. L.; McCorkle, D. C., Marine calcifiers exhibit mixed responses to CO2-induced ocean acidification. *Geology* **2009,** *37* (12), 1131-1134.

171. McCandless, E. L.; Craigie, J. **S.,** Sulfated Polysaccharides in Red and Brown Algae. *Annual Review of Plant Physiology* **1979,** *30*, 41-53.

172. Mann, S., Webb, J., Williams, R. J. P. Biomineralization: Chemical and biochemical perspectives. (VCH Verlagsgesellschaft, 1989)

173. Robbins, L. L.; Knorr, P. O.; Hallock, P., Response of *Halimeda* to ocean acidification: field and laboratory evidence. *Biogeosciences Discuss* **2009,** *6*, 41-53.

174. Kroeker, K. J.; Kordas, R. L.; Crim, R. N.; Singh, G. G., Meta-analysis reveals negative yet variable effects of ocean acidification on marine organisms. *Ecology Letters* **2010,** *13* (11), 1419-1434.

175. Fabry, V. J., Ocean science - Marine calcifiers in a high-CO(2) ocean. *Science* **2008,** *320* (5879), 1020-1022.

176. Johnson, V. R.; Russell, B. D.; Fabricius, K. E.; Brownlee, C.; Hall-Spencer, J. M., Temperate and tropical brown macroalgae thrive, despite decalcification, along natural CO2 gradients. *Global Change Biology* **2012,** *18* (9), 2792-2803.

177. Munday, P. L.; Warner, R. R.; Monro, K.; Pandolfi, J. M.; Marshall, D. J., Predicting evolutionary responses to climate change in the sea. *Ecology Letters* **2013,** *16* (12), 1488-1500.

178. Anderson, J. T.; Inouye, D. W.; McKinney, A. M.; Colautti, R. I.; Mitchell-Olds, T., Phenotypic plasticity and adaptive evolution contribute to advancing flowering phenology in response to climate change. *Proceedings of the Royal Society B-Biological Sciences* **2012,** *279* (1743), 3843-3852.

179. Rodolfo-Metalpa, R.; Martin, S.; Ferrier-Pagès, C.; Gattuso, J.-P., Response of the temperate coral *Cladocora caespitosa* to mid- and long-term exposure to *p*CO_2 and temperature levels projected in 2100. *Biogeosciences Discuss* **2009,** *6*, 7103-7131; Dias, B. B.; Hart, B.; Smart, C. W.; Hall-Spencer, J. M., Modern seawater acidification: the response of foraminifera to high-CO2 conditions in the Mediterranean Sea. *Journal of the Geological Society* **2010,** *167* (5), 843-846; Calosi, P.; Rastrick, S. P. S.; Graziano, M.; Thomas, S. C.; Baggini, C.; Carter, H. A.; Hall-Spencer, J. M.; Milazzo, M.; Spicer, J. I., Distribution of sea urchins living near shallow water CO2 vents is dependent upon species acid–base and ion-regulatory abilities. *Marine Pollution Bulletin* **2013,** *73* (2), 470-484.

180. Skinner, H. C. W., Biominerals. *Mineralogical Magazine* **2005,** *69* (5), 621-641.

181. Xiang, L.; Wen, Y.; Wang, Q.; Jin, Y., Synthesis of dispersive CaCO3 in the presence of MgO2. *Materials Chemistry and Physics* **2006,** *98* (2-3), 236-240; Brecevic, L.; Kralj, D., On calcium carbonates: from fundamental research to application. *Croatica Chemica Acta* **2007,** *80* (3-4), 467-484; Volodkin, D. V.; von Klitzing, R.; Mohwald, H., Pure Protein Microspheres by Calcium Carbonate Templating. *Angewandte Chemie-International Edition* **2010,** *49* (48), 9258-9261; Yan, X.; Li, J.; Möhwald, H., Templating Assembly of Multifunctional Hybrid Colloidal Spheres. *Advanced Materials* **2012,** *24* (20), 2663-2667.

182. Ostwald, W., Studien über die Bildung und Umwandlung fester Körper: Übersättigung und Überkaltung. *Zeitschrift für Physikalische Chemie* **1897,** *22*, 289-330.

183. Cartwright, J. H. E.; Checa, A. G.; Gale, J. D.; Gebauer, D.; Sainz-Díaz, C. I., Calcium Carbonate Polyamorphism and Its Role in Biomineralization: How Many Amorphous Calcium Carbonates Are There? *Angewandte Chemie International Edition* **2012,** *51* (48), 11960-11970.

184. Radha, A. V.; Navrotsky, A., Thermodynamics of Carbonates. In *Geochemistry of Geologic Co2 Sequestration*, DePaolo, D. J.; Cole, D. R.; Navrotsky, A.; Bourg, I. C., Eds. Mineralogical Soc Amer: Chantilly, 2013; Vol. 77, pp 73-121.

185. Kanakis, J.; Malkaj, P.; Petroheilos, J.; Dalas, E., The crystallization of calcium carbonate on porcine and human cardiac valves and the antimineralization effect of sodium alginate. *Journal of Crystal Growth* **2001,** *223* (4), 557-564.

186. Falini, G.; Fermani, S.; Vanzo, S.; Miletic, M.; Zaffino, G., Influence on the formation of aragonite or vaterite by otolith macromolecules. *European Journal of Inorganic Chemistry* **2005,** (1), 162-167.

187. Wehrmeister, U.; Jacob, D. E.; Soldati, A. L.; Loges, N.; Hager, T.; Hofmeister, W., Amorphous, nanocrystalline and crystalline calcium carbonates in biological materials. *Journal of Raman Spectroscopy* **2011,** *42* (5), 926-935.

188. Ariani, A. P.; Wittmann, K. J.; Franco, E., A Comparative study of static bodies inmysid crustaceans: evolutionary implications of crystallographic characteristics. *Biological Bulletin* **1993,** *185* (3), 393-404.

189. Lakshminarayanan, R.; Chi-Jin, E. O.; Loh, X. J.; Kini, R. M.; Valiyaveettil, S., Purification and characterization of a vaterite-inducing peptide, pelovaterin, from the eggshells of Pelodiscus sinensis (Chinese soft-shelled turtle). *Biomacromolecules* **2005,** *6* (3), 1429-1437.

190. Qiao, L.; Feng, Q. L.; Li, Z., Special vaterite found in freshwater lackluster pearls. *Crystal Growth & Design* **2007,** *7* (2), 275-279.

191. Isaure, M. P.; Sarret, G.; Harada, E.; Choi, Y. E.; Marcus, M. A.; Fakra, S. C.; Geoffroy, N.; Pairis, S.; Susini, J.; Clemens, S.; Manceau, A., Calcium promotes cadmium elimination as vaterite grains by tobacco trichomes. *Geochimica Et Cosmochimica Acta* **2010,** *74* (20), 5817-5834.

192. Lowenstam, H. A.; Abbott, D. P., Vaterite: a mineralization product of the hard tissues of a marine organism (Ascidiacea). *Science (New York, N.Y.)* **1975,** *188* (4186), 363-5.

193. Kralj, D.; Brecevic, L.; Nielsen, A. E., Vaterite growth and dissolution in acqueous solution. 1. Kinetics of crystal growth. *Journal of Crystal Growth* **1990,** *104* (4), 793-800.

194. Njegic-Dzakula, B.; Falini, G.; Brecevic, L.; Skoko, Z.; Kralj, D., Effects of initial supersaturation on spontaneous precipitation of calcium carbonate in the presence of charged poly-L-amino acids. *Journal of Colloid and Interface Science* **2010,** *343* (2), 553-563.

195. Falini, G.; Fermani, S.; Gazzano, M.; Ripamonti, A., Oriented crystallization of vaterite in collagenous matrices. *Chemistry-a European Journal* **1998,** *4* (6), 1048-1052; Pouget, E. M.; Bomans, P. H. H.; Goos, J.; Frederik, P. M.; de With, G.; Sommerdijk, N., The Initial Stages of Template-Controlled CaCO3 Formation Revealed by Cryo-TEM. *Science* **2009,** *323* (5920), 1455-1458.

196. Colfen, H.; Antonietti, M., Crystal design of calcium carbonate microparticles using double-hydrophilic block copolymers. *Langmuir* **1998,** *14* (3), 582-589.

197. Kabalah-Amitai, L.; Mayzel, B.; Kauffmann, Y.; Fitch, A. N.; Bloch, L.; Gilbert, P.; Pokroy, B., Vaterite Crystals Contain Two Interspersed Crystal Structures. *Science* **2013,** *340* (6131), 454-457.

198. Demichelis, R.; Raiteri, P.; Gale, J. D.; Dovesi, R., A new structural model for disorder in vaterite from first-principles calculations. *Crystengcomm* **2012,** *14* (1), 44-47.

199. Politi, Y.; Arad, T.; Klein, E.; Weiner, S.; Addadi, L., Sea urchin spine calcite forms via a transient amorphous calcium carbonate phase. *Science* **2004,** *306* (5699), 1161-1164.

200. Poduska, K. M.; Regev, L.; Boaretto, E.; Addadi, L.; Weiner, S.; Kronik, L.; Curtarolo, S., Decoupling Local Disorder and Optical Effects in Infrared Spectra: Differentiating Between Calcites with Different Origins. *Advanced Materials* **2011,** *23* (4), 550-+; Suzuki, M.; Dauphin, Y.; Addadi, L.; Weiner, S., Atomic order of aragonite crystals formed by mollusks. *Crystengcomm* **2011,** *13* (22), 6780-6786.

201. **Sato, M.**; M**atsuda, S.**, Structure of vaterite and infrared spectra. *Zeitschrift für Kristallographie* **1969,** *129*, 405-455.

202. Nakamoto, K.; Fujita, J.; Tanaka, S.; Kobayashi, M., Infrared Spectra of Metallic Complexes. IV. Comparison of the Infrared Spectra of Unidentate and Bidentate Metallic Complexes. *Journal of the American Chemical Society* **1957,** *79* (18), 4904-4908.

203. Qiao, L.; Feng, Q. L.; Liu, Y., A novel bio-vaterite in freshwater pearls with high thermal stability and low dissolubility. *Materials Letters* **2008,** *62* (12-13), 1793-1796.

204. Wolf, G.; Gunther, C., Thermophysical investigations of the polymorphous phases of calcium carbonate. *Journal of Thermal Analysis and Calorimetry* **2001,** *65* (3), 687-698.

205. Radha, A. V.; Forbes, T. Z.; Killian, C. E.; Gilbert, P.; Navrotsky, A., Transformation and crystallization energetics of synthetic and biogenic amorphous calcium carbonate. *Proceedings of the National Academy of Sciences of the United States of America* **2010,** *107* (38), 16438-16443.

206. Peric, J.; Vucak, M.; Krstulovic, R.; Brecevic, L.; Kralj, D., Phase transformation of calcium carbonate polymorphs. *Thermochimica Acta* **1996,** *277*, 175-186.

Acknowledgments

The research leading to these results has received funding from the European Research Council under the European Union’s Seventh Framework Programme (FP7/2007-2013)/ERC Grant Agreement No. [249930-CoralWarm: Corals and global warming: the Mediterranean versus the Red Sea; www. CoralWarm.eu].

I would like to express my gratitude to all the professors, colleagues and students that contributed to the work presented in this thesis. In particular I would like to thanks my supervisor Prof.Giuseppe Falini that gave me the possibility to continue the work started in my master thesis and for his help, his suggestions and his encouragements; Prof. Stefano Goffredo thanks to which I began this path on corals; Dr. Simona Fermani for the support and the useful suggestions; Prof. Francesca Sparla that hosted and followed me in her laboratory with much willingness and for electrophoretic analyses (chapter 4); Dr. Yannicke Dauphin and Prof. Jean-Pierre Cuif for providing some coral samples, for amino acid and AFM analyses (Chapter 2 and 3); Prof. Damir Kralj to hosted me in his laboratory and Dr. Branka Njegić-Džakula to the help and friendship during my abroad period in Zagreb. I would like to express my gratitude also for all the people that collected or send me the samples of the different organisms and the Scientific Diving School for the logistic and technical support.

In the end, I would like to thank my family, my friends, and all those people who supported me with their love and comprehension.

APPENDIX A – Supplementary Informations about Materials and Methods

A.1 Sampling of the organisms and preparation of skeletons

The organisms samples were randomly collected by SCUBA diving. After collection the organisms were dipped in a sodium hypochlorite solution (commercial), changed every 4 days, until the tissue was completely dissolved. Each skeleton was analyzed under a binocular microscope to remove fragment of substratum and calcareous deposit produced by other organisms. Successively, the skeletons were ground in a mortar to obtain a fine and homogeneous powder (grains smaller than 100 µm). The obtained powder was further suspended for 20 min. in a sodium hypochlorite solution (8% *v*/*v*) to eliminate trace of organic material eventually not removed from the first treatment, then the remaining powder was washed with milli-Q water (resistivity 18.2 MΩ cm at 25 °C; filtered through a 0.22 µm membrane) and dried in oven at 37 °C for 24 hr.

A.2 Characterization of the skeleton

X-ray diffractometry. X-ray powder diffraction (XRD) patterns about the skeleton were collected using a PanAnalytical X’Pert Pro equipped with X’Celerator detector powder diffractometer using Cu Kα radiation generated at 40 kV and 40 mA. The diffraction patterns were collected within the 2θ range from 10° to 60° with a step size (Δ2θ) of 0.02° and a counting time of 1200 s.

Thermo-gravimetric analyses. An estimation of the OM content in the coral was determined by thermo-gravimetric analysis (TGA) on a SDT Q600 simultaneous thermal analysis instrument (TA instrument). The analysis was performed in nitrogen flow from 30 to 120 °C with a heating rate of 10 °C/ min, an isothermal at 120 °C for 5 min, and another cycle from 120 to 600 °C with a heating rate of 10 °C/ min.

A.3 Extraction of the organic matrix

Five mL of milli-Q water, in which 2.5 g of powdered coral skeleton were dispersed, were poured in a 40 cm-long osmotic tube for dialysis (MWCO = 3.5 kDa; CelluSep®, MFPI). The sealed tube was put into 1 L of 0.1 M CH_3COOH solution under stirring. The decalcification proceeded for 72 hr. At the end the tube containing the dissolved OM was dialysed against milli-Q water until the final pH was about 6. The obtained aqueous solution containing the OM was lyophilized and weighted.

A.4 Characterization of the organic matrix

SDS-PAGE. SDS-PAGE was performed on 12.5% polyacrylamide gel in a vertical slab gel apparatus (Mini-PROTEAN®, Bio-Rad). For these analyses only the SOM solution before the lyophilisation was utilized. It was filtered and concentrated through Centricon® YM-3 (Amicon, cut off 3 kDa) until a final volume of 1 mL. Different sample volumes were applied for gel lane (10, 15, 20μL). Samples were prepared adding reduced sample buffer 1X (60mM Tris-HCl pH 6.8; 2% SDS; 2.5% β- mercaptoethanol; 10% glycerol; 0.025% bromophenol blue) and then boiled at 100 °C for 5 minutes. The gels ran at constant voltage of 100 V for 1.5 hr at room temperature. Proteins were detected with silver nitrate as staining agent. These proteins may have a pronounced tendency to diffuse out of the gel because they are very acidic, therefore, the gel was immersed in different fixing solutions that involved the simultaneous use of two reagents, formaldehyde and glutaraldehyde, to trap the proteins in the gel before staining. To observe the presence of glycoprotein the PAS (Periodic Acid Schiff) stain was performed.

Aminoacid analyses. Aminoacid analysis was conducted by a chromatographic technique using an amino acid analyzer. The OM material was weighed, then hydrolyzed at 100 °C for 24 hr in 6 M HCl vapor, and analyzed using a Dionex BIOLC amino acid analyzer. Lyophylised IOM and

SOM were hydrolysed with 6N HCl for 24 hr at 110°C. During hydrolysis, complete or partial destruction of several amino acids occurs: tryptophan is destroyed; serine and threonine are partially destroyed. Sulphur amino acids are altered. Amino acid composition of the hydrolysates was determined by high performance liquid chromatography (HPLC) using pre-column derivatization with ortho-phtalaldehyde (OPA) for primary amines and fluorometric detection. Fluorescence intensity of OPA-derivatized aminoacids was monitored with an excitation wavelength of 330 nm and an emission wavelength of 450 nm. The average protein pI of all the OM fractions was calculated from the aminoacid analyses of all the species, following the method described in Sillero and Ribeiro.

Fourier Transform Infrared Spectroscopy (FTIR). Fourier transform infrared spectroscopic analyses were conducted by using a FTIR Nicolet 380 Thermo Electron Corporation working in the range of wave-numbers 4000-400 cm^{-1} at a resolution of 2 cm^{-1}. Disk was obtained mixing little amount (< 1 mg) of SOM or IOM with 100 mg of KBr and applying a pressure of 48.6 psi (670.2 MPa) to the mixture using a hydraulic press.

Aminoacid analyses and FTIR spectra results were submitted to a statistical analysis with Mann-Whitney test.

A.5 Calcium carbonate overgrowth experiments

Transversal section of coral skeletons were placed in a microplate for cellular culture (MICROPLATE 24 well with Lid, IWAKI) or in a Petri dish (d = 3.2 cm) considering the size of different skeletons. The specimens were overlaid with 750 µL or 3360 µL of 10 mM $CaCl_2$ solution respectively. A 30x30x50 cm^3 crystallization chamber was used. Two 25 mL beakers half-full of $(NH_4)_2CO_3$ (Carlo Erba) covered with Parafilm 10 times holed and two Petri dishes (d = 8 cm) full of anhydrous $CaCl_2$ (Fluka) were put inside the chamber. Calcium carbonate crystals were let grow for four days. The overgrown specimens were then lightly rinsed with milli-Q water, dried and examined in the scanning electron microscope (SEM) after coating with gold.

A.6 Calcium carbonate crystallization experiments

A 30x30x50 cm^3 crystallization chamber was used. Two 25 mL beakers half-full of $(NH_4)_2CO_3$ (Carlo Erba) covered with Parafilm 10 times holed and two Petri dishes (d = 8 cm) full of anhydrous $CaCl_2$ (Fluka) were put inside the chamber. Microplates for cellular culture (MICROPLATE 24 well with Lid, IWAKI) containing a round glass cover slip in each well were used. In each well, according to the purpose of experiments, different solutions containing Ca^{2+} ions with or without other additives were poured. In these solutions the OM was added. The experiment proceeded for 4 days. The obtained crystals were washed three times with milli-Q water and then analyzed. All the experiments were conducted at room temperature. The crystallization trials of calcium carbonate in the different conditions were replicated starting from different batches of OM fractions.

A.7 Characterization of $CaCO_3$ precipitates

FTIR spectra of samples in KBr disks were collected at room temperature by using a FTIR Nicolet 380 Thermo Electron Corporation working in the range of wave-numbers 4000-400 cm^{-1} at a resolution of 2 cm^{-1}. A finely ground, approximately 1% (w/w) mixture of the sample in KBr was pressed into a transparent disk using a hydraulic press and applying a pressure of 48.6 psi (670.2 MPa).

Microscopic observations The optical microscope observations of $CaCO_3$ precipitates were made with a Leica microscope equipped with a digital camera. The SEM observations were conducted in a scanning electronic microscope using directly in a Phenom^{TM} microscope (FEI) and after coating with gold using a Hitachi FEG 6400 scanning electron microscope.

APPENDIX B – Side-projects

CROATICA CHEMICA ACTA
CCACAA, ISSN 0011-1643, e-ISSN 1334-417X

Croat. Chem. Acta **86** (1) (2013) 39–47
http://dx.doi.org/10.5562/cca2197

Original Scientific Article

The Influence of a Protein Fragment Extracted from Abalone Shell Green Layer on the Precipitation of Calcium Carbonate Polymorphs in Aqueous Media[†]

Branka Njegić-Džakula,[a] Michela Reggi,[b] Giuseppe Falini,[b] Igor Weber,[c] Ljerka Brečević,[a,*] and Damir Kralj[a,*]

[a]*Laboratory for Precipitation Processes, Ruđer Bošković Institute, P. O. Box 180, HR-10002 Zagreb, Croatia*
[b]*Dipartimento di Chimica "G. Ciamician", Università di Bologna, via Selmi 2, I-40126 Bologna, Italy*
[c]*Laboratory for Electron Microscopy, Ruđer Bošković Institute, P. O. Box 180, HR-10002 Zagreb, Croatia*

RECEIVED OCTOBER 12, 2012; REVISED DECEMBER 11, 2012; ACCEPTED DECEMBER 12, 2012

Abstract. Many living organisms form mineral phases through biologically controlled processes, known as biomineralization. Thus created materials are composites of both, mineral and organic components. The shell of the gastropod mollusc red abalone (*Haliotis rufescens*) consists of calcite and aragonite layers, each of them containing characteristic biopolymers responsible for biomineralization. In this work, the effect of interstitial green sheet polypeptide, GP, extracted from the green layer of the mollusc red abalone shell, on the process of spontaneous precipitation of calcium carbonate polymorphs, was investigated. Three precipitation systems, in which the initial mineralogical composition of the precipitate was different, have been studied. Thus, in system (1) calcite appeared, in system (2) a mixture of calcite and vaterite was found, while in system (3), ASW, only aragonite precipitated. However, the precipitation kinetic measurements, X-ray diffraction, FT-IR spectroscopy, and light and scanning electron microscopy indicated that the addition of GP in the model systems caused the inhibition of precipitation and change of morphology of crystals as a consequence of GP adsorption on the crystal surfaces and its entrapment into the mineral structure. (doi: 10.5562/cca2197)

Keywords: calcium carbonate, calcite, aragonite, vaterite, green sheet polypeptide (GP)

INTRODUCTION

Many organisms are capable to construct a variety of mineral based materials, or biomaterials, by inducing crystallization and deposition of complex inorganic hierarchical structures. A precise control of crystal nucleation and growth, in which biological (macro)molecules play important roles by guiding the process, is essential for the properties of mineralized tissues formed.[1] Although these biologically mediated processes, known as biomineralization, can occur in normal (*e.g.* bone, tooth enamel or shell of the mollusc) and in pathological circumstances (ectopic mineral deposits), the principles governing them are still not well understood.[1–3] However, it is known that the formation of biominerals in organisms is controlled by different processes, sometimes synergic, like the regulation of concentrations of respective ions, formation of initial amorphous and other metastable precursor phases, and the presence of specific biomolecular additives.[4–7]

Calcium carbonate is among the most abundantly produced biominerals that may be formed biogenically in marine organisms, such as molluscs and crustaceans. It occurs in three anhydrous crystalline polymorphs (vaterite, aragonite and calcite) and three hydrated forms (calcium carbonate monohydrate, calcium carbonate hexahydrate and amorphous calcium carbonate), of which calcite is the most stable form under standard conditions. The role of metastable calcium carbonate modifications in the formation of crystalline polymorphs has recently been particularly emphasized.[8–11] It is now well recognized and experimentally confirmed that many organisms, among them molluscs,[12] use amorphous calcium carbonate as a transient (precursor) phase in the process of biomineral development.[13,14] Such a pathway allows efficient transport of ions to the site of minerallization.[8] It has been also suggested,[15,16] that an amorphous phase can direct the formation of the specific polymorph into which it will transform. The mineralization control is mainly achieved by the

---

[†] This article belongs to the Special Issue devoted to the 85th anniversary of *Croatica Chemica Acta*.

* Authors to whom correspondence should be addressed. (E-mails: damir.kralj@irb.hr, brecevic@irb.hr)

involvement of organic matrix proteins,, whose formation is directed in space and time at cellular level.[17,18]

A usual way of studying the organic matrix components is to extract them from the biomineral. The components, as agreed, are classified in two groups depending on their solubility in water solutions,[1] although this distinction in some cases is not generally valid.[19] In many cases the soluble fraction is characterized by the presence of acidic glycoproteins (rich in aspartic and glutamic acid residues) and the insoluble fraction is often formed by macromolecules able to build fibrous structures (chitin in mollusc shells, collagen in bones). The shell of the gastropod mollusc red abalone (*Haliotis rufescens*) consists of calcitic and aragonitic layers, each of them jointed together with characteristic biopolymers. The outer layer of the shell is made of red prismatic calcite and the inner layer, the nacre, is composed of aragonite tablets. Green organic sheets sandwiched between interstitial mineral heterolayers, which differ from nacre, are interspersed through the nacre at irregular intervals.[20,21] The green sheet turned out to be a good model for the study of biomineralization processes of the molluscan shells, even if unique in the abalone shell.[22] Indeed, it shares common features with the nacre organic matrix and the periostracum, and also has similarities to the myostracum. Moreover, it has been demonstrated that the green layer has nucleating properties for calcium carbonate either *in vivo*[22] or *in vitro*.[23]

The green layer is highly insoluble and resistant to chemical and biological agents.[22,23] After its alkaline digestion, water soluble protein fragment (GP) is obtained. The amino acidic composition of GP was found to be similar to the parent green layer and therefore suitable for using it as a soluble analogous of the nucleating green sheet.[23] It is rich in acidic residues, aspartic and glutamic acid, in proline, tyrosyne and tyrosine derivates, that are actually responsible to GP unique fluorescent properties.

In this study, the effects of GP on the process of spontaneous precipitation of calcium carbonate polymorphs were correlated to its concentration and initial supersaturation in simple precipitation model systems, as well as in the system of artificial sea water (ASW). However, it should be kept on mind that the ionic composition of artificial sea water is similar to that of the extrapalial fluid present at the interface between mineral and soft tissue in mollusc shells.[24]

EXPERIMENTAL

Materials and Methods

Experiments were carried out in a thermostated double-walled glass vessel of 20 cm^3 capacity, at a constant temperature of 21 °C. In order to precipitate different calcium carbonate polymorphs, three precipitation systems were investigated:

(1) Precipitation of calcium carbonate was initiated by pouring 10 cm^3 of calcium chloride solution into 10 cm^3 of sodium carbonate solution: the initial concentrations of the reactants were equal, $c_i(\mathrm{Ca}^{2+}) = c_i(\mathrm{CO_3})_{2-} = 1.0 \times 10^{-2}$ mol dm^{-3}. The $\mathrm{CaCl_2}$ solution was prepared by appropriate dilution of a respective stock solution, while the $\mathrm{Na_2CO_3}$ solution was freshly prepared by dissolving anhydrous sodium carbonate in water.[25] An appropriate amount of GP was added to the $\mathrm{Na_2CO_3}$ solution and the GP concentrations used varied in the range 3 ppm $\leq c_i(\mathrm{GP}) \leq$ 14 ppm. During the experiments the reaction vessel was tightly closed by a Teflon cover thus minimizing the exchange of carbon dioxide between the air and the reaction system, and enabling a strict control of supersaturation. The system was mechanically stirred at a constant rate.

(2) The procedure similar to system 1 was applied with the difference that the initial reactant concentrations were higher, $c_i(\mathrm{Ca}^{2+}) = c_i(\mathrm{CO_{32-}}) = 2.0 \times 10^{-2}$ mol dm^{-3}, and the GP concentrations used varied in the range 3 ppm $\leq c_i(\mathrm{GP}) \leq$ 10 ppm.

(3) In this system the precipitation was initiated in a solution that imitated the artificial sea water[2] (ASW) or extrapallial solution of sea water mollusc shell. Identical to the previously described protocols, the volumes of reactants of 10 cm^3 were used: the carbonate solution contained $c(\mathrm{Na_2CO_3}) = 5.0 \times 10^{-3}$ mol dm^{-3}, $c(\mathrm{NaCl}) = 3.198 \times 10^{-1}$ mol dm^{-3} and $c(\mathrm{Na_2SO_4}) = 5.11 \times 10^{-2}$ mol dm^{-3}, while the calcium solution was made up of $c(\mathrm{CaCl_2}) = 9.3 \times 10^{-3}$ mol dm^{-3}, $c(\mathrm{MgCl_2}) = 5.3 \times 10^{-2}$ mol dm^{-3} and $c(\mathrm{KCl}) = 9.0 \times 10^{-3}$ mol dm^{-3}. GP was added into the carbonate solution and the precipitation was initiated by pouring the calcium containing solution into the carbonate solution. The concentrations of GP used in experiments varied in the range 3 ppm $\leq c_i(\mathrm{GP}) \leq$ 20 ppm. In distinction from the previous systems, 1 and 2, the systems were continuously stirred at a constant rate by means of a Teflon-coated magnetic stirring bar.

In all systems the chemicals used to prepare reactant solutions, $\mathrm{CaCl_2}$, $\mathrm{Na_2CO_3}$, $\mathrm{MgCl_2}$, $\mathrm{Na_2SO_4}$, KCl and NaCl, were analytical grade and the deionized water was of high quality (conductivity < 0.055 µS cm^{-1}). The systems used as controls contained the same initial reactant concentrations and volumes, but without GP.

The progress of the precipitation process was followed by measuring pH of the solution during 70 min (systems 1 and 2) and 150 min (ASW system) of the process, using a combined glass-calomel electrode (GK 2401C) connected to a digital pH meter (PHM 290, Radiometer). The samples of precipitate used for the analyses were taken at the end of each experiment, when the total volume of suspension was filtered through a 0.22 µm membrane filter. The precipitate was washed with small portions of water and dried at 50 °C. The mineralogical composition of the dried samples was analyzed by FT-IR spectroscopy (FT-IR Mattson spectrometer, Genesis Series) using KBr pellets and by X-ray powder diffraction, XRD (Philips X'Celerator diffractometer). The diffraction intensities were measured in the angular range $10° \leq 2\theta \leq 60°$ setting a step size $2\theta = 0.05°$ and measuring time of 150 s per step. The calcium carbonate polymorphs were identified by using the FT-IR standards and according to the ICDD Powder Diffraction File.[26] The concentration of total dissolved calcium was determined in the mother liquor by ion chromatography system (ICS-1100, Dionex) fitted with SC16 Analytical Column. The morphology of the crystals was observed by light microscopy (Leika microscope equipped with a digital camera) and by scanning electron microscopy (FEG SEM Hitachi 6400 and Phenom model G2). In some cases the samples used for the SEM observations were coated with gold. Confocal laser scanning microscopy was performed using a Leica TCS SP2 AOBS confocal microscope equipped with an HCX PL APO λ-Blue 63×/1.4 objective (Leica Microsystems). Fluorescence and transmission images were acquired simultaneously. For illumination, the 488 nm line from the Argon-ion gas laser was used and fluorescence was collected in the 500−590 nm range. Confocal fluorescence images were taken using the pinhole size of 114 µm (1 Airy unit), corresponding to an optical section thickness of approximately 360 nm (FWHM).

Extraction of Green Layer Water Soluble Polypeptide (GP)

Shells of red abalones (*Haliotis rufescens*) were purchased from malacology shop. They were collected on the pacific coast, cleaned from the soft tissues and then stored at −4 °C. Nacre shell portion was mechanically separated, cleaned and decalcified in dilute acetic acid containing 0.1 % sodium azide at 20 °C. After decalcification, salts were removed from the remaining insoluble material by exhaustive washing with distilled water. The green interstitial polymer composite sheets were manually separated under the optical microscope. Extraction of GP was achieved by treatment of the green layer with 1.0 mol dm^{-3} NaOH for 24 h. The solubilised material was dialysed against water (MWCO 3.5 kDa) and successively lyophilized.

Treatment of Data

On the basis of the measured pH and the known total initial concentrations of the precipitating components, the molar concentrations and activities of the ionic species present in solution at considerable amounts and at any moment of the precipitation process, were calculated.[27] In the case of the precipitation systems 1 and 2, 11 ionic species were considered: H^+, OH^-, CO_3^{2-}, HCO_3^-, $NaCO_3^-$, $CaCO_3^0$, $CaHCO_3^+$, $CaOH^+$, Ca^{2+}, Na^+ and Cl^-, while in the artificial sea water precipitation system, system 3, the additional species were assumed to exist: SO_4^{2-}, $NaSO_4^-$, $CaSO_4^0$, $NaHCO_3^0$, $MgCO_3^0$, $MgSO_4^0$, $NaCl^0$, Mg^{2+}, K^+, $MgCO_3^0$, $MgHCO_3^+$, $CaCl^+$, $MgCl^+$ and $MgOH^+$.

Detailed calculation procedure, as well as the corresponding equilibrium constants of ionic species can be found in literature.[25,27–31] The protein concentrations were always low in comparison to those of the calcium species and, consequently, calcium-protein complexation was not considered in the calculation procedure.

Supersaturation was expressed as saturation ratio, S:

$$S = [a_{\mathrm{Ca}}\, a_{\mathrm{CO3}} / K_{\mathrm{sp}}^{0}]^{1/2} \qquad (1)$$

where a_{Ca} is the activity of calcium ion, a_{CO3} is the activity of carbonate ion, and K_{sp}^{0} is the thermodynamic equilibrium constant of dissolution ("thermodynamic solubility product") of the corresponding calcium carbonate polymorph.

RESULTS AND DISCUSSION

Three sets of experiments were performed. In each set the initial supersaturation and/or solution composition were varied with the view of obtaining different polymorphic compositions of calcium carbonate precipitates. Thus, it was found that in the control precipitation system in which the initial concentrations of the reactants were $c_i(Ca^{2+}) = c_i(CO_3^{2-}) = 1.0 \times 10^{-2}$ mol dm^{-3} (system 1) the precipitate isolated at the end of the experiment consisted entirely of calcite, while in the system $c_i(Ca^{2+}) = c_i(CO_3^{2-}) = 2.0 \times 10^{-2}$ mol dm^{-3} (system 2) the precipitate consisted of a mixture of calcite and vaterite. Actually, the appearance of metastable polymorph vaterite was expected since its precipitation was a consequence of a higher initial supersaturation in this system. As found earlier,[30] vaterite, if left in contact with the solution, would gradually transform to calcite as a consequence of the solution-mediated transformation process. In the control system in which the artificial sea water was used and the concentrations of reactants were $c(CO_3^{2-}) = 5.0 \times 10^{-3}$ mol dm^{-3} and $c(Ca^{2+}) = 9.3 \times 10^{-3}$ mol dm^{-3} (system 3), ASW system, only aragonite was obtained. Aragonite is relatively stable polymorph especially when in contact with magnesium ions, which promote its nucleation and stabilize it in the solution. The mineralogical composition of precipitates was detected by both, XRD and FT-IR

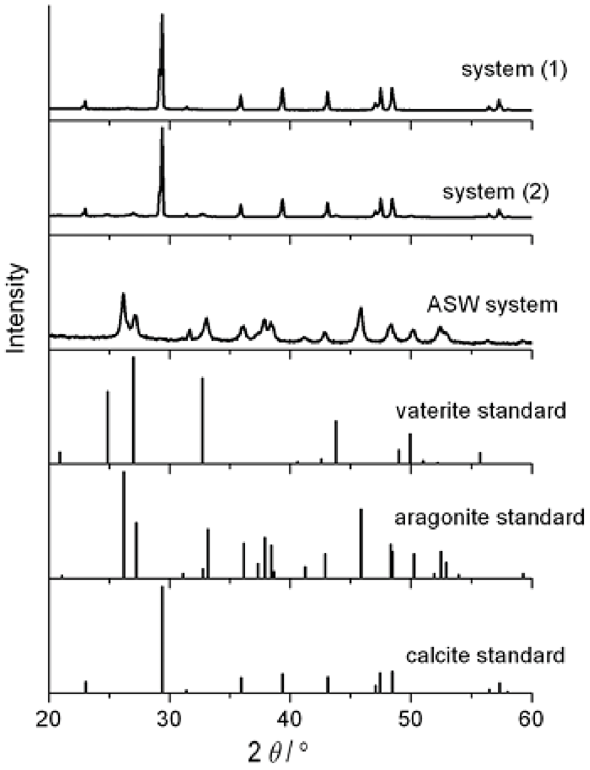

Figure 1. X-ray diffractograms of the calcium carbonate samples isolated from the precipitation model systems of different initial supersaturations and compositions: system 1: $c_i(Ca^{2+}) = c_i(CO_3^{2-}) = 1.0 \times 10^{-2}$ mol dm^{-3}, system 2: $c_i(Ca^{2+}) = c_i(CO_3^{2-}) = 2.0 \times 10^{-2}$ mol dm^{-3} and system 3 (artificial sea water, ASW). The XRD standards are also shown.

spectroscopy. Figure 1 shows the XRD patterns of the samples isolated from all three control systems, which are compared with the XRD patterns of the respective standards of calcium carbonate polymorphs. It is evident that in system 1 only diffraction peaks of calcite were obtained, while in system 2 diffraction patterns of both calcite and vaterite were found. In the case of ASW precipitation system, diffraction peaks distinctive for aragonite, as well as two additional peaks at $2\theta = 31.8°$ and $2\theta = 56.4°$, could be seen. These additional peaks correspond to NaCl, which remained in the precipitate as contamination after separation of aragonite from the suspension and drying the samples.

The mineralogical composition of the precipitates, which were isolated from the systems in which the green layer polypeptide (GP) was added, showed no significant difference from the respective control systems, regardless the GP concentrations used. In the same way as was the case of the control system, the samples of precipitate were isolated after the apparent termination of the growth process.

The kinetics of spontaneous precipitation, in the systems containing different amounts of GP and in the respective control systems, was followed by measuring the solution pH. Figure 2 shows the progress curves of precipitation processes, S_c versus time, recorded in the presence of different GP concentrations. The respective pH versus time curves, from which the supersaturations, S_c, were calculated, are shown in insets. It is evident that in systems 1 (pH$_i$ 10.85), the initial supersaturations expressed with respect to calcite were $S_c = 32.0$. The initial supersaturation in systems 2 (pH$_i$ 10.93) was even higher and was found to be, $S_c = 47.0$ (the initial supersaturation, expressed with respect to vaterite was, $S_v = 24.2$). Since in both systems the initial superstaturation was high, the precipitation expectedly started immediately after mixing the reactants, exhibiting a sudden drop of concentrations of the constituent ions (supersaturation). It should be mentioned that the systems 1 and 2 are supersaturated with respect to amorphous calcium carbonate. However, the increasing addition of GP caused the progressive lowering of the slope of progress curves, which indicated the inhibition of calcium carbonate precipitation. In addition to lowering the slope of progress curves, GP caused an apparent termination of precipitation (crystal growth) at different supersaturations: at higher GP concentration, the supersaturation at which no growth occurred was higher as well.[*] In system 1 with GP concentration of 3 ppm and 6 ppm, this apparent termination of crystal growth at specific critical supersaturations, so-called “dead zone”, was observed at $S_c \approx 2.6$ and $S_c \approx 6.1$, respectively. Any increase of GP concentration above 6 ppm just slightly increased the S_c value and presumably not additionally influenced the growth kinetics and mechanism. According to the model of interactions between dissolved additives and growing crystal, proposed by Cabrera and Vermilyea,[32] the appearance of the dead zone and termination of crystal growth in the solution still supersaturated with respect to the specific crystal phase, is assumed to be a consequence of the adsorption of GP molecules at the calcite crystal surfaces. On the other hand, in system 2 the “dead zone” plateau was not observed within the range of GP concentrations investigated. Since in this system calcite appeared in a mixture with vaterite, the observed inhibition of crystal growth is probably the result of GP interactions with crystals of both polymorphs.

In the ASW systems (pH$_i \approx 10.20$) the initial supersaturation was, $S_c = 9.5$ (with respect to aragonite, $S_a = 8.0$). Since in this system magnesium ions, known as extremely strong inhibitors of calcium carbonate (particularly of calcite) precipitation, were present in concentrations 5.7 times higher than Ca^{2+} concentration, a long induction times were observed (control system:

---

[*] Actually, growth termination in the systems with different addition of GP is more pronounced at the respective pH versus time curves.

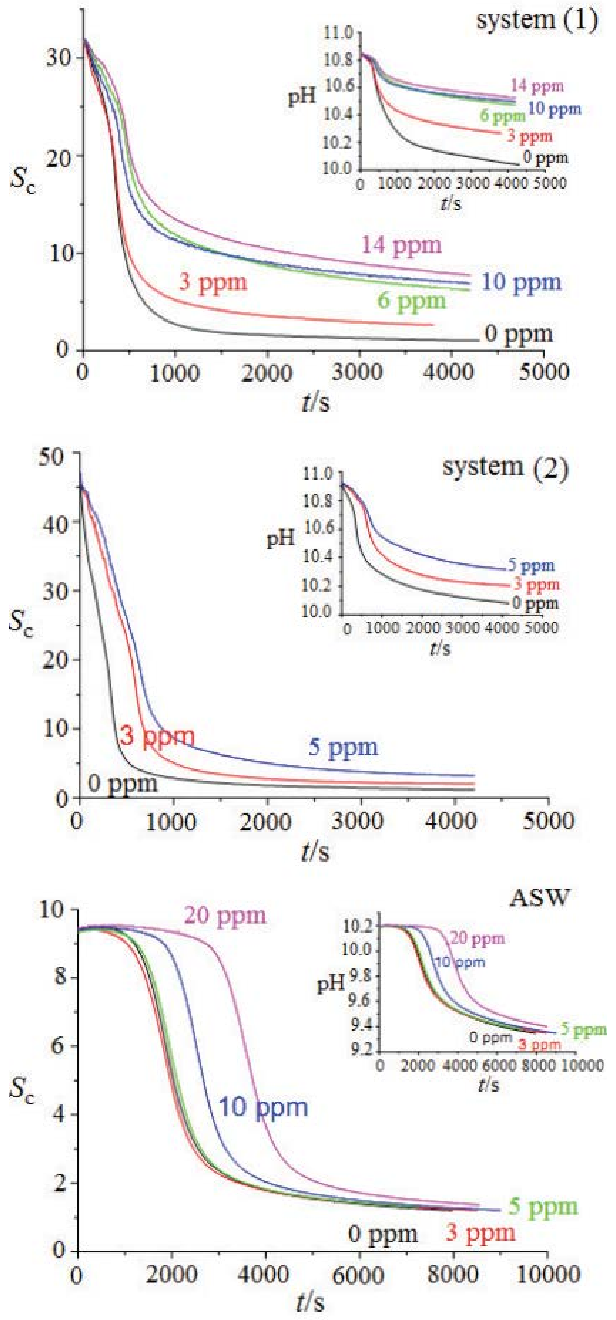

Figure 2. Progress curves, S_c versus time, of calcium carbonate precipitated in the systems of different initial supersaturations and composition: system 1: $c_i(Ca^{2+})$ = $c_i(CO_3^{2-})$ = 1.0 × 10^{-2} mol dm^{-3}, system 2: $c_i(Ca^{2+})$ = $c_i(CO_3^{2-})$ = 2.0 × 10^{-2} mol dm^{-3} and system 3 (artificial sea water, ASW). Concentrations of GP added into the systems are indicated.

$t_{ind} \approx 1500$ s). However, after the addition of increasing concentrations of GP, the induction times respectively increased, thus indicating the inhibition of the nucleation process.

Since the experimental results of the kinetics of precipitation in the presence of GP peptide demonstrated the overall retardation of nucleation (evident in the ASW system) and growth processes (more marked in the systems 1 and 2 than in ASW), the adsorption of GP on the growing calcium carbonate crystals (particularly calcite) seems to be a prevailing inhibition mechanism. Since the above data suggest an inhibition of crystal growth, due to the adsorption of GP onto the crystal surfaces, a change in the crystal sizes and morphologies is expected. Figure 3 shows low magnification scanning electron microscopy (SEM) micrographs of the crystals of spontaneously precipitated calcium carbonate polymorphs formed in systems 2, containing 0 ppm, 3.0 ppm or 10.0 ppm of GP. In all these systems the precipitate consisted of calcite and vaterite, the former appeared as rhombohedral crystals, while the latter appeared as spherulites.[28,30,33] The vaterite particles are actually aggregates of primary crystallites of 25−35 nm in size. The size of primary crystallites was estimated earlier[34] from the observed broadening of the diffraction lines of vaterite compared to calcite using the Scherrer equation. Figure 4 shows low magnification SEM micrographs of the crystals formed in systems 1 in which only calcite precipitated in the shape of rhombohedral crystals. Only in the presence of the highest concentrations of GP, some spherulitic vaterite crystallites have appeared. The crystals were about the same size within the whole range of GP concentrations investigated.

With these low magnification observations (Figures 3 and 4) it was not possible to observe the changes of crystal morphology caused by the presence of GP. However, the influence of GP on the crystal morphology was observed when high magnification SEM micrographs (Figure 5) were analyzed. They revealed textural differences between the crystals precipitated in the control system 1 and the GP containing systems 1. In the control system the calcite crystals with well expressed, regular {104} faces and edges were observed, while the crystals grown in the presence of 10 ppm GP expressed curved edges and new crystalline faces, different from the stable {104} ones. The appearance of new faces is certainly the consequence of the adsorption of soluble green layer peptides, most probably through the carboxylate groups of their acidic residues (aspartic and glutamic acids) on crystalline planes exposing calcium ions.[27,35–41]

As previously confirmed by mineralogical analysis, aragonite was the only calcium carbonate polymorph precipitated in the systems that mimic the composition of principle components of sea water. High magnification SEM micrographs (Figure 6) show that aragonite precipitated in a form of irregular aggregates of an average dimension of 2 μm. These crystals did not show the typical acicular morphology of synthetic

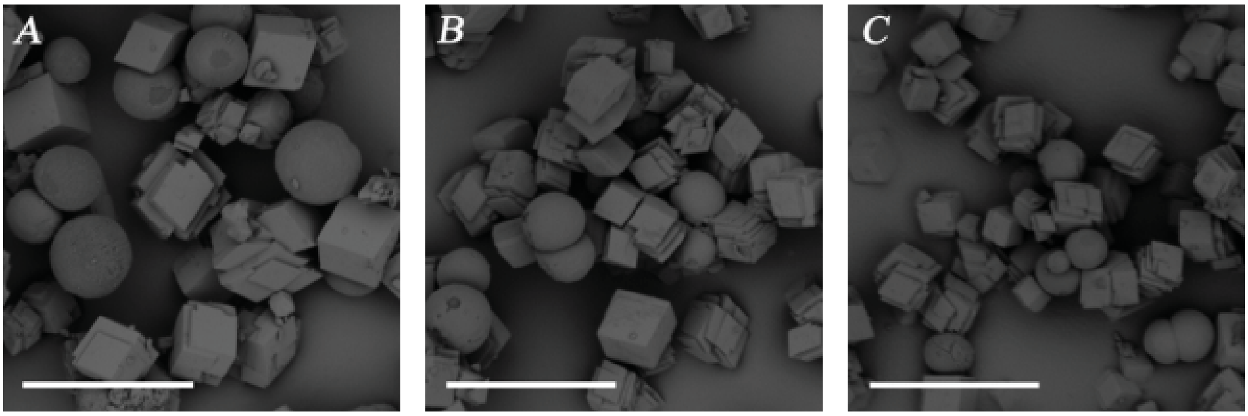

Figure 3. SEM micrographs of calcium carbonate samples isolated from the precipitation system 2: $c_i(\mathrm{Ca}^{2+}) = c_i(\mathrm{CO}_3^{2-}) = 2.0 \times 10^{-2}$ mol dm^{-3}. The concentrations of green layer peptide added to the systems are: A) 0 ppm, B) 3 ppm and C) 10 ppm. Scale bar 40 μm.

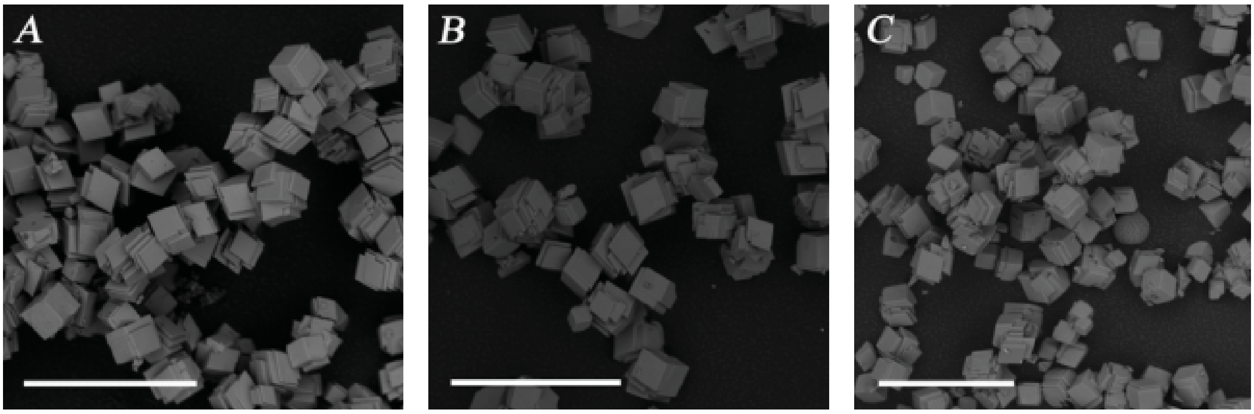

Figure 4. SEM micrographs of calcium carbonate samples isolated from the precipitation system 2: $c_i(\mathrm{Ca}^{2+}) = c_i(\mathrm{CO}_3^{2-}) = 1.0 \times 10^{-2}$ mol dm^{-3}. The concentrations of green layer peptide added to the systems are: A) 0 ppm, B) 3 ppm and C) 10 ppm. Scale bar 40 μm.

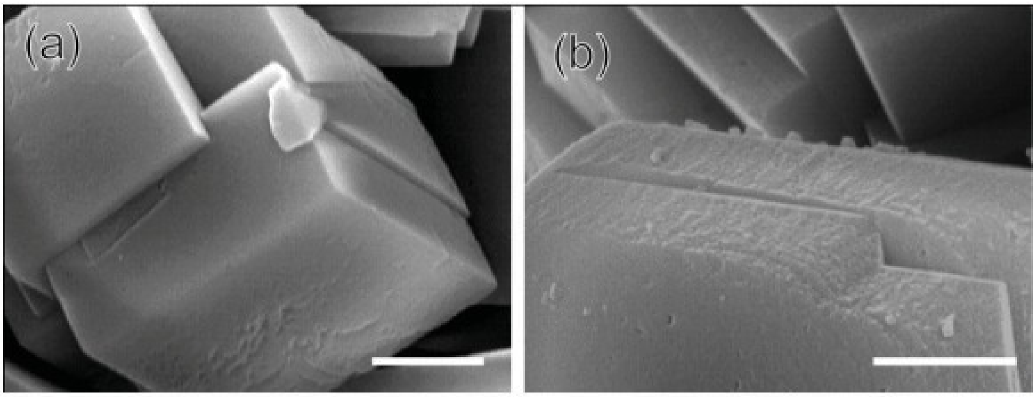

Figure 5. High magnification SEM micrographs of calcite samples isolated from the precipitation system 1: $c_i(\mathrm{Ca}^{2+}) = c_i(\mathrm{CO}_3^{2-}) = 1.0 \times 10^{-2}$ mol dm^{-3}. a) control system; b) c(GP) = 10 ppm. Scale bar 1 μm.

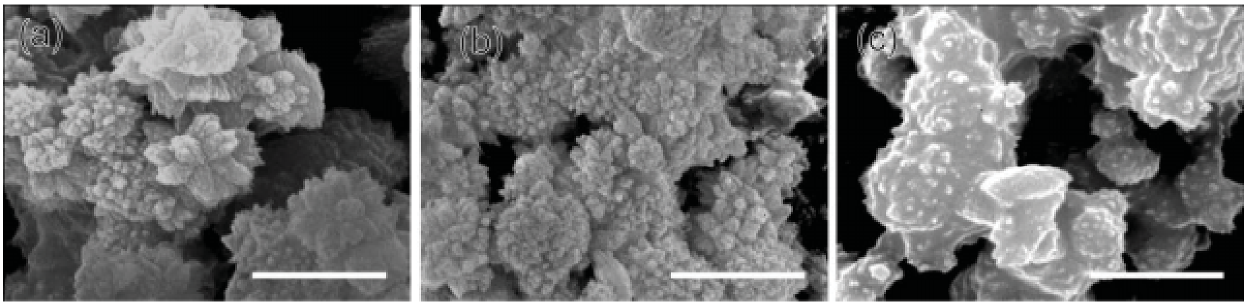

Figure 6. High magnification SEM micrographs of calcium carbonate samples isolated from the ASW precipitation system: $c_i(Ca^{2+}) = 9.3 \times 10^{-3}$ mol dm^{-3}, $c_i(CO_3^{2-}) = 5.0 \times 10^{-3}$ mol dm^{-3}. The concentrations of green layer peptide added to the systems are: a) 0 ppm, b) 3 ppm and c) 10 ppm. Scale bar 200 nm.

aragonite. Only a few elongated needle-like crystals were observed. They appeared organized in radial way and emerging from a seeding crystallization point. The addition of GP did not change the average dimension of the aggregates. However, the progressive increase of the GP concentration, up to 10 ppm, caused a reduction of the size of acicular crystals and aragonite appeared more having a tablet-like structure. Just the minor changes in morphology, but still a disappearance of sharp edges and additional reduction of curving of the faces could be observed.

The results of precipitation kinetics and morphological observations of calcite and aragonite crystals, formed in the presence of soluble fraction of green organic sheets, pointed out to the interactions between dissolved macromolecules and mineral surfaces.[42] However, calcite crystals interact with GP predominantly during the growth stage, while aragonite crystals predominantly during nucleation. Moreover GP seems to alter the morphology of aragonite crystals at larger

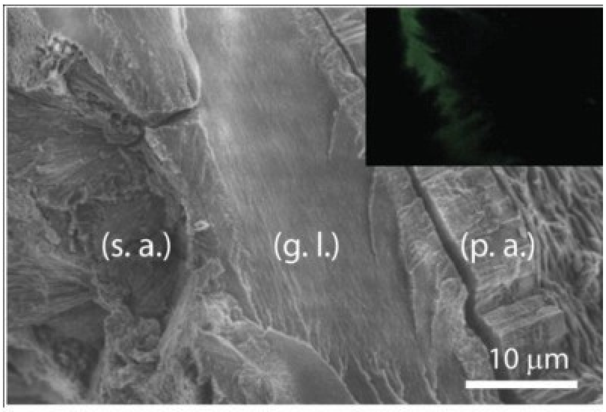

Figure 7. SEM micrographs of a fragment of abalone shell nacre, containing the green sheet. The layers of spherulitic aragonite (s. a.), green layer (g. l.) and prismatic aragonite (p. a.) are indicated. The inset shows a fluorescent image (λ_{ex} = 488 nm) of a similar shell fragment in which a green fluorescence coincide with the green layer.

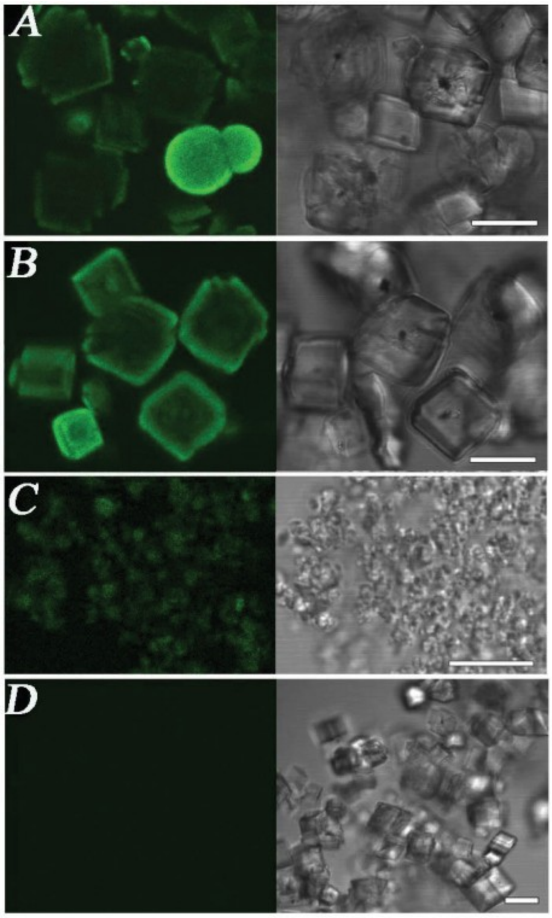

Figure 8. Confocal laser scanning microscopy of calcium carbonate crystals precipitated in: (A) system 2 ($c_i(Ca^{2+}) = c_i(CO_3^{2-}) = 2.0 \times 10^{-2}$ mol dm^{-3}) in the presence of 10 ppm GP, (B) system 1 ($c_i(Ca^{2+}) = c_i(CO_3^{2-}) = 1.0 \times 10^{-2}$ mol dm^{-3}) in the presence of 14 ppm GP, (C) system ASW ($c_i(Ca^{2+}) = 9.3 \times 10^{-3}$ mol dm^{-3}, $c_i(CO_3^{2-}) = 5.0 \times 10^{-3}$ mol dm^{-3}) in the presence of 10 ppm GP and (D) system 1 ($c_i(Ca^{2+}) = c_i(CO_3^{2-}) = 1.0 \times 10^{-2}$ mol dm^{-3}) without GP. Left − the fluorescence images, excitation at λ_{ex} = 488 nm and detection at 500−590 nm; right − the images in the transmitted light. Scale bars: 10 µm (A, B, C) and 20 µm (D).

extent than that of calcite crystals, so the aragonite crystals reduce their growth along the acicular axis and become more plate like. These findings of stronger interactions of GP with aragonite crystals than with calcite is of relevance in understanding the abalone biomineralization. *In vivo* the green organic sheets are actually interspersed through the nacre, thus demarcating the interruption of nacre synthesis and serve as a substrate for nucleation and the resumption of crystal growth. Prismatic and spherulitic aragonite phases precede and follow the deposition of the sheets as could be seen from the SEM micrograph of a section of abalone shell nacre (Figure 7).

In order to detect and observe a possible distribution of GP in the synthetic crystals as well, the confocal laser scanning microscopy was used to analyse the calcite, vaterite and aragonite crystals precipitated in the presence of GP. In agreement with the SEM observations, the rhombohedral calcite crystals and vaterite spherulites are observed in samples of system 2, predominantly calcite in system 1 and aragonite in ASW system. Figure 8. shows that all polymorphs precipitated in the presence of GP exert a green fluorescence after excitation at λ_{ex} = 488 nm. However, both calcite and vaterite, display incorporation of GP predominantly in the surface and the intensity of the GP fluorescence is much stronger in the case of vaterite spherulites (Figure 8A). On the other hand, the calcite crystals formed in the precipitation system 1 (Figure 8B) have a significantly more intense fluorescent layer at their surface than the equivalent crystallites grown under conditions of system 2. Likely explanation for the observed differences in fluorescence intensity is related, not only to different concentrations of GP added to the respective systems, but also to significantly higher specific surface area of vaterite particles, that is, in turn, responsible for preferential adsorption of GP. The aragonite crystallites, precipitated in the ASW system containing 10 ppm GP, are shown in Figure 8c in which weaker flourescence labeling (in comparisson to vaterite and calcite!) could be observed.

The crystals obtained in the appropriate control systems, grown in the absence of GP, show no fluorescent labeling. As an example, Figure 8d shows the precipitate formed in system 1, without the addition of GP.

CONCLUSION

The effects of the interstitial green sheet polypeptide (GP), the protein fragment extracted from the green sheets interdispersed in the nacre of abalone shells, on the spontaneous precipitation of $CaCO_3$ were investigated in three precipitation systems.

It was found that in the model systems, with no GP, different polymorphs of calcium carbonate precipitated. Thus, in system 1, ($c_i(Ca^{2+}) = c_i(CO_3^{2-}) = 1.0 \times 10^{-2}$ mol dm^{-3}) the initial precipitate consisted entirely of calcite, while in system 2, ($c_i(Ca^{2+}) = c_i(CO_3^{2-}) = 2.0 \times 10^{-2}$ mol dm^{-3}) a mixture of vaterite and calcite was formed. In system 3 (ASW, artificial sea water) only aragonite precipitated.

The mineralogical composition of the precipitates, isolated from the systems into which GP was added, showed no significant difference from the respective control systems, regardless the GP concentrations used.

The results also show that GP is able to control the precipitation of calcium carbonate by its adsorption on the crystal surfaces and entrapment into the mineral structure thus modifying their morphology. The adsorption of GP at all three polymorphs, vaterite, calcite and aragonite, was additionally corroborated by the confocal laser scanning microscopy.

Acknowledgements. The financial support from the Ministry of Science, Education and Sports of the Republic of Croatia (project No. 098-0982904-2951) is gratefully acknowledged.

REFERENCES

1. H. A. Lowenstam and S. Weiner, *On Biomineralization*, Oxford University Press, New York, 1989.
2. P. M. Dove, J. J. De Yoreo, and S. Weiner, *Biomineralization*, Mineralogical Society of America, Washington, DC, 2003.
3. S. Weiner, J. Mahamid, Y. Politi, Y. Ma, and L. Addadi, *Front. Mater. Sci. China* **3** (2009) 104−108.
4. S. Mann, *Angew. Chem., Int. Ed*. **39** (2000) 3392−3406.
5. L. Addadi, D. Joester, F. Nudelman, and S. Weiner, *Chem.-Eur. J.* **12** (2006) 981−987.
6. F. C. Meldrum and H. Colfen, *Chem. Rev.* **108** (2008) 4332−4432.
7. F. Nudelman and N. A. J. M. Sommerdijk, *Angew. Chem. Int. Ed.* **51** (2012) 6582−6596.
8. S. Weiner, I. Sagi, and L. Addadi, *Science* **309** (2005) 1027−1028.
9. A. Neira-Carrillo, D. F. Acevedo, M. C. Miras, C. A. Barbero, D. Gebauer, H. Cölfen, and J. L. Arias, *Langmuir* **24** (2008) 12496−12507.
10. D. Gebauer, A. Völkel, and H. Cölfen, *Science* **322** (2008) 1819−1822.
11. E. M. Pouget, P. H. H. Bomans, J. A. C. M. Goos, P. M. Frederik, G. De With, and N. A. J. M. Sommerdijk, *Science* **323** (2009) 1455−1458.
12. I. M. Weiss, N. Tuross, L. Addadi, and S. Weiner, *J. Exp. Zool.* **293** (2002) 478−491.
13. J. C. Marxen, W. Becker, D. Finke, B. Hesse, and M. Epple, *J. Molluscan Stud.* **69** (2003) 113−121.
14. A. Sugawara, T. Nishimura, Y. Yamamoto, H. Inoue, H. Nagasawa, and T. Kato, *Angew. Chem., Int. Ed.* **45** (2006) 2876−2879.
15. Y. Politi, Y. Levi-Kalisman, S. Raz, F. Wilt, L. Addadi, S. Weiner, and I. Sagi, *Adv. Funct. Mater.* **16** (2006) 1289−1298.
16. B. Hasse, H. Ehrenberg, J. C. Marxen, W. Becker, and M. Epple, *Chem. Eur. J.* **6** (2000) 3679−3685.
17. L. Addadi, J. Moradian, E. Shay, N. G. Maroudas, and S. Weiner, *Proc. Natl. Acad. Sci. USA* **84** (1987) 2732−2736.
18. F. Nudelman, B. A. Gotliv, L. Addadi, and S. Weiner, *J. Struct. Biol.* **153** (2006) 176−187.

19. C. Du, G. Falini, S. Fermani, C. Abbott, and J. Moradian-Oldak, *Science* **307** (2005) 1450−1454.
20. J. Erasmus, P. A. Cook, and N. Sweijd, *J. Shellfish Res*. **13**(1994) 493−501.
21. X. Su, A. M. Belcher, C. M. Zaremba, D. E. Morse, G. D.Stucky, and A. H. Heuer, *Chem. Mater.* **14** (2002) 3106−3117.
22. A. M. Belcher, X. H. Wu, R. J. Christensen, P. K. Hansma, G. D.Stucky, and D. E. Morse, *Nature* **381** (1996) 56−58.
23. G. Falini, G. Sator, D. Fabri, P. Vergni, S. Fermani, A. M.Belcher, G. D. Stucky, and D. E. Morse, *J. Struct. Biol.* **173** (2011) 128−137.
24. S. L. Tracy, C. J. P. Francois, and H. M. Jennings, *J. Cryst.Growth* **193** (1993) 374−381.
25. D. Kralj, Lj. Brečević, and A. E. Nielsen, *J. Cryst. Growth* **104**(1990) 793−800.
26. Powder diffraction file, inorganic volume, Table Nos. 01-072-1937 for calcite; 00-005-0453 for aragonite; 01-72-0506, for vaterite, International Centre for Diffraction data, Swarthmore, PA, USA.
27. B. Njegić-Džakula, Lj. Brečević, G. Falini, and D. Kralj, *Cryst.Growth Des.* **9** (2009) 2425−2434.
28. D. Kralj, Lj. Brečević, and A. E. Nielsen, *J. Cryst. Growth* **143** (1994) 269−276.
29. D. Kralj and Lj. Brečević, *Colloids Surf*. **96** (1995) 287−293.
30. D. Kralj, Lj. Brečević, and J. Kontrec, *J. Cryst. Growth* **177** (1997) 248−257.
31. L. N. Plummer and E. Busenberg, *Geochim. Cosmochim. Acta* **46** (1982) 1011−1040.
32. N. Cabrera and D. A. Vermilyea, in: R. H. Doremus, B. W. Rob- erts, and D. Turnbull (Eds.), *Growth and Perfection of Crystals*, Wiley, New York, 1958.
33. Lj. Brečević and D. Kralj, *Croat. Chem. Acta* **80** (2007) 467−484.
34. Lj. Brečević, V. Nöthig-Laslo, D. Kralj, and S. Popović, *J. Chem. Soc., Faraday Trans.* **92** (1996) 1017−1022.
35. B. Njegić-Džakula, G. Falini, Lj. Brečević, Ž. Skoko and D. Kralj, *J. Colloid Interface Sci.* **343** (2010) 553−563.
36. F. Manoli and E. Dalas, *J. Cryst. Growth* **222** (2001) 293−297.
37. F. Manoli, J. Kanakis, P. Malakaj, and E. Dalas, *J. Cryst. Growth* **236** (2002) 363–370.
38. H. Tong, W. T. Ma, L. L. Wang, P. Wan, J. M. Hu, and L. X. Cao, *Biomaterials* **25** (2004) 3923–3929.
39. D. Volkmer, M. Fricke, T. Huber, and N. Sewald, *Chem. Commun.* (2004) 1872−1873.
40. A. J. Xie, Y. H. Shen, C. Y. Zhang, Z. W. Yuan, X. M. Zhu, and Y. M. Yang, *J. Cryst. Growth* **285** (2005) 436−443.
41. H. Cölfen, *Curr. Opin. Colloid Interface Sci.* **8** (2003) 23–31.
42. A. Adamiano, S. Bonacchi, N. Calonghi, D. Fabbri, G. Falini, S. Fermani, D. Genovese, D. Kralj, M. Montalti, B. Njegić-Džakula, L. Prodi, and G. Sartor, *Chem. Eur. J.* **18**(2012),14367−14374.

Nanoscale

RSC Publishing

PAPER

View Journal | View Issue

Cite this: Nanoscale, 2013, 5, 6944

Morphological and mechanical characterization of composite calcite/SWCNT–COOH single crystals†

Matteo Calvaresi,*[a] Giuseppe Falini,*[a] Luca Pasquini,*[b] Michela Reggi,[a]
Simona Fermani,[a] Gian Carlo Gazzadi,[c] Stefano Frabboni[cd] and Francesco Zerbetto*[a]

Received 29th March 2013
Accepted 17th May 2013

DOI: 10.1039/c3nr01568h

www.rsc.org/nanoscale

A growing number of classes of organic (macro)molecular materials have been trapped into inorganic crystalline hosts, such as calcite single crystals, without significantly disrupting their crystalline lattices. Inclusion of an organic phase plays a key role in enhancing the mechanical properties of the crystals, which are believed to share structural features with biogenic minerals. Here we report the synthesis and mechanical characterization of composite calcite/SWCNT–COOH single crystals. Once entrapped into the crystals SWCNT–COOH appeared both as aggregates of entangled bundles and nanoropes. Their observation was possible only after crystal etching, fracture or FIB (focused ion beam) cross-sectioning. SWCNT–COOHs occupied a small volume fraction and were randomly distributed into the host crystal. They did not strongly affect the crystal morphology. However, although the Young's modulus of composite calcite/SWCNT–COOH single crystals was similar to that of pure calcite their hardness increased by about 20%. Thus, SWCNT–COOHs provide an obstacle against the dislocation-mediated propagation of plastic deformation in the crystalline slip systems, in analogy with the well-known hardness increase in fiber-reinforced composites.

1 Introduction

The huge diversity of hierarchical micro-/nano-structures existing in biological systems is increasingly becoming a source of inspiration for materials scientists and engineers to create the next-generation of advanced functional materials.[1,2] Among biological materials, hard tissues, or biominerals, based on calcium carbonate ($CaCO_3$) continue to be one of the most attractive models for artificially structured composites.[3–6] This is because they are stiff and tough at the same time, an uncommon combination of mechanical properties.[7–9] This property allowed them to be the building material of mollusk shells, egg shells and sea urchin spines, among many other calcified tissues.[10,11] These biominerals are actually composite materials in which biological macromolecules are entrapped in the mineral phase. In many cases, they can be described as agglomerations of mineral nano-crystals separated by an inter-crystalline macromolecular matrix.[12,13] They can diffract as single crystals or polycrystalline aggregates depending on the crystallographic alignment of nano-crystals.[14] The sea urchin spine diffracts as a single crystal of calcite and yet fractures as a glassy material.[15] It comprises a highly oriented array of Mg–calcite nanocrystals in which macromolecules are embedded.[16] The nacre is formed by stacked tables of aragonite that are sandwiched between layers of organic material. Each tablet diffracts as a single crystal, but the arrays of tablets do not show crystallographic registration.[17] In these highly organized hierarchical structures different inter-crystalline materials are used to increase strength and toughness.[18,19] Low amounts of amorphous calcium carbonate and/or organic matrix are used to transfer load via the high shear zones among the mineral nanocrystals.[20] Indeed, nacre is ∼3000 times more fracture resistant than pure aragonite, its main component.[21] Recently, biologically inspired synthetic composite calcite/organic (macro)molecule single crystals have been prepared. Sulfonated polystyrene nano-spheres were entrapped into calcite crystals and this improved their elasticity and hardness.[4] Kim et al. reported the synthesis of single crystals of calcite containing a considerable amount of 13 wt% (approximately 30 vol%) of 20 nm anionic diblock copolymer micelles that have structural and mechanical properties analogous to those of natural biominerals.[6]

In the nanocomposite field, an extremely interesting material is represented by carbon nanotubes (CNTs).[22] Their mechanical[23,24] (high strength and toughness) and physicochemical properties[25,26] (high surface area, electrical and

---

[a] Dipartimento di Chimica "G. Ciamician", Alma Mater Studiorum Università di Bologna, Via F. Selmi 2, 40126 Bologna, Italy. E-mail: matteo.calvaresi3@unibo.it; giuseppe.falini@unibo.it; francesco.zerbetto@unibo.it

[b] Dipartimento di Fisica e Astronomia, Alma Mater Studiorum Università di Bologna, Viale Berti-Pichat 6/2, 40127 Bologna, Italy. E-mail: luca.pasquini@unibo.it

[c] CNR-Institute of Nanoscience-S3, Via G. Campi 213/a, Modena 41100, Italy

[d] Dipartimento di Fisica, Università di Modena e Reggio Emilia, Via G. Campi 213/a, Modena 41100, Italy

† Electronic supplementary information (ESI) available. See DOI: 10.1039/c3nr01568h

thermal conductivity, and low weight) make them very attractive fillers to realize new functional nanocomposite materials.[24,26–29] Exploiting their outstanding tensile strength and resilience, CNTs are commonly used to improve the mechanical properties of polymers by developing new polymer/CNT nanocomposites.[24,26–29] CNTs have also been combined with a variety of inorganic compounds to give a new and very promising class of functional materials that combine the multiphase characteristics of nanocomposites with the synergistic functions of hybrid frameworks.[27] It is known that carbon nanomaterials can affect calcium carbonate crystallization[30–37] and that pristine and functionalized CNTs can be adsorbed onto the surface of $CaCO_3$ crystals,[33] or that CNTs can be coated by $CaCO_3$.[31] CNTs can also be incorporated into the $CaCO_3$ matrix.[34] In this scenario, it is reasonable to have high expectations for materials obtained by CNT doping of calcite. Despite the interest in CNT and $CaCO_3$-based composites, materials containing both CNTs and $CaCO_3$ have so far been scarcely reported,[30–34] and their mechanical properties have never been characterized.

2 Experimental

2.1 Materials and preparation of the composite calcite/SWCNT–COOH single crystals

Single wall carbon nanotubes functionalized with carboxylate groups (SWCNT–COOH) were purchased from Cheap Tubes Inc © (USA), and were used as supplied (diameter 1–2 nm; length 0.5–2.0 mm, purity > 90 wt%, COOH content 2.73 wt%). A saturated solution of SWCNT–COOH in 10 mM $CaCl_2$ was prepared by successive steps of stirring, sonication and centrifugation. First in a volume of 5 ml of a 10 mM $CaCl_2$ solution 10 mg of SWCNT–COOH were dispersed by vigorous stirring for 3 hours. After this step the solution was sonicated for 30 min in a bath sonicator using a power of 40 W. Finally the solution was centrifuged at 5000g for 10 minutes. The obtained solution of SWCNT–COOH in 10 mM $CaCl_2$ was stored at 4 °C and successively used for calcium carbonate precipitation experiments. The obtained suspension was stable for days and no precipitation of SWCNT–COOH was observed. $CaCO_3$ crystals were precipitated on glass coverslips placed at the base of a solution of $CaCl_2\$2H_2O$ and SWCNT–COOH through exposure to ammonium carbonate vapor for up to 4 days. The starting and final pH of the crystallizing solution was 5.4 and 8.6, crystals were observed with a scanning electron microscope (FEG Hitachi 6400) using a tension of 15 kV.

FIB (focused ion beam) microsectioning techniques were carried out on a Dual-Beam (FEI Strata DB235M) apparatus combining a Ga-ion FIB and an SEM on the same platform. FIB cross-sections were milled with an ion energy of 30 keV and imaged with the SEM at 15 keV electron energy. EDX (energy dispersive X-ray) analysis was performed at 15 keV electron energy with an EDAX spectrometer. X-ray powder diffraction (XRD) patterns were recorded using a Philips X'Celerator diffractometer with Cu Ka (1.5814 Å) radiation. The samples were scanned for 2q angles between 20° and 60°, with a resolution of 0.02°.

The mechanical properties of single crystals of pure calcite and calcite/SWCNT–COOH were measured using a Nano-indentation Tester, model NHT-TTX by CSM Instruments, equipped with a Berkovich diamond tip, operating in continuous stiffness measurement mode to a maximum applied load of 30 mN. The instrumented (I_T) values of the elastic Young's modulus (E_{IT}) and hardness (H_{IT}) as well as the stiffness S were determined as a function of the indentation depth by Oliver–Pharr dynamic analysis of the loading portion of the curve.[38] The crystals were embedded at room temperature using a fast polymerising cold curing resin based on methyl methacrylate, Technovit 5071 (Buehler), and were then lightly polished using colloid alumina (average size of 1 mm, PACE Technologies) to give a clean, smooth and flat surface for indentation.

3 Results and discussion

In this work we develop an effective procedure for trapping functionalized CNTs into single crystals of calcite. We used single wall carbon nanotubes (SWCNTs) functionalized with COOH groups (SWCNT–COOH) to facilitate the dissolution of CNTs in water. The solubility of SWCNT–COOH is a function of pH, being favored by alkaline conditions.[39] The presence of calcium ions favors SWCNT–COOH aggregation when exposing carboxylate groups. Thus, to compromise these effects the dissolution of SWCNT–COOH was carried out in 10 mM $CaCl_2$ at pH 5.4. At this pH value the carboxylic groups are only partially ionized (pK_a z 4.3). Calcium carbonate single crystals entrapping SWCNT–COOH were precipitated at room temperature by controlled diffusion of CO_2 and NH_3 vapors into the 10 mM $CaCl_2$ solution respectively.

2.2 Characterization and instruments

In the FTIR analysis each powdered sample (approximately 0.1 mg) was mixed with about 10 mg of anhydrous KBr. The mixtures were pressed into 7 mm diameter discs. Pure KBr discs were used as background. The analysis was performed at 2 cm^{-1} resolution using a Nicolet 380 FT-IR spectrometer.

Crystals were initially examined directly in wells by an optical microscope (Leika optical microscope connected to a CCD digital camera). The dried glass coverslips covered with crystals were glued to SEM aluminum stubs. After gold coating, the saturated with SWCNT–COOH. This simple method has the advantage of inducing nucleation and growth of calcite single crystals under conditions of low supersaturation.[40]

Under these conditions the growth of single crystals of calcite, eventually entrapping SWCNT–COOH, is favored. The synthesized composite CNT/CaCO$_3$ crystals were characterized for their mineralogy, morphology and mechanical properties.

The mineralogical composition of the precipitates was analyzed by X-ray powder diffraction (XRD) and Fourier transform infrared spectroscopy (FTIR), Fig. 1. Both techniques revealed that the calcium carbonate precipitated only in the form of calcite, both in the absence and in the presence of SWCNT–COOH.

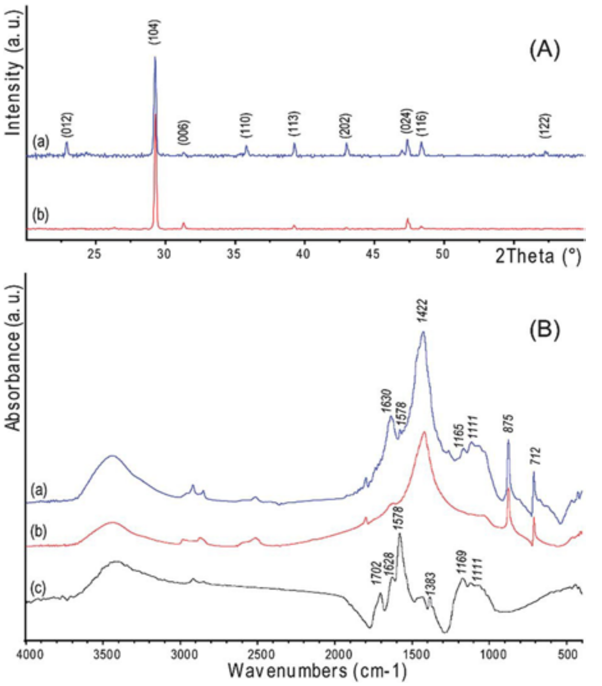

Fig. 1 (A) X-ray powder diffraction patterns of calcium carbonate precipitated in the presence (a) of SWCNT–COOH and in its absence (b). The Miller indices of each diffraction peak are indicated, according to the calcite hexagonal unit cell. (B) FTIR spectra of calcium carbonate precipitated in the presence of SWCNT–COOH (a) and in its absence (b) and of pure SWCNT–COOH (c).

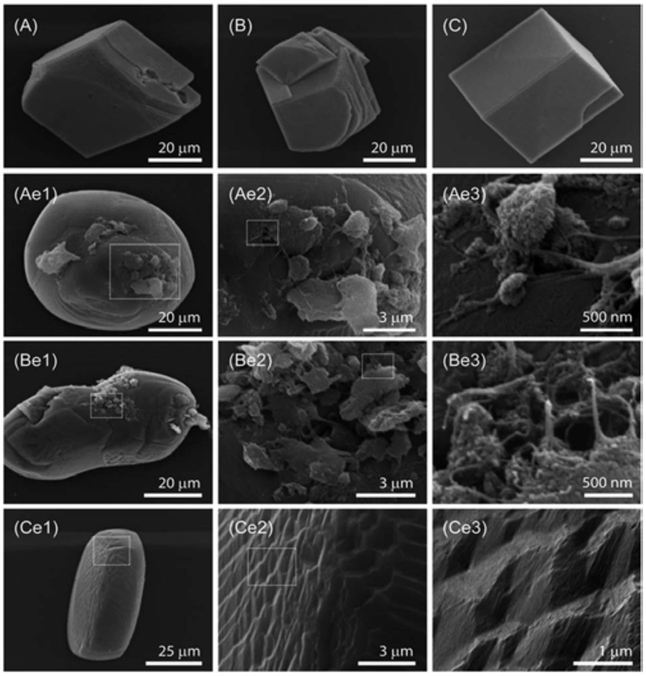

Fig. 2 Scanning electron microscopy pictures. (A) Single crystal and (B) aggregate of calcite/SWCNT–COOH; (C) single crystal of pure calcite. (Ae1-3), (Be1-3) and (Ce1-3) increasing magnifications of a single crystal of calcite/SWCNT–COOH, an aggregate of calcite/SWCNT–COOH and a single crystal of calcite, respectively, observed after treatment with a solution of 0.1 M HCl for 2 minutes. The dotted square indicates the enlarged region. These crystals are representative of the entire sample population.

In the XRD patterns all the peaks observed were assigned to calcite. Moreover, the absence of a broad band between 20º and 40º of 2Q excluded the presence of amorphous phases. In the FTIR spectrum of the calcite/SWCNT–COOH composite strong absorption bands due to calcite at 1420 cm^{-1} (n_3), 875 cm^{-1} (n_2) and 713 cm^{-1} (n_4) were observable together with those due to the SWCNT–COOH, at 1702 cm^{-1}, 1578 cm^{-1}, 1165 cm^{-1} and 1111 cm^{-1}. The latter bands were very weak and did not show any significant shift with respect to those observed in the FTIR spectrum of pure SWCNT–COOH. The sharpness of the peaks in the XRD profile and the n_2/n_4 peak intensity ratio of about 3.4 in the FTIR spectrum of the calcite/SWCNT–COOH composite suggest the presence of a high atomic order in the mineral phase.[41,42] The morphological investigation showed that in the absence of SWCNT–COOH calcite crystals precipitated showing the typical rhombohedral habit (Fig. 2C). In these crystals, having an average size of 50 mm, only {10.4} faces are observable. In the presence of SWCNT–COOH the morphology and shape of calcite crystals were slightly modified.

The crystals appeared as single particles (Fig. 2A) and as particles with irregular intergrown morphologies (Fig. 2B). These crystals showed additional {hk0} faces together with {10.4} ones and thus appeared elongated in the direction of the crystallographic c-axis. This indicates that stabilization of {hk0} crystalline planes is present associated with the presence of SWCNT–COOH (Fig. 1). However, in these crystals the presence of SWCNT–COOH was not directly observable. Only after acidic etching of the crystals the SWCNT–COOHs were clearly observed (Fig. 2Ae1–3 and Be1–3). They appeared as patches, formed by aggregated and entangled bundles of SWCNT–COOH, partially embedded in the surface (Fig. 2Ae1–3 and Be1–

3). In the control experiment, these forms were absent on the surface of etched pure calcite crystals (Fig. 2Ce1–3). The direct visualization of the SWCNT–COOH in the single crystals of calcite was achieved either by SEM imaging on mechanically fractured crystals or by FIB (focused ion beam) microsectioning

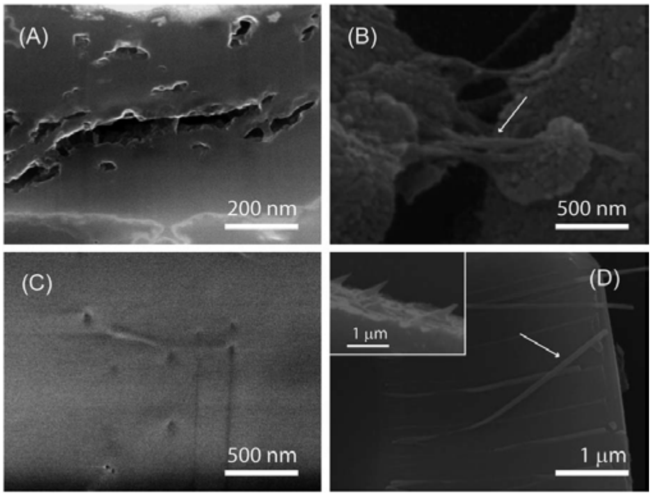

Fig. 3 SEM images of FIB cross-sections of the cavities (A) and holes (C) generated by the partial pulling out of the SWCNT–COOH previously present as entangled bundles and as nanoropes, respectively. (B and D) SEM images of fractured single crystals of calcite showing entangled bundles and nanoropes of SWCNT–COOH, respectively. In the inset in (D) calcified nanoropes emerging from a calcite crystal are shown. The arrows indicate SWCNT–COOH.

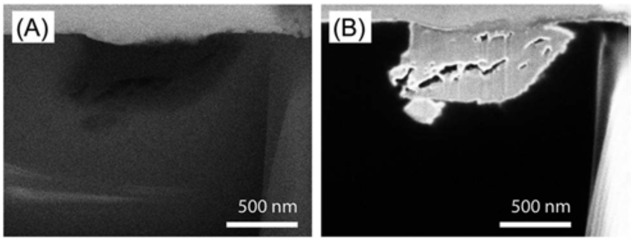

Fig. 4 (A) Backscattered-electron SEM image of the FIB cross-section. (B) Secondary electron FIB image of the same region.

followed by SEM imaging (Fig. 3). The analyses of FIB cross-sections were carried out on polished {10.4} faces of calcite (Fig S1 in the ESI†), the same as those used for the nanoindentation measurements. Both methods of sectioning showed that only a small volume of the crystal was occupied by the SWCNT–COOH. They were observed as aggregates of entangled bundles and nanoropes (Fig. 3 and S2 in the ESI†). In fact, due to attracting van der Waals forces SWCNT–COOHs can entangle themselves forming aggregates (Fig. 3A and B) or they can generate strands of bundles (Fig. 3C and D), called nanoropes, in which the CNTs parallelise.[43] The locations of entangled bundles and nanoropes of SWCNT–COOH in the crystal appeared as partially empty cavities (Fig. 3A) and holes (Fig. 3C), respectively. This is because during the FIB milling process entangled bundles and nanoropes were partially pulled out from the calcitic structure.[44,45] The size and shape of the cavities generated by the entangled bundles are very different, reflecting the diversity of possible aggregation and entanglement processes of SWCNT–COOH bundles. In contrast, the SWCNT–COOH nanoropes generate holes with diameters of about 20 nm. The entangled bundles as well the nanoropes are strictly associated with the mineral phase.

The presence of SWCNT–COOH entangled bundles in the crystal was further confirmed by backscattered-electron SEM imaging (Fig. 4A), where the darker area indicates a lower atomic number material (nanotubes) with respect to the surroundings (calcite), and FIB ion-imaging (Fig. 4B). The latter technique is extremely sensitive to the electrical nature of the material: bright regions indicate a conductive nature (nanotubes) while dark regions indicate an insulating nature (calcite).

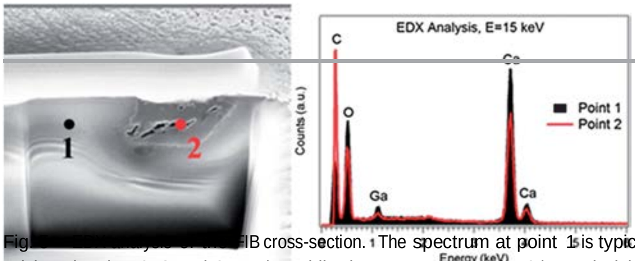

Fig. 5 EDX analysis of the FIB cross-section. The spectrum at point 1 is typical of calcite, showing C, O and Ca peaks, while the spectrum at point 2 is much richer in C (nanotube rich region). Both spectra show a small Ga peak originating from the FIB processing.

averaged over three different crystals of the same type. The uncertainty reported in the table is the standard error

Material	E_{IT} (GPa)	H_{IT} (GPa)	S (mN nm^{-1})
Calcite	56 ± 3	4.00 ± 0.30	0.057 ± 0.002
Calcite/SWCNT–COOH	59 ± 2	4.90 ± 0.15	0.059 ± 0.002

In Fig. 5 the EDX analysis of a FIB cross-section in a region hosting SWCNT–COOH entangled bundles is illustrated. It is possible to observe that elemental analysis showed a higher content of carbon (from the nanotubes) in a point inside the SWCNT–COOH cavity (2) with respect to a point in the external calcite matrix (1).

Having developed a successful protocol for producing calcite/SWCNT–COOH crystals with composite structures, their mechanical properties were measured using nanoindentation, and were compared to control calcite crystals grown in the absence of the SWCNT–COOH. The values of the elastic modulus (E_{IT}), hardness (H_{IT}) and stiffness (S) were determined as a function of the indentation depth by analyzing the load/depth oscillations superimposed to the loading portion of the curve.

From the data reported in Table 1 and Fig. 6, it appears that the two samples exhibit the same value of the modulus E_{IT} and stiffness S within the measurement uncertainty. Since the modulus of SWCNTs is about an order of magnitude higher than that of calcite, this observation is compatible with the presence of only a "modest" volume fraction of SWCNT–COOH in the calcite crystal matrix. Differently, the hardness is increased by about 20% in the calcite/SWCNT–COOH composite with respect to the control calcite sample. We can explain this effect by suggesting that SWCNT–COOH provides an obstacle to the dislocation-mediated propagation of plastic deformation in the crystalline slip systems,[44] in analogy with the well-known hardness increase in fiber-reinforced composites.[45]

SEM images (Fig. 3) suggest possible toughening mechanisms associated with CNT pullout, CNT fracture, CNT bridging and CNT crack deflection, as have been proposed by many authors for similar CNT-based nanocomposites.[46,47] Reinforcement of inorganic crystals with CNTs therefore offers a simple route for generating new, tough, inorganic composite materials.[47] They will open new routes for the application of inorganic crystals, overcoming the actual limits represented as

‡ These are the values obtained on calcite microparticles embedded in the epoxy. The epoxy–calcite interfaces affect the value of E giving values lower than for pure bulk calcite. The reduced modulus with respect to bulk calcite is likely an effect of the matrix, which has a much lower modulus (about 3 GPa). In fact, we observed a decrease of the modulus with increasing indentation depth. The measured hardness values (∼4 GPa) differ from that measured for geologic single crystal calcite Iceland spar (∼3 GPa). Other than the epoxy effect a diversity in purity, crystallographic texture and crystallite size between synthetic and geological calcite crystals could explain this difference. The modulus and hardness data we measured on bulk aragonite, calcite, fused silica, sea urchin spine, nacre, and other reference materials with our instruments using the same protocols are fully consistent with the literature.

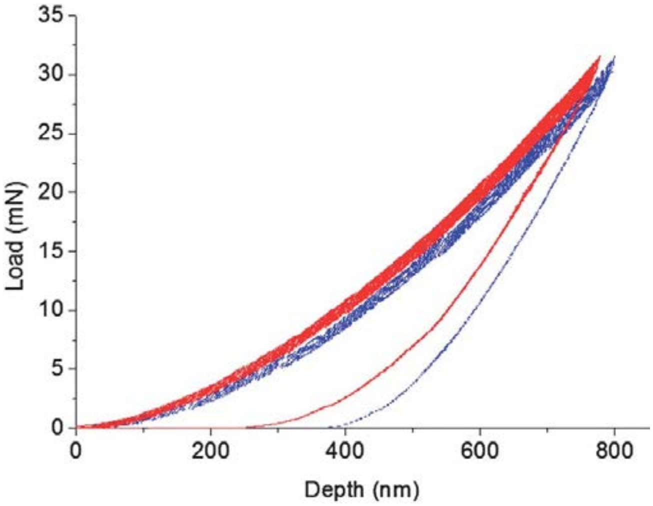

Fig. 6 Load–displacement curves for nanoindentation experiments conducted in continuous stiffness measurement mode on (a) the calcite/SWCNT–COOH composite (red solid curve) and (b) to the calcite control crystal (dashed blue curve).

being stiff but not very tough. CNT nanoropes, well dispersed within the matrix, play a positive role in improving the mechanical properties[48] of the nanocomposites, while macroscopic agglomerates may have a detrimental effect. CNTs exhibit an enormous surface area being several orders of magnitude larger than the surface of conventional fillers. This surface area acts as an interface for stress transfer, but is also responsible for the strong tendency of the CNTs to form agglomerates. The homogeneous dispersion of individual CNTs or small bundle CNTs within a matrix remains a complex hurdle to overcome. New protocols to improve the dispersion state of the CNTs in the crystal and reduce their aggregation will be tested in the future. Further characterization of the calcite/SWCNT–COOH composite is certainly warranted. In particular, it will be interesting to assess the amount of transfer of the electronic properties of CNTs to the new composite and the modification of CNT properties upon confinement.[49,50] Calcium carbonate ($CaCO_3$) has received considerable attention in recent years, not only because of its significance as the main building material of exoskeletons[10,11] but also because it has various applications in industry, such as, for instance, pigment and fillers for rubber, paper, plastics and paints.[51] The calcite/SWCNT–COOH nanocomposite can improve the performance of the common calcium carbonate filler and new applications, deriving from the properties of the CNTs, can be envisioned, for example as antistatic fillers or scaffold materials in tissue engineering.[52] For technological application it is possible to scale up the synthesis of the nanocomposite using "batch precipitation" protocols.[53]

4 Conclusions

This research, which is inspired by studies on natural biominerals, shows that following an easy experimental procedure it is possible to trap SWCNT–COOHs into single crystals of calcite. The combination of these two mechanically and chemically dissimilar materials produces a composite single crystal of calcite with a significant increase of the hardness, even if the content of the SWCNT–COOHs is very low. This result highlights the role of CNTs in improving the mechanical properties also of inorganic crystals.

Notes and references

1 H.-B. Yao, H.-Y. Fang, X.-H. Wang and S.-H. Yu, Chem. Soc. Rev., 2011, 40, 3764–3785.
2 S. Kim and C. B. Park, Adv. Funct. Mater., 2013, 23, 10–25.
3 N. A. J. M. Sommerdijk and G. de With, Chem. Rev., 2008, 108, 4499–4550.
4 Y.-Y. Kim, L. Ribeiro, F. Maillot, O. Ward, S. J. Eichhorn and F. C. Meldrum, Adv. Mater., 2010, 22, 2082–2086.
5 A. S. Schenk, I. Zlotnikov, B. Pokroy, N. Gierlinger, A. Masic, P. Zaslansky, A. N. Fitch, O. Paris, T. H. Metzger, H. Cölfen, P. Fratzl and B. Aichmayer, Adv. Funct. Mater., 2012, 22, 4668–4676.
6 Y. Y. Kim, K. Ganesan, P. Yang, A. N. Kulak, S. Borukhin, S. Pechook, L. Ribeiro, R. Kröger, S. J. Eichhorn, S. P. Armes, B. Pokroy and F. C. Meldrum, Nat. Mater., 2011, 10, 890–896.
7 J. W. Morse, R. S. Arvidson and A. Luttge, Chem. Rev., 2007, 107, 342–381.
8 G. M. Carter, J. L. Henshall and R. J. Wakeman, J. Mater. Sci. Lett., 1993, 12, 407–410.
9 T. Y. Wong and R. C. Bradt, Mater. Chem. Phys., 1992, 30, 261–266.
10 L. Addadi and S. Weiner, Angew. Chem., Int. Ed., 1992, 31, 153–169.
11 G. Falini, S. Albeck, S. Weiner and L. Addadi, Science, 1996, 271, 67–69.
12 S. Weiner and L. Addadi, Annu. Rev. Mater. Res., 2011, 41, 21–40.
13 H. Cölfen and M. Antonietti, Angew. Chem., Int. Ed., 2005, 44, 5576–5591.
14 F. Meldrum and H. Cölfen, Chem. Rev., 2008, 108, 4332–4432.
15 P. O'Neill, Science, 1981, 213, 646–648.
16 J. Seto, Y. Ma, S. A. Davis, F. Meldrum, A. Gourrier, Y.-Y. Kim, U. Schilde, M. Sztuckig, M. Burghammer, S. Maltsev, C. Jäger and H. Cölfen, Proc. Natl. Acad. Sci. U. S. A., 2012, 109, 3699–3704.
17 S. Weiner, Y. Talmon and W. Traub, Int. J. Biol. Macromol., 1983, 5, 325–328.
18 X. Su, S. A. Kamat and H. Heuer, J. Mater. Sci., 2000, 35, 5545–5551.
19 F. Song, A. K. Soh and Y. L. Bai, Biomaterials, 2003, 24, 3623–3631.
20 P. Fratzl and R. Weinkamer, Prog. Mater. Sci., 2007, 52, 1263–1334.
21 J. D. Currey, Proc. R. Soc. London, Ser. B, 1977, 196, 443–463.
22 M. S. Dresselhaus, G. Dresselhaus and P. Avouris, in Carbon Nanotubes: Synthesis, Structure, Properties, and Applications. Topics in Applied Physics, Springer-Verlag, Heidelberg, 2000, vol. 80.

23 A. Peigney, Nat. Mater., 2003, 2, 15–16.
24 X. Zhang, Q. Zeng, H. Dong, D. Zhao, L. Cai, W. Zhou and S. Xie, Nanoscale, 2011, 3, 3731–3736.
25 T. W. Ebbesen, H. J. Lezec, H. Hiura, J. W. Bennett, H. F. Ghaemi and T. Thio, Nature, 1996, 382, 54–56.
26 F. Meng, J. Zhao, Y. Ye, X. Zhang and Q. Li, Nanoscale, 2012, 4, 7464–7468.
27 D. Eder, Chem. Rev., 2010, 110, 1348–1385.
28 S. Desbief, N. Hergué, O. Douhéret, M. Surin, P. Dubois, Y. Geerts, R. Lazzaroni and P. Leclère, Nanoscale, 2012, 4, 2705–2712.
29 J. Foroughi, G. M. Spinks, S. R. Ghorbani, M. E. Kozlov, F. Safaei, G. Peleckis, G. G. Wallace and R. H. Baughman, Nanoscale, 2012, 4, 940–945.
30 R. E. Anderson and A. R. Barron, Main Group Chem., 2005, 4, 279–289.
31 Y. Liu, R. Wang, W. Chen, X. Chen, Z. Hu, X. Cheng and H. J. Xin, Chem. Lett., 2006, 35, 200–201.
32 D. Tasis, S. Pispas, C. Galiotis and N. Bouropoulos, Mater. Lett., 2007, 61, 5044–5046.
33 W. Li and C. Gao, Langmuir, 2007, 23, 4575–4582.
34 W. E. Ford, A. Yasuda and J. M. Wessels, Langmuir, 2008, 24, 3479–3485.
35 M. Calvaresi, G. Falini, S. Bonacchi, D. Genovese, S. Fermani, M. Montalti, L. Prodi and F. Zerbetto, Chem. Commun., 2011, 47, 10662–10664.
36 S. Kim, S. H. Ku, S. Y. Lim, J. H. Kim and C. B. Park, Adv. Mater., 2011, 23, 2009–2014.
37 X. Wang, H. Bai, Y. Jia, L. Zhi, L. Qu, Y. Xu, C. Li and G. Shi, RSC Adv., 2012, 2, 2154–2160.
1583.
39 Y.-T. Shieh, G.-L. Liu, H.-H. Wu and C.-C. Lee, Carbon, 2007, 45, 1880–1890.
40 J. Gomez-Morales, A. Hernandez-Hernandez, G. Sazaki and J. M. Garcia-Ruiz, Cryst. Growth Des., 2010, 10, 963–969.
41 E. Beniash, J. Aizenberg, L. Addadi and S. Weiner, Proc. R. Soc. London, Ser. B, 1997, 264, 461–465.
42 S. Raz, S. Weiner and L. Addadi, Adv. Mater., 2000, 12, 38–42.
43 L. Zejian and L.-C. Qin, Carbon, 2005, 43, 2146–2151.
44 C. Kearney, Z. Zhao, B. J. F. Bruet, R. Radovitzky, M. C. Boyce and C. Ortiz, Phys. Rev. Lett., 2006, 96, 255505.
45 A. G. Evans and F. W. Zok, J. Mater. Sci., 1994, 29, 3857–3896.
46 B. Fiedler, F. H. Gojny, M. H. G. Wichmann, M. C. M. Nolte and K. Schulte, Compos. Sci. Technol., 2006, 66, 3115–3125.
47 J. Cho, F. Inam, M. J. Reece, Z. Chlup, I. Dlouhy, M. S. P. Shaffer and A. R. Boccaccini, J. Mater. Sci., 2011, 46, 4770–4779.
48 X. Liu, W. Lu, O. M. Ayala, L.-P. Wang, A. M. Karlsson, Q. Yang and T. W. Chou, Nanoscale, 2013, 5, 2002–2008.
49 W. Plank, R. Pfeiffer, C. Schaman, H. Kuzmany, M. Calvaresi, F. Zerbetto and J. Meyer, ACS Nano, 2010, 4, 4515–4522.
50 X. Liu, H. Kuzmany, P. Ayala, M. Calvaresi, F. Zerbetto and T. Pichler, Adv. Funct. Mater., 2012, 22, 3202–3208.
51 F. W. Tegethoff, J. W. Rohleder and E. Kroker, Calcium carbonate: from the Cretaceous period into the 21st century, Birkhäuser, 2001.
52 E. Heister, E. W. Brunner, G. R. Dieckmann, I. Jurewicz and A. B. Dalton, ACS Appl. Mater. Interfaces, 2013, 5, 1870–1891.
53 L. Brecevic and D. Kralj, Croat. Chem. Acta, 2007, 80, 467–484.